

NASA/CR—2017-219573



# Development of Experimental Icing Simulation Capability for Full-Scale Swept Wings

## Hybrid Design Process, Years 1 and 2

*Gustavo Fujiwara and Mike Bragg*  
*University of Washington, Seattle, Washington*

*Chris Triphahn, Brock Wiberg, and Brian Woodard*  
*University of Illinois, Urbana, Illinois*

*Eric Loth*  
*University of Virginia, Charlottesville, Virginia*

*Adam Malone and Bernard Paul*  
*Boeing Commercial Airplanes, Mukilteo, Washington*

*David Pitera, Pete Wilcox, and Abdi Khodadoust*  
*Boeing Research & Technology, Huntington Beach, California*

## NASA STI Program . . . in Profile

Since its founding, NASA has been dedicated to the advancement of aeronautics and space science. The NASA Scientific and Technical Information (STI) Program plays a key part in helping NASA maintain this important role.

The NASA STI Program operates under the auspices of the Agency Chief Information Officer. It collects, organizes, provides for archiving, and disseminates NASA's STI. The NASA STI Program provides access to the NASA Technical Report Server—Registered (NTRS Reg) and NASA Technical Report Server—Public (NTRS) thus providing one of the largest collections of aeronautical and space science STI in the world. Results are published in both non-NASA channels and by NASA in the NASA STI Report Series, which includes the following report types:

- TECHNICAL PUBLICATION. Reports of completed research or a major significant phase of research that present the results of NASA programs and include extensive data or theoretical analysis. Includes compilations of significant scientific and technical data and information deemed to be of continuing reference value. NASA counter-part of peer-reviewed formal professional papers, but has less stringent limitations on manuscript length and extent of graphic presentations.
- TECHNICAL MEMORANDUM. Scientific and technical findings that are preliminary or of specialized interest, e.g., “quick-release” reports, working papers, and bibliographies that contain minimal annotation. Does not contain extensive analysis.
- CONTRACTOR REPORT. Scientific and technical findings by NASA-sponsored contractors and grantees.
- CONFERENCE PUBLICATION. Collected papers from scientific and technical conferences, symposia, seminars, or other meetings sponsored or co-sponsored by NASA.
- SPECIAL PUBLICATION. Scientific, technical, or historical information from NASA programs, projects, and missions, often concerned with subjects having substantial public interest.
- TECHNICAL TRANSLATION. English-language translations of foreign scientific and technical material pertinent to NASA's mission.

For more information about the NASA STI program, see the following:

- Access the NASA STI program home page at <http://www.sti.nasa.gov>
- E-mail your question to [help@sti.nasa.gov](mailto:help@sti.nasa.gov)
- Fax your question to the NASA STI Information Desk at 757-864-6500
- Telephone the NASA STI Information Desk at 757-864-9658
- Write to:  
NASA STI Program  
Mail Stop 148  
NASA Langley Research Center  
Hampton, VA 23681-2199



# Development of Experimental Icing Simulation Capability for Full-Scale Swept Wings

## Hybrid Design Process, Years 1 and 2

*Gustavo Fujiwara and Mike Bragg  
University of Washington, Seattle, Washington*

*Chris Triphahn, Brock Wiberg, and Brian Woodard  
University of Illinois, Urbana, Illinois*

*Eric Loth  
University of Virginia, Charlottesville, Virginia*

*Adam Malone and Bernard Paul  
Boeing Commercial Airplanes, Mukilteo, Washington*

*David Pitera, Pete Wilcox, and Abdi Khodadoust  
Boeing Research & Technology, Huntington Beach, California*

Prepared under Cooperative Agreement NNX12AB04A

National Aeronautics and  
Space Administration

Glenn Research Center  
Cleveland, Ohio 44135

## Acknowledgments

The authors would like to thank NASA for providing the funding for this project under NASA Award Number NNX12AB04A.

Trade names and trademarks are used in this report for identification only. Their usage does not constitute an official endorsement, either expressed or implied, by the National Aeronautics and Space Administration.

*Level of Review:* This material has been technically reviewed by expert reviewer(s).

Available from

NASA STI Program  
Mail Stop 148  
NASA Langley Research Center  
Hampton, VA 23681-2199

National Technical Information Service  
5285 Port Royal Road  
Springfield, VA 22161  
703-605-6000

This report is available in electronic form at <http://www.sti.nasa.gov/> and <http://ntrs.nasa.gov/>

## Contents

Executive Summary .....	1
1.0 Introduction.....	3
2.0 Task 1: Selection of Aircraft and Baseline Flight Icing Conditions .....	5
2.1 Task 1.1: Aircraft Wing.....	5
2.2 Task 1.2: Baseline Flight and Icing Conditions.....	6
3.0 Task 2: Baseline Simulations and Wing Section Selection .....	6
3.1 Task 2.1: 3D Reynolds-Averaged Navier–Stokes Calculations for Clean Flight Baseline .....	6
3.2 Task 2.2: LEWICE3D for Iced Flight Baseline.....	8
3.3 Task 2.3: Spanwise Wing Sections Selection for Analysis .....	9
4.0 Task 3: Design and Simulation of 2D Hybrid Airfoils .....	13
4.1 Task 3.1: Integrate 2D Tunnel Effects and Flaps Into 2D Hybrid Design .....	13
4.2 Task 3.2: Perform 2D Scaling Analysis and Develop Tradeoffs.....	15
4.3 Task 3.3: Design 2D Hybrid Airfoil Sections With Trailing-Edge Flaps.....	15
4.4 Task 3.4: Verify Model Design With 2D RANS To Improve Clean Flight Baseline Correlation.....	16
4.5 Task 3.5: Apply LEWICE to Compare Ice Shapes to Iced Flight Baseline .....	19
5.0 Task 4: Design and Simulation of 3D Icing Research Tunnel (IRT) Hybrid Models .....	25
5.1 Task 4.1: Validate and Assess 3D RANS for High Blockage in the IRT.....	25
5.2 Task 4.2: Translate 2D Hybrid Airfoils Into 3D IRT Models .....	26
5.3 Task 4.3: Refine Design and Flap Schedule With 3D RANS Simulations .....	31
5.4 Task 4.4: Apply DES- $k\omega$ to IRT Models to Assess Method and Flow Physics .....	37
5.5 Task 4.5: Apply LEWICE3D to IRT Models and Perform Comparisons .....	37
5.6 Task 4.5: Perform 3D Similitude Studies .....	44
5.7 Task 4.6: Document and Deliver Process and Conceptual Design of Models .....	47
6.0 Summary, Conclusions, and Recommendations.....	48
6.1 Summary and Conclusions .....	48
6.2 Recommendations .....	49
Appendix A.—Nomenclature .....	51
Appendix B.—Numerical Methodology for Aerodynamic Simulations in the Icing Research Tunnel .....	53
B.1 Numerical Inflow Conditions for the Icing Research Tunnel Empty Test Section .....	53
B.2 Validation With a High-Lift Test Article in the Icing Research Tunnel .....	58
Appendix C.—3D Swept Hybrid Wing Design Method for Icing Wind Tunnel Tests .....	65
Appendix D.—Large-Scale Swept-Wing Icing Simulations in the NASA Glenn Icing Research Tunnel Using LEWICE3D.....	83
Appendix E.—Full-Scale and Hybrid Model Airfoil Section Coordinates for Inboard, Midspan, and Outboard Stations.....	101
References.....	111

## List of Tables

Table I.—Task List and Schedule.....	4
Table II.—Common Research Model (CRM) Characteristics Compared With Similar Commercial Aircraft.....	5
Table III.—CRM65 Characteristics Compared With Similar Commercial Aircraft .....	6
Table IV.—Baseline Icing Conditions and Case Identifiers.....	7
Table V.—Inboard, Midspan, and Outboard Full-Scale Normal Airfoils and Respective Hybrid Airfoil Designs.....	16
Table VI.—Streamwise Wrap Distances From Highlight to Attachment Line Locations for Clean Flight Baseline (CFB).....	32

Table VII.—Midspan Model Flow Field and Icing Condition Comparisons of Iced Flight Baseline (IFB) With Icing Research Tunnel (IRT) Simulations for Three Cases .....	37
Table E.1.—CRM65 Full-Scale Wing Station Chord Length .....	101
Table E.2.—Coordinates for 2D Full-Scale Airfoils for Inboard, Midspan, and Outboard Stations .....	101
Table E.3.—Coordinates for Inboard, Midspan and Outboard Hybrid Model Sections With Flaps .....	106
Table E.4.—Flap Pivot Points for Inboard, Midspan, and Outboard Models .....	110

## List of Figures

Figure 1.—Common Research Model (CRM) wing and body (WB).....	5
Figure 2.—OVERFLOW analysis of CRM65 showing pressure coefficient contours $C_p$ where Mach number is 0.37, Reynolds number based on mean aerodynamic chord $(Re)_{mac}$ is 20 million, and angle of attack $\alpha$ is $4.4^\circ$ .....	7
Figure 3.—LEWICE3D ice shape results for CRM65. Droplet median volumetric diameter $(MVD) = 20 \mu\text{m}$ , $V = 232 \text{ kn}$ , alt. = 10,000 ft, liquid water content $(LWC) = 0.55 \text{ g/m}^3$ , static temperature = $-4^\circ\text{C}$ , 45-min exposure (Ref. 1). .....	8
Figure 4.—Icing parameters determined from MATLAB code to analyze LEWICE3D data.....	9
Figure 5.—LEWICE3D data analysis displaying ice thickness on horn (a) and horn angle (b) at selected stations along span (20, 64, and 83 percent) for CRM65 case WB33 $T = -4$ , where $T = -4^\circ$ , $t = 45 \text{ min}$ , Mach number $M = 0.36$ , angle of attack $\alpha = 3.7^\circ$ , liquid water content $LWC = 0.551 \text{ g/m}^3$ , and median volumetric diameter $MVD = \mu\text{m}$ . .....	10
Figure 6.—Three spanwise stations of CRM65 selected for this study. SOB is side of body and $\eta$ is spanwise position. ....	11
Figure 7.—CRM65 and selected three stations (Inboard, Midspan, and Outboard) cut in perpendicular direction (Ref. 11).....	11
Figure 8.—Inboard perpendicular cut extrapolation (Ref. 11). (a) Original and assumed Inboard perpendicular cuts. (b) Extrapolation scheme showing Inboard cut location. ....	12
Figure 9.—CRM65 with Icing Research Tunnel (IRT) test sections at three selected spanwise stations (Ref. 11). (a) Oblique view. (b) Top view. ....	12
Figure 10.—Hybrid airfoil geometric variables (Ref. 11). Here, $c_0$ is full-scale chord, $c_{hyb}$ is hybrid-scale chord, $C_{m0}$ is zero-angle-of-attack pitching moment coefficient, $\alpha$ is angle of attack, and $\gamma$ is nose-droop angle. ....	14
Figure 11.—Integrated hybrid airfoil design workflow (Ref. 11). In step 5, $C_{m0}$ is zero-angle-of-attack pitching moment. ....	15
Figure 12.—Midspan hybrid airfoil design with flap. Here, $c_0$ is full-scale chord, $c_{hyb}$ is hybrid-scale chord, $C_{m0}$ is zero-angle-of-attack pitching moment coefficient, and $\gamma$ is nose-droop angle.....	16
Figure 13.—Two-dimensional (2D) mesh utilized for 2D Reynolds-averaged Navier–Stokes (RANS) simulations.....	17
Figure 14.—Two-dimensional (2D) Reynolds-averaged Navier–Stokes (RANS) bracketing cases for Midspan model (Ref. 11) showing angle of attack $\alpha$ and flap angle $\delta$ . ....	18
Figure 15.—Two-dimensional (2D) aerodynamic calibration for the Midspan model. 2D Reynolds- averaged Navier–Stokes (RANS) wrap distances stretched from normal to streamwise direction and clean flight baseline (CFB) taken in streamwise direction. ....	19
Figure 16.—Midspan LEWICE full-scale and hybrid design results for case WB33 $T = -4$ (from Table IV, extracted from Fujiwara) (Ref. 11). (a) Collection efficiency. (b) Ice shape. ....	20
Figure 17.—Inboard model LEWICE simulations: Case WB33 $T = -4$ (from Table IV) (Ref. 11). IFB is iced flight baseline and FS is full scale. (a) Pressure coefficient distribution. (b) Collection efficiency. (c) Ice shape.....	22

Figure 18.—Midspan model LEWICE simulations: Case WB33 $T = -4$ (from Table IV) (Ref. 11). IFB is iced flight baseline and FS is full scale. (a) Pressure coefficient distribution. (b) Collection efficiency. (c) Ice shape.....	23
Figure 19.—Outboard model LEWICE simulations: Case WB33 $T = -4$ (from Table IV) (Ref. 11). IFB is iced flight baseline and FS is full scale. (a) Pressure coefficient distribution. (b) Collection efficiency. (c) Ice shape.....	24
Figure 20.—Midspan model installation in Icing Research Tunnel (IRT) test section. (a) Test section dimensions drawn to model scale. (b) Computational fluid dynamics (CFD) test section extended upstream and downstream of the Midspan model location. ....	25
Figure 21.—Anisotropic tetrahedral grid elements between trailing edge of main element and leading edge of flap.....	26
Figure 22.—Hybrid wing design method workflow (Refs. 11 and 40). ....	27
Figure 23.—Icing Research Tunnel (IRT) Midspan hybrid wing model. (a) Hybrid airfoil extruded parallel to leading edge, then trimmed at ends. (b) IRT Midspan model compared with full-scale CRM65 geometry (Ref. 11). ....	28
Figure 24.—Inboard hybrid wing model 3D RANS simulation in Icing Research Tunnel (IRT) indicating pressure coefficient $C_p$ where angle of attack $\alpha = 3.67^\circ$ , flap angle $\delta = 6^\circ$ , and Reynolds number $Re = 3.45 \times 10^7$ .....	29
Figure 25.—Lifting-line theory representation of swept-wing model bounded by sidewalls.....	30
Figure 26.—Inboard hybrid wing model 3D RANS simulation in the Icing Research Tunnel (IRT) indicating pressure coefficient $C_p$ and attachment line location at angle of attack $\alpha = 3.67^\circ$ and flap angle $\delta = 6^\circ$ . ....	30
Figure 27.—Outboard model 3D aerodynamic calibration plot with 2D and 3D data in streamwise direction. ....	33
Figure 28.—Midspan model 3D aerodynamic calibration plot. 2D and 3D data in streamwise direction. ....	33
Figure 29.—Inboard model 3D aerodynamic calibration plot. 3D data in streamwise direction. ....	34
Figure 30.—Outboard hybrid wing model 3D RANS simulation in Icing Research Tunnel (IRT) indicating pressure coefficient $C_p$ where angle of attack $\alpha = 3.67^\circ$ , flap angle $\delta = 13^\circ$ , and Reynolds number $Re = 1.59 \times 10^7$ .....	35
Figure 31.—Midspan hybrid wing model 3D RANS simulation in IRT indicating pressure coefficient $C_p$ where angle of attack $\alpha = 3.67^\circ$ , flap angle $\delta = 15^\circ$ , and Reynolds number $Re = 1.60 \times 10^7$ . ....	35
Figure 32.—Pressure coefficient $C_p$ streamwise cuts at $Y = -6, 0, +6$ in. for (a) Outboard, (b) Midspan, and (c) Inboard models compared with streamwise cuts from CRM65 for case WB33.....	36
Figure 33.—Inboard model LEWICE3D simulations, case WB33 $T = -4$ where angle of attack $\alpha$ is $3.67^\circ$ and flap angle $\delta$ is $6^\circ$ . (a) IRT (Icing Research Tunnel) ice shapes. (b) IRT ice shape compared with iced flight baseline (IFB). (c) IRT collection efficiency compared with IFB. ....	39
Figure 34.—Midspan model LEWICE3D simulations, case WB33 $T = -4$ where angle of attack $\alpha$ is $3.67^\circ$ and flap angle $\delta$ is $15^\circ$ . (a) IRT (Icing Research Tunnel) ice shapes. (b) IRT ice shape compared with iced flight baseline (IFB). (c) IRT collection efficiency compared with IFB. ....	40
Figure 35.—Outboard model LEWICE3D simulations, case WB33 $T = -4$ where angle of attack $\alpha$ is $3.67^\circ$ and flap angle $\delta$ is $11^\circ$ . (a) IRT (Icing Research Tunnel) ice shapes. (b) IRT ice shape compared with iced flight baseline (IFB). (c) IRT collection efficiency compared with IFB. ....	41
Figure 36.—Midspan model ice shapes for case WB33 $T = -4$ where angle of attack $\alpha$ is $3.67^\circ$ and flap angle $\delta$ is $15^\circ$ at Icing Research Tunnel (IRT) pressures and iced flight baseline (IFB) at pressure altitude. ....	42
Figure 37.—Midspan model ice shapes for case WB47 $T = -6$ where angle of attack $\alpha$ is $4.36^\circ$ and flap angle $\delta$ is $16^\circ$ at Icing Research Tunnel (IRT) pressures and iced flight baseline (IFB) at pressure altitude. ....	42

Figure 38.—Midspan model ice shapes for case WB71 $T = -6$ where angle of attack $\alpha$ is $4.40^\circ$ and flap angle $\delta$ is $15^\circ$ at Icing Research Tunnel (IRT) pressures and iced flight baseline (IFB) at pressure altitude. ....	42
Figure 39.—Midspan model comparison of (a) local collection efficiency $\beta$ and (b) convective heat transfer coefficient $h_c$ for case WB33 $T = -4$ in Icing Research Tunnel (IRT) at IRT (local) and iced flight baseline (IFB) (altitude) pressures.....	43
Figure 40.—Effect of attachment line location on centerline ice shape of Midspan model compared with iced flight baseline (IFB) (condition WB33 $T = -4$ ). (a) Different flap angles $\delta$ where angle of attack $\alpha = 3.67^\circ$ . (b) Different angles of attack $\alpha$ where flap angle $\delta = 5.0^\circ$ .....	44
Figure 41.—Pressure coefficient $C_p$ contour for case WB47 $T = -6$ at angle of attack $\alpha = 4.36^\circ$ and flap angle $\delta = 16^\circ$ .....	45
Figure 42.—Midspan model spanwise attachment location for case WB47 $T = -6$ at angle of attack $\alpha = 4.36^\circ$ and flap angle $\delta = 16^\circ$ .....	45
Figure 43.—Comparison of Midspan model scaled and unscaled ice shapes for case WB47 $T = -6$ in Icing Research Tunnel (IRT).....	46
Figure 44.—Comparison of $\beta$ and $h_c$ for case WB47 $T = -6$ in Icing Research Tunnel (IRT) for scaled and unscaled icing conditions. (a) Local collection efficiency, $\beta$ . (b) Heat transfer coefficient, $h_c$ . ..	46
Figure B.1.—Top view of Icing Research Tunnel (IRT). ....	53
Figure B.2.—Icing Research Tunnel (IRT) description and computational boundary conditions. (a) Heat exchanger (HX) showing six sets of HX tubes. (b) Velocity field (ft/sec) for one HX tube set. (c) Velocity field (ft/sec) at HX exit, assuming all six tube sets have same outflow. ....	54
Figure B.3.—Icing Research Tunnel (IRT) corner D computational mesh. (a) Overview of corner D mesh. (b) IRT corner D turning vanes mesh.....	55
Figure B.4.—Side view of Icing Research Tunnel (IRT) full contraction computational mesh. ....	55
Figure B.5.—Comparison of computational meshes used in Icing Research Tunnel (IRT) simulations. (a) Full contraction. (b) Truncated contraction. ....	56
Figure B.6.—Full Icing Research Tunnel (IRT) simulation domain showing upstream (contraction region) cut and downstream (test section) cut. ....	56
Figure B.7.—Turbulent kinetic energy (TKE) ( $m^2/sec^2$ ) comparison at upstream and downstream Icing Research Tunnel (IRT) cuts. (a) Upstream cut from full contraction domain. (b) Downstream cut from full contraction. (c) Downstream cut from truncated contraction. ....	57
Figure B.8.—McDonnell Douglas Aerospace multi-element airfoil (MEA). (a) Two-dimensional cross-section geometry. (b) Test model installed in the Icing Research Tunnel (IRT). ....	58
Figure B.9.—Computational mesh for the multi-element airfoil (MEA) at angle of attack $\alpha = 0^\circ$ . (a) Complete computational mesh with model in Icing Research Tunnel (IRT) test section. (b) 2D mesh around model. (c) Detailed view of T-Rex unstructured cells.....	59
Figure B.10.—Comparison of 2D multi-element airfoil (MEA) in Icing Research Tunnel (IRT) computational meshes. (a) Surface resolution for 2D – BL mesh. (b) Surface resolution for 2D – $2 \times AS$ mesh.....	60
Figure B.11.—Three-dimensional multi-element airfoil (MEA) in Icing Research Tunnel (IRT) computational mesh. (a) Top view. (b) Isometric view.....	61
Figure B.12.—Mach (M) contours at centerline cut of 3D – BL simulation.....	62
Figure B.13.—Two-dimensional (2D) and three-dimensional (3D) grid resolution study for multi-element airfoil (MEA) in Icing Research Tunnel (IRT). (a) Pressure coefficient $C_p$ on MEA slat. (b) $C_p$ on MEA main element. (c) $C_p$ on MEA flap.....	63
Figure B.14.—Two-dimensional (2D) and three-dimensional (3D) comparison of simulations to experimental data for multi-element airfoil (MEA) in Icing Research Tunnel (IRT). (a) Pressure coefficient $C_p$ on MEA slat. (b) $C_p$ on MEA main element. (c) $C_p$ on MEA flap.....	64



# **Development of Experimental Icing Simulation Capability for Full-Scale Swept Wings Hybrid Design Process, Years 1 and 2**

Gustavo Fujiwara and Mike Bragg  
University of Washington  
Seattle, Washington 98195

Chris Triphahn, Brock Wiberg, and Brian Woodard  
University of Illinois  
Urbana, Illinois 61801

Eric Loth  
University of Virginia  
Charlottesville, Virginia 22903

Adam Malone and Bernard Paul  
Boeing Commercial Airplanes  
Mukilteo, Washington 98275

David Pitera, Pete Wilcox, and Abdi Khodadoust  
Boeing Research & Technology  
Huntington Beach, California 92647

## **Executive Summary**

This report presents key results from the first 2 years of a program to develop experimental icing simulation capabilities for full-scale swept wings. This investigation was undertaken as part of a larger collaborative research effort on ice accretion and aerodynamics for large-scale swept wings. Ice accretion and the resulting aerodynamic effect on large-scale swept wings presents a significant airplane design and certification challenge to airframe manufacturers, certification authorities, and research organizations alike. While the effect of ice accretion on straight wings has been studied in detail for many years, the available data on swept-wing icing are much more limited, especially for larger scales.

The primary goal of the program involved developing a process for designing icing wind tunnel models that generate representative, full-scale ice accretion on a large swept wing. These full-scale swept wings cannot be tested directly in icing wind tunnels due to physical size limitations, so this program presents a method for acquiring full-scale ice shapes using truncated wing models representing sections of a full-scale wing. The research objectives included selecting a wing geometry and icing conditions that fit with both NASA and Federal Aviation Administration (FAA) program goals and industry interest, developing and documenting the model design and testing methodology for icing wind tunnel models based on the selected wing geometry, and completing computer simulations of the models in the Icing Research Tunnel (IRT) at NASA Glenn Research Center.

A swept-wing aircraft geometry representative of modern commercial transport aircraft was required for the entire swept-wing icing program. Options were considered, and the Common Research Model (CRM) geometry was selected. Boeing provided the CRM design for a joint experimental effort with

NASA, and the geometry has been studied extensively in the American Institute of Aeronautics and Astronautics (AIAA) Drag Prediction Workshops along with various wind tunnel tests. Additionally, the geometry is publicly available and unrestricted for worldwide distribution. However, the CRM represents a large transport aircraft similar in size to a Boeing 777. That wing size presented several technical challenges for ice-accretion studies, so the baseline model for this work is a 65 percent scale version of the CRM, or the CRM65, which is similar in size to a Boeing 757. Next, the baseline icing conditions were selected based on industry perspective and the FAA's icing certification requirements. A large matrix of generic icing mission scenarios was reviewed, and a subset of icing conditions was selected by the team. Computational fluid dynamics (CFD) and icing simulations were generated for those conditions using the CRM65 geometry. The icing simulation tool LEWICE3D requires CFD-generated flow fields, which were created using the CFD code OVERFLOW. These simulations set the standard, or baseline, for all the subsequent work described in this report and are referred to as the "clean flight baseline" (CFB) and "iced flight baseline" (IFB).

Next, the segments or sections of the CRM65 that would be tested in the IRT had to be selected. The ice shapes from the IFB simulations were analyzed to investigate ice thickness and ice-shape horn angle across the span of the wing. With those results and some considerations regarding actual aircraft operations, three stations were selected that could create ice shapes representative of the entire wing. Although not directly a part of this project, NASA planned to build (and has subsequently built and tested) models based on these designs, so minimizing the number of models required to adequately describe the full-span ice shape was an important consideration. These three locations, referred to as "Inboard," "Midspan," and "Outboard," are located at approximately 20, 64, and 83 percent of the span measured from the centerline of the aircraft.

Even segments of the CRM65 are far too large to be tested directly in the IRT. The size of the wing sections had to be reduced to fit in the IRT, but complete geometric scaling was not desirable for this swept-wing icing testing. Icing scaling methods are not sufficiently validated for swept wings, so the leading edge of the wing where ice accretes needed to retain its original size. However, the trailing edge of the model could be truncated subject to aerodynamic constraints. This design process had been utilized in the past for creating truncated or hybrid airfoil models, but significant effort was required to expand this technique to swept wings. The location of the attachment line (the three-dimensional (3D) equivalent of the stagnation point) was shown to be a primary driver of the ice accretion, so the hybrid models were designed to match the attachment line location based on the aerodynamic simulations from the CFB. Throughout the model design process, numerous two-dimensional (2D) and 3D CFD simulations were performed to ensure that the hybrid models would perform in the icing tunnel in such a way that they were representative of the CRM65 wing in free-air flight. Additionally, LEWICE and LEWICE3D simulations were performed in order to compare predicted IRT ice shapes with the IFB. The primary tradeoffs identified during the hybrid model design process involved balancing IRT turntable load limits and blockage considerations (upper limit on size) with the risk of flow separation on the upper surface of the model as it transitions from the full-scale leading edge to the truncated trailing edge (lower limit on size).

The general swept-wing hybrid design methodology was verified using the simulation tools described, and the designs for these three specific models were delivered to NASA for use in construction of the actual icing wind tunnel models. A significant lesson learned throughout this process is that the substantial time spent using 2D CFD simulations to verify the hybrid wing designs might not have been the best use of resources. The usefulness of those simulations was shown to be marginal after 3D CFD simulations were performed. In the future, a direct-to-3D methodology might prove more efficient for designing similar hybrid swept-wing models.

## 1.0 Introduction

Three-dimensional (3D) computational and experimental icing simulation tools are becoming increasingly common in icing analysis for modern transport airplanes. However, validation data are very limited, particularly for large-scale swept wings that are typical of modern commercial airplanes. Thus it is difficult to determine how much confidence can be placed in results from computational fluid dynamics (CFD) codes used in design, and particularly in certification. Furthermore, an understanding of the icing effects on swept-wing aerodynamics is critical to evaluating the accuracy to which ice accretion must be predicted by computational tools or simulated in aerodynamic testing to quantify the aircraft performance degradation due to ice accretion. In addition, basic swept-wing aerodynamic effects such as the spanwise flow and configuration dependence play an important role. An understanding of these effects as well as scale effects, including Reynolds and Mach numbers, is needed in order to develop lower-cost aerodynamic test techniques for iced swept wings and validate CFD simulation tools used to predict the aerodynamics of iced wing configurations. All of these factors have provided motivation for collaborative research efforts in this arena involving the authors of this report as well as the Federal Aviation Administration (FAA) and Office National d'Etudes et de Recherches Aérospatiales (ONERA). This overall research effort is described in detail by Broeren et al. (Ref. 1).

Significant research has been performed by other investigators in the area of swept-wing icing, but the studies have primarily been at low Reynolds number for relatively simple ice geometries. Little ice accretion geometry information for large-scale swept wings of modern design exists in the public domain. High-Reynolds-number aerodynamic data from swept wings with ice accretions is also not available in the public domain and is an objective of the overall research program.

The goal of the work conducted under this cooperative agreement is to provide a design method for swept-wing icing wind tunnel models that can be used to produce full-scale ice accretion for wings that are representative of modern commercial transport aircraft. A database of ice-accretion geometry will then be used for icing simulation tool development and validation. The ice-accretion geometry will also be used to generate artificial ice shapes for use in aerodynamic tests.

Icing wind tunnels are not of sufficient size to accommodate a full-scale aircraft wing, and ice accretion scaling is not sufficiently developed for the testing of small-scale 3D models. Thus an alternative method is to use hybrid or truncated models, which retain the full-scale leading-edge geometry (and full-scale leading-edge flow field) while significantly reducing the chord length and usually the maximum thickness of the model. This method was developed in the 1990s, but its application is limited to straight wings of moderate size. A hybrid model design for large swept wings requires further understanding and extension of this method such that hybrid swept-wing models can be built for various spanwise stations with full-scale leading edges and reduced chord length to reduce the model size and wind tunnel blockage (Refs. 2, 3, and 4). The extended hybrid or truncated design method is then applied to specific spanwise segments or stations of the full-scale wing, which are selected to test in the icing tunnel based upon the desired objectives. For this research, three spanwise stations of a full-scale wing were selected as cases for the hybrid model design with the goal of developing a full-span ice shape on the entire wing leading edge. Ice-accretion geometries at these three spanwise stations can be interpolated and/or extrapolated into a full-span ice shape that could be used for aerodynamic testing.

The sections of this report are arranged following the project tasks as given in Table I. The aircraft wing selection, icing conditions, and baseline simulations (both flow field and icing) are discussed, as is the selection of the three spanwise stations of the wing. The design process leading to the final two-dimensional (2D) and 3D model designs is explained in detail. Acronyms and symbols used in the text are listed in Appendix A. Appendix B to Appendix E provide additional information on topics relevant to this work that

were not specifically part of the defined task list and design process. Appendix B describes the work performed to validate the application of the commercial CFD code Fluent to the models and wind tunnels described in this work. Further details of swept wings in wind tunnels are explored in Appendix C, including the effects of the wind tunnel sidewalls, model sweep angle, model aspect ratio, and wind tunnel blockage. Additionally, several spanwise load control techniques are discussed. In Appendix D, the effects of several model design parameters on the ice shapes are investigated. Appendix E includes airfoil coordinates for both the main element and the flap for each of the three hybrid models.

Task 4.4 was intentionally postponed to year 3 of the project to allow the team to provide additional support to model design and construction within the first 2 years. This work will be described in the final report.

TABLE I.—TASK LIST AND SCHEDULE<sup>a</sup>

Task	Description	Calendar year 2012				Calendar year 2013			
		Quarter				Quarter			
		1	2	3	4	1	2	3	4
1	Aircraft and conditions selection	1							
1.1	Choose aircraft wing	x---x							
1.2	Choose baseline flight and icing conditions	x---x							
2	Baseline icing simulations and selection of sections	2							
2.1	Three-dimensional (3D) Reynolds-averaged Navier–Stokes (RANS) for clean baseline flow	x---	---x						
2.2	LEWICE3D for baseline ice shapes		x---x						
2.3	Choose three spanwise sections			x---x					
3	Design and simulation in two-dimensional (2D) tunnel	3							
3.1	Integrate 2D tunnel effects and flaps into 2D hybrid design method	x---	---x						
3.2	Perform scaling analysis and develop tradeoffs					x---	---x		
3.3	Design 2D truncated sections and segmented trailing-edge flaps			x---	---	---x			
3.4	Verify model design with 2D RANS to improve clean flight baseline (CFB) correlation				x---	---x			
3.5	Apply LEWICE2D to compare ice shapes to iced flight baseline (IFB)				x---	---x			
4	Design and simulation in 3D tunnel	4							
4.1	Validate and assess 3D RANS- $k\omega$ for high blockage in Icing Research Tunnel (IRT)			x---	---	---	---x		
4.2	Translate above 2D truncated airfoil sections into a 3D IRT models				x---	---	---x		
4.3	Refine design and flap schedule with 3D RANS- $k\omega$					x---	---	--x	
4.4	Apply DES- $k\omega$ to IRT models to assess method and flow physics						x---	---x	
4.5	Apply LEWICE3D to IRT models and compare; perform 3D similitude studies						x---	--x	
4.6	Document and deliver process and conceptual design of models						x---	---x	

<sup>a</sup>Green shading indicates task is complete. Gray shading indicates task was moved to year 3.

## 2.0 Task 1: Selection of Aircraft and Baseline Flight Icing Conditions

This section describes the selection of a swept-wing geometry and baseline icing conditions for the study.

### 2.1 Task 1.1: Aircraft Wing

The first step in the process of studying swept-wing icing was to select a swept-wing geometry to use for the studies. The two main requirements were that it had to be a publicly available geometry without any restrictions on usage or distribution, and it had to represent a modern large transport class aircraft. The Common Research Model (CRM) was identified as meeting these requirements and was selected for this work. The CRM is a commercial transport class configuration with a contemporary transonic supercritical wing design. Table II presents basic characteristics of the CRM as compared with other commercial aircraft; details of the design can be found in Vassberg (Ref. 5). The CRM has also been used for the AIAA Drag Prediction Workshop, and aerodynamic testing has been performed in various wind tunnels with different model configurations (Refs. 6 to 9). As Figure 1 shows, only the CRM fuselage and wing were considered in this work.

TABLE II.—COMMON RESEARCH MODEL (CRM) CHARACTERISTICS  
COMPARED WITH SIMILAR COMMERCIAL AIRCRAFT<sup>a</sup>  
[From Ref. 1]

Airplane	Span, ft	Mean aerodynamic chord, ft	Area, ft <sup>2</sup>	Aspect ratio	Taper ratio	Sweep, c/4, deg
CRM	192.8	23.0	4,130	9.0	0.28	35
Airbus A330–200/300	198.0	23.9	3,892	9.5	0.22	30
Boeing 777–200	199.9	26.5	4,389	8.7	0.27	31
Boeing 787–9	197.0	20.6	3,880	9.6	0.18	32
Boeing 747–400	211.4	29.8	5,417	7.7	0.28	37

<sup>a</sup>Data for existing wide-body airplanes were compiled from publicly available sources that may use different conventions to define the geometric parameters.

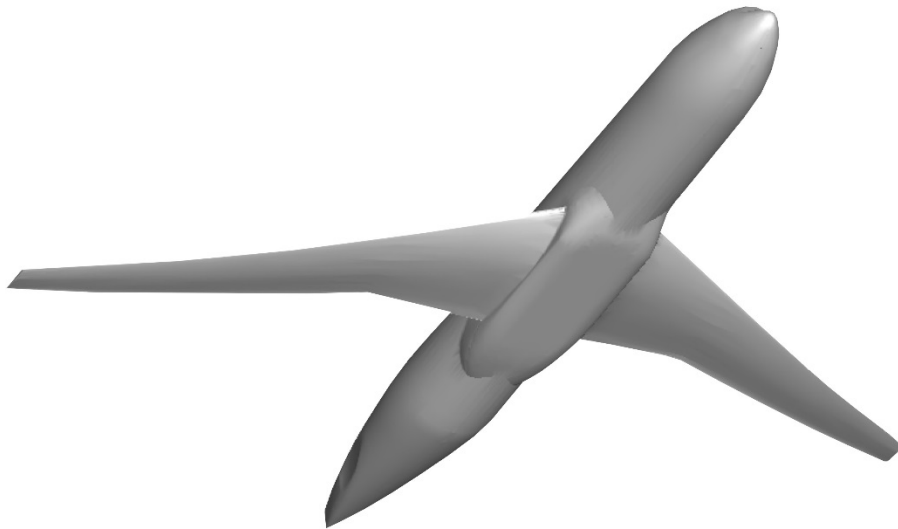


Figure 1.—Common Research Model (CRM) wing and body (WB).

TABLE III.—CRM65 CHARACTERISTICS COMPARED WITH SIMILAR COMMERCIAL AIRCRAFT<sup>a</sup>  
[From Ref. 1]

Airplane	Span, ft	Mean aerodynamic chord, ft	Area, ft <sup>2</sup>	Aspect ratio	Taper ratio	Sweep, c/4, deg
CRM65	125.3	15.0	1,745	9.0	0.28	35
Airbus A320	112.0	14.1	1,320	9.5	0.22	25
Boeing 737–800	112.6	13.0	1,341	8.7	0.27	25
Boeing 757–200	124.8	16.7	1,847	9.6	0.18	25

<sup>a</sup>Data for existing single-aisle airplanes were compiled from publicly available sources that may use different conventions to define the geometric parameters.

Early on in this research, it was determined that even the hybrid model of the CRM would be too large to fit in the Icing Research Tunnel (IRT) and that reference size would need to be reduced. However, it could not be reduced so much that important ice characteristics that depend on having a large leading edge are no longer accurately captured. To address these two sizing constraints, a 65 percent scale version of the CRM was selected to serve as the full-scale reference swept-wing geometry. Throughout the rest of this document, “full-scale wing” will refer to the 65 percent scale CRM wing (CRM65). Table III shows that this version of the model is still representative of modern commercial aircraft. Note how the CRM65 is similar in size to a B757–200 but the wing sweep is still comparable to the wide-body airplanes.

## 2.2 Task 1.2: Baseline Flight and Icing Conditions

A substantial set of realistic icing mission scenarios were identified for the certification of a typical large transport aircraft based upon the U.S. Code of Federal Regulations (CFR) Title 14, Part 25, Appendix C, Continuous Maximum Icing (Ref. 10). After reviewing those conditions, a subset of the scenarios was determined to be adequate for determining the ice shapes of interest and was chosen for the baseline icing conditions. Table IV shows a summary of the baseline icing conditions (Ref. 11). The case identifier comes from the CFD calculations indicating that only the wing and body (WB) of the CRM65 were included in the analysis. There are six main aerodynamic conditions, identified by WB and the corresponding case number, for which a few different temperatures were identified for analysis for each case. Throughout this document, cases are identified with the case number and a temperature (in °C) to indicate the icing conditions.

## 3.0 Task 2: Baseline Simulations and Wing Section Selection

This section describes the study’s CFD simulations, the use of LEWICE3D to determine the IFB, and the selection of the wing segments to be analyzed.

### 3.1 Task 2.1: 3D Reynolds-Averaged Navier–Stokes Calculations for Clean Flight Baseline

After determining the baseline icing conditions, CFD simulations were performed on the CRM65 using each of the six sets of aerodynamic conditions. The 3D Reynolds-averaged Navier–Stokes (RANS) code OVERFLOW (Ref. 6) was utilized for the analysis. This tool has been validated (Ref. 6) within Boeing on a wide variety of configurations, including past analysis of the CRM (Refs. 6 to 9). The calculations were performed only on the wing and body of the CRM65. An example of the OVERFLOW analysis on the CRM65 is shown in Figure 2. The calculations for the six different aerodynamic conditions of Table IV are referred to as the “clean flight baseline” (CFB). These six flow field solutions from OVERFLOW were then used to guide the hybrid design. At each of the selected spanwise stations, the hybrid design process was performed with the goal of matching flow field characteristics from the OVERFLOW simulations on the CRM65. This process will be discussed in further detail in Tasks 3 and 4.

TABLE IV.—BASELINE ICING CONDITIONS AND CASE IDENTIFIERS

[Adapted from Ref. 11]

[Median volumetric diameter for each condition was 20  $\mu\text{m}$ .]

[Langmuir D droplet distribution was used for subsequent computational simulations.]

Condition	Phase <sup>a</sup>	Weight <sup>b</sup>	Flaps	Altitude, ft	Static ambient pressure, $P_{amb}$ , kPa	Static ambient temp., $T_{amb}$ , °C	Mach number, M	True airspeed, kn	Angle of attack, $\alpha$ , deg	Liquid water content, $\text{g/m}^3$	$\Delta t$ , min
WB25 $T = -40$	Climb	Nominal	Up	30,000	30.124	-40	0.81	484.5	1.68	0.200	0.32
WB33 $T = -4$	Hold	LGW	Up	10,000	69.702	-4	0.36	232.1	3.67	0.551	45
WB33 $T = -6$	Hold	LGW	Up	10,000	69.702	-6	0.36	231.2	3.67	0.509	45
WB33 $T = -13$	Hold	LGW	Up	10,000	69.702	-13	0.36	228.2	3.67	0.361	45
WB33 $T = -25$	Hold	LGW	Up	10,000	69.702	-25	0.36	222.9	3.67	0.175	45
WB39 $T = -20$	Hold	LGW	Up	22,000	42.824	-20	0.46	284.5	3.64	0.210	45
WB39 $T = -25$	Hold	LGW	Up	22,000	42.824	-25	0.46	281.7	3.64	0.175	45
WB39 $T = -30$	Hold	LGW	Up	22,000	42.824	-30	0.46	278.8	3.64	0.140	45
WB41 $T = -6$	Hold	HGW	Up	5,000	84.319	-6	0.35	225.1	4.38	0.509	45
WB41 $T = -13$	Hold	HGW	Up	5,000	84.319	-13	0.35	222.1	4.38	0.361	45
WB41 $T = -25$	Hold	HGW	Up	5,000	84.319	-25	0.35	216.9	4.38	0.175	45
WB47 $T = -6$	Hold	HGW	Up	15,000	57.209	-6	0.43	271.4	4.36	0.509	45
WB47 $T = -13$	Hold	HGW	Up	15,000	57.209	-13	0.43	267.8	4.36	0.361	45
WB47 $T = -25$	Hold	HGW	Up	15,000	57.209	-25	0.43	261.5	4.36	0.175	45
WB71 $T = -6$	ETOPS Hold	Nominal	---	1,500	95.956	-6	0.32	203.2	4.40	0.509	15
WB71 $T = -13$	ETOPS Hold	Nominal	---	1,500	95.956	-13	0.32	200.5	4.40	0.361	15
WB71 $T = -25$	ETOPS Hold	Nominal	---	1,500	95.956	-25	0.32	195.8	4.40	0.175	15

<sup>a</sup>ETOPS is extended range operation twin-engine operational performance standard.

<sup>b</sup>LGW is low gross weight; HGW is high gross weight.

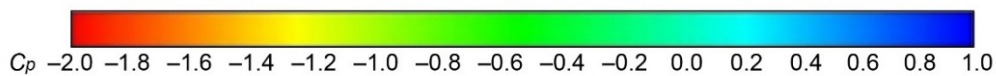
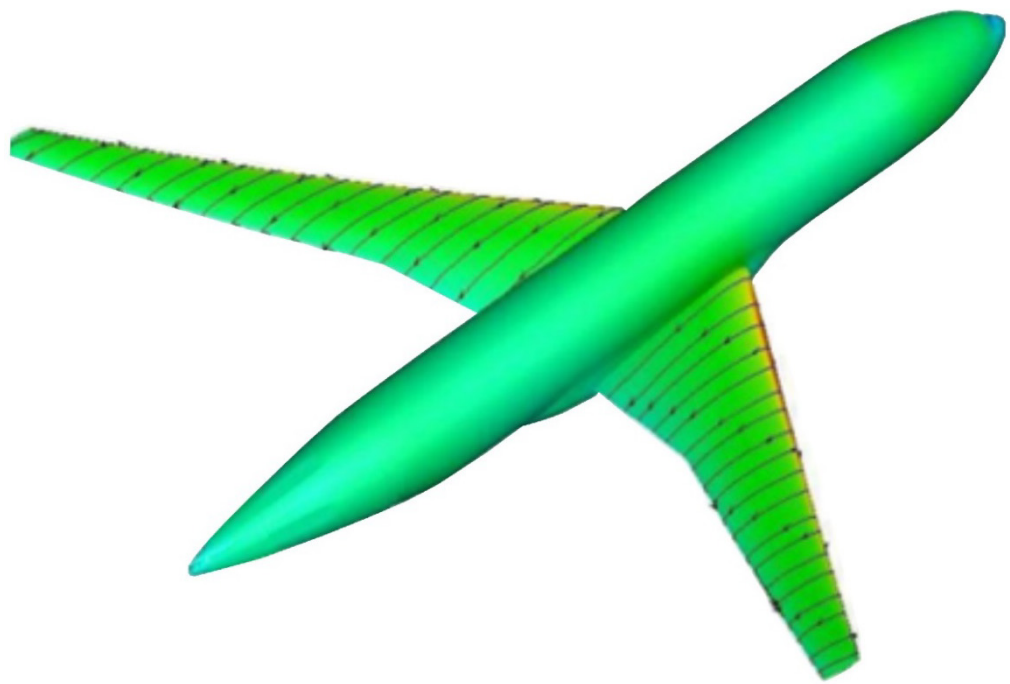


Figure 2.—OVERFLOW analysis of CRM65 showing pressure coefficient contours  $C_p$  where Mach number is 0.37, Reynolds number based on mean aerodynamic chord  $(Re)_{mac}$  is 20 million, and angle of attack  $\alpha$  is 4.4°.

### 3.2 Task 2.2: LEWICE3D for Iced Flight Baseline

The flow fields generated by OVERFLOW were then used in LEWICE3D (Ref. 12) for the 17 different icing conditions listed in Table IV in order to establish the iced flight baseline (IFB). These results included the ice shape geometries and collection efficiencies for each case. Ice shapes at numerous spanwise locations were provided along with partial lofts of the ice shapes along the wingspan. LEWICE3D calculations were performed using the CFB conditions including the CRM65 wing and body. Figure 3 contains an example of the information provided by LEWICE3D. The ice shapes from this analysis are considered the “gold standard” at the spanwise stations selected for the hybrid design process, meaning that the ice shapes produced by LEWICE3D on the hybrid models are expected to match those from the IFB in order for the design to be considered reasonable or accurate. This process of analyzing the hybrid models using LEWICE3D is discussed further in Section 4.5.

The original IFB was established using a Boeing-modified version of LEWICE3D. This proprietary version of LEWICE3D includes some source code changes and is based on an older version (TRAJMC3D version 2.2) than the version used (TRAJMC3D version 2.47) (Ref. 13) in this research to predict the ice shapes on the hybrid wing models as they would be installed in the IRT test section. In order to have a flight baseline set of ice shapes consistent with the ice shapes that would be produced for the IRT simulations, a new set of baseline ice shapes using the OVERFLOW flow-field solutions was generated with the same version of LEWICE3D (TRAJMC3D version 2.47). This new set of baseline ice shapes, called the revised IFB, ensures that no differences in IRT and baseline ice shapes are due to changes in LEWICE3D trajectory or icing physics models. All IFB ice shapes shown or discussed in this report are taken from the revised IFB, which includes the same cases listed in Table IV. Therefore, any reference to the IFB hereafter refers to the revised IFB.

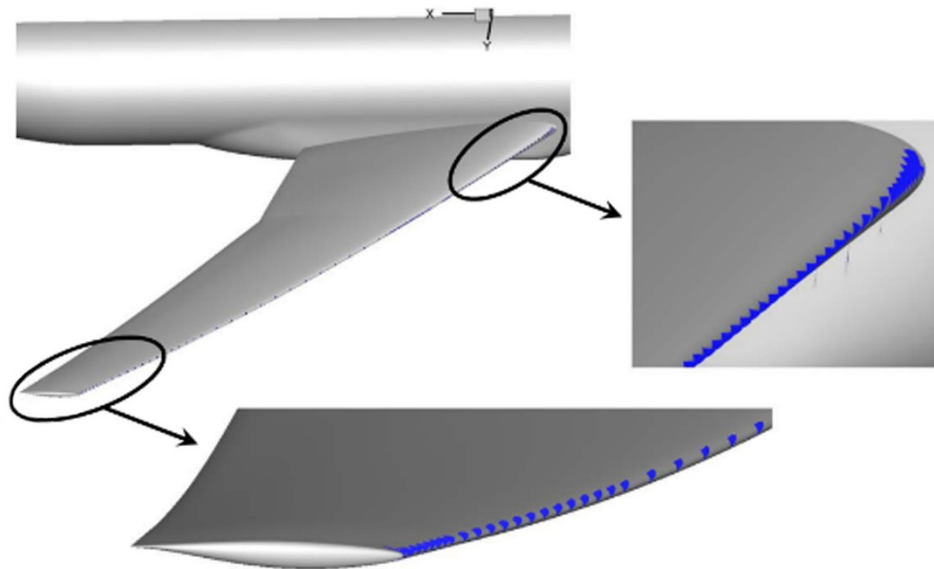


Figure 3.—LEWICE3D ice shape results for CRM65. Droplet median volumetric diameter ( $MVD$ ) = 20  $\mu\text{m}$ ,  $V$  = 232 kn, alt. = 10,000 ft, liquid water content ( $LWC$ ) = 0.55  $\text{g}/\text{m}^3$ , static temperature =  $-4$   $^{\circ}\text{C}$ , 45-min exposure (Ref. 1).



### 3.3 Task 2.3: Spanwise Wing Sections Selection for Analysis

Once the wing geometry for this project was selected and the baseline CFD and icing analysis were performed, the specific spanwise stations for the hybrid model designs were selected. The goal was to select the minimum number of locations along the wing necessary to interpolate and extrapolate an ice shape across the entire span of the wing. The hybrid design process was applied to these sections of the full-scale wing in order to create airfoils with full-scale leading-edge geometries and flow fields. These new airfoils were extruded with the same leading-edge sweep angle as the full-scale wing to create 3D wind tunnel models for testing in the icing wind tunnel. These models are similar to a wing due to their sweep, but they have a constant cross section and zero twist representing only one station of the swept-wing geometry. Since the design, fabrication, and testing of large-scale models can be expensive, it was desirable to select only three stations to represent the ice on the entire swept wing. To select these three stations, the team analyzed the IFB data and considered real aircraft characteristics.

To analyze the six flight cases with multiple temperatures for each of the cases from the IFB, a MATLAB code was written to determine the ice horn length and horn angle. This code is similar to the NASA code THICK (Ref. 14). Using this code, every LEWICE ice shape cut perpendicular to the leading edge could be investigated for each IFB case. The parameters identified with this code are shown in Figure 4. The ice horn length is defined as the distance from the center of the leading-edge radius to the horn tip, and the horn angle is defined as the angle between the chord line and a line along the horn length. A parameter called ice thickness on the horn was defined, as well as the horn length minus the distance from center of the leading-edge radius to the surface of the wing.

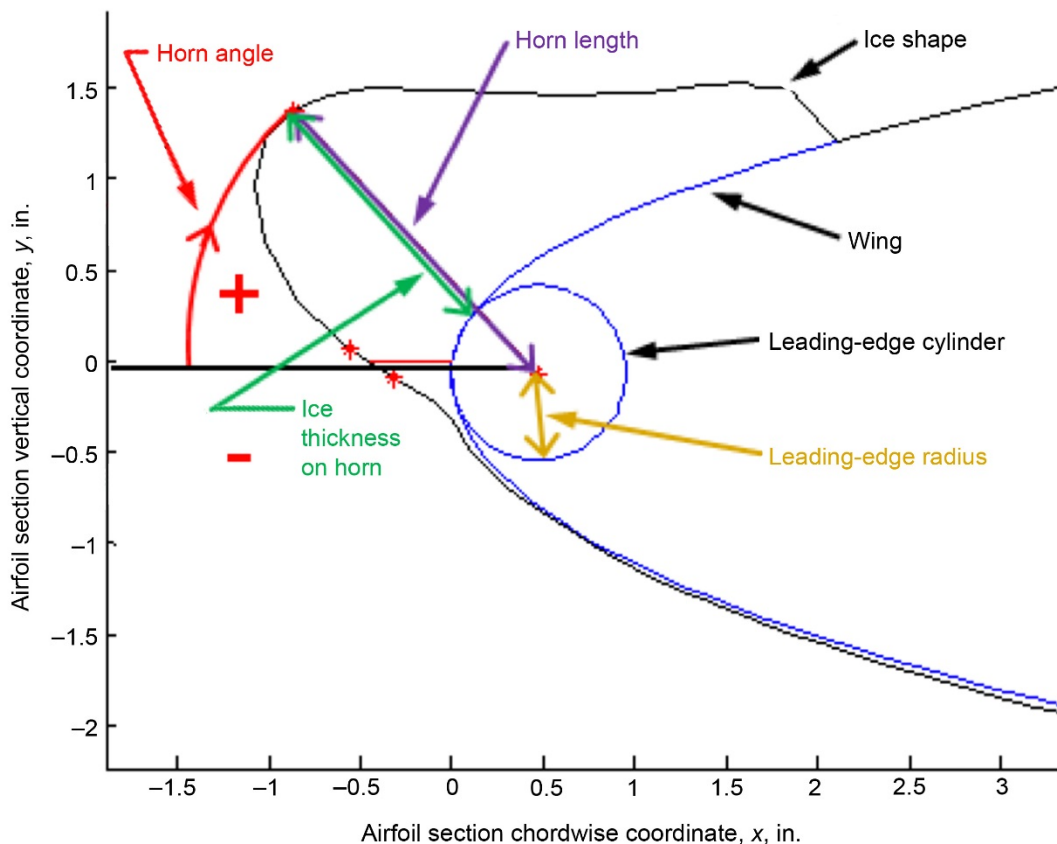


Figure 4.—Icing parameters determined from MATLAB code to analyze LEWICE3D data.

The size of the ice horn and the angle of that horn were determined for each ice shape as a function of span. This analysis was repeated for all 17 cases of the IFB, and a recommendation for the three spanwise stations was formulated. Generally, the horn length changed gradually and nearly linearly across the span for all of the cases analyzed, while the horn angle tended to dip near the 20 percent station and then increase almost linearly toward the wing tip. Warmer cases showed larger ice thicknesses on the horn, such as the WB33  $T = -4$  case displayed in Figure 5.

Recommendations for the stations at 20, 64, and 83 percent of the wing semispan were discussed and selected with NASA. They correspond to nominal wing butt line (WBL) positions of 151.378, 481.208, and 624.067 in. on the CRM65, respectively, and are shown in Figure 6. The 20 percent station was selected for having the minimum horn angle for most IFB cases analyzed and for its large physical size, which challenged the design of a swept-wing model capable of fitting inside the IRT. Despite being located near the wing root, it was still not too close to the side of body (SOB) (10 percent of the span or WBL = 75.189 in.). The 83 percent station represents the junction between the heated and unheated portion of a wing had this been a real aircraft, although ice protection systems are not included in this study. The 64 percent station was selected because one more station was needed between the 20 and 83 percent stations to help characterize ice accretion across the entire wingspan. It was conveniently observed that one of the icing cases from the IFB (WB33  $T = -4$ ) that was considered more important due to its larger ice accretions presented a horn angle inflection point that corresponded to the 64 percent station, as seen in Figure 5, so this station was selected even though this behavior was not observed in the other 16 IFB simulations.

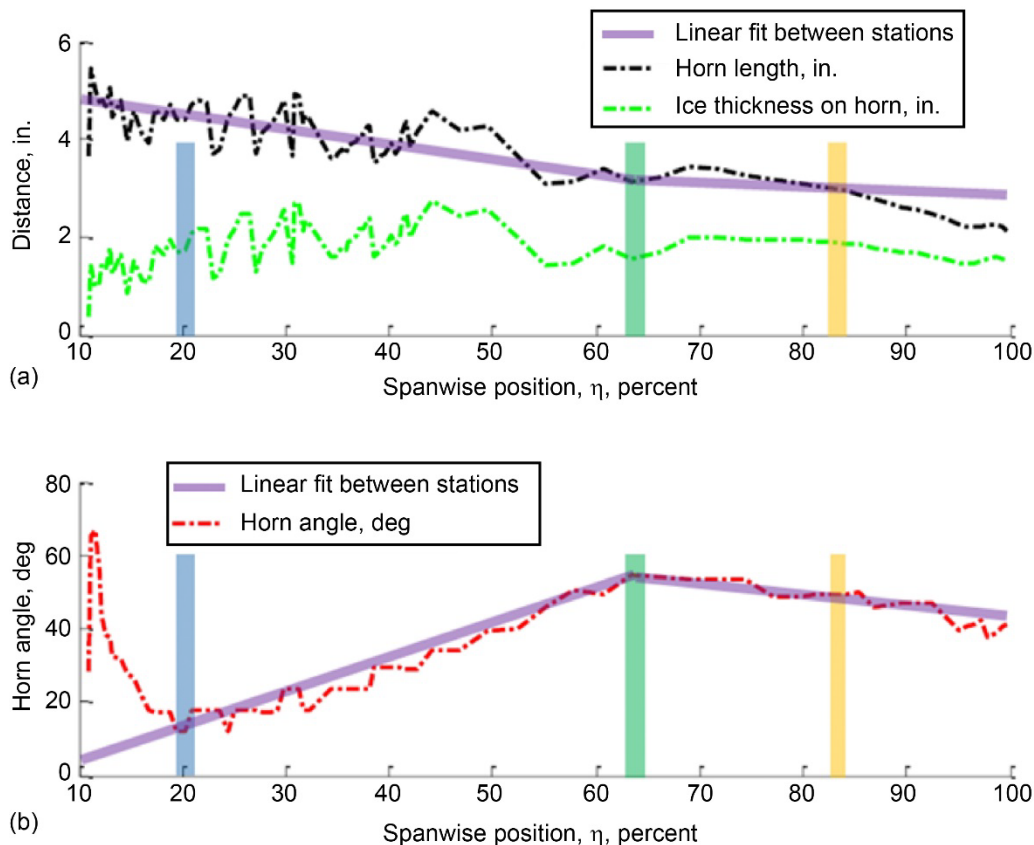


Figure 5.—LEWICE3D data analysis displaying ice thickness on horn (a) and horn angle (b) at selected stations along span (20, 64, and 83 percent) for CRM65 case WB33  $T = -4$ , where  $T = -4^\circ$ ,  $t = 45$  min, Mach number  $M = 0.36$ , angle of attack  $\alpha = 3.7^\circ$ , liquid water content  $LWC = 0.551$  g/m<sup>3</sup>, and median volumetric diameter  $MVD = 20$   $\mu$ m.

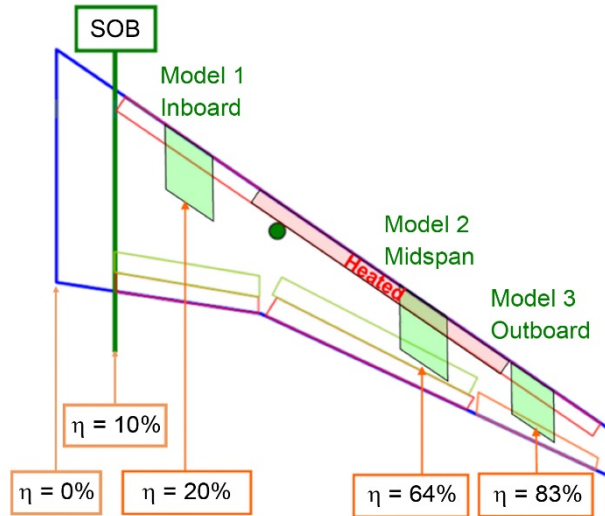


Figure 6.—Three spanwise stations of CRM65 selected for this study. SOB is side of body and  $\eta$  is spanwise position.

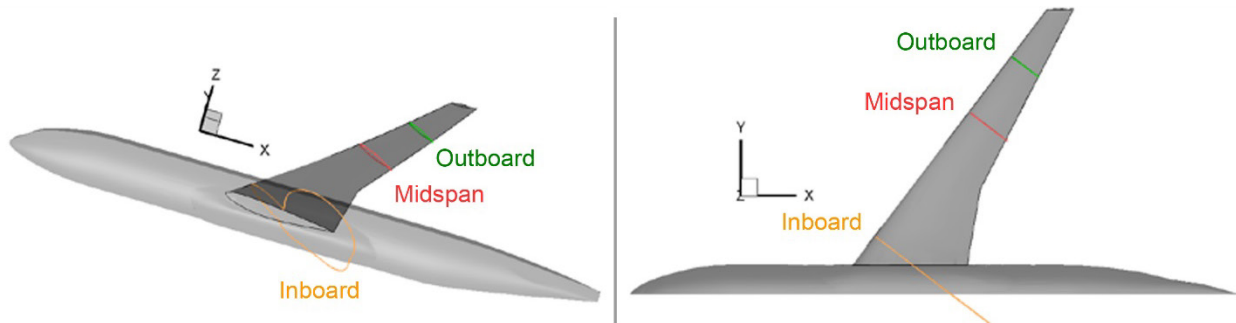


Figure 7.—CRM65 and selected three stations (Inboard, Midspan, and Outboard) cut in perpendicular direction (Ref. 11).

Because the reference wing was swept, the models were designed utilizing the stations in the normal direction, applying simple swept-wing theory as discussed by McLean (Ref. 15). The three selected stations and the respective airfoils in the direction perpendicular to the wing leading edge are displayed in Figure 7.

It is noticeable from Figure 7 that the Inboard perpendicular cut intersects the fuselage, but because the hybrid airfoil design retains only the leading edge of the full-scale cut, there is little impact in replacing the trailing-edge portion of the Inboard cut that corresponds to the fuselage intersection by an assumed extrapolated trailing edge, seen in Figure 8.

To illustrate the challenges involved in designing each of the three models to fit inside the IRT test section, Figure 9 shows the IRT test section (20 by 9 by 6 ft) overlaid on each of the wing stations of the CRM65 geometry. Both top and rear views are displayed to scale.

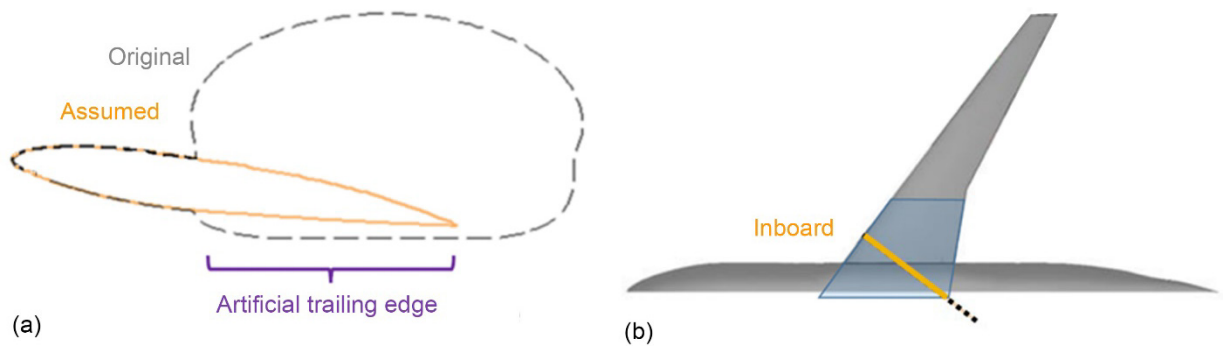


Figure 8.—Inboard perpendicular cut extrapolation (Ref. 11). (a) Original and assumed Inboard perpendicular cuts. (b) Extrapolation scheme showing Inboard cut location.

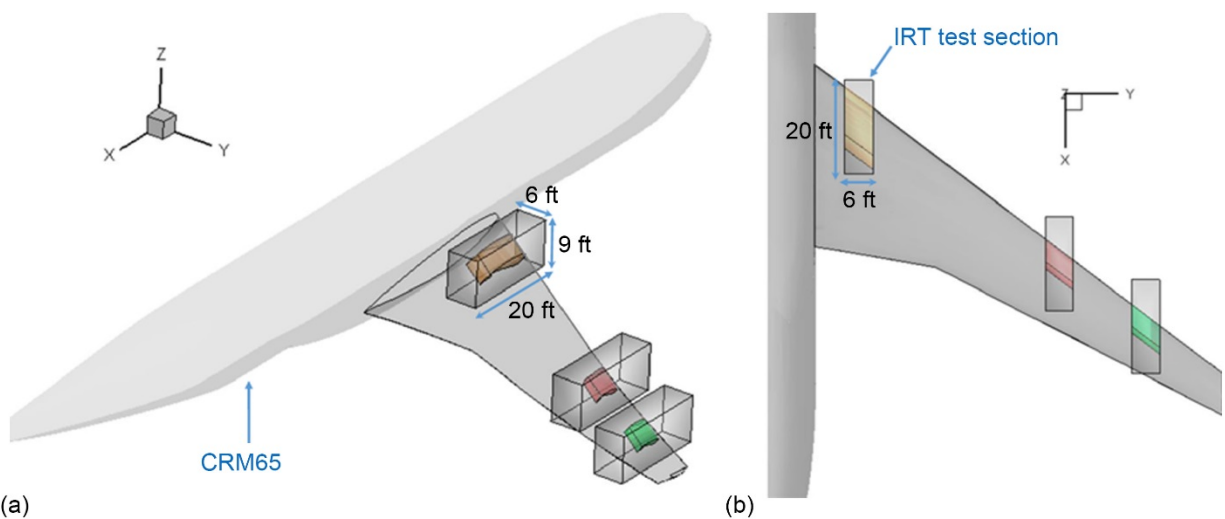


Figure 9.—CRM65 with Icing Research Tunnel (IRT) test sections at three selected spanwise stations (Ref. 11). (a) Oblique view. (b) Top view.

The computational simulations for the aerodynamic flow field and ice accretions for the CFB and IFB were performed on the CRM65, whose wing shape includes the bending and twist that a real wing would see under a 1-g load in flight. Early in the project, researchers identified how complex it would be to manufacture the artificial ice shapes to fit onto the leading edge of the CRM65 wing wind tunnel model for later design, fabrication, and testing to quantify the aerodynamic effect of the experimentally measured ice accretions. To address this issue, an unbent CRM65 wing was generated for utilization in future aerodynamic wind tunnel tests. This geometry was referred to as the “unsheared CRM65 wing,” which maintained the same twist of the CRM65 wing but had the leading-edge points brought to a straight line, as there was no dihedral along the wing leading edge.

At the time of the selection of these three stations, only the CRM65 geometry was available, so the airfoil coordinates of the selected stations were extracted from the CRM65, and 3D matrix rotations were done to remove the local “dihedral” from the airfoil coordinates. By the time the unsheared CRM65 became available, the hybrid models were already far into the design process. The extracted cuts from the unsheared CRM65 were compared with the CRM65 models, and it was concluded that they were close enough that it would not be justifiable to restart the design process of the hybrid models.

Although the nominal spanwise locations of the 20, 64, and 83 percent stations on the CRM65 based on the CRM reference semispan corresponded to 151.378, 481.208, and 624.067 in., respectively, the actual locations of the CRM65 stations utilized for the hybrid model designs were 151.178, 483.768, and 627.387 in., based on the measurements of the CAD model utilized.

To design the wind tunnel wing models for each of the three selected spanwise stations that could fit inside the test section and also reproduce the ice accretion of the full-scale wing, the design method process was broken down into 2D and 3D designs, as discussed in Sections 4.0 and 5.0, respectively.

## **4.0 Task 3: Design and Simulation of 2D Hybrid Airfoils**

This section describes the 2D design process, including integration of 2D tunnel effects, design of 2D hybrid airfoil sections with trailing-edge flaps, and application of LEWICE to compare the resulting ice shapes to the IFB.

### **4.1 Task 3.1: Integrate 2D Tunnel Effects and Flaps Into 2D Hybrid Design**

A hybrid airfoil is defined as one that has a full-scale airfoil leading edge and a shortened (or truncated) trailing edge. The hybrid airfoil design method was first introduced by Saeed et al. (Refs. 2 to 4), who explored the design of single-element airfoils in free air that matched full-scale circulation in an attempt to match the full-scale ice accretion (Refs. 2 and 3) and performed an experimental validation with a simple hinged flap (Ref. 4) in the IRT compared with LEWICE results. Fujiwara et al. (Refs. 11 and 16) further studied this subject by performing parametric studies of hybrid airfoil design variables to identify key parameters that control ice accretion matching. Fujiwara et al. also extended the hybrid airfoil design method to include the effects of flaps, wind tunnel walls, viscosity, and computational predictions of the resulting ice shapes using LEWICE. A brief summary of the hybrid airfoil nomenclature and design process is presented below.

Three main geometrical parameters (Ref. 17) describe a hybrid airfoil: the hybrid scale factor, the upper leading-edge extents, and the lower leading-edge extents. The hybrid scale factor is defined as the full-scale chord divided by the hybrid chord and represents the factor by which the baseline geometry is shortened. The upper and lower leading-edge extents are the chordwise lengths of the full-scale leading edge that are maintained, given as a percent of the full-scale chord length. Figure 10 shows an example of a hybrid airfoil with 10 percent lower and 5 percent upper leading-edge extent and a scale factor of 2. Because ice shapes that grow on the nose of the hybrid model are correlated to the full-scale baseline airfoil, the hybrid angle of attack is measured relative to the full-scale airfoil chord line rather than the hybrid airfoil chord line. Note that the full-scale and hybrid airfoils are both at zero angle of attack in Figure 10. The slight negative incidence angle observed in the full-scale airfoil is due to the reference wing local twist angle, extracted perpendicular to the leading edge. This is done to allow referencing back to the overall aircraft angle of attack when dealing with the various icing cases.

Two additional design variables determine the aft section geometry: the nose-droop angle  $\gamma$  and the quarter-chord zero-angle-of-attack pitching-moment coefficient  $C_{m0}$ . The nose-droop angle is the angle formed by the full-scale airfoil chord line and the line connecting the leading and trailing edges of the hybrid airfoil. Alternatively, it can be interpreted as the elevation of the trailing edge with respect to the leading edge. A more positive nose-droop angle causes a lower trailing-edge elevation or more camber, shifting more load to the aft of the hybrid airfoil. The quarter-chord zero-angle-of-attack pitching-moment coefficient affects the camber line curvature of the aft hybrid section without changing the elevation of the trailing edge, such that a more positive  $C_{m0}$  will result in a less cambered aft section and, therefore,

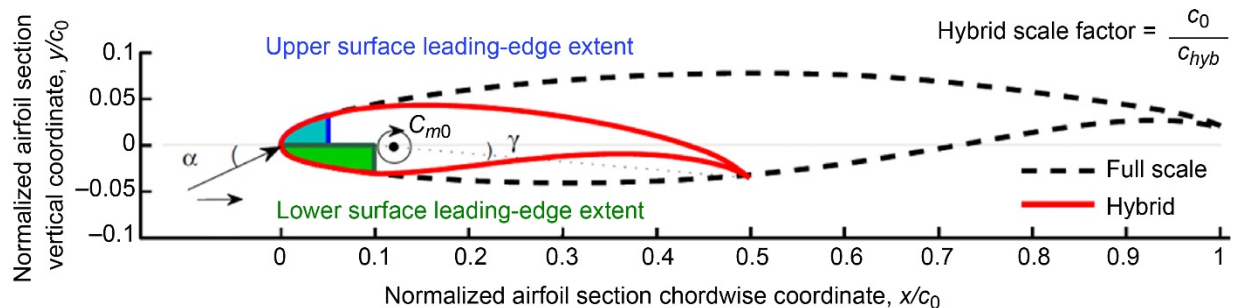


Figure 10.—Hybrid airfoil geometric variables (Ref. 11). Here,  $c_0$  is full-scale chord,  $c_{hyb}$  is hybrid-scale chord,  $C_{m0}$  is zero-angle-of-attack pitching moment coefficient,  $\alpha$  is angle of attack, and  $\gamma$  is nose-droop angle.

reduced aft loading. Values of  $C_{m0}$  can be both negative and positive, but  $C_{m0}$  is usually negative. Both parameters are illustrated for the hybrid airfoil of Figure 10 with a nose-droop angle of  $\gamma = +4^\circ$  and  $C_{m0} = -0.30$ .

A hybrid airfoil is designed to reproduce the full-scale leading-edge ice accretion by controlling the leading-edge flow field (and thus the heat transfer) and droplet impingement at a specific angle of attack with a model using a much shorter chord and, consequently, lower wind tunnel blockage. The computational integrated design workflow is presented in Figure 11. The 2D hybrid model design process is largely automated (steps 1 to 5) using several existing codes, providing a fairly rapid design. The process starts with the analysis of the inviscid flow field and calculation of the pressure distribution  $C_p$  around the full-scale airfoil with XFOIL (Ref. 18). Next, the droplet trajectories and local collection efficiency  $\beta$  are computed with AIRDROP (Ref. 19). Once the droplet impingement limits are known, the user can determine the upper and lower full-scale leading-edge extents to be maintained for the hybrid airfoil. PROFOIL (Ref. 17) is then used to design the aft section airfoil using an inverse airfoil design method. The two most important design variables are the zero-angle-of-attack pitching-moment coefficient  $C_{m0}$  and the nose-droop angle  $\gamma$ , which determine the aft camber and trailing-edge height, as discussed in Figure 10. The aft section of the hybrid airfoil is merged with the leading edge of the full-scale airfoil at the user-prescribed leading-edge extents. Once the hybrid airfoil is designed, it is analyzed with XFOIL and AIRDROP to determine the resulting  $C_p$  and  $\beta$  distributions in comparison with the full-scale airfoil. Adjustments in the design parameters often need to be made in order to perfect the hybrid design, making this an iterative process (Ref. 20). In the case of a single-element hybrid airfoil,  $C_{m0}$  and nose-droop angle  $\gamma$  are varied until a good match is obtained. In the case of a flapped hybrid airfoil, the main element is designed through the same process, with the subsequent addition of an external flap geometry. Four additional design parameters exist when adding a flap: gap, overlap, flap airfoil geometry, and size relative to the main element. Adding a flap is optional and is often done to allow for testing of the model at different conditions from the specified design point (due to the unreliability of modeling wind tunnel effects, the limitations of the CFD, and modeling tools) by modifying the flow field and altering the stagnation point (or attachment point) on the leading edge of the model with the flap deflection. Since all steps thus far use inviscid models, the hybrid design is then evaluated using a RANS CFD code (ANSYS Fluent) (Ref. 21) to ensure that no significant flow separation that could potentially affect the hybrid model performance occurs, and to include the effects of the wind tunnel wall proximity on the hybrid model (Ref. 22). If predicted flow separation is acceptable, the final step is to compare the ice shapes produced by the hybrid airfoil with the full-scale airfoil. This is done using LEWICE (Ref. 23).

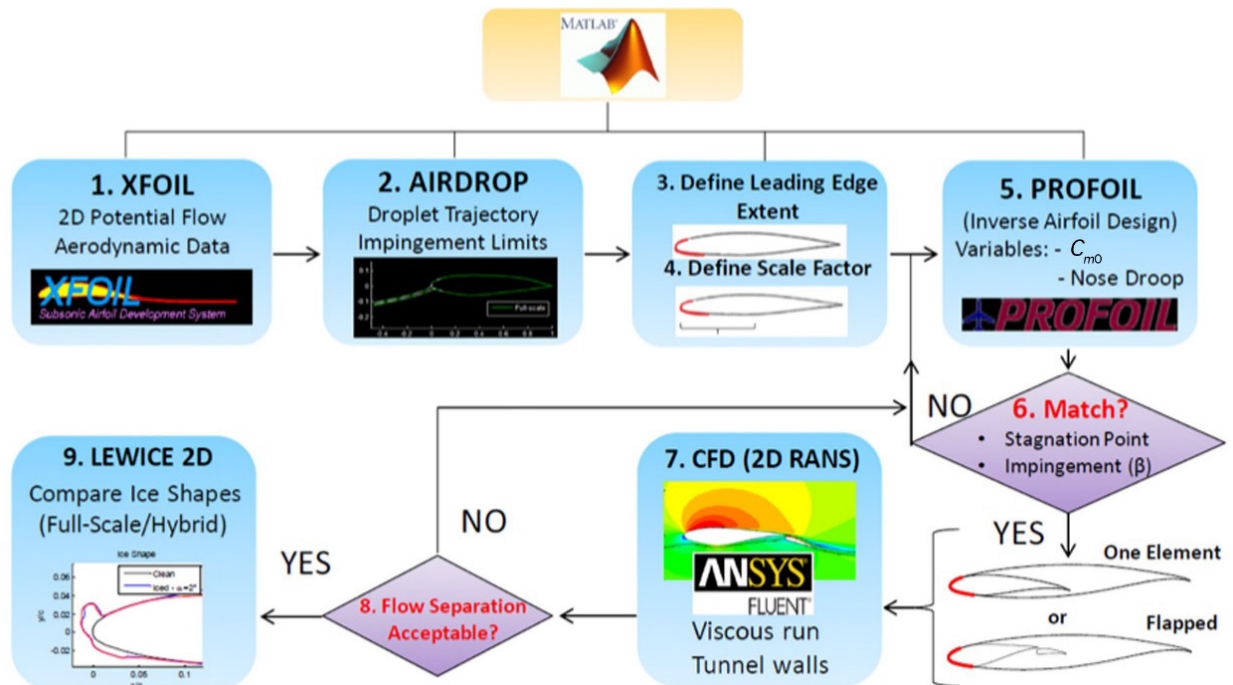


Figure 11.—Integrated hybrid airfoil design workflow (Ref. 11). In step 5,  $C_{m0}$  is zero-angle-of-attack pitching moment coefficient.

#### 4.2 Task 3.2: Perform 2D Scaling Analysis and Develop Tradeoffs

When the proposal for this project was originally written, it was assumed that the IRT wind tunnel models would be designed with some scale of the full-scale airfoil leading edge (either smaller, equal to 100 percent, or larger) and a redesigned trailing edge. During the hybrid airfoil design process described in Section 4.1, the advantages and disadvantages of selecting a certain scale for the leading edge were evaluated. A tradeoff was identified between requiring less scaling of the icing conditions by designing a model with a leading edge size closer to the full scale and potentially requiring velocity scaling if full-scale leading-edge models would pose a limit to the achievable wind tunnel speed due to blockage.

It was decided during the design process that a 100 percent full-scale leading edge with a truncated trailing edge would be used and that velocity scaling requirements that could arise from potentially unachievable speeds in the wind tunnel would be dealt with later for the IRT tests.

An initial study on icing scaling was done based on NASA’s Manual of Scaling Methods (Ref. 24). NASA later took the lead to further develop the velocity scaling for the IRT tests for years 3 and 4 of this project.

#### 4.3 Task 3.3: Design 2D Hybrid Airfoil Sections With Trailing-Edge Flaps

The 2D hybrid airfoil design method previously described was used to design the Inboard, Midspan, and Outboard models. Flaps were included to provide more testing flexibility and reach the full set of target icing conditions. The flap geometry was a modified National Advisory Committee for Aeronautics (NACA) 6412 with a more circular leading-edge geometry so that flap gap and overlap could be kept fairly constant over a range of flap deflection using the same flap pivoting point. The flap chord corresponded to 25 percent of the total hybrid chord,  $c_{hyb}$ , and both gap and an overlap were set to 1.5 percent of the total hybrid chord. The Midspan model is presented in Figure 12 as an example.

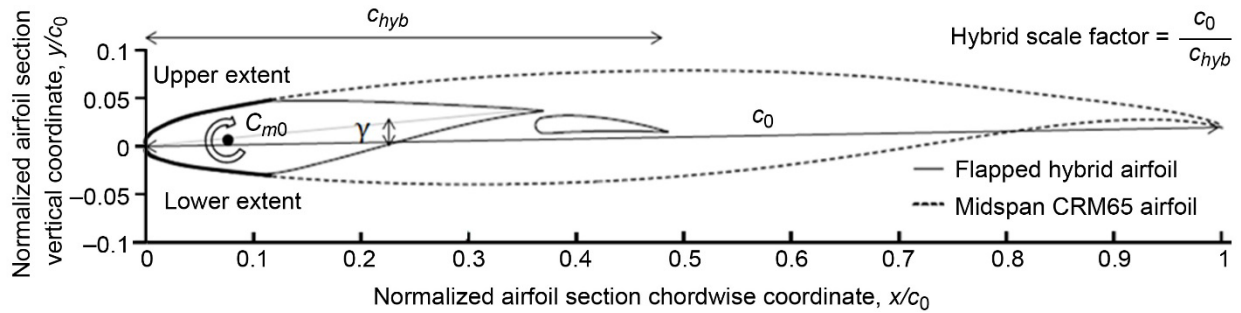

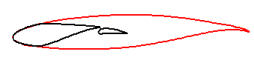
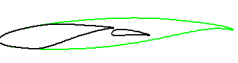


Figure 12.—Midspan hybrid airfoil design with flap. Here,  $c_0$  is full-scale chord,  $C_{hyb}$  is hybrid-scale chord,  $C_{m0}$  is zero-angle-of-attack pitching moment coefficient, and  $\gamma$  is nose-droop angle.

TABLE V.—INBOARD, MIDSPAN, AND OUTBOARD FULL-SCALE NORMAL AIRFOILS AND RESPECTIVE HYBRID AIRFOIL DESIGNS

Model name	Inboard	Midspan	Outboard
CRM65 spanwise location, $\eta$ , %	20	64	83
Full-scale normal chord, $c_0$ , in. (m)	297.88 (7.566)	122.72 (3.117)	91.27 (2.318)
Upper leading-edge $x/c_0$ extent, %	4	10	17
Lower leading-edge $x/c$ extent, %	6	10	15
Nose-droop angle, $\gamma$ , deg	-11.5	-5.5	-3.5
Zero-angle-of-attack pitching moment coefficient, $C_{m0}$	-0.12	-0.05	-0.08
Scale factor	2.25	2	1.5
Full-scale maximum thickness, <sup>a</sup> in. (%)	38.2 (12.8)	14.0 (11.4)	10.2 (11.1)
Hybrid maximum thickness, <sup>a</sup> in. (%)	19.2 (6.4)	9.2 (7.5)	8.2 (9.0)
Full-scale/hybrid airfoils (normal to leading edge)			

<sup>a</sup>All thickness ratios calculated based on full-scale chord.

The 2D hybrid airfoil designs went through an iterative process, as described in Section 4.1. To be considered complete, the designs had to show the capability of reaching all the stagnation points of the target test conditions with some safety margin. This was checked with the 2D RANS simulations for the hybrid airfoils, as described in Section 4.4, and later with the 3D RANS simulations for the IRT hybrid wing models, as described in Section 5.3.

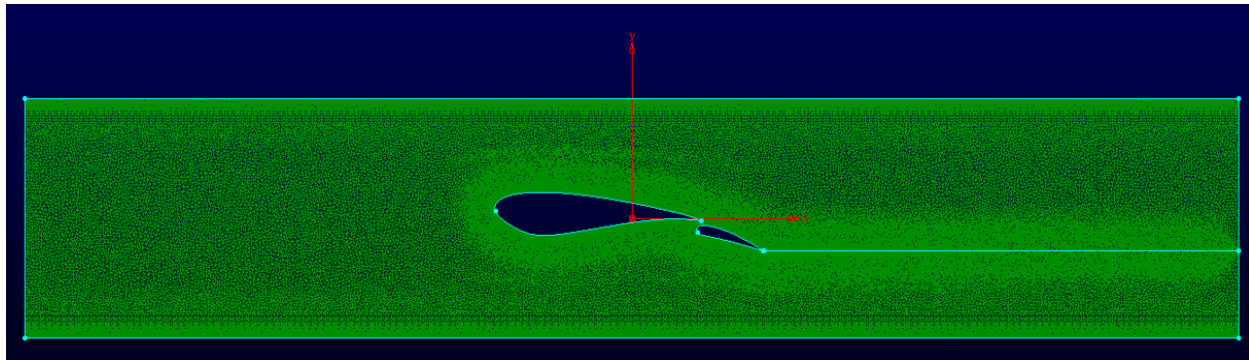
The final 2D hybrid airfoil designs can be seen in Table V with the full-scale and respective hybrid design parameters displayed (Ref. 16). The airfoil coordinates for these three sections and the associated flaps are provided in Appendix E.

#### 4.4 Task 3.4: Verify Model Design With 2D RANS To Improve Clean Flight Baseline Correlation

The design of the three models with external flaps required 2D RANS flow solutions to verify that the corresponding range of stagnation point locations could be reached within a safety margin (step 7 of Figure 11).

Figure 13 provides a schematic of the IRT mesh utilized for the solutions. The rectangular fluid domain representing the IRT stretched 576 in. (or 48 ft) in the  $x$ -direction (along the airfoil chord) and 108 in. (or 9 ft) in the  $y$ -direction (along the airfoil thickness). The grids were generated utilizing Pointwise with about 470,000 nodes, where anisotropic grid cells were used to solve the boundary-layer





**Flow conditions:**

$P = 94.743 \text{ Pa}$   
 $V = 77.2 \text{ m/s}$   
 $\rho = 1.28543 \text{ kg/m}^3$   
 $T = 267 \text{ K}$

**Dimensions of IRT used:**

Length: 48 ft or 576 in.  
 Height: 9 ft or 108 in.  
 Nodes: ~470,000

**Boundary conditions:**

Inlet: Velocity inlet  
 Outlet: Pressure outlet  
 All other surfaces: Viscous walls

Figure 13.—Two-dimensional (2D) mesh utilized for 2D Reynolds-averaged Navier–Stokes (RANS) simulations.

region. ANSYS Fluent (Ref. 21) was the solver, and  $k-\omega$  SST (shear stress transport) was the turbulence model utilized for the solutions. The inlet velocity was set to 77.2 m/s, with an operating pressure of 94.7 kPa and air density of 1.285 kg/m<sup>3</sup>. Each flapped hybrid was modeled in the IRT test section with walls present above and below, simulating the sides of the IRT test section. The meshing strategy used was validated on a two-element NACA 23012 airfoil with a 20 percent chord NACA 23012 external flap (Refs. 25 to 27). The turbulence parameters at the inlet were determined by scaling values obtained computationally by Clark et al. (Ref. 28) for an empty IRT test section, resulting in a turbulent kinetic energy of  $k = 1.08 \text{ m}^2/\text{s}^2$  and specific turbulence dissipation rate of  $\omega = 47.34 \text{ s}^{-1}$  (Ref. 28). This corresponds to a streamwise test section velocity of 188 kn (96.9 m/s), which is typical in the IRT.

To minimize the number of runs, two bracketing aerodynamic cases comprising the required range of stagnation point locations were run per model: a case reaching a stagnation point higher than the highest stagnation point required and a case reaching lower than the lowest. Target stagnation points were extracted from the corresponding stations of the CFB 3D RANS solutions done with OVERFLOW for the CRM65 in free air. Figure 14 illustrates the process of checking the solutions for the two bracketing cases of the Midspan model. No flow separation was observed.

The two bracketing cases help determine whether the design was acceptable or not. Once this was achieved for all three models, additional 2D RANS simulations in between the two bracketing cases were done to obtain the 2D aerodynamic calibration (aerocal) plots, which determine what speeds, angles of attack, and flap deflections are necessary to match certain target flight conditions.

For each model and station, the aerocal gives the wrap distance (also called arc length),  $s$ , measured along the airfoil surface from the highlight (forwardmost point when the aircraft angle of attack is zero) to the stagnation point versus the model angle of attack,  $\alpha$ , at several flap deflections,  $\delta$ . Negative values of  $s$  correspond to positions below the model highlight (on the lower surface of the model). The attachment line locations from the Inboard, Midspan, and Outboard stations of the CRM65 wing are also plotted for the six critical icing scenarios of the CFB as a reference. The aerocal serves two purposes. First, it shows whether the flapped-hybrid design at a given station is effective in reaching all the stagnation point locations required for the IFB test cases. Second, it serves as a tool for predicting what flap deflections will be required by the 3D model to match attachment line locations at the centerline of the IRT to those of the CFB for a desired angle of attack. The flap angle predicted by the 2D aerocal serves as the starting

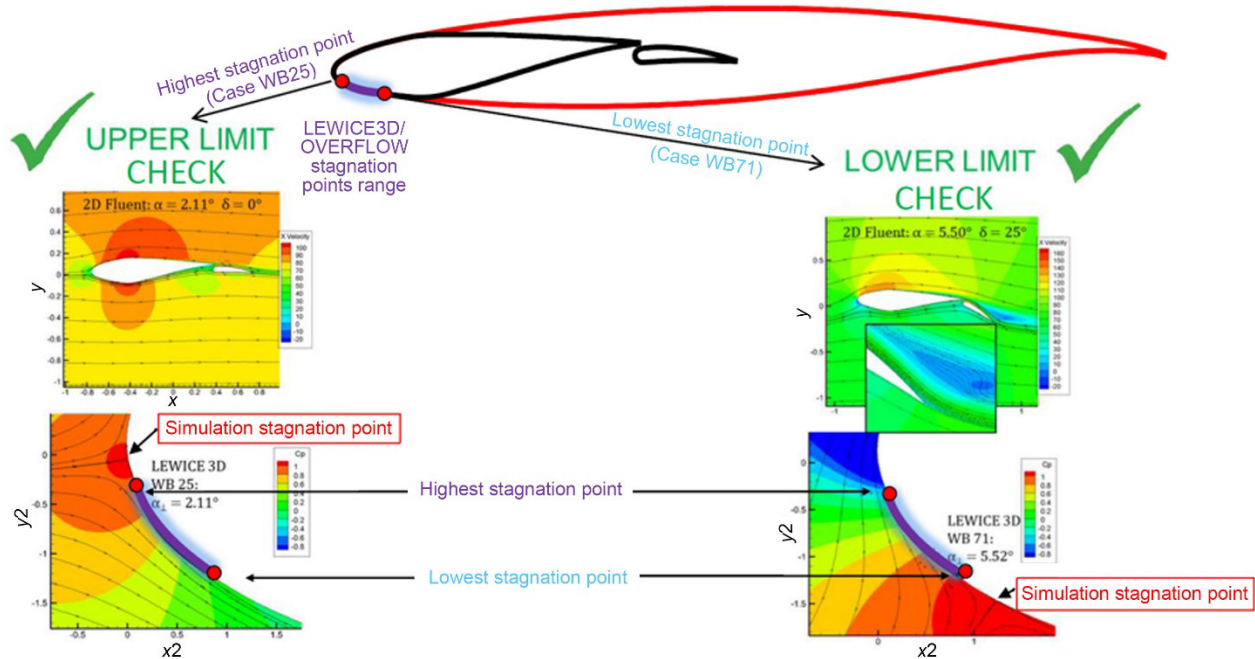


Figure 14.—Two-dimensional (2D) Reynolds-averaged Navier–Stokes (RANS) bracketing cases for Midspan model (Ref. 11) showing angle of attack  $\alpha$  and flap angle  $\delta$ .

point for the iterative matching of centerline attachment line position in 3D CFD simulations, reducing the number of iterations needed.

Aerocal plots were constructed for each of the three 2D hybrid designs using the standard set of test section conditions described above. Various angles of attack were simulated for a set of fixed flap deflections. Figure 15 shows an example of a 2D aerocal plot for the final design of the Midspan model. On the  $y$ -axis, the streamwise wrap distance  $s$  of the stagnation point location relative to the highlight is plotted, and the  $x$ -axis is the angle of attack for multiple flap deflections. The CFB cases' streamwise wrap distances from the 3D OVERFLOW simulations are also included in the figure. The data on this plot labeled IRT model simulation, 2D RANS come from a 2D simulation originally generated in the normal direction. To transform it to streamwise direction, the wrap distances and angles of attack of the 2D RANS lines were divided by cosine of the leading-edge sweep angle ( $37.2^\circ$ ). The flap deflections did not need to be corrected as they are defined perpendicularly to the hinge line, which is the same in 2D or 3D. The plot served to check that the airfoil was designed such that any of the baseline conditions could be reached roughly with flap deflections between  $0^\circ$  and  $20^\circ$ . The 2D aerocal data for the other stations are included on the 3D aerocal plots in Section 5.3.

It is important to notice that although the 2D aerodynamic calibration plots are useful to determine the angle of attack and flap schedule expected for the 3D hybrid wing model inside the wind tunnel, it may not agree with either the CFB (free air) or the 3D RANS data for the hybrid wing inside the tunnel. Recall that the 2D cuts were taken in the normal direction to the leading edge assuming all conditions under which simple sweep theory (Ref. 15) (infinite-span untapered swept-wing characteristics) holds true. The 3D data from the CFB were extracted in the streamwise direction for later comparison with the actual 3D simulation of the IRT model. In addition to the differences due to extracting the 2D data in the normal direction and stretching it to the streamwise direction for comparison with 3D data extracted directly in the streamwise direction, mismatches might arise due to flow three-dimensionalities that deviate largely

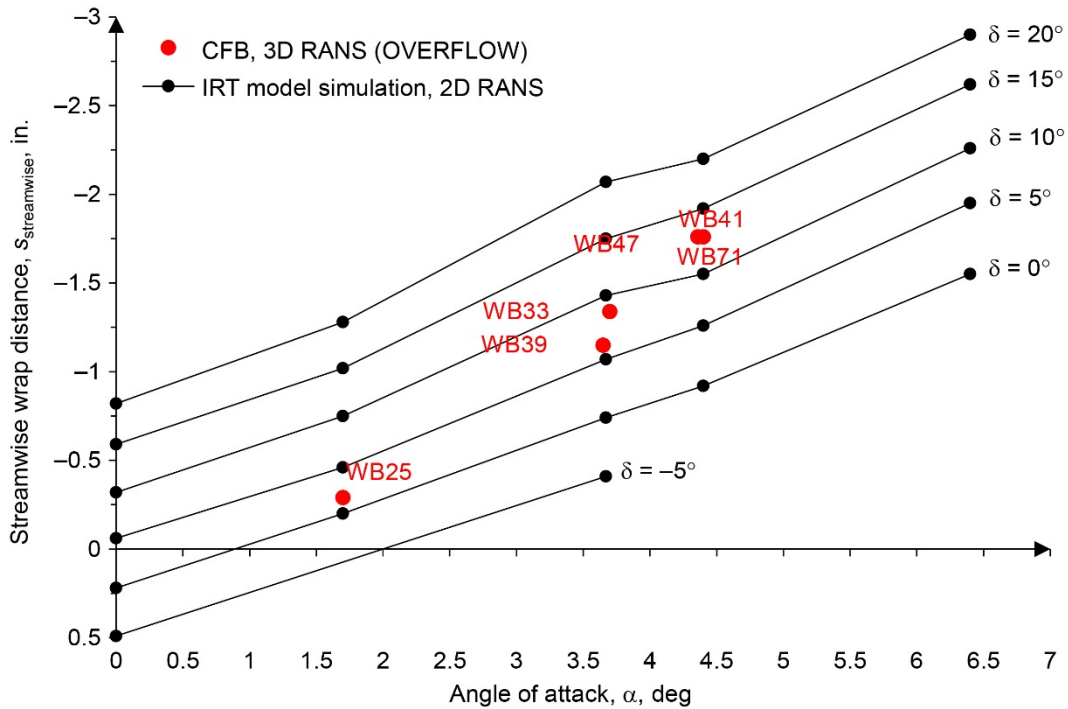


Figure 15.—Two-dimensional (2D) aerodynamic calibration for the Midspan model. The 2D Reynolds-averaged Navier–Stokes (RANS) wrap distances stretched from normal to streamwise direction and clean flight baseline (CFB) taken in streamwise direction.

from these assumptions, such as proximity to the side of body or wing-tip flow features. In this sense, the 2D RANS aerocal plots provide limited information beyond the initial angle of attack and flap schedule estimate in terms of the 3D hybrid wing model design performance. Thus, a similar process is repeated in 3D with higher fidelity tools in Section 5.3 to include the effects that cannot be accounted for in 2D simulations, such as the interaction between the model and tunnel floor and ceiling, and the three-dimensionalities in the swept-wing flow field.

#### 4.5 Task 3.5: Apply LEWICE to Compare Ice Shapes to Iced Flight Baseline

While the aerodynamic characteristics ( $C_p$  distributions over the leading edge) and impingement characteristics (droplet trajectories that define local collection efficiency  $\beta$ ) are important parameters for comparing the full-scale and hybrid airfoils, the most important comparison between the full-scale and hybrid designs is the ice shape itself. To make this comparison, LEWICE version 3.2.2, developed by NASA, was used on each of the hybrid designs to predict the ice shapes and collection efficiencies (Ref. 23).

From the aerodynamic perspective, matching the stagnation point location between the full-scale and hybrid airfoils has been shown (Refs. 11 and 16) to have the strongest effect toward matching the ice accretions, while matching  $C_p$  suction peak magnitude was shown to be secondary. Results have further indicated that the closer to the leading edge the lift is generated, the less circulation is required to match the same stagnation point location, such that hybrid airfoils do not have to maintain the full-scale circulation to yield good ice shape matching (Refs. 11 and 16). From the droplet impingement perspective, matching stagnation point location also yields a satisfactory match in local collection efficiency between full-scale and hybrid designs. The local collection efficiency represents the water mass flux distribution impinging on the airfoil surface and is calculated by LEWICE (Ref. 23) in the

calculation of the ice shape. The local collection efficiency plotted versus wrap distance curve provides the upper and lower impingement limits as well as the maximum value and location of the maximum local collection efficiency  $\beta$ .

To perform the ice accretion comparisons between the full-scale and hybrid airfoils, it is important to quantify how well two ice shapes match. Six common parameters are used to describe ice shapes quantitatively (Ref. 29). The three parameters that most significantly affect the aerodynamics are horn length, horn angle, and maximum ice thickness; the other three variables (stagnation thickness, impingement length, and maximum width) help quantify the ice shape (Refs. 30 and 31). Although it is possible to quantify the ice shape match numerically, the comparisons were done subjectively by visually inspecting the ice shapes according to these parameters.

A hybrid design airfoil that matched the stagnation point of the full-scale airfoil yielded a match in both the local collection efficiency distribution and the overall ice shape. LEWICE simulations were done for the full-scale and hybrid airfoils to show this, utilizing the same flow and icing conditions for both the hybrid and full-scale airfoils. The solutions from LEWICE consisted of the 2D-panel method (inviscid) for the flow field, which was updated as the geometry of the clean airfoil was changed by the added ice shape that grew over the geometry. The automatic time stepping option was utilized.

Figure 16 presents an example of the collection efficiency and ice shape generated by LEWICE for the 2D full-scale and hybrid design for the Midspan station. The icing conditions for the case correspond to condition WB33  $T = -4$  °C with a normal freestream velocity of 95.35 m/s (corresponding to the streamwise freestream velocity of 119.41 m/s), a freestream pressure of 69.702 kPa, a droplet median volumetric diameter ( $MVD$ ) = 20  $\mu\text{m}$ , liquid water content ( $LWC$ ) = 0.551  $\text{gm}^3$ , and an icing time of 45 min, as described in Table IV. The droplet size distribution utilized was the Langmuir D, described in the LEWICE manual (Ref. 23).

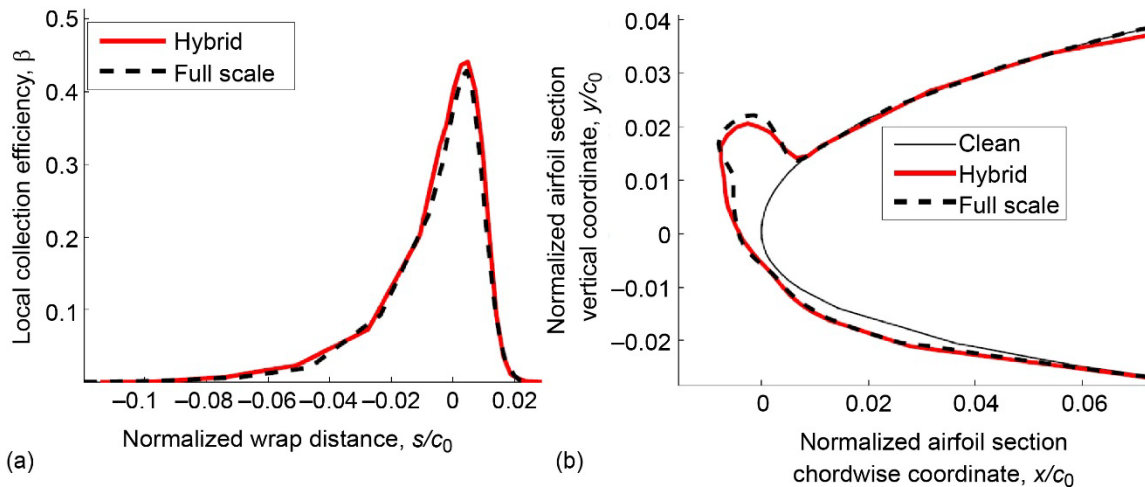


Figure 16.—Midspan LEWICE full-scale and hybrid design results for case WB33  $T = -4$  (from Table IV, extracted from Fujiwara) (Ref. 11). (a) Collection efficiency. (b) Ice shape.

The pressure distributions, collection efficiencies, and ice shapes for the three stations for condition WB33  $T = -4$  ( $T = -4$  °C) obtained with LEWICE were also compared with the LEWICE3D solutions from the IFB. It is important to keep in mind that differences in physical models exist between LEWICE and LEWICE3D. First, LEWICE uses a 2D-panel method (inviscid) to solve the 2D aerodynamic flow field, which is used to calculate the droplet trajectories, resulting in a collection efficiency around the geometry. The surface roughness and heat transfer coefficient are estimated to perform thermodynamic and ice growth calculation. The flow field is then updated as the ice grows in subsequent time steps, and the process is repeated for the duration of the user-specified icing time. LEWICE3D utilizes a 3D RANS (viscous) solution as input for the droplet trajectories that is not updated for the ice growth calculation, such that the ice shape is computed in a single-step method. Another major difference is that the LEWICE3D roughness model utilizes different correlations based on the leading-edge radius, causing differences in heat transfer coefficients that can yield disparities in ice shapes for cases when the temperature is closer to freezing (warmer cases) (Ref. 32). A more detailed discussion of the physical model differences between the two codes is presented by Wiberg (Ref. 13).

Figure 17, Figure 18, and Figure 19 present the pressure distributions, collection efficiencies, and ice shapes for case WB33  $T = -4$ , described in Table IV, for the Inboard, Midspan, and Outboard models, respectively. All droplet distributions were Langmuir D (Ref. 23). Each plot shows results for LEWICE and LEWICE3D full-scale (FS) and hybrid designs. Simple sweep theory (Ref. 15) was used to compare LEWICE3D data for each of the streamwise cuts with the data for the 2D perpendicular cut by dividing the 3D  $C_p$  data of the streamwise cut by  $(\cos^2 \Lambda)$  since the dynamic pressure in the normal direction is based on velocity squared, and dividing 3D local collection efficiency,  $\beta$ , for the streamwise cut by  $(\cos \Lambda)$ , as shown in the derivation of Wiberg (Ref. 13). Note that the collection efficiency values increase from the Inboard to the Outboard model due to the decreasing model thicknesses, as expected for thinner airfoils (Ref. 33). Also, the Inboard full-scale pressure distribution of Figure 17(a) presents a discontinuity due to the intersection of the perpendicular cut on the wing with the side of body (detailed in Figure 8).

All three models showed good agreement between the full-scale and hybrid ice shapes. The differences in ice shapes encountered between LEWICE and LEWICE3D arise in part from the different icing physics models and three-dimensionality of 3D flow solutions. The LEWICE ice shapes obtained served as a preliminary prediction of the ice shapes of the 3D hybrid models, later calculated using 3D RANS and LEWICE3D inside the IRT (Ref. 13), as discussed in Section 5.0.

A number of lessons were learned from the 2D hybrid airfoil design. First, once the full-scale airfoil is defined and its impingement limits are known from the CFB target, define the necessary hybrid scale factor to design a model that can fit inside the icing wind tunnel available. Next, try to maintain close to the same portion of the full-scale leading edge defined by the full-scale impingement limits. Next, redesign a truncated leading edge for the hybrid airfoil that meets the necessary hybrid scale factor and matches the full-scale stagnation points for the extreme target cases with flap deflections that present margins from flow separation of at least about  $5^\circ$  in the 2D RANS simulations that include upper and lower wind tunnel walls. Check for ice-shape matching performance with LEWICE. Finally, keep in mind that the 2D hybrid airfoil design is only part of the 3D hybrid wing process and that 3D computational analyses are needed to achieve a satisfactory final 3D hybrid wing, as described in Section 5.0.

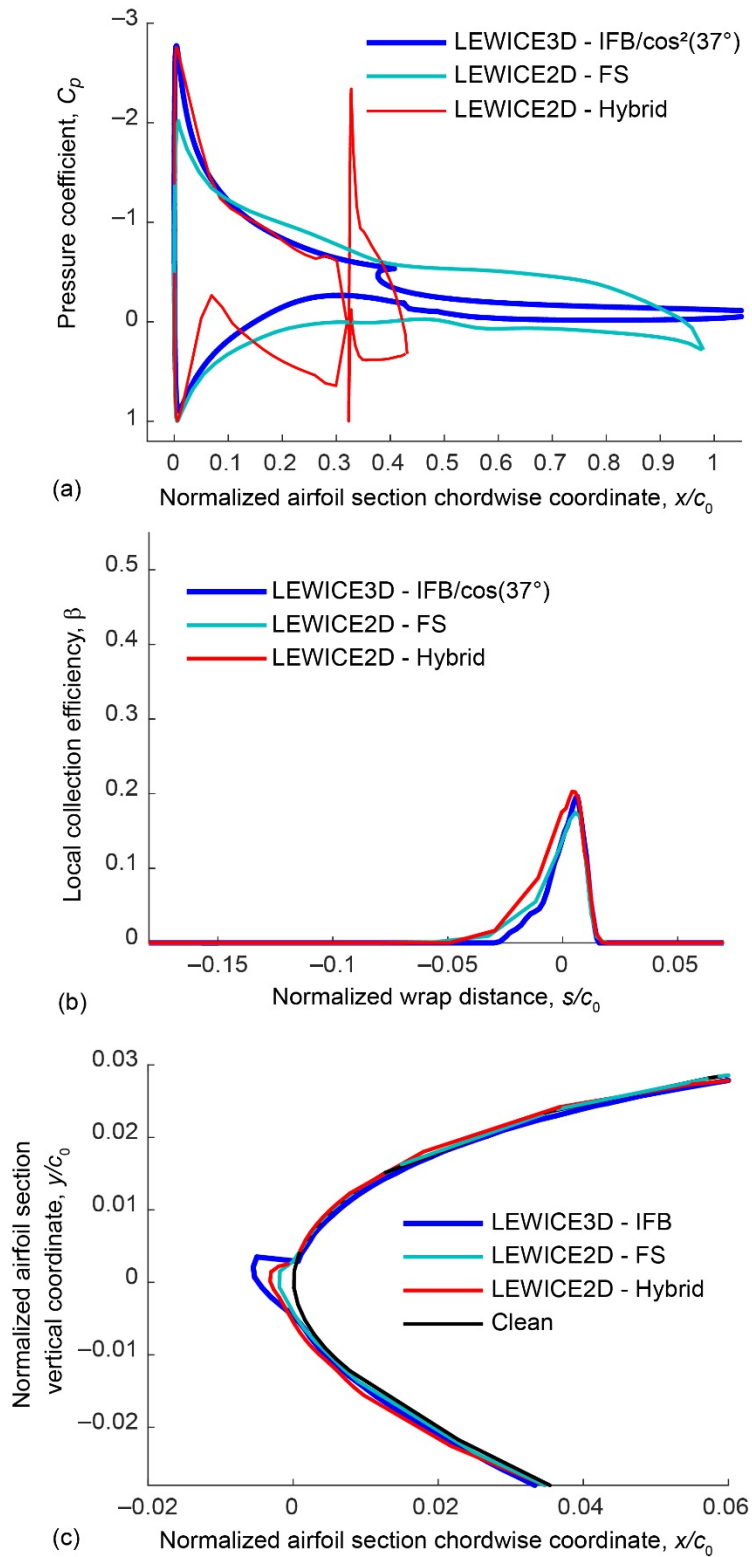


Figure 17.—Inboard model LEWICE simulations: Case WB33  $T = -4$  (from Table IV) (Ref. 11). IFB is iced flight baseline and FS is full scale. (a) Pressure coefficient distribution. (b) Collection efficiency. (c) Ice shape.

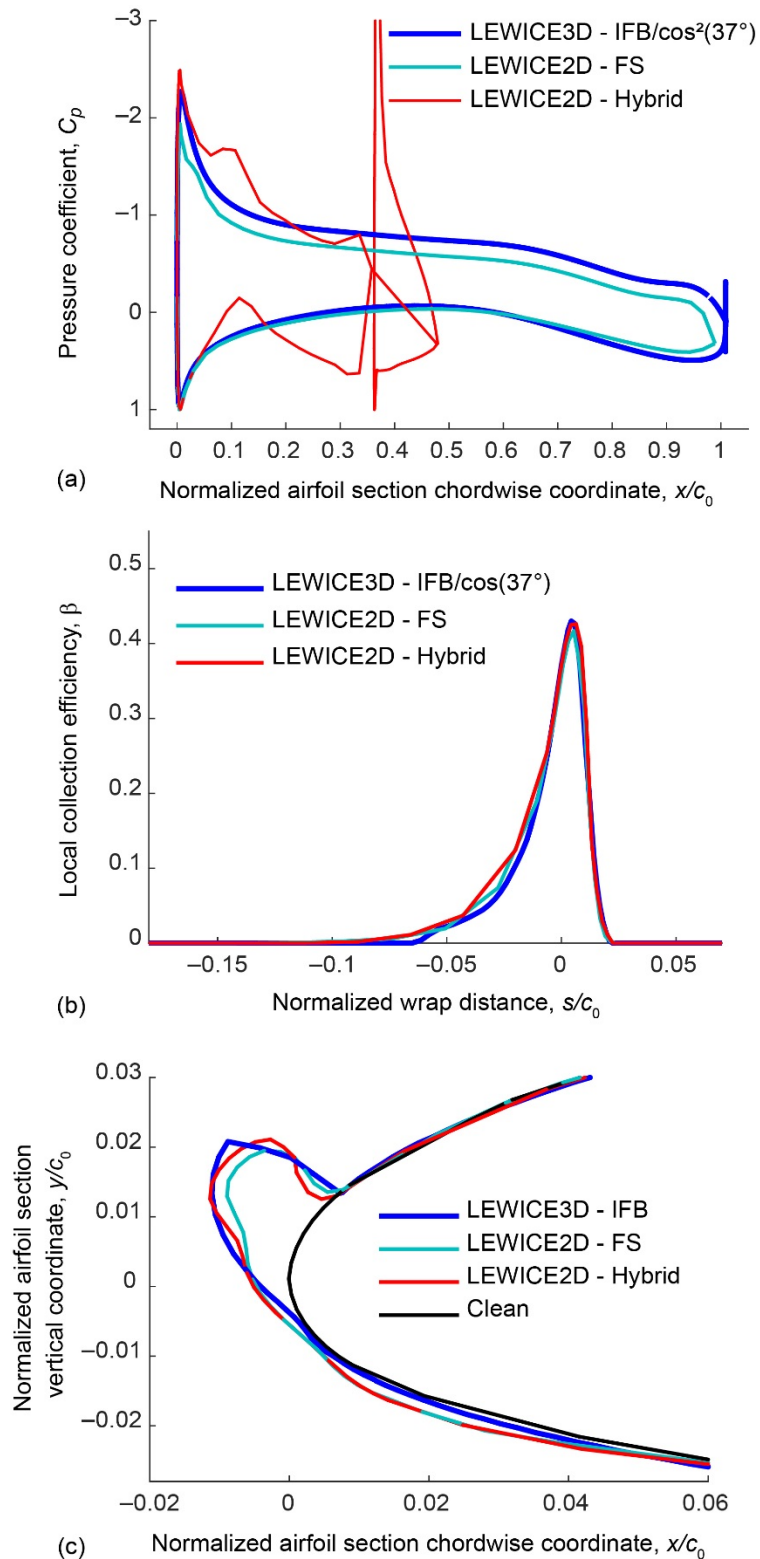


Figure 18.—Midspan model LEWICE simulations: Case WB33  $T = -4$  (from Table IV) (Ref. 11). IFB is iced flight baseline and FS is full scale. (a) Pressure coefficient distribution. (b) Collection efficiency. (c) Ice shape.

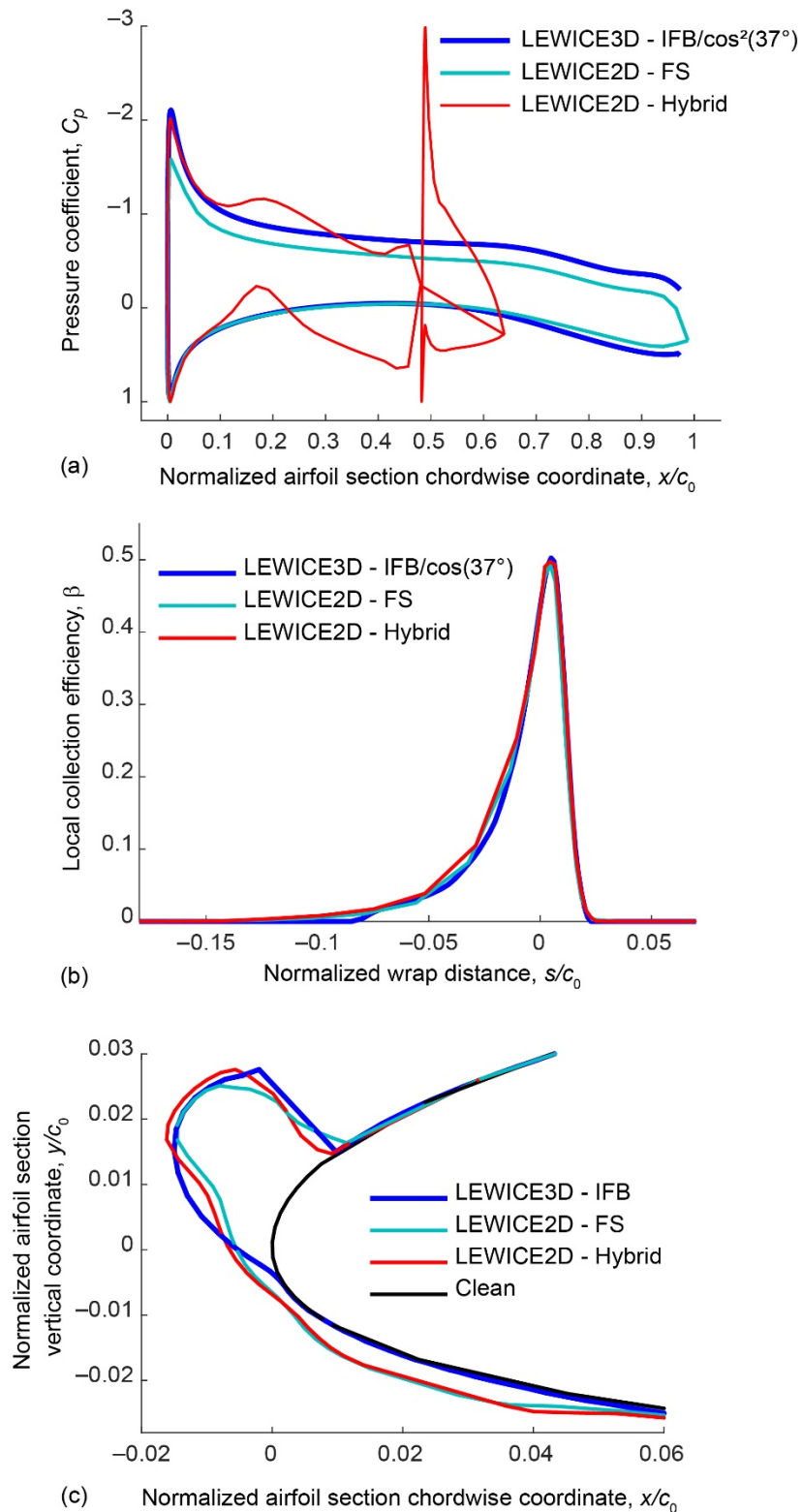


Figure 19.—Outboard model LEWICE simulations: Case WB33  $T = -4$  (from Table IV) (Ref. 11). IFB is iced flight baseline and FS is full scale. (a) Pressure coefficient distribution. (b) Collection efficiency. (c) Ice shape.



## 5.0 Task 4: Design and Simulation of 3D Icing Research Tunnel (IRT) Hybrid Models

A design method for a straight, untapered hybrid wing can be as straightforward as the extrusion of a hybrid airfoil, a design method well documented by Saeed et al. (Ref. 2) and further explored by Fujiwara et al. (Ref. 16). The design of a swept, hybrid wing, however, introduces design challenges related to the three-dimensionality of swept-wing flow fields (Ref. 15) and ice shapes (Refs. 34 and 35). Fujiwara et al. (Ref. 16) discuss this method extensively. This section presents the major findings of the developed method and its application to the design of the three hybrid wing models.

After completion of the 2D design for the hybrid airfoils (Section 4.0), they were translated into 3D hybrid wing models for further study and comparison with the IFB. Section 5.0 details how this was done utilizing both 3D CFD tools and LEWICE3D.

### 5.1 Task 4.1: Validate and Assess 3D RANS for High Blockage in the IRT

The same CFD code that was used during the 2D RANS simulations, ANSYS Fluent (Ref. 21), was utilized to study the 3D hybrid wing models. Fluent has been used for simulations for the AIAA Drag Prediction Workshop with results comparable to other commercially available codes (Refs. 36 to 38). For this application, the code was validated using data from another multi-element airfoil (MEA) that was tested in the IRT. Pressure distribution data are available from a straight-wing model that utilized the McDonnell Douglas Aerospace MEA and spanned from wall to wall. The details of this validation study are presented in Appendix B, including grid resolution studies and pressure comparisons.

Based on those studies, the swept-wing models were simulated in a modified version of the IRT geometry. Clark et al. (Ref. 28) performed a CFD simulation of the IRT empty geometry from the heat exchanger (HX) to the test section to assess the turbulence levels experienced in the test section, as shown in Appendix B. To simplify the CFD meshes, rather than keeping the contraction and expansion sections of the IRT, the constant-area test section was extended upstream and downstream of the actual test section by 20 ft (Refs. 33 and 39) and the turbulence values found by Clark et al. (Ref. 28) were scaled to account for the different velocities between simulations, as further explained in this section. Figure 20(a) shows the Midspan model in the actual IRT test section (6 by 9 by 20 ft). Figure 20(b) shows the computational test section for CFD purposes. The grid for these 3D models consisted of anisotropic elements from all wall and model surfaces that were formed with a growth rate of 1.2. The smallest element spacing was  $1.3 \times 10^{-4}$  in. in order to maintain  $y^+$  less than 1. The Inboard, Midspan, and Outboard models had approximately 24, 17, and 17 million nodes, respectively. The grid near the intersection of the trailing edge of the main element and the leading edge of the flap is illustrated in Figure 21.

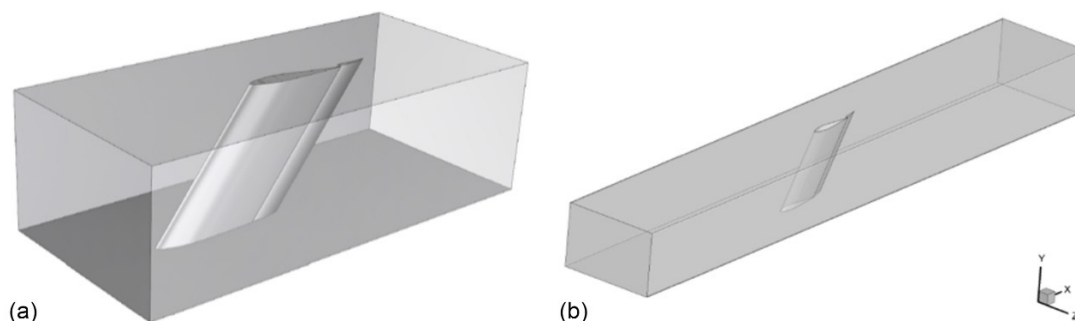


Figure 20.—Midspan model installation in Icing Research Tunnel (IRT) test section. (a) Test section dimensions drawn to model scale. (b) Computational fluid dynamics (CFD) test section extended upstream and downstream of the Midspan model location.

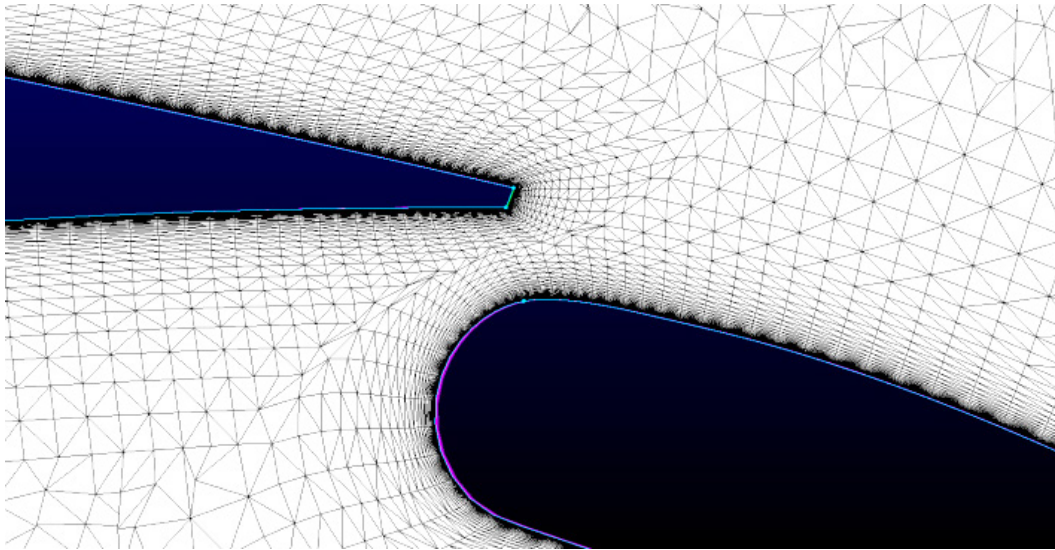


Figure 21.—Anisotropic tetrahedral grid elements between trailing edge of main element and leading edge of flap.

The boundary condition for the inlet was a constant velocity, and a pressure outlet boundary condition was applied. The no-slip condition was applied to the walls and model surfaces. The two-equation RANS turbulence model  $k-\omega$  SST was utilized with inlet turbulence specified based on previous work. The inlet values for the turbulence parameters  $k$  and  $\omega$  were determined using the results of an empty IRT flow simulation performed by Clark et al. (Ref. 28) in which a 3D RANS analysis was used to estimate the flow in the new 2012 configuration of the IRT. Clark et al. simulated the IRT from the exit of the HX to the center of the test section including the turning vanes, spray bars, and contraction nozzle. These results were produced using Fluent. To perform flow approximations at velocities other than those used by Clark et al.,  $k$  and  $\omega$  were scaled using the relations

$$k = k_0 \left( \frac{V^2}{V_0^2} \right) \qquad \omega = \omega_0 \left( \frac{V}{V_0} \right)$$

where  $V_0$ ,  $k_0$ , and  $w_0$  are the tunnel velocity, turbulent kinetic energy, and specific turbulence dissipation rate produced by Clark et al., respectively. Additionally, a second-order upwind scheme was used to solve for momentum and temperature, and all other parameters were solved for using a first-order upwind scheme.

## 5.2 Task 4.2: Translate 2D Hybrid Airfoils Into 3D IRT Models

A hybrid wing model can be designed to represent either a section of the reference wing or a single spanwise station. For a section, the 3D leading-edge geometry from the full-scale wing is maintained while a 3D truncated aft section is redesigned. For this project, the wing model was designed to represent a single spanwise station on the CRM65, shown by Fujiwara et al. (Ref. 40), such that the hybrid airfoil is simply extruded across the wind tunnel test section to create a hybrid wing model. This constant section design method was selected for two primary reasons: first, because it simplifies the design of the 3D hybrid wing model, and second, because only the center portion of the IRT wing model ice accretion data is acquired experimentally, which is more representative of a single spanwise station of the CRM65.

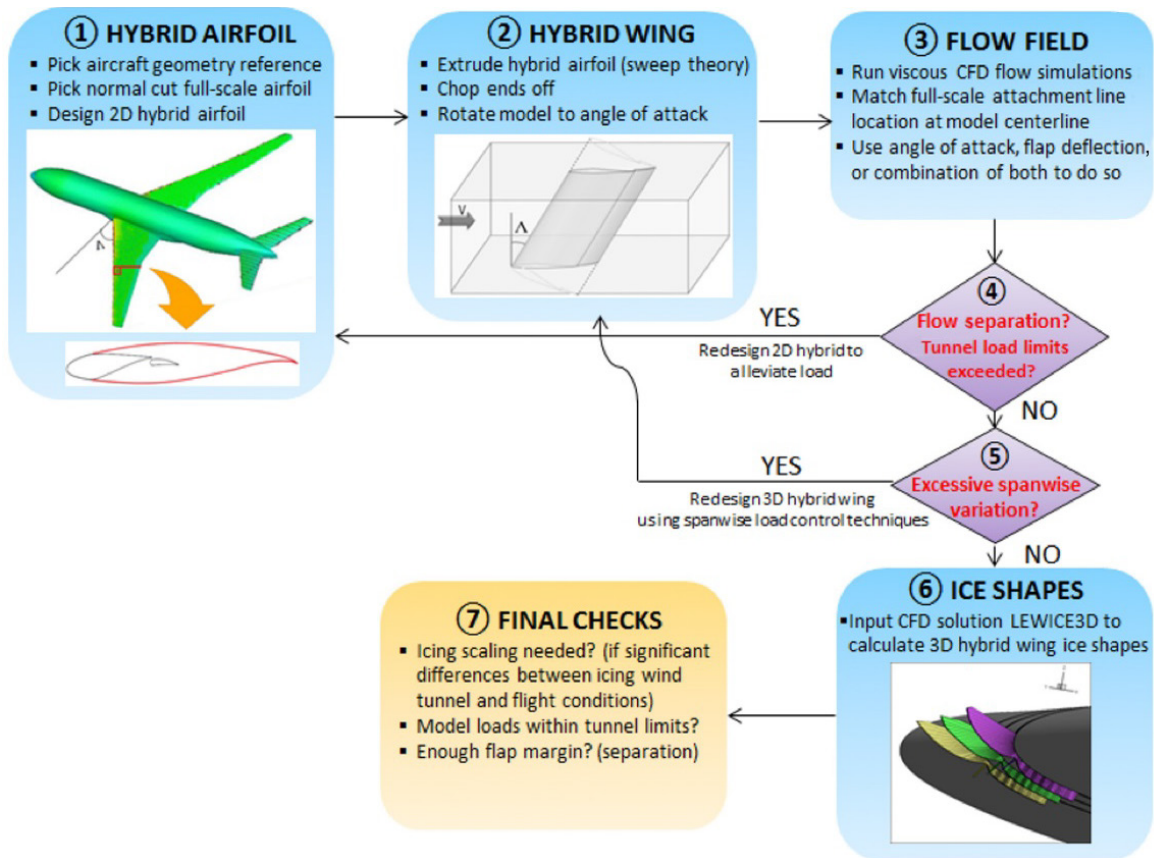


Figure 22.—Hybrid wing design method workflow (Refs. 11 and 40).

The hybrid wing model design method utilized for the present work is presented in the workflow of Figure 22. The first step is to define the aircraft reference geometry and establish the set of aerodynamic and icing conditions to be replicated. The hybrid wing design starts with the design of a 2D hybrid airfoil from a normal-to-leading-edge cut of the full-scale airfoil of the CRM65 to match the stagnation point location for that full-scale airfoil cut. While the stagnation point location information was obtained from the CFD solution (3D OVERFLOW) done on the CRM65, the full-scale airfoil geometries were extracted from the unshored CRM65. The details and design tradeoffs of this first step are described in Section 4.0 of this report, and in more detail in Fujiwara et al. (Ref. 16). To properly represent a swept wing in 2D with simple sweep theory (Ref. 15), the hybrid airfoil is designed for a full-scale airfoil that is cut in the direction normal to the leading edge of the full-scale wing.

The second step requires extruding the designed hybrid airfoil in the direction parallel to the full-scale leading edge, maintaining the same wing leading-edge sweep angle. The ends of the hybrid wing model are trimmed in the streamwise direction to create a model that spans from floor to ceiling in the IRT, as shown for the Midspan hybrid wing model in Figure 23(a). A size perspective of this same model in comparison with the CRM65 is presented in Figure 23(b). Once the hybrid wing geometry is created, the model is then rotated to the desired angle of attack for the CFD simulations that will assess the similarity between the full-scale and hybrid wing's flow field near the region of interest. The order of operations for this portion of the design is important. The 3D geometry must be created first, and then the entire swept hybrid model must be rotated to the desired angle of attack. First rotating the hybrid airfoil to the desired angle of attack and then extruding it to a 3D model generates a 3D model geometry that differs from the full-scale wing because of the model sweep angle in the extrusion.

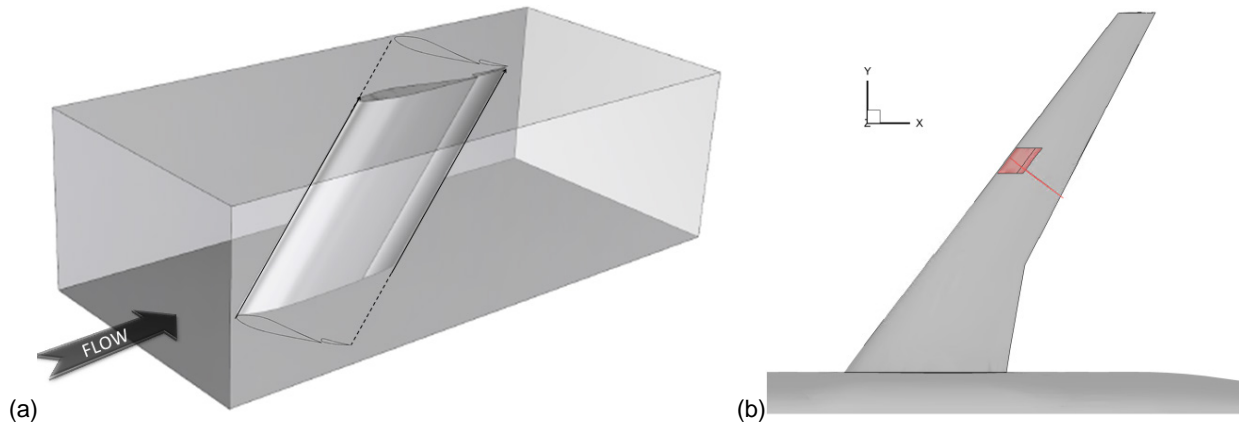


Figure 23.—Icing Research Tunnel (IRT) Midspan hybrid wing model. (a) Hybrid airfoil extruded parallel to leading edge, then trimmed at ends. (b) IRT Midspan model compared with full-scale CRM65 geometry (Ref. 11).

The third step is similar to the iterative process done in 2D for the hybrid airfoil. Instead of varying the hybrid airfoil geometry and flap deflection to match the full-scale airfoil stagnation point location, the criterion utilized is to vary the hybrid wing angle of attack and/or flap deflection to match the full-scale attachment line point at the centerline cut of the model inside the tunnel with 3D viscous CFD simulations. Wiberg et al. (Ref. 41) showed results further supporting the idea that matching the full-scale wing section attachment line location at the centerline of the tunnel generates satisfactory ice shapes for the 3D hybrid model (Ref. 41). To narrow the number of critical baseline cases that drive the design of the hybrid wing model, it is assumed that if the hybrid model is capable of reaching the farthest attachment line location at the tunnel centerline, it is capable of reaching all others as well. The cases requiring the attachment line location to be the lowest on the leading edge are considered the most aggressive scenarios because they require the largest circulation, and hence impose the highest risk of flow separation to the hybrid wing. Fujiwara et al. show in the 2D hybrid airfoil design method that a unique combination of angle of attack and flap deflection does not exist for reaching the same stagnation point location (Ref. 16). Instead, there is one corresponding flap deflection for each angle of attack that reaches the same stagnation point location, with very distinct loads. The more frontloaded the model, the smaller the load required to reach the same stagnation point. Based on that, if flow separation is observed during step 4 on the main element of the hybrid wing but not on the flap, it means some of the load can be transferred from the main element to the flap by increasing the flap deflection and decreasing the main element camber, while reaching the same attachment line location for that particular angle of attack. The analogy applies if separation occurs on the flap and not on the main element. This is done iteratively until the farthest attachment line location is reached with no flow separation, within the tunnel load limits.

Once this is achieved, the fifth step is to observe how much the attachment line location on the hybrid wing model changes across the span. If variation is significant, then spanwise load control techniques can be considered. These are discussed in Fujiwara et al. (Ref. 40) (included as Appendix C). Otherwise, the 3D ice shapes are calculated in step 6 using LEWICE3D and compared with the full-scale ice shapes. For this project, the hybrid wing model ice shapes were only investigated near the centerline region of the model because this is where the model is designed to reach the full-scale attachment line location and where the icing cloud at the IRT is most uniform. If the icing wind tunnel cannot reach the flight icing conditions (density, velocity, etc.), icing scaling must be used to correct for the different operating conditions. A similitude method is described in Section 5.6 as well as in Wiberg et al. (Ref. 41) (included as Appendix D). Otherwise, the hybrid wing is considered complete.

The wind tunnel sidewalls are an important topic from the hybrid wing model design perspective because they affect the attachment line location, the risk of flow separation, and, ultimately, the model performance to reproduce full-scale ice shapes. A discussion of the applications of this effect is presented by Wiberg et al. (Ref. 41) and Wiberg (Ref. 13).

The flow field of an untwisted swept-back wing model confined by sidewalls, like the IRT hybrid models designed for this project, shows a very pronounced 3D feature of increasing outboard load, as shown in Figure 24 for the RANS solution for the Inboard hybrid wing model at  $\alpha = 3.67^\circ$ , with a flap deflection of  $6^\circ$ , run at approximately 120 m/s. The circulation increases farther outboard on the model, leading to higher suction peaks noted by the lower pressure blue color on the upper surface of the model.

This phenomenon occurs naturally in swept-back wings due to the induced upwash by the stations upstream of the outboard region (Ref. 42) but is particularly enhanced for a model bounded by walls because of the symmetry condition imposed by the sidewalls (Refs. 31 and 41). A lifting line representation of the swept-wing model inside the IRT is shown in Figure 25, placing three horseshoe vortices A, B, and C, each composed of two trailing-edge vortices connected by a bound vortex, on the wing and on two mirrored images at each side of the wall. It can be observed that the right trailing vortex of the horseshoe vortex C, which primarily contributes to decreasing the outboard local angle of attack by inducing downwash at the wing tip, is cancelled by its image C". The bound vortex of C" also induces a greater upwash on the wing outboard region, thus increasing the outboard load even more. The inboard region sees a much lower effect since the vortices are inducing upwash to the left of the left mirrored image, away from the wing inboard region. Note that both mirror images distort the flow condition attempted to be reproduced in the neighborhood of the model with this three-segment kinked wing, as opposed to the continuous swept-back wing expected in the neighborhood of the model, as in Figure 23(b). This explains the observed load variation across the span, which initiated the investigations here presented for the use of spanwise load control techniques.

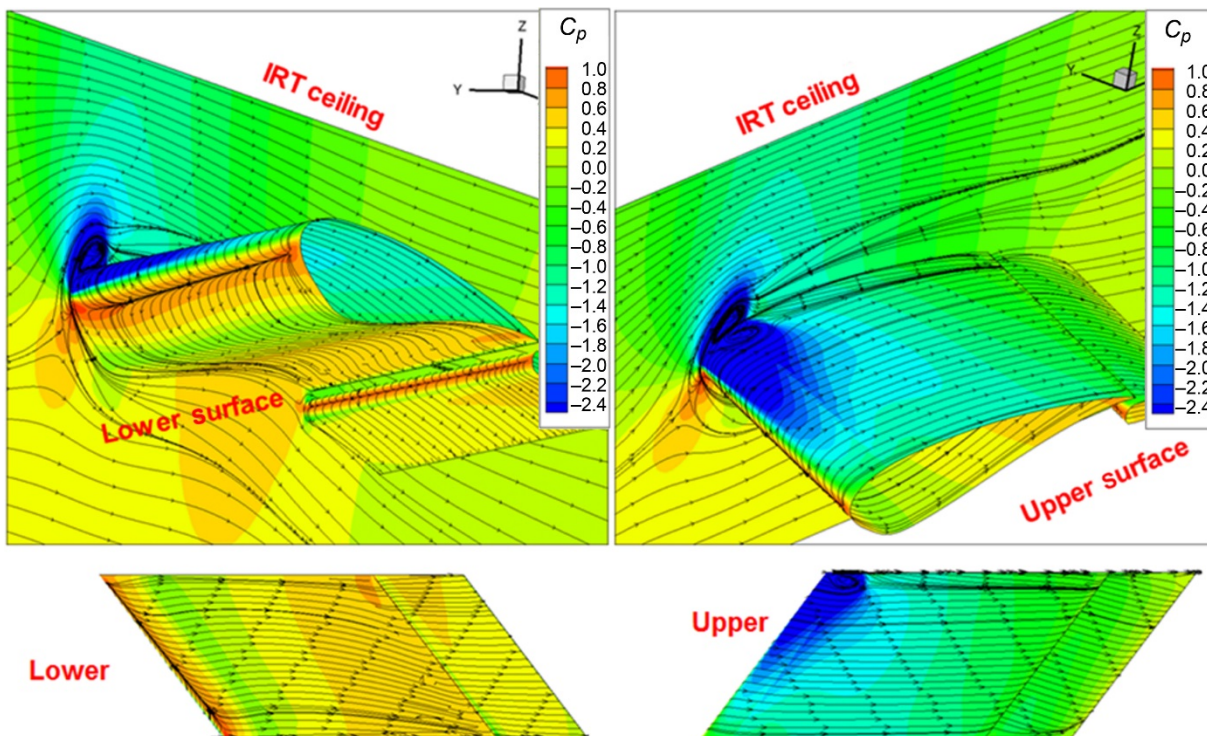


Figure 24.—Inboard hybrid wing model 3D RANS simulation in Icing Research Tunnel (IRT) indicating pressure coefficient  $C_p$  where angle of attack  $\alpha = 3.67^\circ$ , flap angle  $\delta = 6^\circ$ , and Reynolds number  $Re = 3.45 \times 10^7$ .

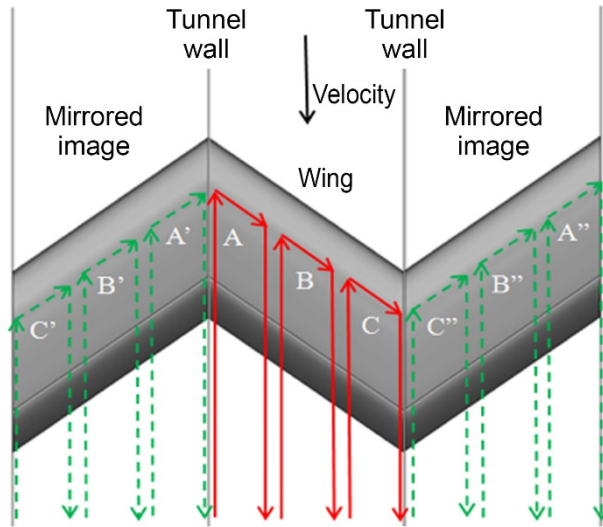


Figure 25.—Lifting-line theory representation of swept-wing model bounded by sidewalls.

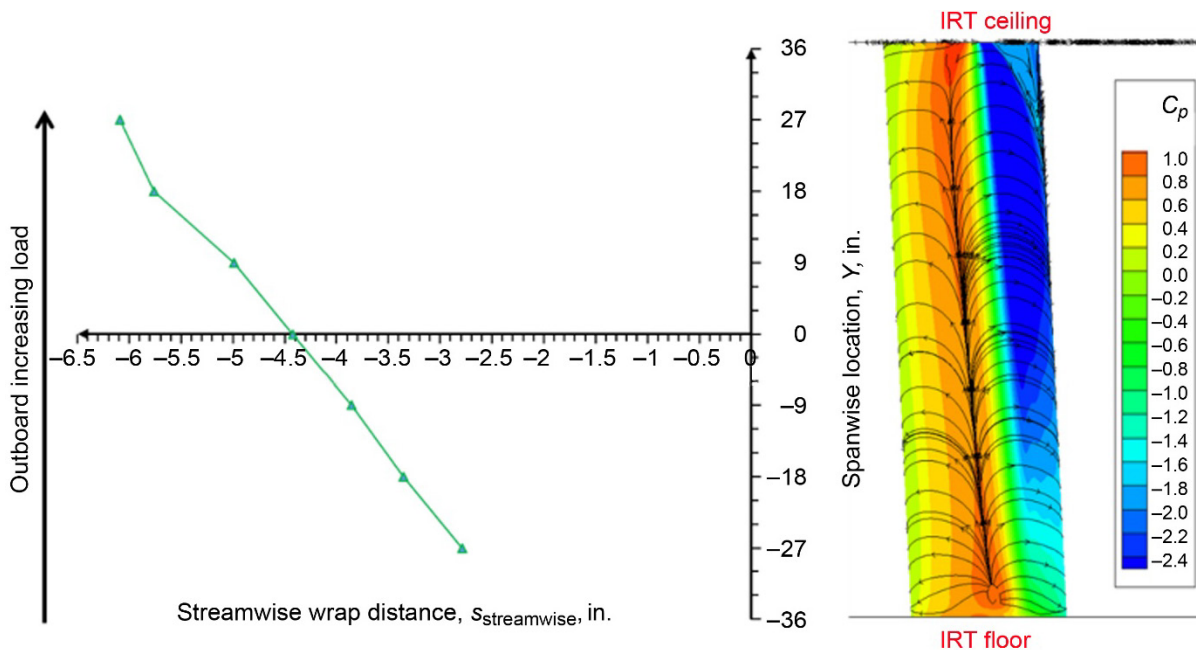


Figure 26.—Inboard hybrid wing model 3D RANS simulation in the Icing Research Tunnel (IRT) indicating pressure coefficient  $C_p$  and attachment line location at angle of attack  $\alpha = 3.67^\circ$  and flap angle  $\delta = 6^\circ$ .

The influence of spanwise load variation on the attachment line location can be observed in Figure 26. The abscissa presents the dimensional wrap distance in inches from the model’s frontmost point, also referred to as the “highlight,” to the attachment line. The ordinate presents the spanwise position in inches, with the IRT floor at  $-36$  in. and ceiling at  $+36$  in. The CFD RANS solution with pressure contours for the same case is shown at the right.

The attachment line moves a significant distance around the leading edge of the model across the entire span from floor to ceiling. However, the ice shapes will only be documented in approximately the 6 in. above and below the tunnel centerline due to the time required for documentation and the questionable

uniformity of the icing cloud away from the centerline. With that reasoning, the attachment line location over only the center 12 in. of the IRT was considered when determining if the variation was acceptable. For the Inboard model, the attachment line location varies by approximately 0.75 in. over that spanwise distance, and the attachment line for the Midspan and Outboard models changes by less than 0.4 in. Considering that the streamwise chord of the Inboard model is approximately 162 in., these variations were deemed acceptably small. Reference 16 (included as Appendix C) describes computational studies to further understand and mitigate the variation in attachment line location on these swept models. However, the complications those mitigation techniques would have imposed on the model design were determined to be not worth the additional effort.

The size of the hybrid designs are ultimately constrained by two competing factors:

**(1) IRT load and overall dimensions limit scale factor (lower limit)**

The upper limit for the hybrid wing model dimension is bounded by the size of the IRT test section. But the maximum IRT load acceptable on the aerodynamic force balance and turntable also provide an upper bound for the model. The higher the scale factor, the smaller the model and, consequently, the less wind tunnel blockage it presents. Shorter models also lead to lower loads as they generate circulation closer to the leading edge, as observed in 2D hybrid airfoils (Ref. 16). An aircraft manufacturer often uses full-scale leading-edge models to investigate anti-icing system design and requirements. In this case, maintaining a full-scale leading edge is critical, so scaling down the model is not an option.

**(2) Risk of flow separation limits scale factor (upper limit)**

Unfortunately, models cannot have arbitrarily large scale factors, posing a lower limit for the size of the models. Models with higher scale factors have shorter aft sections to transition from the full-scale leading edge to the truncated trailing edge. This presents a challenge to make a smooth geometric transition from leading edge (thick) to trailing edge and diminishes the chord length available to recover pressure, which increases the risk of flow separation on the model.

### **5.3 Task 4.3: Refine Design and Flap Schedule With 3D RANS Simulations**

As described previously, the hybrid airfoil from which the swept models were extruded was designed in 2D using sweep theory (Ref. 15). This design was validated using 2D RANS simulations used to calculate the stagnation point locations of different angles of attack and flap deflections that generated the aerocal plots described in Section 4.4. These 2D aerocals were used to estimate what flap angle was needed to match IRT centerline attachment line positions on the swept models to those of the full-scale CRM65 wing at the respective station assuming the model is at the same angle of attack as the reference wing station.

When 3D flow simulations in the IRT were performed, the centerline attachment line position on the model was measured in the streamwise direction (consistent with the CFB OVERFLOW data extracted, Table VI) and added to the aerocal plots. These are referred to as “3D aerocal plots.” This does not imply that all the information on these plots is from 3D simulations, but rather that they include some single-point 3D results. The bulk of the simulations on a given aerocal were generally from 2D simulations (in the normal direction), which were used to cover a larger range of configurations due to the computational efficiency of running 2D RANS simulations. Overlaying the 3D simulation results at the tunnel centerline on the 2D results allows trends between 2D and 3D to be identified. The 2D data can then be used more effectively to predict 3D behavior for  $\alpha$ - $\delta$  pairs that have not yet been run.

The 3D aerocal plot for the Outboard station is given in Figure 27. Outboard RANS simulations performed in 2D are shown in black and are connected by lines of constant flap deflection. The 3D RANS simulations of the Outboard hybrid in the IRT are shown as blue triangles and are labeled for their respective flap deflections. Attachment line positions for the Outboard station of the CFB from the OVERFLOW solutions, Table VI, are represented by red circles and are labeled for each respective WB case.

TABLE VI.—STREAMWISE WRAP DISTANCES FROM HIGHLIGHT TO ATTACHMENT LINE LOCATIONS FOR CLEAN FLIGHT BASELINE (CFB)

Case	Angle of attack, $\alpha$ , deg	CFB, 3D RANS (OVERFLOW), streamwise wrap distance $s_{\text{streamwise}}$ , in.		
		Inboard	Midspan	Outboard
WB25	1.7	-1.85	-0.29	-0.21
WB52	2.1	-3.00	-0.61	-0.33
WB39	3.6	-4.32	-1.15	-0.85
WB33	3.7	-4.32	-1.34	-0.85
WB41	4.4	-4.81	-1.76	-1.15
WB47	4.4	-4.81	-1.76	-1.15
WB71	4.4	-4.81	-1.76	-1.15

The 3D RANS simulations for the Outboard hybrid wing aerocal were performed with the purpose of matching the stagnation point positions of the Outboard station that presented the largest streamwise wrap distances, as shown in Table VI. This was done to minimize the number of 3D RANS simulations needed to check that the hybrid wing model was capable of reaching all target conditions. In addition, a flap margin study was performed to ensure that the model could reach wrap distances greater than those listed in Table VI before stalling. This was done to allow for uncertainty in the CFD simulations modeling the tunnel effects and in anticipation of issues that could occur during the test.

The 2D RANS simulations predicted a flap deflection of about  $10^\circ$  for the Outboard model to match conditions WB33/39 ( $s_{\text{streamwise}} = -0.85$  in.) and about  $12^\circ$  to match conditions WB 41/47/71 ( $s_{\text{streamwise}} = -1.15$  in.), which provided approximately the same results as the 3D RANS simulations. The word “approximately” is used intentionally because the 3D RANS simulations were not performed at the exact flap deflections represented by the red circles of the CFB. Instead, because the 3D simulations were very time-consuming, the simulations were done at a few key chosen conditions that would show that the hybrid wing design could match the target stagnation point locations with some margin. The 3D RANS results are indicated in Figure 27 by the blue triangles.

The 3D aerocal plot for the Midspan station is displayed in Figure 28. The 2D RANS simulations that form the basis of the aerocal are shown in black and are connected by lines of constant flap angle. Simulations performed using 3D RANS in the IRT are designated with blue triangles and are individually labeled to identify the corresponding flap angle. Finally, the attachment line position at the Midspan station of the CFB based on the OVERFLOW solutions are represented with red markers and labeled based on the corresponding case identifier. Because the intent of many of the 3D simulations was to match centerline attachment line positions with the reference wing at the respective station, most of the 3D results are clustered near the CFB data.

The 2D RANS simulations predicted a flap deflection of about  $9^\circ$  for the Midspan model to match condition WB33 ( $s_{\text{streamwise}} = -1.34$  in.) and about  $13^\circ$  to match conditions WB 41/47/71 ( $s_{\text{streamwise}} = -1.76$  in.), whereas the 3D RANS simulations predicted about  $13^\circ$  and  $17^\circ$ , respectively. Although the Midspan model was similar in size to the Outboard model, its corresponding CFB target stagnation point was farther down the leading edge, requiring more lift to be generated by the Midspan model in comparison with the Outboard model. Higher lift caused a larger interaction between the model surface pressure and the wind tunnel sidewall (IRT ceiling), explaining the larger deviation between the 2D and 3D RANS simulations for the Midspan model. This was a particularly important lesson learned when designing the Inboard model.

The 3D aerocal plot for the Inboard station is displayed in Figure 29. The Inboard model was significantly different than its predecessors, and the 2D to 3D design process was well understood at the time the calculations were performed. After noticing how the 2D RANS and 3D RANS data differed for the other two models, and particularly for the Inboard model, 2D aerocal simulations were not performed on this model, so no 2D data are shown on the plot.



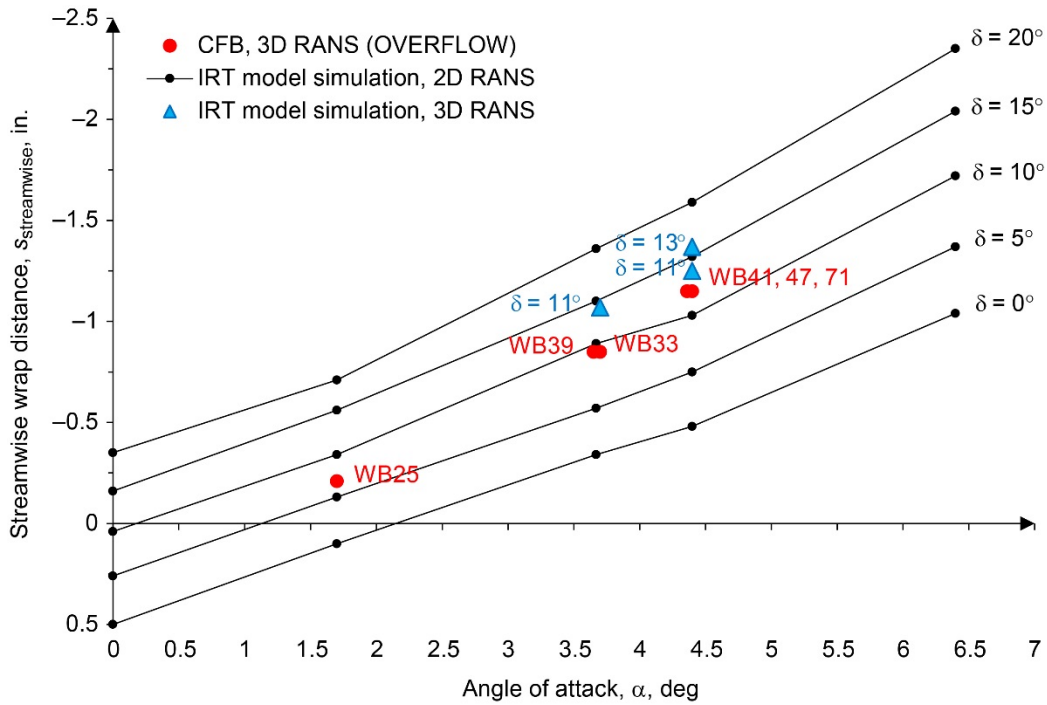


Figure 27.—Outboard model 3D aerodynamic calibration plot with 2D and 3D data in streamwise direction.

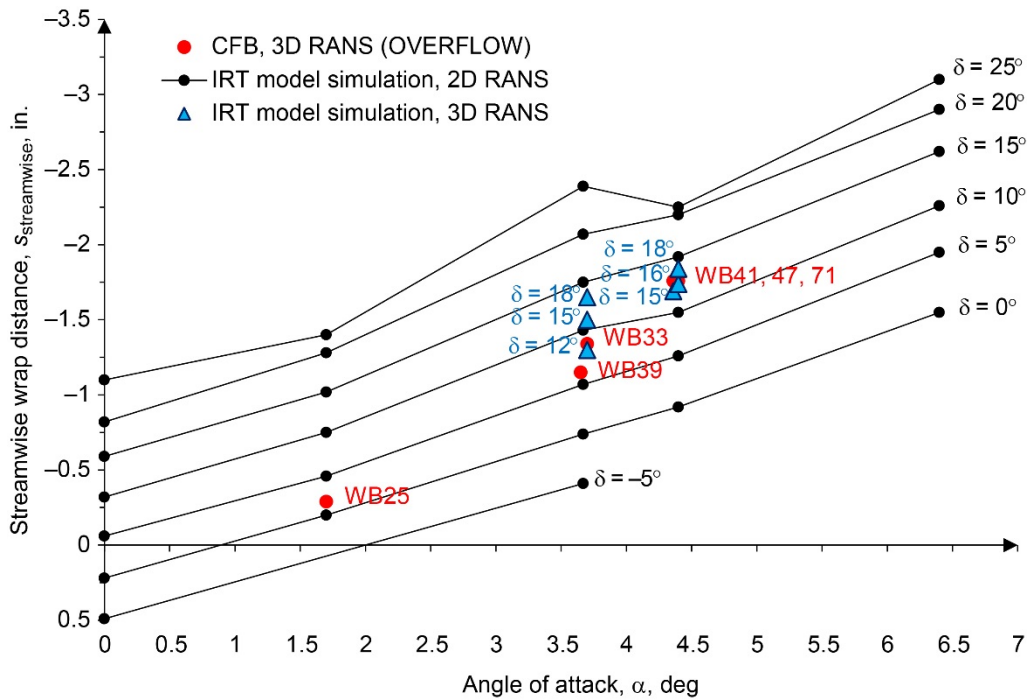


Figure 28.—Midspan model 3D aerodynamic calibration plot with 2D and 3D data in streamwise direction.

The 3D RANS simulations predicted a flap deflection of about  $6^\circ$  for the Inboard model to match conditions WB33/39 ( $s_{\text{streamwise}} = -4.32$  in.) and about  $5^\circ$  to match conditions WB 41/47/71 ( $s_{\text{streamwise}} = -4.81$  in.). It is important to note that the 3D RANS simulations performed for the Inboard model were never fully converged (five decades' decay in the continuity equation residuals). This could be due to the generation of poor meshes and lack of experience in better meshing techniques, the solver

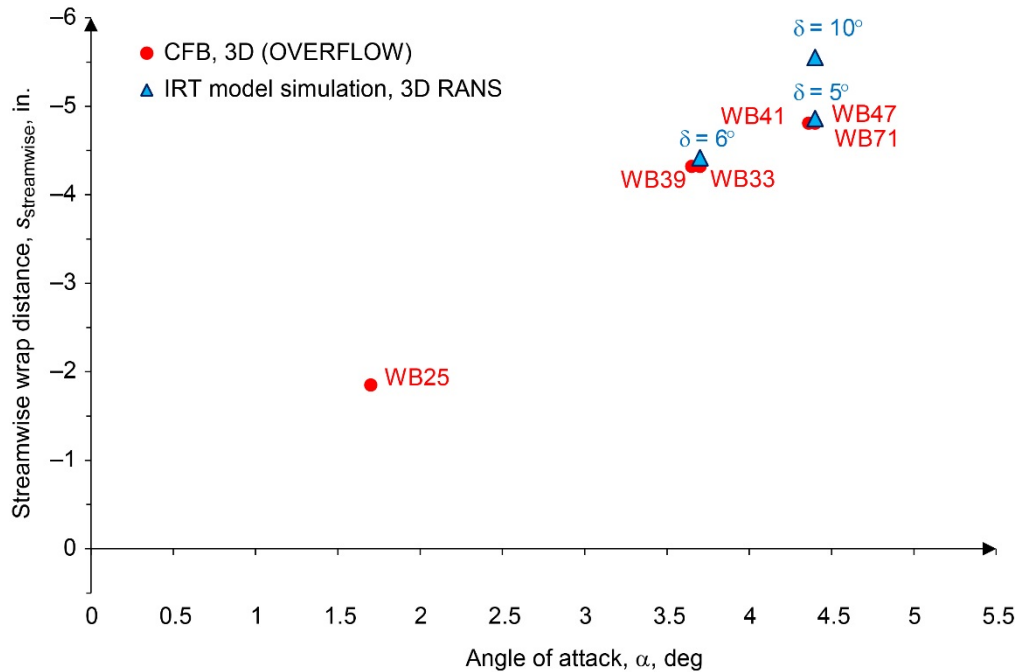


Figure 29.—Inboard model 3D aerodynamic calibration plot with 3D data in streamwise direction.

used (ANSYS Fluent 14.6), or the convergence difficulty where portions of the flow field were separated near the model-tunnel ceiling region. These factors combined yielded the least amount of confidence in the predicted flap deflections needed for the Inboard model to match the target conditions of Table VI, based on the 3D RANS simulations performed.

An alternative method for designing this model, discussed in the recommendations of Section 6.2, can minimize the time spent on the 2D hybrid airfoil design. This approach can save significant time spent on 2D RANS simulations to give more focus to the 3D design that is more representative of the actual 3D swept hybrid wing inside the wind tunnel section.

The 3D RANS simulation solutions of the Outboard, Midspan, and Inboard hybrid models in the IRT were processed in many ways, a few of which are presented in Figure 27, Figure 28, and Figure 29, where the models were simulated with different angles of attack and flap deflections, most of them targeting the conditions listed on Table IV and Table VI. Figure 30 features pressure contours and streamlines on the Outboard model in the IRT with multiple view angles of a 3D RANS simulation targeting condition WB33 (Table IV) with an angle of attack of  $\alpha = 3.67^\circ$  and a flap deflection of  $\delta = 13^\circ$ . Figure 31 shows the same for the Midspan model, with an angle of attack of  $\alpha = 3.67^\circ$  and a flap deflection of  $\delta = 15^\circ$ . As displayed, the flow is well behaved in almost the entire domain, with the only major area of concern being at the leading edge of the upper surface of the model where it meets the wall. As with nearly all other hybrid simulations performed (for all three models), a separation bubble can be seen in the junction of the model with the IRT. Figure 32 presents a comparison of pressure distributions from both 3D RANS simulations in the IRT over three spanwise positions and OVERFLOW solutions of the CFB at the corresponding sections. Negative  $y$ -valued lines represent those cuts below the centerline of the tunnel, while positive values indicate cuts above the tunnel centerline, which has a position of zero. Values are in inches. The pressure distribution varies significantly over the span of the tunnel, with an increasing load toward the top of the model, where the highest pressure cut shows signs of flow separation. Overall, the hybrid models nearly match the pressure distribution of the CFB near the leading edge. An example of the 3D RANS simulations for the Inboard model was shown in Figure 24.

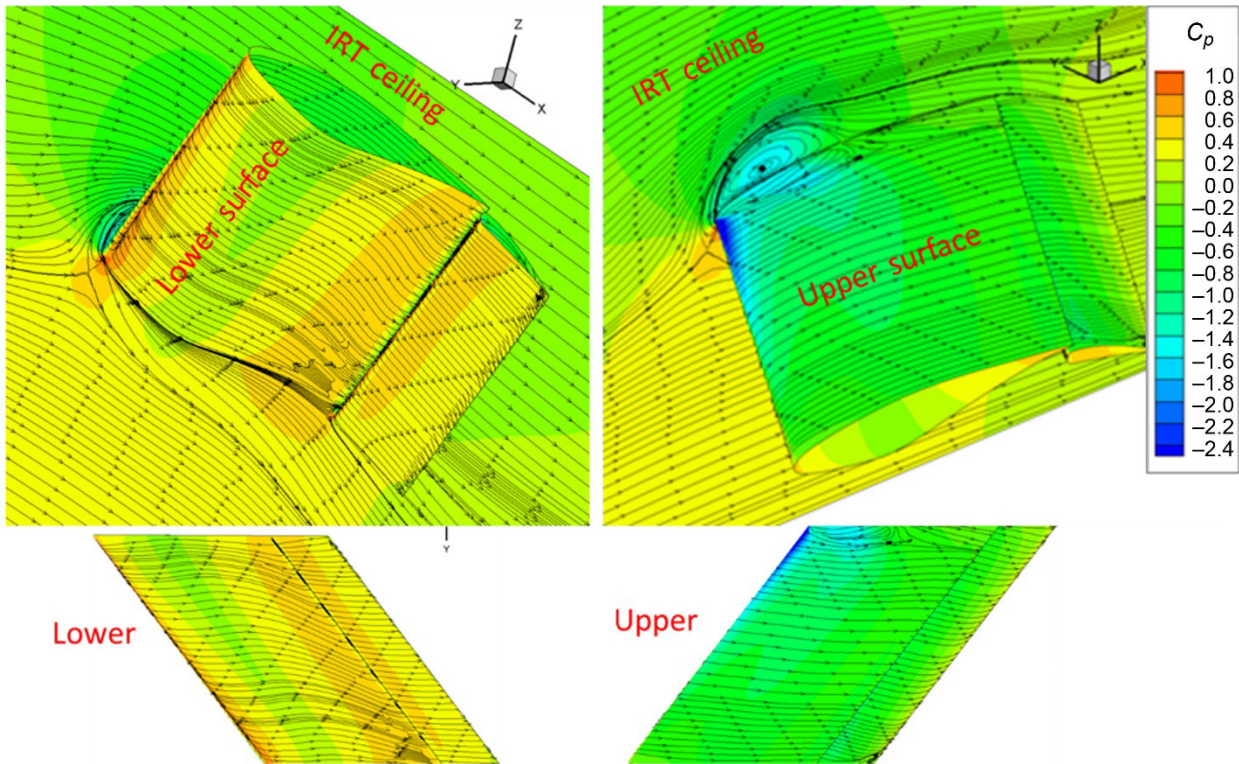


Figure 30.—Outboard hybrid wing model 3D RANS simulation in Icing Research Tunnel (IRT) indicating pressure coefficient  $C_p$  where angle of attack  $\alpha = 3.67^\circ$ , flap angle  $\delta = 13^\circ$ , and Reynolds number  $Re = 1.59 \times 10^7$ .

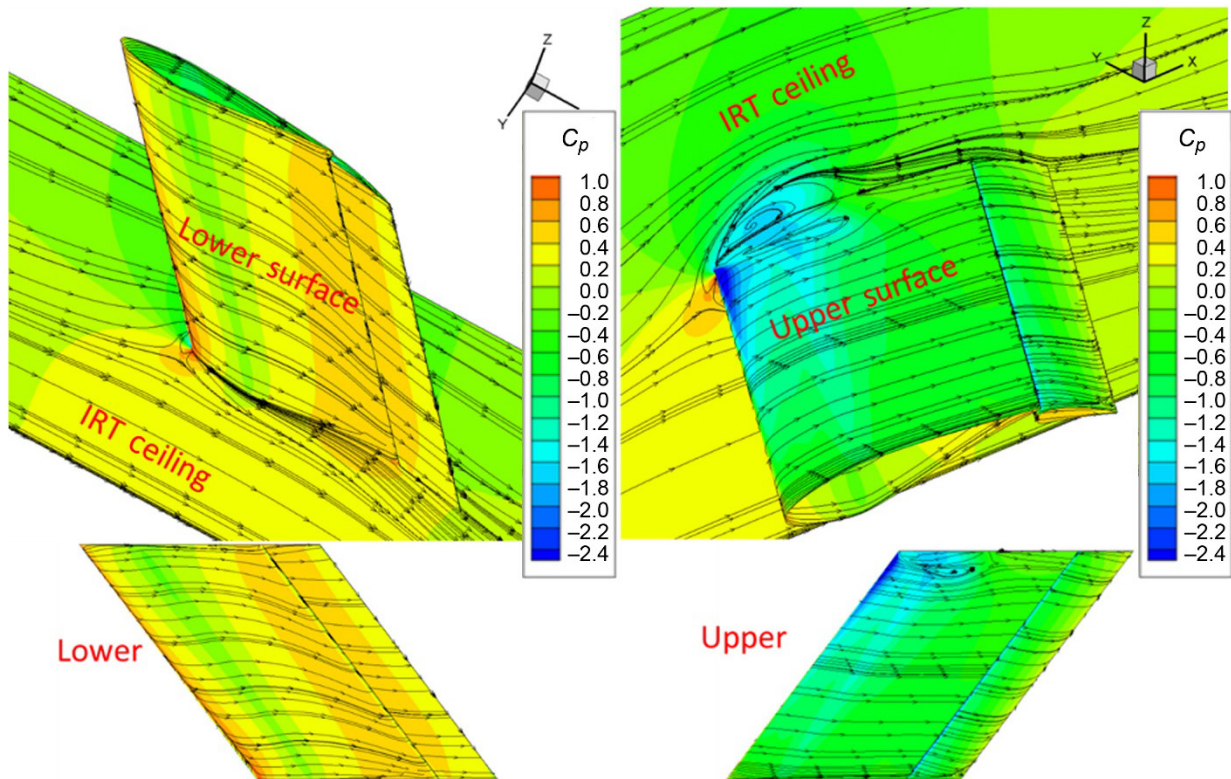


Figure 31.—Midspan hybrid wing model 3D RANS simulation in Icing Research Tunnel (IRT) indicating pressure coefficient  $C_p$  where angle of attack  $\alpha = 3.67^\circ$ , flap angle  $\delta = 15^\circ$ , and Reynolds number  $Re = 1.60 \times 10^7$ .

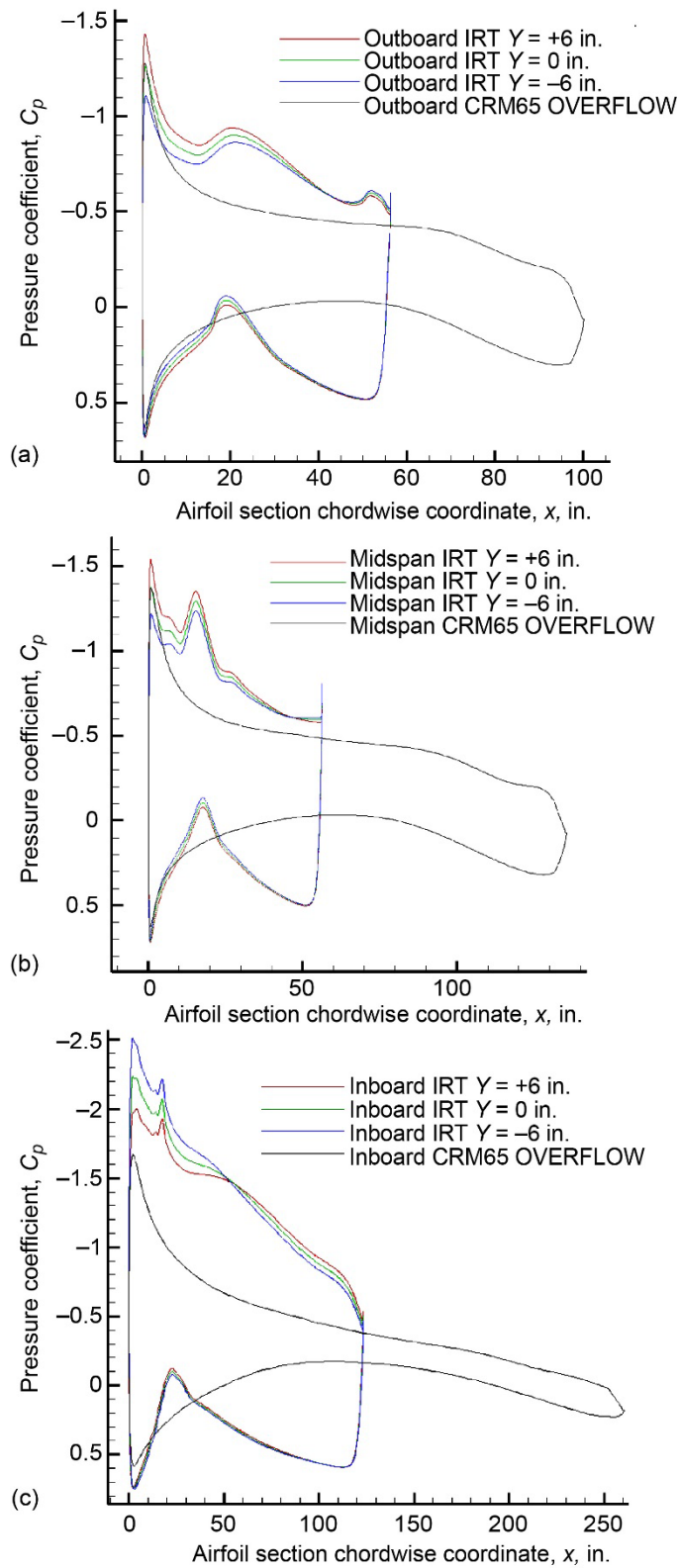


Figure 32.—Pressure coefficient  $C_p$  streamwise cuts at  $Y = -6, 0, +6$  in. for (a) Outboard, (b) Midspan, and (c) Inboard models compared with streamwise cuts from CRM65 for case WB33.

#### 5.4 Task 4.4: Apply DES- $k\omega$ to IRT Models to Assess Method and Flow Physics

This task was moved to year 3.

#### 5.5 Task 4.5: Apply LEWICE3D to IRT Models and Perform Comparisons

To validate the swept hybrid model designs, flow field and icing simulations were performed on each of the three models for selected conditions of Table IV. The flow fields were generated with Fluent, as described previously, and the ice shapes were then generated using LEWICE3D (TRAJMC3D version 2.47). Comparing the resulting ice shapes near the centerline of the IRT to those from the respective IFB case at the appropriate station allowed evaluation of the performance of the hybrid wing models in predicting the full-scale ice accretion.

Three test cases were selected for evaluating the models. Case WB33  $T = -4$  was selected because it had an attachment line location, airspeed, and angle of attack near the average of all the cases, making it a good candidate for general testing. Case WB71  $T = -6$  was selected for having the largest IFB aircraft angle of attack and an attachment line location that was farthest down the leading edge, requiring the most aggressive  $\alpha$  and  $\delta$  settings in the tunnel. The warmer temperatures for these two cases also produce glaze ice shapes with large upper horns that were sensitive to the local heat transfer coefficient, making it easier to determine when a good ice shape match was achieved. Case WB47  $T = -6$  was also used in this research because the flight speed for this case exceeds the assumed IRT test section velocity limit of 250 kn (128.6 m/s). This provided an opportunity to investigate icing scaling methods in the case of the wind tunnel conditions being unable to match flight velocity. Results are shown for case WB 33  $T = -4$  for all three models; additional cases are shown only for the Midspan model to illustrate the comparison. Table VII compares the conditions for the IRT simulations with those from the baseline analyses for the cases described above.

TABLE VII.—MIDSPAN MODEL FLOW FIELD AND ICING CONDITION COMPARISONS OF ICED FLIGHT BASELINE (IFB) WITH ICING RESEARCH TUNNEL (IRT) SIMULATIONS FOR THREE CASES

Condition	Case					
	WB33 $T = -4$		WB47 $T = -6$		WB71 $T = -6$	
	IFB	IRT	IFB	IRT	IFB	IRT
Static pressure, $P_{amb}$ , kPa	69.702	90.011	57.209	88.658	95.956	91.882
Air density, $\rho$ , kg/m <sup>3</sup>	0.9027	1.1653	0.7464	1.1563	1.2519	1.1984
Reynolds number based on model chord, $Re_c$ , $\times 10^6$	28.9	16.0	28.1	17.2	35.2	14.5
Airspeed, $V$ , m/s	119.41	119.41	139.6	128.61	104.51	104.51
Static temperature, $T_{amb}$ , °C	-4	-4	-6	-6	-6	-6
Mach number (M)	0.363	0.363	0.426	0.393	0.319	0.319
Liquid water content, g/m <sup>3</sup>	0.551	0.551	0.509	0.467	0.509	0.509
Median volumetric diameter, $\mu\text{m}$	20	20	20	20.88	20	20
Droplet distribution	Langmuir D	10-bin IRT	Langmuir D	10-bin IRT	Langmuir D	10-bin IRT
Icing time, min	45	45	45	53.3	15	15
Angle of attack, $\alpha$ , deg	3.67	3.67	4.36	4.36	4.4	4.4
Flap angle, $\delta$ , deg	NA	15	NA	16	NA	15

While the LEWICE3D simulations for the IFB were performed at pressure altitude listed on Table IV and utilized a Langmuir D (Ref. 23) droplet size distribution consistent with that found in flight conditions, the hybrid wing models were simulated utilizing the IRT pressure and the 10-bin IRT droplet size distribution based on the values measured experimentally inside the IRT by Papadakis et al. (Ref. 43) in 2004,<sup>1</sup> with the exception of the Inboard hybrid wing model, which had to be simulated utilizing a monodisperse droplet size distribution due to memory limitations of the Taub supercomputer cluster at the University of Illinois. The differences between the CFB/IFB simulations and those done in the IRT are detailed in Table VII.

Figure 33, Figure 34, and Figure 35 show comparisons in ice shape and collection efficiency between the LEWICE3D simulations of the IFB and the three models in the IRT for case WB33  $T = -4$ . The ice shapes for the IRT hybrid wing models are shown in 3D view for Figure 33(a) for the Inboard model, Figure 34(a) for the Midspan model, and Figure 35(a) for the Outboard model, where the squares indicate the stagnation point location for the respective cuts near the centerline of the tunnel. The same three ice shapes near the centerline of the tunnel are also displayed in 2D view in comparison with the corresponding IFB ice shape in Figure 33(b), Figure 34(b), and Figure 35(b) for the Inboard, Midspan, and Outboard models, respectively. Overall, good agreement was observed in the ice shape comparison, meaning horn lengths were within about 20 percent and horn angles were within the variation of the three cuts near the centerline ( $\pm 6$  in.). Local collection efficiencies between the IFB and IRT simulations are displayed in Figure 33(c), Figure 34(c), and Figure 35(c) for the Inboard, Midspan, and Outboard models, respectively, in which location and magnitude of the collection efficiency peak were in good agreement, with the exception of the Inboard model, which presented the poorest agreement among the three models. This could be attributed to a few different factors, including the lack of a satisfactorily converged CFD 3D RANS solution for the Inboard model, the inability to simulate the model with a 10-bin IRT droplet distribution in LEWICE3D, and higher pressure and density at the IRT that led to higher heat transfer coefficients and larger horn lengths.

Figure 36, Figure 37, and Figure 38 show the centerline ice shapes on the Midspan model for the three cases detailed in Table VII as well as the ice shapes at 6 in. above and below the centerline. The effect of the spanwise variation in the attachment line on the ice shape can be seen in Figure 33 to Figure 38. These variations were no larger than the variation between the centerline ice shape from the IRT simulations and the IFB. Generally, the agreement between ice shapes from the IFB and the hybrid models is quite good.

---

<sup>1</sup>Although it was later determined that the 10-bin IRT droplet size distribution is not really representative of the actual IRT spray system, it was deemed appropriate for the model-design simulations.

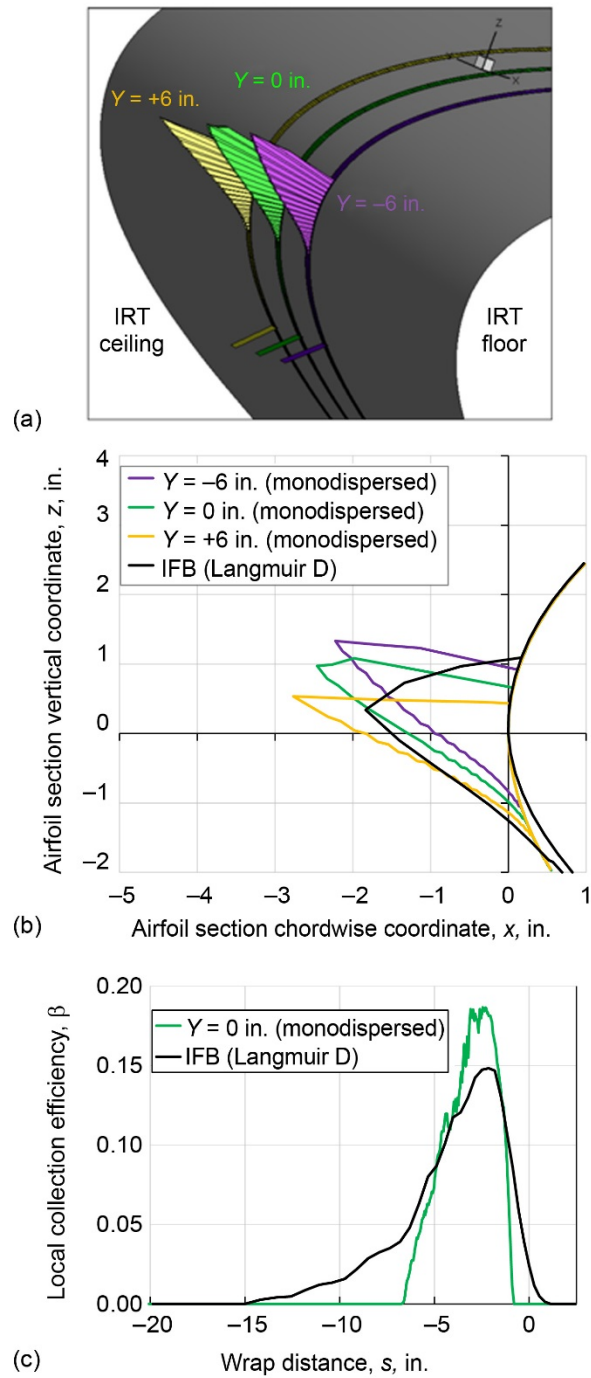


Figure 33.—Inboard model LEWICE3D simulations, case WB33  $T = -4$  where angle of attack  $\alpha$  is  $3.67^\circ$  and flap angle  $\delta$  is  $6^\circ$ . (a) IRT (Icing Research Tunnel) ice shapes. (b) IRT ice shape compared with iced flight baseline (IFB). (c) IRT collection efficiency compared with IFB.

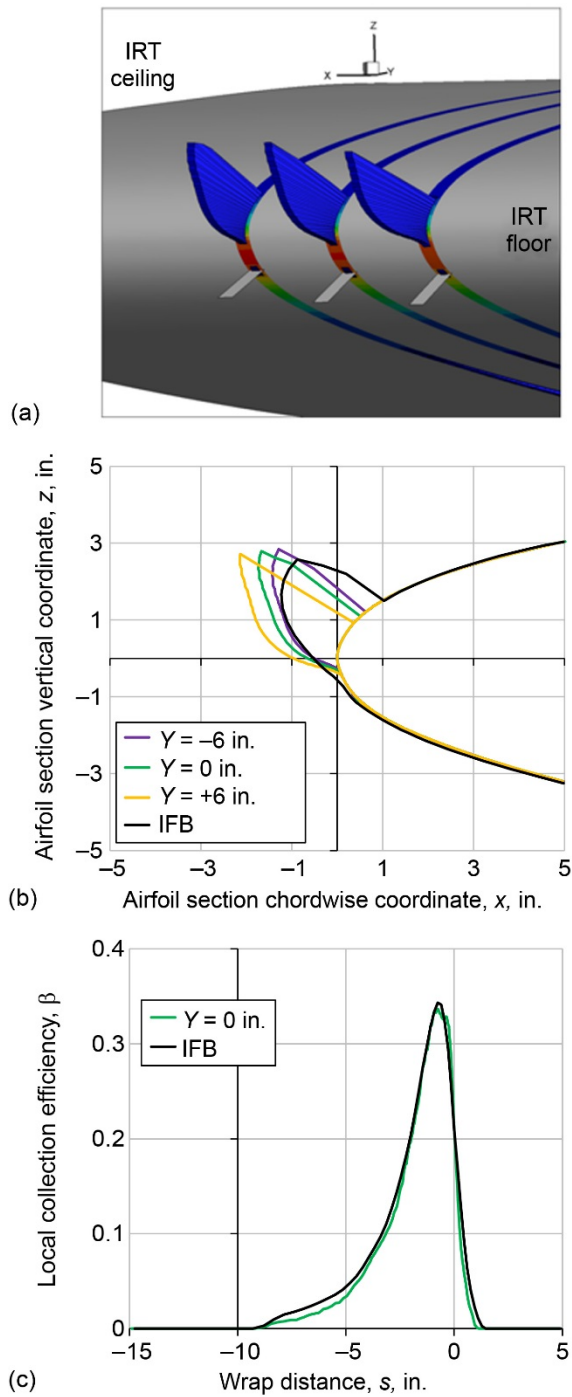


Figure 34.—Midspan model LEWICE3D simulations, case WB33  $T = -4$  where angle of attack  $\alpha$  is  $3.67^\circ$  and flap angle  $\delta$  is  $15^\circ$ . (a) IRT (Icing Research Tunnel) ice shapes. (b) IRT ice shape compared with iced flight baseline (IFB). (c) IRT collection efficiency compared with IFB.



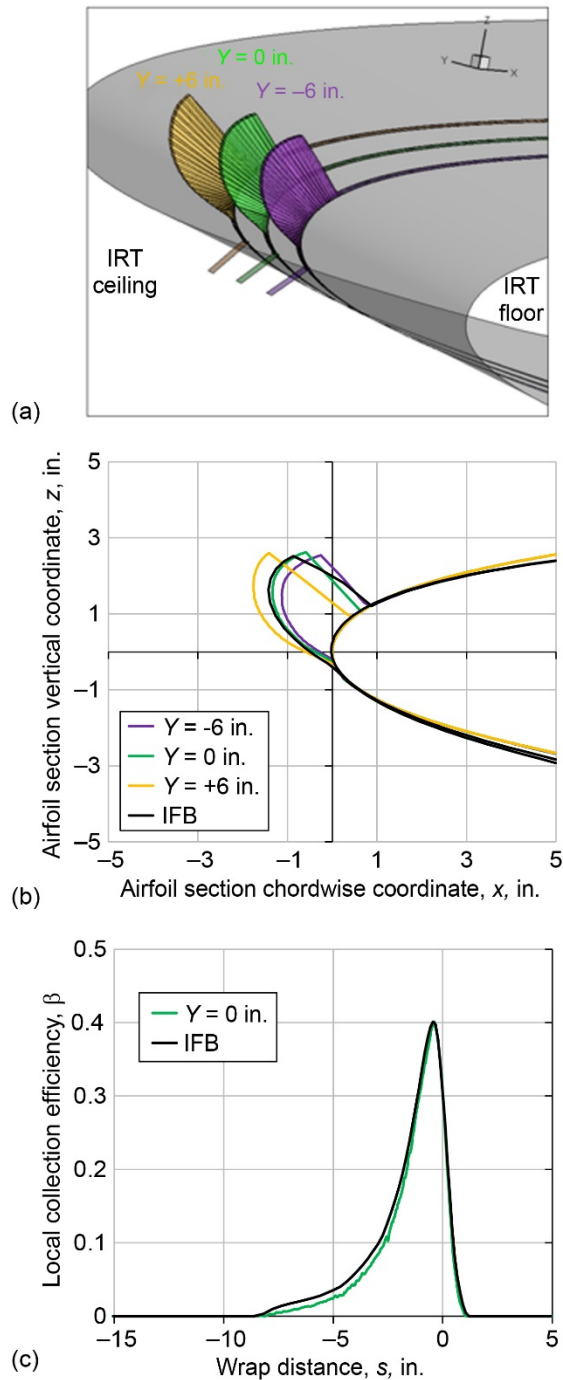


Figure 35.—Outboard model LEWICE3D simulations, case WB33  $T = -4$  where angle of attack  $\alpha$  is  $3.67^\circ$  and flap angle  $\delta$  is  $11^\circ$ . (a) IRT (Icing Research Tunnel) ice shapes. (b) IRT ice shape compared with iced flight baseline (IFB). (c) IRT collection efficiency compared with IFB.

The discrepancies seen in Figure 36, Figure 37, and Figure 38 between the hybrid model ice accretions and those from the IFB can be attributed to a few different factors. First, the simulations done for the hybrid models were performed at IRT pressure, while the IFB simulations were done at pressure altitude. Other factors also play a role in causing the different ice accretions. To explain some of the discrepancies between the hybrid models and the IFB, the local collection efficiency and heat transfer coefficient for case WB33  $T = -4$  are presented in Figure 39 for simulations done for the hybrid models utilizing both the local IRT pressure and the pressure altitude of the IFB.

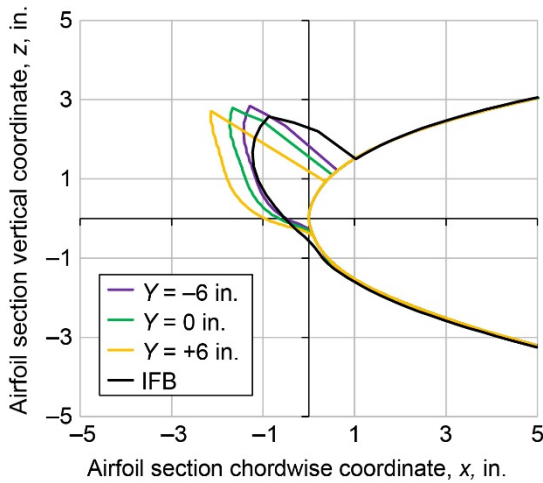


Figure 36.—Midspan model ice shapes for case WB33  $T = -4$  where angle of attack  $\alpha$  is  $3.67^\circ$  and flap angle  $\delta$  is  $15^\circ$  at Icing Research Tunnel (IRT) pressures and iced flight baseline (IFB) at pressure altitude.

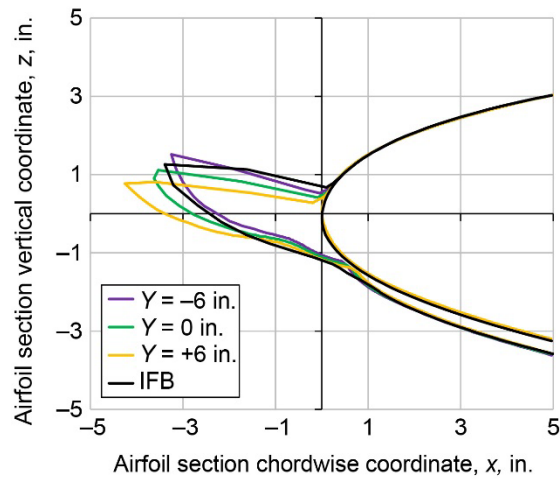


Figure 37.—Midspan model ice shapes for case WB47  $T = -6$  where angle of attack  $\alpha$  is  $4.36^\circ$  and flap angle  $\delta$  is  $16^\circ$  at Icing Research Tunnel (IRT) pressures and iced flight baseline (IFB) at pressure altitude.

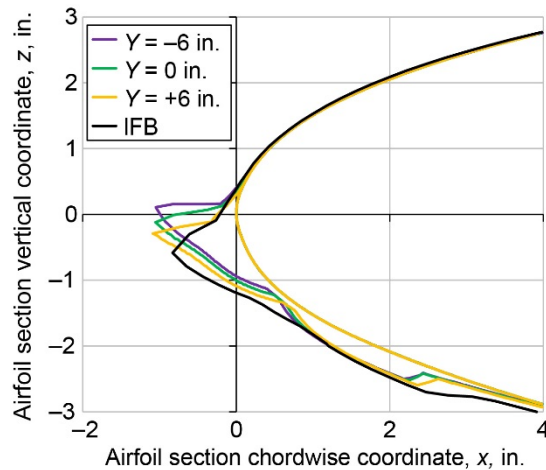


Figure 38.—Midspan model ice shapes for case WB71  $T = -6$  where angle of attack  $\alpha$  is  $4.40^\circ$  and flap angle  $\delta$  is  $15^\circ$  at Icing Research Tunnel (IRT) pressures and iced flight baseline (IFB) at pressure altitude.

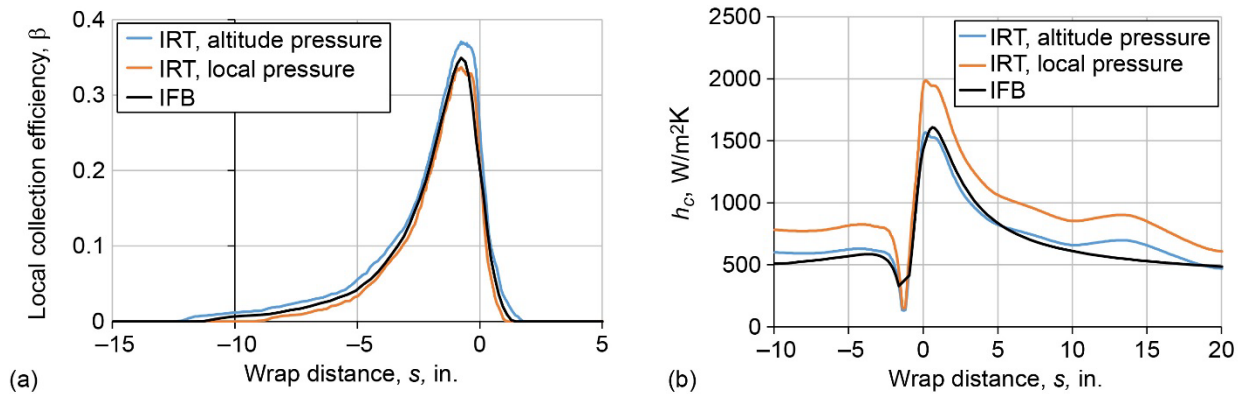


Figure 39.—Midspan model comparison of (a) local collection efficiency  $\beta$  and (b) convective heat transfer coefficient  $h_c$  for case WB33  $T = -4$  in Icing Research Tunnel (IRT) at IRT (local) and iced flight baseline (IFB) (altitude) pressures.

When running the LEWICE3D simulation of the IRT model at the same pressure as the flight condition (IFB), the local collection efficiency peak,  $\beta_{\max}$ , on the IRT model is somewhat higher than that of the IFB, whereas the heat transfer coefficient,  $h_c$ , is well matched. This results in a larger horn due to the extra impinging mass of water in the horn area of the model upper surface. The  $\beta_{\max}$  value is likely larger due to the lower maximum thickness of the hybrid model as compared with the baseline airfoil. For a hybrid model, geometry similitude is achieved by retaining the full-scale geometry at the leading edge, but the full-scale geometry can only be maintained over a small portion of the airfoil, up to the leading-edge extents. The leading-edge extents are generally selected based on the expected impingement limits. Beyond these points the leading edge is blended with the redesigned aft section of the model. Because the leading-edge extents rarely extend to the point of maximum thickness on the airfoil, this usually results in a hybrid model with a lower maximum thickness than the reference airfoil. The differences between the thickness of the hybrid and the thickness of the full-scale airfoil are shown in Table V. For the Inboard model, the difference in total thickness is significant, resulting in loss of about half of the total full-scale thickness. Streamlines and droplet trajectories upstream of a thick geometry are influenced more than for a thinner body. Thus, icing cloud droplets impinge on the leading edge of the airfoil at a lesser rate for thicker airfoils in comparison with thinner ones. For this reason, hybrid models often result in higher  $\beta_{\max}$  than the reference geometry for the same conditions because the hybrid is substantially thinner than the reference geometry it represents. Such a trend of higher  $\beta_{\max}$  for the hybrid models compared with the corresponding full-scale stations was seen in the icing simulation results for cases WB33  $T = -4$ , WB47  $T = -6$ , and WB71  $T = -6$  (see Figure 36, Figure 37, and Figure 38).

Additionally, when the IRT model is simulated at the local atmospheric pressure, the effects are reversed with a well-matched  $\beta$  distribution but considerably higher  $h_c$ . This also leads to a larger horn on the IRT model than the IFB because more of the water that impinges near the horn region is frozen due to the higher heat transfer. The increase in magnitude of the heat transfer is caused by the higher density of the air at the IRT and is the most apparent effect of altitude. Thus, attempting to match either the IFB  $\beta$  by simulating the IRT model at the IFB pressure or to match the IFB  $h_c$  by simulating the IRT model at the local elevation pressure yields similar ice accretions that both have longer horns than the IFB.

The ice shapes for the Outboard and Inboard models at their design angle of attack and flap deflection were shown in Figure 35 and Figure 33. The ice shape on the Outboard model matches the IFB well at the centerline of the IRT. As discussed previously, the Inboard model ice shapes have a longer horn length compared with the IFB due to the difference in total thickness of the model compared with the full-scale baseline.

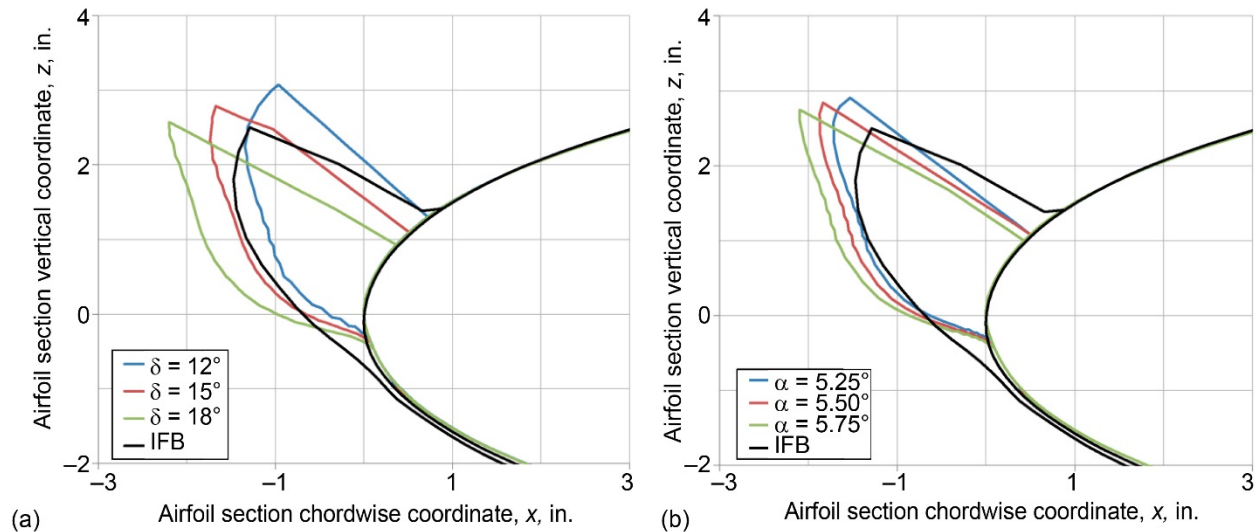


Figure 40.—Effect of attachment line location on centerline ice shape of Midspan model compared with iced flight baseline (IFB) (condition WB33  $T = -4$ ). (a) Different flap angles  $\delta$  where angle of attack  $\alpha = 3.67^\circ$ . (b) Different angles of attack  $\alpha$  where flap angle  $\delta = 5.0^\circ$ .

The effect of the position of the attachment line is illustrated in Figure 40 for the Midspan model. For the same input flow conditions, the changing angle of attack or flap deflection angle changes the location of the attachment line at the centerline of the IRT. As discussed previously in the 2D analysis, the attachment line location has a first-order effect on the ice shape that forms on the airfoil or wing. Either method for changing the attachment line location (changing the geometric angle of the model or moving the flap) can be used. Figure 40 illustrates the ice shape variations that result from changing the attachment line location.

The appendixes include additional LEWICE3D calculations for studies that investigated spanwise ice shape variation due to changes in attachment line location, the necessity of setting the proper geometric angle of attack compared with simply setting the desired attachment line location, and formation of ice shapes for stations along the baseline model for locations other than the three for which models are being constructed.

## 5.6 Task 4.5: Perform 3D Similitude Studies

A preliminary investigation of one similitude method was performed for a single test case on the Midspan model. The IRT flow and icing conditions for case WB47  $T = -6$  were adjusted to match several dimensionless parameters according to the method summarized by Tsao and Lee (Ref. 44). The modified inertia parameter,  $K_0$ , for the IRT is matched to the full-scale value in order to maintain droplet trajectory similitude. This was done by adjusting the MVD for the IRT simulation. Next, the stagnation point freezing fraction,  $n_0$ , was matched by adjusting LWC. Finally, the accumulation parameter,  $A_c$ , was matched to maintain water catch similitude by adjusting icing exposure time,  $\tau$ . Tsao and Lee also recommend matching the Weber number,  $We_L$ , with characteristic length being the leading-edge diameter,  $L = d$ . This was not possible because the leading edge of the model is fixed at full scale and the test section velocity was assumed to be limited to 250 kn due to model blockage. The equations defining these parameters in terms of air and water properties and the test conditions are summarized in Wiberg et al. (Ref. 41) (included as Appendix D). The interested reader can refer to Anderson's (Ref. 24) work for a complete description of these formulations.

A flow simulation including viscous effects using Fluent (Ref. 21) was run for the unscaled conditions of case WB47 T-6 at the associated baseline angle of attack of  $\alpha = 4.36^\circ$  and a flap angle of  $\delta = 16^\circ$  in order to match the attachment line location of the CFB at the IRT centerline. It was assumed that the IRT test section velocity is limited to 250 kn (128.6 m/s) for this run so the baseline airspeed was not matched. This results in an airspeed of  $V = 139.60$  m/s for the flight baseline and  $V = 128.61$  m/s in the IRT test section. Figure 41 shows  $C_p$  contours with streamtraces on the model surface.

A large separation bubble similar to previous results is present at the ceiling junction. This region is slightly larger due to the higher model loading that results from the higher  $\alpha$  corresponding to case WB47 compared with case WB33. The flow was inspected in detail to ensure that no separation occurred in the region of interest for icing simulations. Figure 42 shows the attachment line position with the span of the model. The attachment line location from the CRM65 is well matched at the IRT centerline ( $y = 0$  in.).

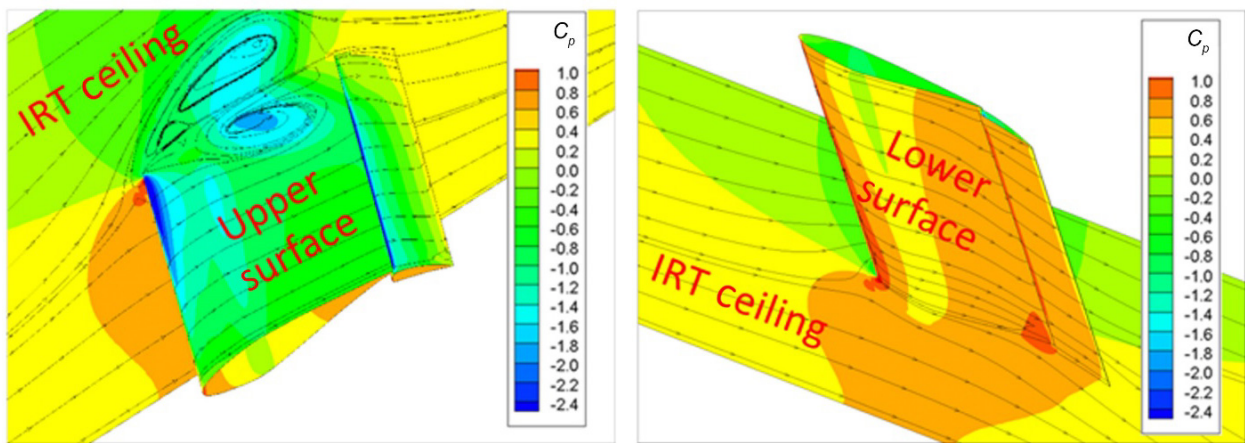


Figure 41.—Pressure coefficient  $C_p$  contour for case WB47  $T = -6$  at angle of attack  $\alpha = 4.36^\circ$  and flap angle  $\delta = 16^\circ$ .

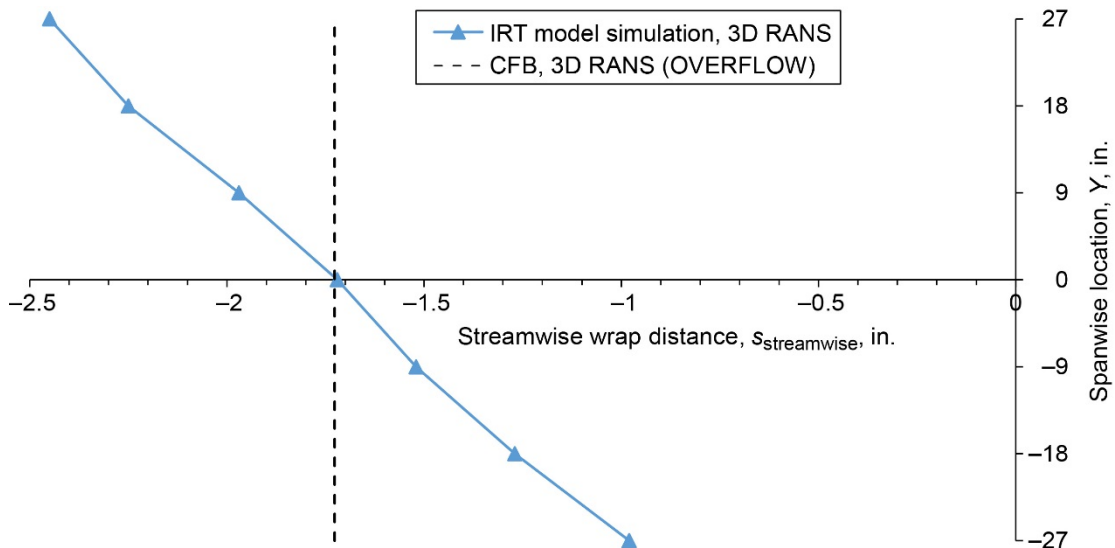


Figure 42.—Midspan model spanwise attachment location for case WB47  $T = -6$  at angle of attack  $\alpha = 4.36^\circ$  and flap angle  $\delta = 16^\circ$ .

The method described previously and outlined in Appendix D was used to determine a set of icing conditions to investigate icing scaling. LEWICE3D was then used to generate ice accretions using both the unscaled baseline conditions and the scaled conditions. These conditions are given in Table VII and corresponding ice shapes are compared with the IFB ice shape for case WB47  $T = -6$  in Figure 43.

Surprisingly, the IRT ice shape with the unscaled conditions matches the IFB ice shape better than that with scaled conditions. To understand why this may be, consider the  $\beta$  and  $h_c$  distributions shown in Figure 44.

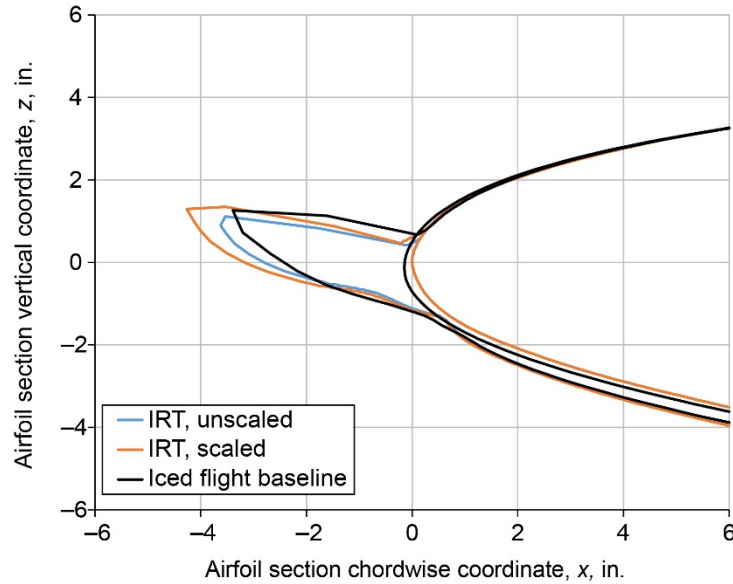


Figure 43.—Comparison of Midspan model scaled and unscaled ice shapes for case WB47  $T = -6$  in Icing Research Tunnel (IRT).

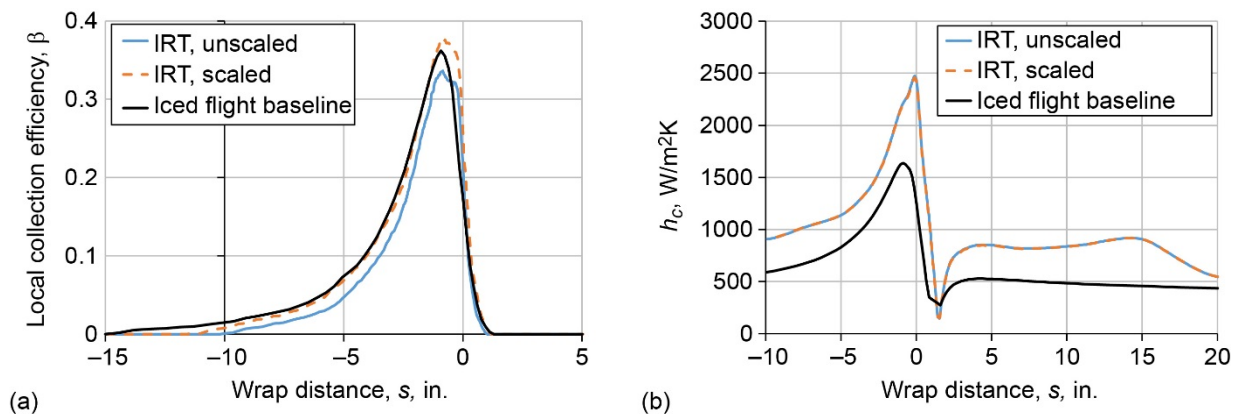


Figure 44.—Comparison of  $\beta$  and  $h_c$  for case WB47  $T = -6$  in Icing Research Tunnel (IRT) for scaled and unscaled icing conditions. (a) Local collection efficiency,  $\beta$ . (b) Heat transfer coefficient,  $h_c$ .

Comparing the collection efficiency distributions in Figure 44 reveals that the droplet trajectory similitude, attempted by matching  $K_0$ , was largely successful. The  $\beta$  distribution from the scaled conditions matches well except for a slightly higher  $\beta$  from about  $s = 0$  to  $-1$  in., whereas the unscaled collection efficiency is low throughout most of the leading-edge region. Careful examination of Figure 44 reveals that the scaled and unscaled case  $h_c$  distributions are exactly the same, the respective curves being coincident. Though equal, the  $h_c$  for the scaled and unscaled cases are significantly higher than that of the IFB. With a combined low  $\beta$  and high  $h_c$  distribution, the ice thickness of the unscaled shape approximately matches that of the IFB. The  $\beta$  of the scaled case matches that of the IFB well except for the overshoot from about  $s = 0$  to  $-1$  in. Nevertheless, the high  $h_c$  of the scaled case compared with that of the IFB results in ice that is thicker than the IFB, though the horn angle is perhaps matched better. This brings into question whether an effort should be made to directly match  $h_c$  rather than the more general matching of  $n_0$ .

The heat transfer coefficient is higher in the IRT than in the IFB due to the higher air density at the lower altitude. While  $h_c$  is not matched directly in the scaling method used, it is taken into account in the matching of the freezing fraction at the stagnation point,  $n_0$ , which is a function of  $h_c$  through the air energy transfer parameter and the relative heat factor. This process is described in detail in Appendix D of Wiberg (Ref. 13). To match  $h_c$  directly would require that the test section velocity be scaled by the factor by which air densities are mismatched. In the context of a large-scale swept-wing model, this is actually a favorable constraint because, given the higher density of air at the elevation of the IRT, the test section velocity would need to be lowered in order to match  $h_c$ . Due to blockage effects, it is often the case that the true airspeed of the reference case cannot be matched in the tunnel, requiring the tests to be performed at lower velocities. Lowering the IRT test section velocity simultaneously reduces loading while allowing  $h_c$  to be matched directly, perhaps improving ice shape agreement. However, this precludes surface water dynamics similitude because, with reduced velocity and a full-scale leading edge, the Weber number of the scaled conditions will not match that of the reference case. This highlights the classic challenge of icing similitude: the scaling of icing conditions is limited to a small set of parameters over which the operator has control, namely  $MVD$ ,  $LWC$ ,  $\tau$ ,  $T$ , and perhaps  $V$ . Furthermore, there are often additional constraints on these parameters due to tunnel capabilities, such as a limit on test section velocity due to blockage. This short list of variables over which the icing test designer has control limits the allowable number of dimensionless parameters that can practically be adjusted in the tunnel in order to scale the conditions for similitude with the reference case.

Despite the droplet trajectory similarity enforced by matching  $K_0$ , the local collection efficiency,  $\beta$ , for the scaled conditions is somewhat mismatched in the region from about  $s = 0$  to  $-1$  in. A similar trend was found in the ice shapes for case WB33  $T = -4$ , shown in Figure 36, and WB47  $T = -6$ , shown in Figure 37, though in these cases no scaling was attempted. However, the higher collection efficiency near  $\beta_{\max}$  is likely due to the reduced thickness of the hybrid model as compared with the full-scale reference wing, as discussed previously.

## 5.7 Task 4.6: Document and Deliver Process and Conceptual Design of Models

The delivery of this report on the design process of hybrid models for icing wind tunnel tests concludes the work performed during years 1 and 2 of this project. Additional articles and model geometry coordinates that supplement this documentation are presented in the appendixes.

## 6.0 Summary, Conclusions, and Recommendations

### 6.1 Summary and Conclusions

The research presented in this report is part of a collaborative research effort conducted by NASA, the Federal Aviation Administration (FAA), Office National d'Etudes et de Recherches Aérospatiales (ONERA), Boeing, and the Universities of Washington, Illinois, and Virginia to address the technical challenges associated with swept-wing icing and its effects on aircraft aerodynamic performance and flight safety. The work presented in this report covered a method for designing icing wind tunnel models capable of reproducing the full-scale swept-wing ice accretion of a particular spanwise station with reduced size and tunnel blockage. Such models are called hybrid because they retain a portion of the full-scale wing leading edge and replace the full-scale trailing edge with a truncated section of reduced chord. The hybrid design method was introduced in the 1990s for straight wings of moderate sizes and was extended and further explored in this report to allow for the design of hybrid models for large swept wings.

The 65 percent scale of the Common Research Model (CRM65) was selected as the aircraft reference geometry, representing a modern swept-wing transport aircraft. A subset of icing mission scenarios was then selected to adequately represent the flight phases that determine the critical ice shapes, consistent with those of the U.S. Code of Federal Regulations (CFR) Title 14, Part 25, Appendix C, Continuous Maximum Icing. Computational fluid dynamics (CFD) simulations were done to obtain the aerodynamic solutions and ice accretion calculations of the reference aircraft in free air (flight conditions) known as the clean flight baseline (CFB) and iced flight baseline (IFB), respectively. Both CFB and IFB were then defined as the target baseline data to be reproduced by the hybrid models within the icing wind tunnel. Three stations of the CRM65 were selected at the spanwise positions 20, 64, and 83 percent and named Inboard, Midspan, and Outboard, respectively. The hybrid model design was then utilized to design models at these stations to be tested in the NASA Glenn Icing Research Tunnel (IRT). The hybrid design method utilized was broken down into two stages: a two-dimensional (2D) hybrid airfoil design method and a three-dimensional (3D) swept-wing design method. The 2D design method extended the method originally developed by Saeed et al. (Ref. 2) and further explored other parameters and their effects on the hybrid airfoil design. The 3D design method established a consistent process of translating 2D hybrid airfoils into hybrid swept wings.

Several lessons were learned with the design of hybrid models to match full-scale ice accretions in icing wind tunnels. The following findings from the 2D and 3D hybrid model design studies and method were shown in this report:

- Matching stagnation or attachment line location on the leading edge of the hybrid wing model is the first-order parameter in matching ice shape.
- The sweep angle is the primary cause for attachment line spanwise variation.
- A significant portion of the model issues (3D flow separation, spanwise load variation, model and wall interaction, and 3D flap effectiveness) were only captured in 3D viscous aerodynamic evaluations, so they should be included in the design process at the earliest stage possible.
- To keep both wind tunnel blockage and model loads to a minimum, models should have the largest scale factor (smallest chord) that allows reaching all attachment line locations without significant flow separation.
- If model loads still exceed the IRT limits even with the largest possible scale factor, then tunnel airspeeds should be decreased to not exceed loads. Velocity scaling methods for icing similitude will then be required.



The following additional conclusions from Fujiwara et al. (Ref. 16), Wiberg et al. (Ref. 41), and Fujiwara et al. (Ref. 40) are related to the hybrid design but not shown in this report:

- Spanwise load/attachment line variation will exist in floor-to-ceiling (no gap) models for an untwisted swept wing.
- The need for spanwise load control techniques must be evaluated considering the variation of simulated ice shapes across the span in the accreted region of interest. Ice shape uniformity across the entire span may not be required or expected.
- Model twist is more effective than segmented flaps for controlling spanwise load variations, as twist can be implemented to affect the circulation closer to the leading edge.
- The effectiveness of spanwise segmented flaps for changing spanwise load heavily depends on model aspect ratio.
- Ceiling gaps can help unload the model but do not effectively change the spanwise load variation.

Significant time was spent analyzing the hybrid models using a 2D Reynolds-averaged Navier–Stokes (RANS) code, but the flow around these models is highly 3D, so the usefulness of these calculations was marginal. For a swept wing in a wind tunnel, there may be 3D relief effects that are missed in the 2D analysis. Wall–wing junction separation effects can also undermine the accuracy of the 2D-based design. Moving more quickly in the design process to the 3D RANS simulations could reduce the time required for each iteration of the model. Section 6.2 describes how a direct-to-3D methodology might be employed.

In conclusion, the primary goals of this portion of the project were all completed, which should substantially improve the study of swept-wing icing. The wing geometry and baseline icing conditions selected during this process have been and will continue to be utilized throughout the swept-wing icing research project primarily supported by the FAA and NASA. The stations of the CRM65 that were selected will allow ice shapes to be produced in the IRT that can be extrapolated to full span and accurately represent free-flight icing. Finally, a method for designing hybrid icing wind tunnel models for large-scale swept wings was developed and applied to design three models for the 20, 64, and 83 percent spanwise stations of the CRM65.

## **6.2 Recommendations**

The current hybrid wing design method can be computationally expensive due to the number of iterations that might be required to generate a satisfactory model. Simultaneously matching full-scale attachment line location with minimum or no flow separation within the wind tunnel load limits and producing good full-scale ice accretion agreement fundamentally requires 3D analysis tools; 2D tools are insufficient. Thus, a direct 3D design approach utilizing the lessons learned from the extended 2D hybrid airfoil design method might yield a more efficient design method, starting directly from the 3D full-scale leading-edge geometry and designing the 3D truncated aft section with an integrated flap, if any. Guided by 3D CFD RANS, wing optimization techniques that parameterize the 3D hybrid wing geometry of the main element, the twist distribution along the hybrid wing model span, and the flap deflection might help reduce local flow separation while maintaining the full-scale attachment line location as an objective function for a larger portion of the hybrid wing model span than just the center line cut.



## Appendix A.—Nomenclature

### Acronyms

AIAA	American Institute of Aeronautics and Astronautics
CFB	clean flight baseline
CFD	computational fluid dynamics
CFR	Code of Federal Regulations
CRM	Common Research Model
CRM65	65 percent scale CRM wing
ETOPS	extended range operation twin-engine operational performance standard
FAA	Federal Aviation Administration
FS	full scale
HGW	high gross weight
HX	heat exchanger
IFB	iced flight baseline
IRT	Icing Research Tunnel
LGW	low gross weight
LWC	liquid water content
MAC	mean aerodynamic chord
MEA	multi-element airfoil
MVD	median volumetric diameter
NACA	National Advisory Committee for Aeronautics
ONERA	Office National d'Etudes et de Recherches Aérospatiales
RANS	Reynolds-averaged Navier–Stokes
SOB	side of body
SST	shear stress transport
TAS	true airspeed
WB	wing and body configuration (Common Research Model)
WBL	wing butt line
2D	two-dimensional
3D	three-dimensional

### Symbols

$A_c$	accumulation parameter
$C_{m0}$	zero-angle-of-attack pitching moment coefficient
$C_p$	pressure coefficient
$c$	chord
$c_0$	full-scale chord
$c_{hyb}$	hybrid-scale chord
$h_c$	heat transfer coefficient

$K_0$	modified inertia parameter
$k$	turbulent kinetic energy
$M$	Mach number
$n_0$	stagnation point freezing fraction
$Nu_a$	Nusselt number of air
$P_{amb}$	static ambient pressure
$Re_c$	Reynolds number based on model chord
$Re_{mac}$	Reynolds number based on mean aerodynamic chord
$s$	wrap distance (arc length) from highlight to attachment point
$T_{amb}$	static ambient temperature
$t$	time
$V$	velocity
$x$	airfoil section chordwise coordinate
$Y$	spanwise location
$y$	airfoil section vertical coordinate
$y^+$	dimensionless wall distance
$z$	airfoil section vertical coordinate
$We_L$	Weber number based on leading-edge diameter
$We_\delta$	Weber number based on droplet diameter
$\alpha$	angle of attack
$\beta$	local collection efficiency
$\beta_{max}$	local collection efficiency peak
$\gamma$	nose-droop angle
$\delta$	flap angle
$\Lambda$	wing leading-edge sweep angle
$\eta$	spanwise position
$\rho$	air density
$\tau$	icing exposure time
$\omega$	specific turbulence dissipation

## Appendix B.—Numerical Methodology for Aerodynamic Simulations in the Icing Research Tunnel

### B.1 Numerical Inflow Conditions for the Icing Research Tunnel Empty Test Section

In all the computational fluid dynamics (CFD) predictions shown herein, ANSYS Fluent software was used with a Reynolds-averaged Navier–Stokes (RANS) solution based on the  $k-\omega$  turbulence model. The computational domain was based on a subset of the entire Icing Research Tunnel (IRT), seen schematically in Figure B.1. It was important to develop accurate inflow conditions of the flow field near the end of the contraction section so that the mean and turbulent flow properties in the test section, with and without a model, could be simulated. Since no experimental flow-field profiles were available for the IRT at the end of the contraction section, the flow was first simulated starting upstream of the heat exchangers (HXs) all the way to the test section. Details of the empty tunnel simulation methodology and results, including validation with experimental test section data, are described by Clark et al. (Ref. 28). The computational grid uses three sections to produce detailed flow properties at the test section: 1) the HX region, 2) the turning vane region, and 3) the region from settling chamber to test section.

The computational domain for the HX region starts at the inlet to the HX of the IRT and stops just before the flow is turned (Figure B.1). A photograph of the HX exit is presented in Figure B.2(a). Due to limits in computational resources, the HX, with all the individual spanwise tube circular cross sections included, was simulated two-dimensionally as shown in Figure B.2(b), with an arrow indicating the end of a splitter plate. The downstream cross-sectional plane from this HX domain is shown in Figure B.2(c), which is a simple linear composite of the single set of tubes from Figure B.2(b), reproduced and stacked on top of one another. This outflow plane result was used as an input to the contraction turning vane region (corner D), which is the bottom left-hand corner seen in Figure B.1, between the HX and the spray bars.

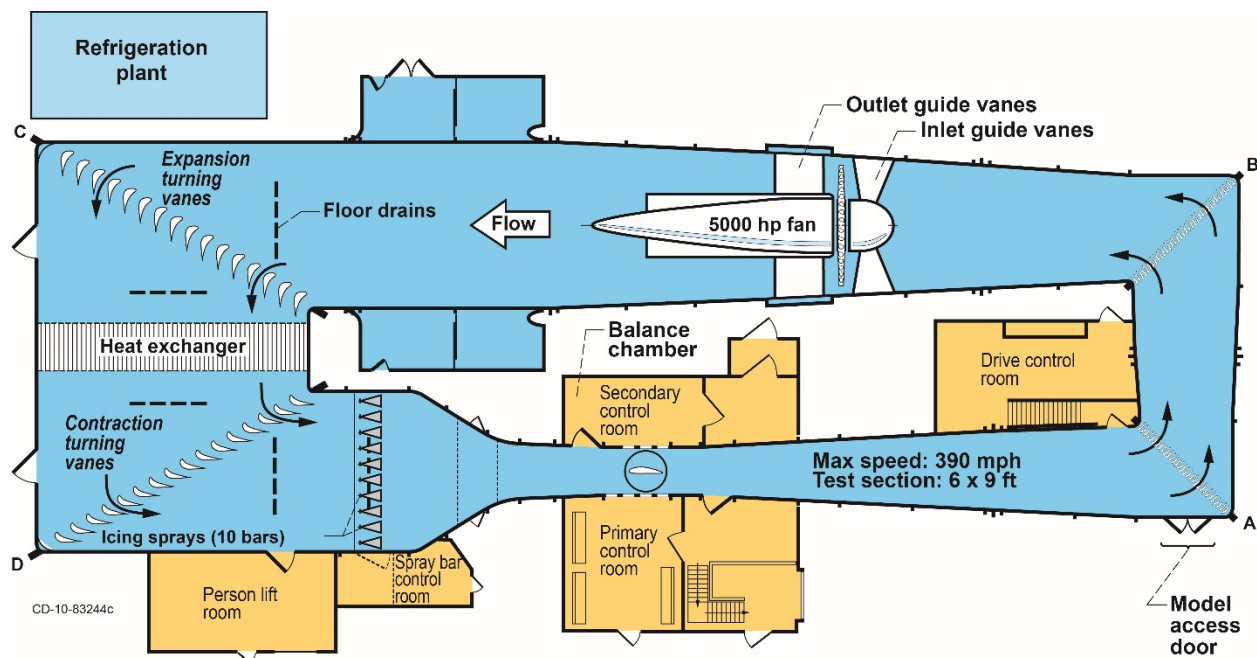


Figure B.1.—Top view of Icing Research Tunnel (IRT).

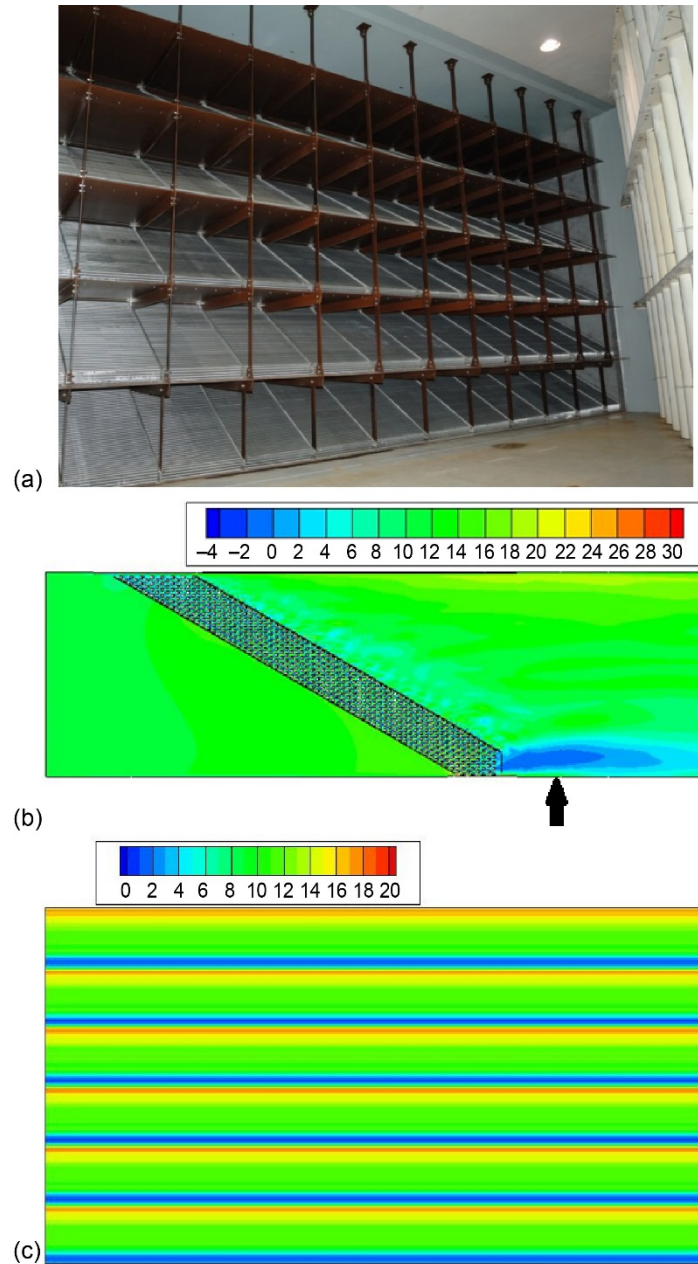


Figure B.2.—Icing Research Tunnel (IRT) description and computational boundary conditions. (a) Heat exchanger (HX) showing six sets of HX tubes. (b) Velocity field (ft/sec) for one HX tube set. (c) Velocity field (ft/sec) at HX exit, assuming all six tube sets have same outflow.

Results from 2D HX simulations (velocity field of Figure B.2(c) as well as the associated  $k$  and  $\omega$  fields) were used as input flow parameters for corner D simulations. The corner D computational domain extended downstream of the turning vanes, ending just short of the spray bars upstream of the test section. Figure B.3(a) shows a slice of the 3D computational grid used for corner D, while Figure B.3(b) is a zoom-in view that provides details of the mesh around the turning vanes. Exit conditions from the corner D mesh were used as input conditions for the contraction and test section part of the IRT.

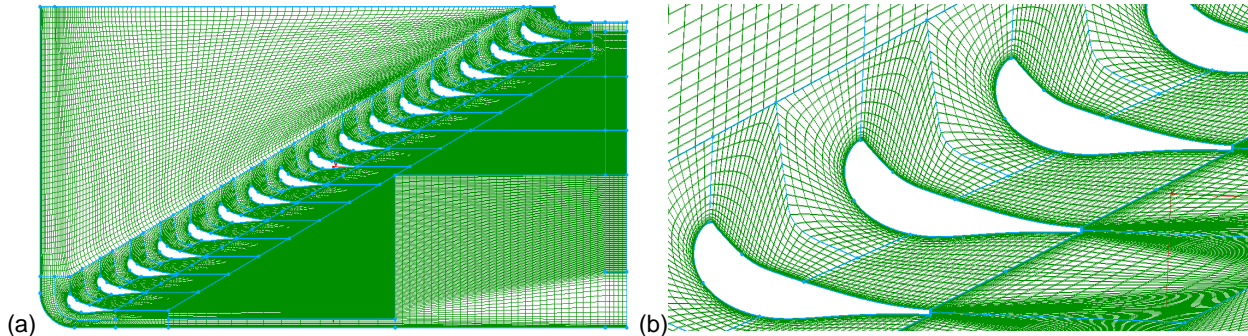


Figure B.3.—Icing Research Tunnel (IRT) corner D computational mesh. (a) Overview of corner D mesh. (b) IRT corner D turning vanes mesh.

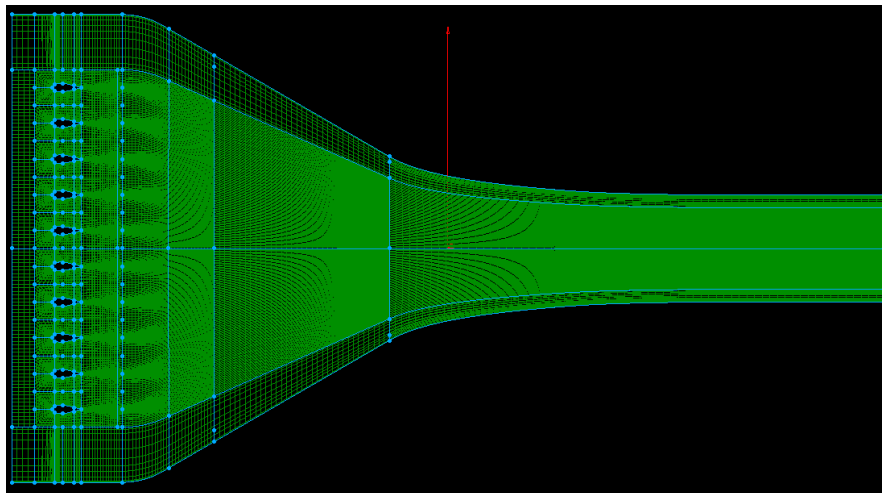


Figure B.4.—Side view of Icing Research Tunnel (IRT) full contraction computational mesh.

The final piece of the IRT grid modeled the tunnel spray bars, contraction region, and test section, ending at the centerline of the turntable (this grid was termed the “full contraction”). This grid can be seen in Figure B.4, showing the different features and general mesh density along the path of the tunnel. Figure B.5(a) shows the grid for the full contraction (which also contained the spray bars and half of the test section, and which had a node count of 11.4 million). To reduce the number of nodes necessary to simulate the empty tunnel, a truncated computational domain was defined to start just short of the end of the contraction. This smaller mesh was termed the “truncated contraction” as shown in Figure B.5(b) and reduced the node count of the empty tunnel mesh to 500,000.

In order to retain the test section prediction fidelity of the full contraction domain with the truncated contraction, a plane was sliced in the solution of the full contraction simulation at the entrance to the truncated contraction and used as inflow conditions for the smaller truncated contraction domain. To ensure this method worked properly, both contraction sections were simulated at the same conditions and cut at the two green planes seen in Figure B.6.

Mean velocity was investigated at the downstream cut plane for both domains of Figure B.5, and the truncated domain yielded a velocity distribution within 1 percent of that for the full domain (with only 5 percent of the total number of grid points). The corresponding prediction for the turbulent kinetic energy, which is more sensitive, is shown in Figure B.7. Comparing the downstream cuts, the truncated contraction domain exhibited very similar flow features to the full contraction, deviating slightly at the walls in the downstream cut. Therefore, the truncated contraction was deemed to be a reasonable representation for flow-field predictions while avoiding the large number of grid points associated with the spray bar and full contraction.

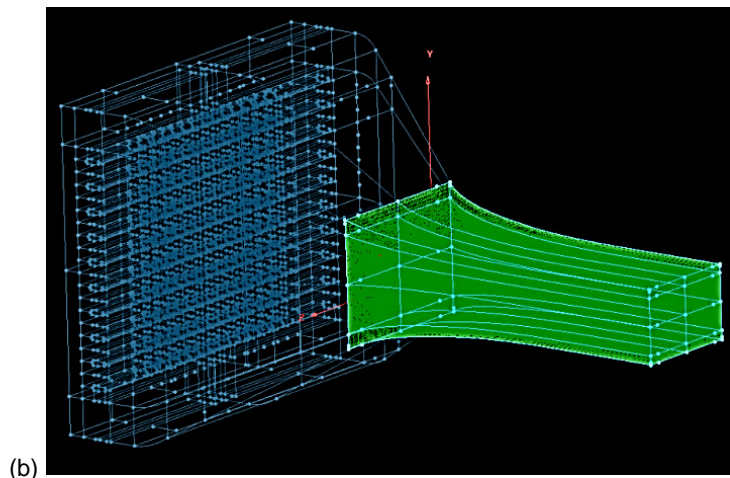
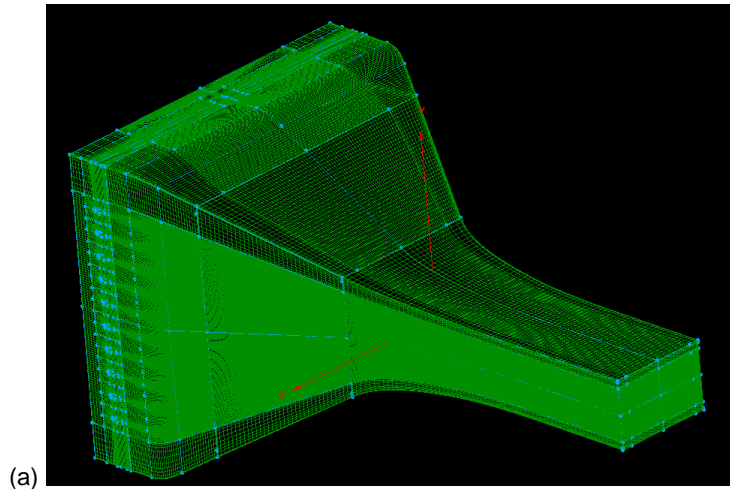


Figure B.5.—Comparison of computational meshes used in Icing Research Tunnel (IRT) simulations. (a) Full contraction. (b) Truncated contraction.

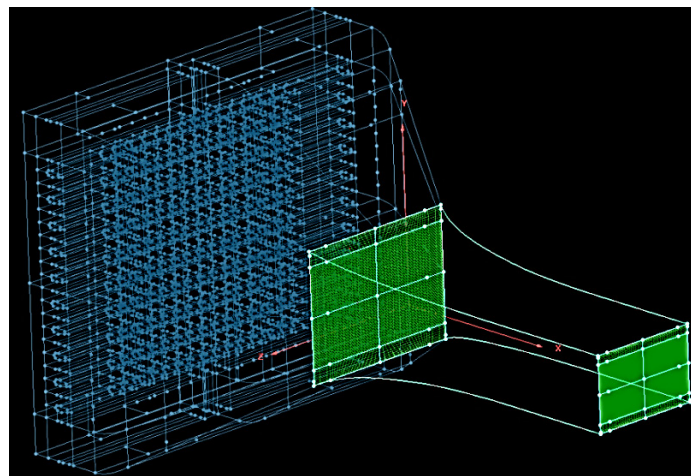


Figure B.6.—Full Icing Research Tunnel (IRT) simulation domain showing upstream (contraction region) cut and downstream (test section) cut.



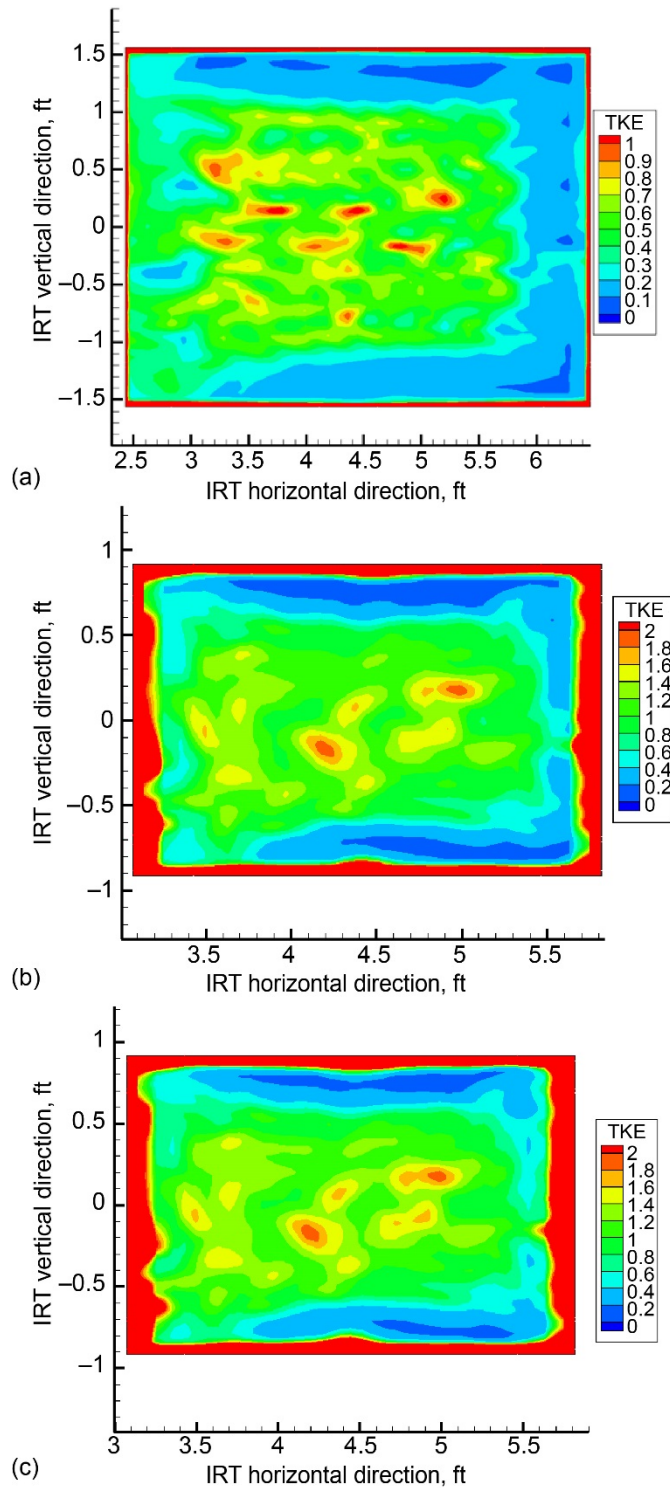


Figure B.7.—Turbulent kinetic energy (TKE) ( $\text{m}^2/\text{sec}^2$ ) comparison at upstream and downstream Icing Research Tunnel (IRT) cuts. (a) Upstream cut from full contraction domain. (b) Downstream cut from full contraction. (c) Downstream cut from truncated contraction.

## B.2 Validation With a High-Lift Test Article in the Icing Research Tunnel

With a suitable starting mesh, a high-blockage test article could be evaluated in the IRT. The model chosen was the McDonnell Douglas Aerospace multi-element airfoil (MEA). This model was selected to validate the present RANS approach as it has relatively high blockage and lift combined with a complex geometry and is associated with detailed experimental data available (Ref. 46). The airfoil model geometry can be seen in Figure B.8(a) with deployed slat and flap. A model created using this section can be seen in Figure B.8(b), where it is being tested in the IRT. This particular test article had a stowed chord length of 36 in. and was tested at a Reynolds number (based on this chord length) of approximately 8 million.

To understand how computational mesh density affects simulations, a grid resolution study was performed using the MEA in the IRT. The computational domain for 2D MEA simulations comprised the truncated contraction, as described previously, the test section with model, and the diffuser. An example of this domain with the MEA in the test section at an angle of attack of  $0^\circ$  can be seen in Figure B.9(a). The baseline 2D grid was made up of 91,000 nodes and included a baffle that connected the trailing edge of the flap to the interface where the test section met the diffuser. The baffle produced a high resolution mesh aft of the flap that allowed the wake of the model to be captured accurately. The baseline test section mesh is shown in Figure B.9(b) and includes the IRT sidewalls, MEA, and wake baffle. The test section mesh contained T-Rex™ cells, an example of which is shown in Figure B.9(c) on the lower surface of the main element of the MEA.

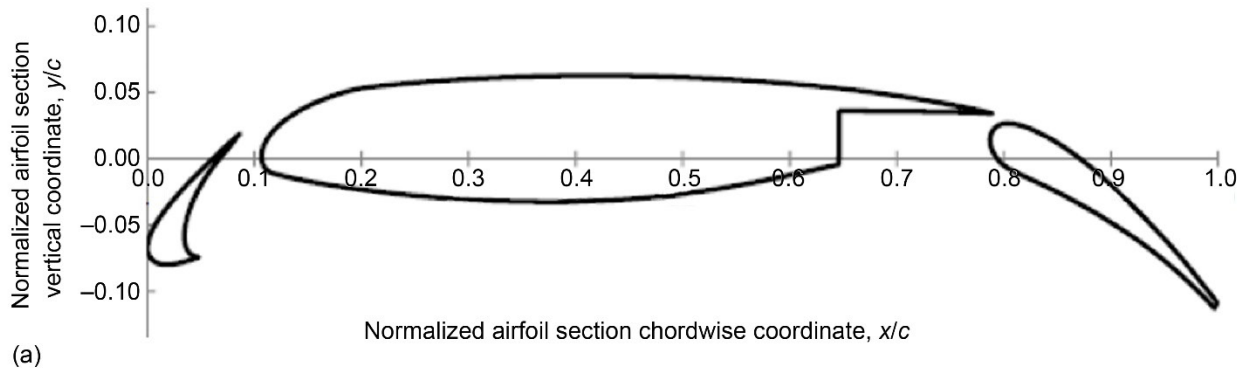


Figure B.8.—McDonnell Douglas Aerospace multi-element airfoil (MEA). (a) Two-dimensional cross-section geometry. (b) Test model installed in the Icing Research Tunnel (IRT).

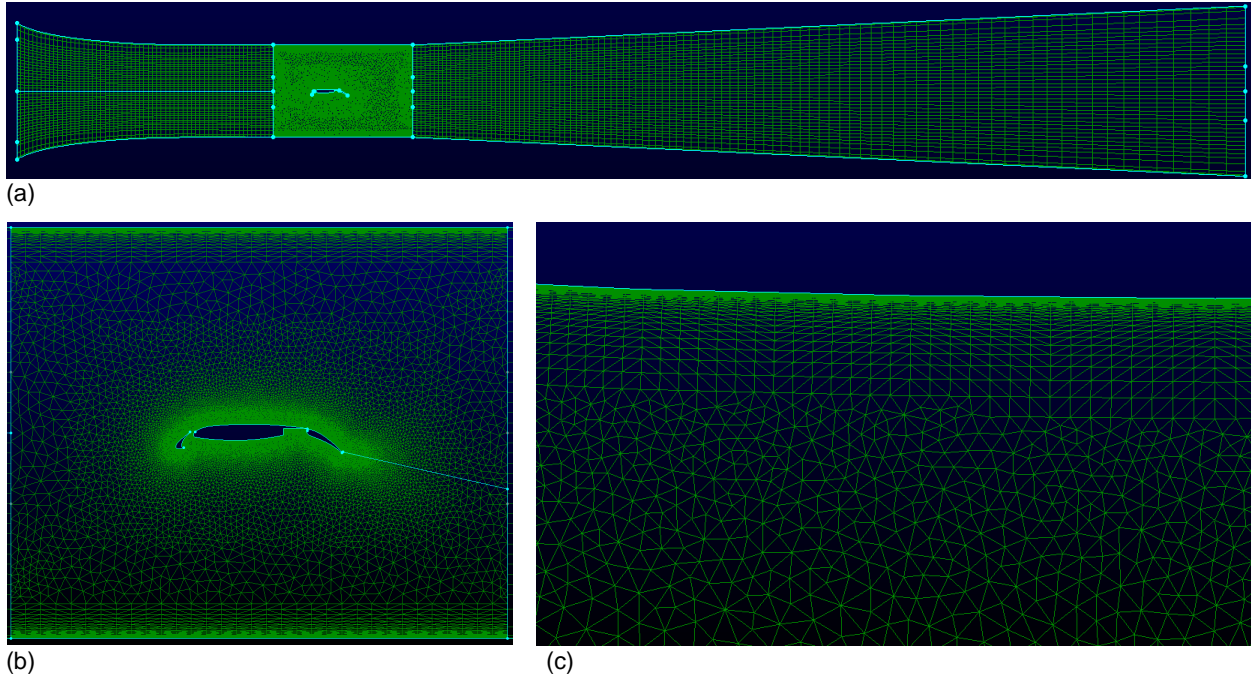
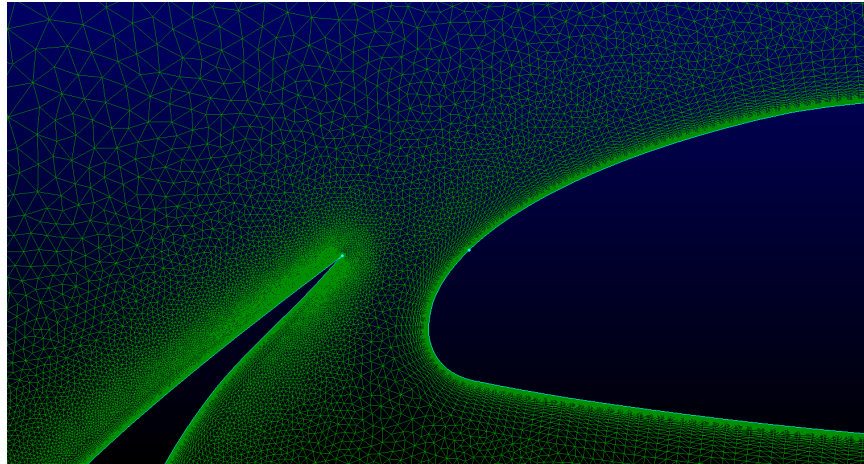


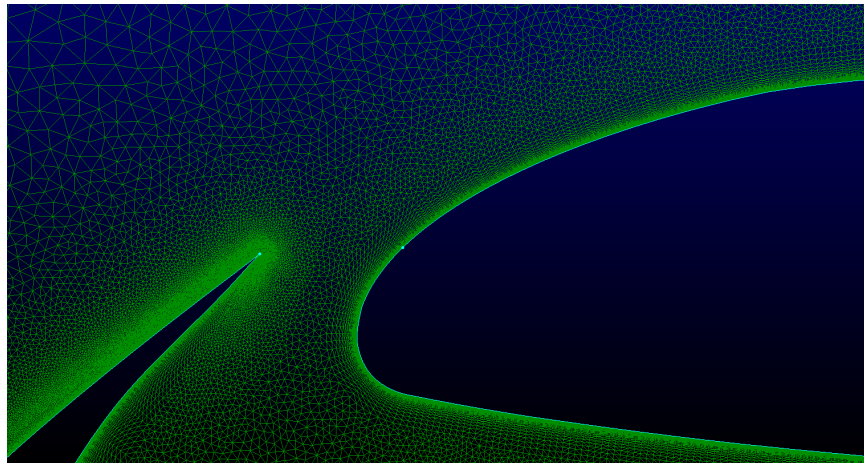
Figure B.9.—Computational mesh for the multi-element airfoil (MEA) at angle of attack  $\alpha = 0^\circ$ . (a) Complete computational mesh with model in Icing Research Tunnel (IRT) test section. (b) Two-dimensional mesh around model. (c) Detailed view of T-Rex unstructured cells.

The baseline mesh was termed the “2D – BL” and had a node count of 91,000. The slat, main element, and flap had 300, 600, and 400 surface nodes, respectively. The initial  $y$  spacing off the airfoil surfaces was  $2.388 \times 10^{-4}$  in., giving a  $y^+$  value slightly less than 1. While many mesh configurations were studied, two others were of particular interest. A modified version of the baseline mesh with double the node count on the airfoil surfaces was named “2D – 2×AS” and comprised 154,000 nodes. The baseline grid with double the surface node count on the IRT walls was given the name “2D – 2×OS” and had 95,000 nodes in the computational domain. Figure B.10(a) is a closeup of the baseline mesh in between the leading-edge slat and main element of the MEA. This image can be compared with Figure B.10(b), where the node count has been doubled on the surfaces of the MEA airfoil.

Grid resolution studies involving 3D simulations utilized an alternate geometry for the tunnel walls. In particular, the 3D IRT tunnel was modeled by a straight and constant area test section that spanned 20 ft upstream and downstream from the test section inlet and outlet, respectively. This domain with the MEA model in the test section is shown in Figure B.11. Drawing on conclusions from the 2D grid resolution study, two 3D simulations were performed using a grid termed “3D – Coarse” and another termed “3D – BL,” which is considered the 3D baseline.

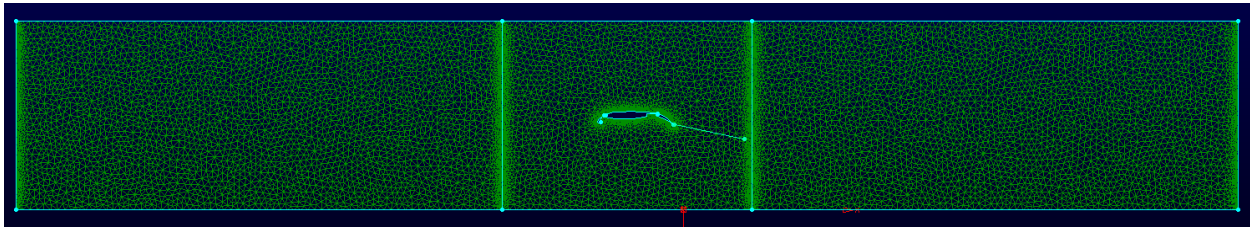


(a)

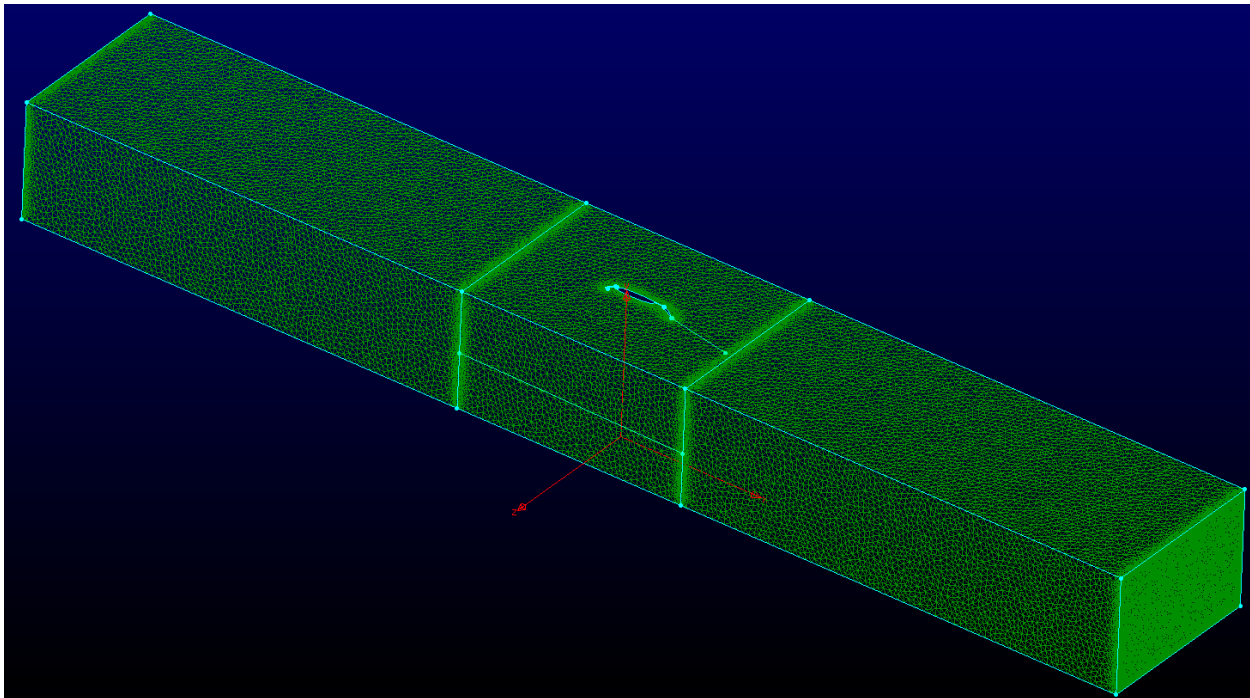


(b)

Figure B.10.—Comparison of 2D multi-element airfoil (MEA) in Icing Research Tunnel (IRT) computational meshes. (a) Surface resolution for 2D – BL mesh. (b) Surface resolution for 2D – 2 $\times$ AS mesh.



(a)



(b)

Figure B.11.—Three-dimensional multi-element airfoil (MEA) in Icing Research Tunnel (IRT) computational mesh.  
 (a) Top view. (b) Isometric view.

Using the previously described domains and meshes, the two-equation RANS turbulence model  $k-\omega$  SST was utilized with inlet turbulence specified at a plane located at 17 ft upstream of the start of the test section (i.e., upstream of where the contraction section would end). The mean velocity and turbulence values at this inflow plane were assumed to be uniform with the latter, given by  $k = 2.58 \text{ m}^2/\text{sec}^2$  and  $\omega = 73.22 \text{ 1/sec}$ . These turbulence values were obtained by velocity scaling average  $k$  and  $\omega$  values produced by Clark et al. (Ref. 28). Figure B.12 provides an image of the flow field, with streamlines and Mach contours, at the centerline of the IRT for the 3D – BL solution. As expected, flow separation can be seen behind the slat and under the main element in the stow recess.

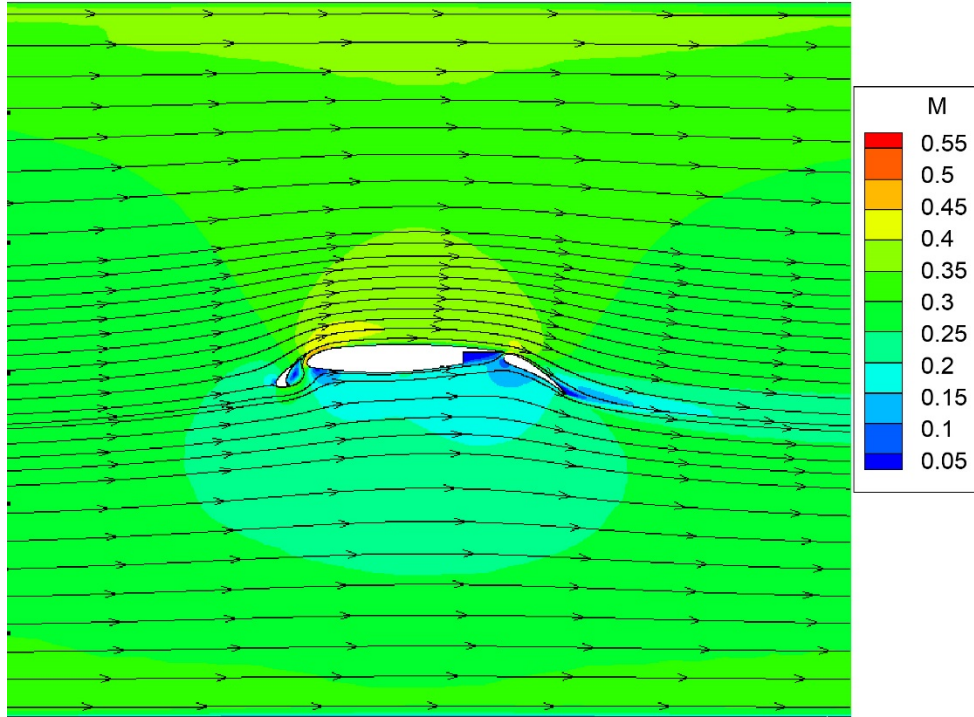
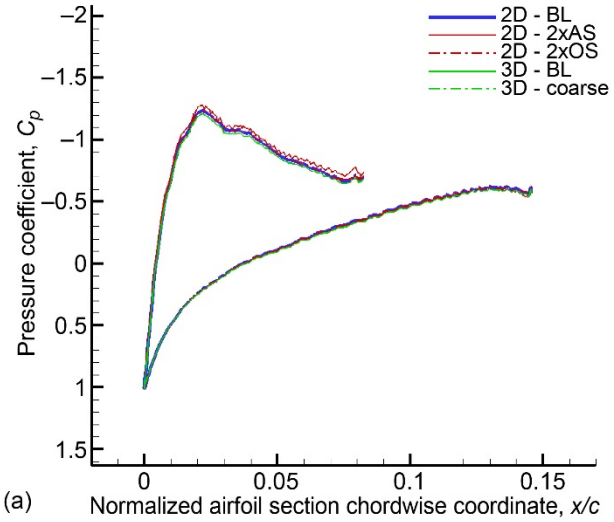


Figure B.12.—Mach (M) contours at centerline cut of 3D – BL simulation.

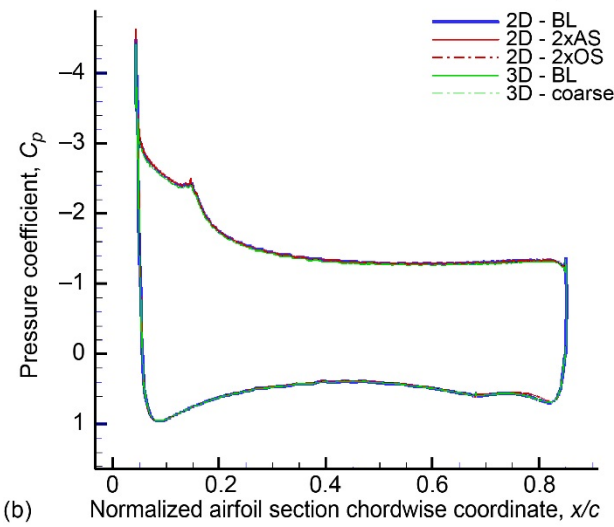
Results for both 2D and 3D grid resolution studies are presented in Figure B.13 in the form of pressure coefficient distributions over the surfaces of the MEA model. These results indicate that the baseline grids for both 2D and 3D were sufficiently resolved to produce grid-independent flow fields.

Experimental data, as well as CFD simulation results (Ref. 45), were compared with the 2D and 3D baseline mesh solutions for the MEA in the IRT. This comparison is shown in Figure B.14, with results for the slat in (a), the main element in (b), and the flap in (c). The 2D MEA baseline simulation was performed using two different turbulence models to note the effects on the solution. The Spalart-Allmaras (termed “2D – BL – SA” in Figure B.14) turbulence model was used in one 2D simulation, with the Menter SST model serving as the baseline for all other simulations performed. The pressure distribution on the slat is only included for the upstream (convex) surface for simplicity. The pressure peak on the slat showed differences when comparing experimental data to simulation results and even when comparing both sets of CFD solutions. This can be attributed to the traditional difficulty of using RANS techniques to predict large separated flow regions. The main element pressure distributions, however, compared well between CFD and experiments. Flap pressure distributions showed some differences in pressure peak locations but had close magnitudes and proved quite alike on the lower surface.

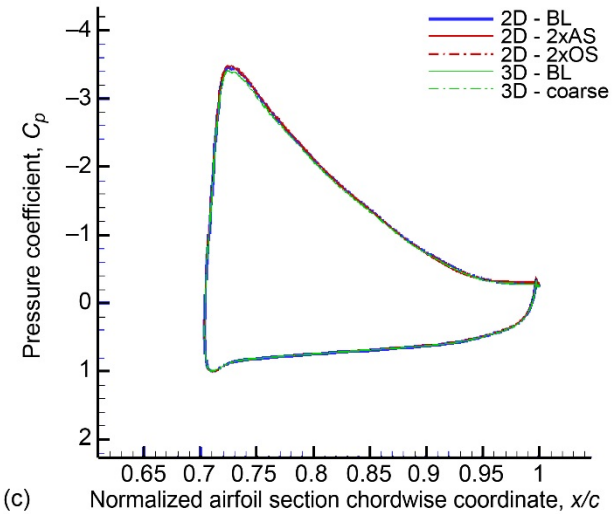
These results for a validation airfoil model show that the CFD methodology employed provides accurate solutions when compared with experimental data. This methodology was then applied to hybrid icing models in the IRT.



(a)



(b)



(c)

Figure B.13.—Two-dimensional (2D) and three-dimensional (3D) grid resolution study for multi-element airfoil (MEA) in Icing Research Tunnel (IRT). (a) Pressure coefficient  $C_p$  on MEA slat. (b)  $C_p$  on MEA main element. (c)  $C_p$  on MEA flap.

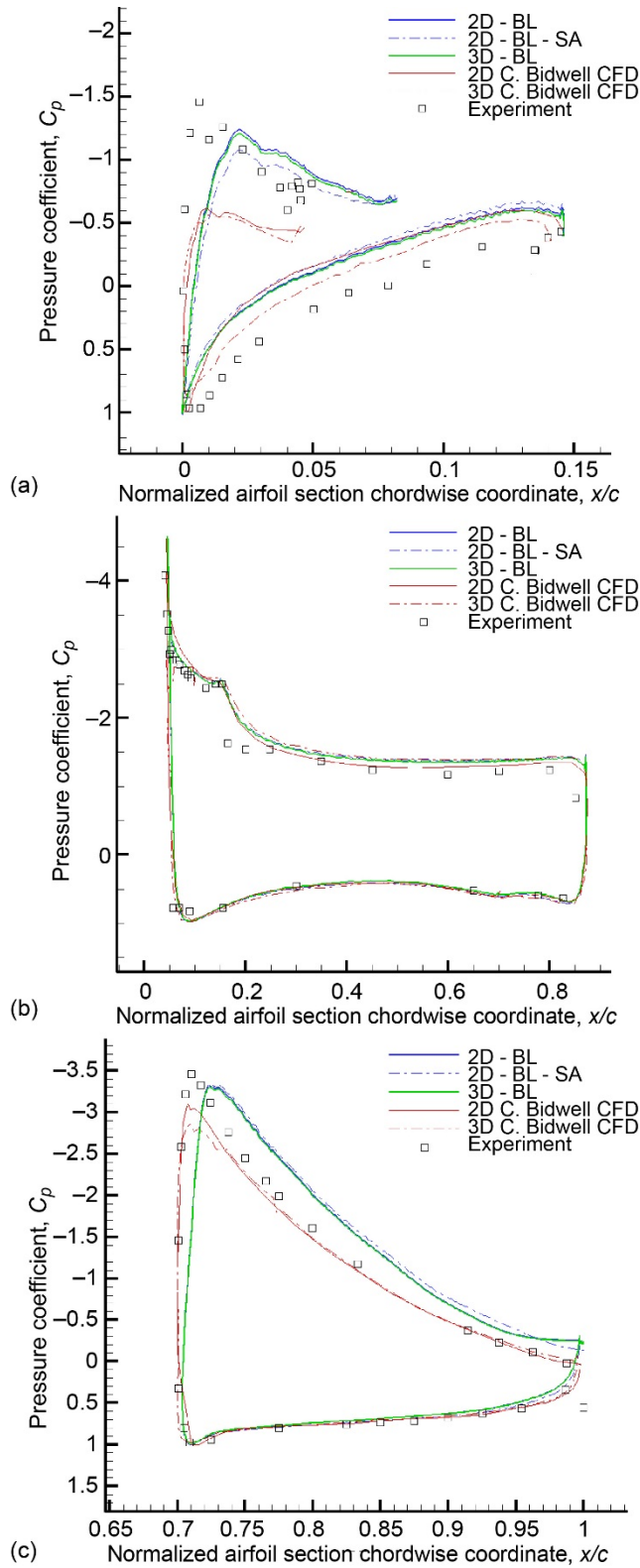


Figure B.14.—Two-dimensional (2D) and three-dimensional (3D) comparison of simulations to experimental data for multi-element airfoil (MEA) in Icing Research Tunnel (IRT). (a) Pressure coefficient  $C_p$  on MEA slat. (b)  $C_p$  on MEA main element. (c)  $C_p$  on MEA flap.



## **Appendix C.—3D Swept Hybrid Wing Design Method for Icing Wind Tunnel Tests**

Reprinted by permission of the American Institute of Aeronautics and Astronautics, Inc., from “3D Swept Hybrid Wing Design Methods for Icing Wind Tunnel Tests,” Gustavo E.C. Fujiwara, Brock D. Wiberg, Brian S. Woodard, and Michael B. Bragg (Ref. 40).

# 3D Swept Hybrid Wing Design Method for Icing Wind Tunnel Tests

Gustavo E. C. Fujiwara<sup>1</sup>, Brock D. Wiberg<sup>2</sup>, Brian S. Woodard<sup>3</sup> and Michael B. Bragg<sup>4</sup>

*University of Illinois at Urbana-Champaign, Urbana, Illinois 61801, USA*

A 3D swept hybrid wing design method using hybrid airfoils is presented for the purpose of icing wind tunnel testing of large commercial aircraft. Hybrid airfoils are those that present the same leading-edge geometry of the full-scale aircraft wing with a redesigned truncated aft section, such that models can fit inside icing wind tunnels and still reproduce full-scale flowfield and ice accretion with reduced chord. The effects of tunnel sidewalls, model sweep angle, aspect ratio, and wind tunnel blockage are presented. Attachment line location is used as a first-order parameter for matching full-scale ice shapes, and methods for controlling its spanwise variation are assessed including the use of gap between model and tunnel wall, aerodynamic twist, and segmented flaps. Finally, model design tradeoffs are presented between competing performance parameters such as full-scale ice accretion agreement, wind tunnel load/speed limits, and model manufacturing/operational complexity.

## Nomenclature

AR	=	Aspect ratio
$\alpha$	=	Airfoil angle of attack
$c_{fs}$	=	Full-scale chord
$c_{hyb}$	=	Hybrid airfoil chord
$C_p$	=	Pressure coefficient
$C_l$	=	Lift coefficient
$C_{m0}$	=	Quarter-chord zero-angle of attack pitching moment coefficient
CRM	=	Common research model
CRM65	=	65% scaled common research model
$\delta$	=	Flap deflection, positive down
$h/c$	=	Tunnel height over model chord
$\eta$	=	Wing spanwise position
LE	=	Leading edge
RANS	=	Reynolds-averaged Navier-Stokes equations
SF	=	Scale factor (full-scale chord divided by hybrid chord)
$s/c$	=	Normalized surface length coordinate
TE	=	Trailing edge
$x$	=	Horizontal coordinate
$x/c$	=	Normalized horizontal coordinate
$y$	=	Vertical coordinate
$y/c$	=	Normalized vertical coordinate

---

<sup>1</sup> Graduate Research Assistant, Department of Aerospace Engineering, Member AIAA.

<sup>2</sup> Graduate Research Assistant, Department of Aerospace Engineering, Member AIAA.

<sup>3</sup> Post Doctoral Researcher, Department of Aerospace Engineering, Member AIAA.

<sup>4</sup> Professor of Aerospace Engineering, currently Dean of Engineering at the University of Washington, Seattle, WA, Fellow AIAA.

## I. Introduction

AIRCRAFT icing is a topic of major importance for the safety and operation of any aircraft that might experience icing conditions during flight.<sup>1,2,3,4</sup> In the United States, the Federal Aviation Administration (FAA) requires commercial aircraft manufacturers to demonstrate that all aircraft can safely operate during icing conditions, through a set of flight tests during the certification stage, as described in the Icing Design Envelopes<sup>5</sup> of 14 CFR Parts 25 and 29 Appendix C. This is often expensive and challenging to find the appropriate icing test conditions.<sup>6</sup> Thus, both computational methods and icing wind tunnel experiments are utilized to provide a controlled and repeatable environment during design and certification of aircraft ice-protection systems to mitigate risks, reduce costs, and validate the existing computational icing tools.

However, the existing icing wind tunnel facilities cannot accommodate large wings such as those found on modern commercial aircraft without requiring dramatic scaling.<sup>7</sup> Scaling can be performed through two different methods.<sup>7</sup> One geometrically scales the entire geometry to fit inside the tunnel test section and then scales the icing conditions to obtain icing similitude. The other maintains the same leading edge of the full-scale wing and replaces the aft section with a truncated trailing edge that produces a similar flowfield around the leading edge with a significantly shorter chord, reducing model size and tunnel blockage. This type of model is referred to as a hybrid<sup>8</sup> and its biggest advantage lies in the fact that it is designed to produce full-scale ice shapes, such that the need for icing scaling<sup>9,10</sup> can be reduced or even eliminated.

A design method for a straight, untapered hybrid wing can be as straight forward as the extrusion of a hybrid airfoil, whose design method is well documented by Saeed et al.<sup>11</sup> and further explored by Fujiwara et al.<sup>12</sup> A broad set of experimental data is available in the literature under airfoil and straight wing icing. The design of a swept, hybrid wing, on the other hand, introduces design challenges related to the three-dimensionality of swept wing flowfields<sup>13</sup> and ice shapes,<sup>14</sup> for which there is a lack of experimental data.<sup>15</sup> In order to meet this need and help better understand the fundamental 3D icing physics on large, swept wings such as those found in large commercial transport aircraft, a collaborative research effort is being performed by NASA, the FAA, the French Aerospace Organization (ONERA), and the University of Illinois at Urbana-Champaign (UIUC), with the contribution of Boeing. An overview of this project is given by Broeren et al.<sup>16</sup>

The work presented in this paper is part of this larger effort. The objective of the work presented here is to establish a design method for large hybrid swept wings that replicate the full-scale ice accretions through icing wind tunnel tests. Another paper by Wiberg et al.<sup>17</sup> covers in further details the flow and icing simulations of a hybrid, swept-wing model and the use of icing scaling to compensate for the differences between the flight and the icing wind tunnel conditions. The hybrid wing models were designed to be tested in the 6 by 9 ft test section of the NASA Glenn Icing Research Tunnel (IRT),<sup>18</sup> vertically mounted with a span of 6 ft. Fluent<sup>19</sup> was used to calculate the model flowfield and LEWICE3D<sup>20,21</sup> used for the droplet impingement and ice accretion calculations.

## II. Methods

### Reference Wing

For this research, the Common Research Model (CRM)<sup>22</sup> was selected as the baseline wing. The CRM was designed by Boeing as part of collaboration with NASA to represent a typical modern wide-body commercial transport, whose geometry,<sup>22</sup> computational<sup>23,24,25,26,27,28</sup> and experimental data<sup>29,30</sup> are publicly available. The CRM was designed for a cruise Mach number of 0.85 at a Reynolds number of 40 million. It has an aspect ratio of  $AR = 9.0$ , a taper ratio of 0.275, and a washout of 8.2 degrees from the side of body to wing tip.<sup>22</sup> Since the CRM would require a very large reduction in chord in order to fit the models into the IRT and avoid high blockage, and later objectives of the overall project require that artificial ice shapes be created and aerodynamically tested on a high Reynolds number semispan geometry in the ONERA F1 tunnel, the reference geometry was scaled down to 65% of its original size, and referred to as the CRM65 in the remainder of this paper. The CRM65 has a semispan of 62.66 ft (19.10 m), a chord of 25.4 ft (7.74 m) at the side of body, and 5.82 ft (1.77 m) at the wing tip. The mean aerodynamic chord is 14.94 ft (4.55 m), and the wing area is 1,745 ft<sup>2</sup>. The wing is swept 35° at quarter-chord and is tapered with a Yehudi break at 37% of the span.

### Flight Baseline

After the aircraft reference geometry was determined, Boeing<sup>31</sup> evaluated several scenarios specified by Appendix C of the 14 CFR Part 25 and 29 and determined a subset of cases that would envelop the most critical ice

shape conditions.<sup>17</sup> Six different aerodynamic conditions were identified, with different temperatures that led to a matrix of 17 icing conditions. In order to simulate these icing cases, aerodynamic flow solutions must first be generated, and then later those solutions are used by the ice accretion simulations.

The Clean Flight Baseline (CFB) is the set of aerodynamic solutions provided by Boeing using CFD RANS code OVERFLOW,<sup>32,35</sup> whose velocity fields were input to LEWICE3D<sup>20</sup> to generate the Iced Flight Baseline (IFB) with droplet trajectories and ice shapes on the CRM65. Both CFB and IFB were used as the target references when designing the 3D hybrid-wing models.

### Hybrid Airfoil Design

A hybrid airfoil presents the same full-scale leading edge as the reference geometry with a redesigned aft section that is considerably shorter than the full-scale. The upper and lower extents maintained from the full-scale geometry are based on the estimated full-scale impingement limits, and are given as a percent of the chord (including both the main element and flap). The hybrid scale factor, SF, is defined as the full-scale chord divided by the total hybrid-model chord, representing the factor by which the baseline geometry is shortened. The nose droop angle,  $\gamma$ , is the angle between the full-scale chord and the hybrid airfoil chord. It determines the elevation of the trailing edge with respect to the full-scale chord line. A more positive nose droop angle causes a lower trailing edge elevation or more camber, shifting the load towards the aft of the hybrid. The quarter-chord zero-lift pitching moment coefficient,  $C_{m0}$ , determines the camber line curvature of the aft of the hybrid section.<sup>34</sup> A more negative  $C_{m0}$  will result in a more cambered aft section, therefore, increasing aft loading. Values of  $\gamma$  can be either positive or negative, while  $C_{m0}$  is usually negative.<sup>35,36</sup> A more detailed discussion on the 2D hybrid airfoil design method is presented by Fujiwara et al.,<sup>12</sup> where matching stagnation point location is shown to be of first order for matching full-scale ice shapes.

A flapped hybrid airfoil was designed for a single airfoil cut of the CRM65 located at spanwise position  $\eta = 64\%$  of the semispan (called Midspan model) with  $SF = 2$ , upper and lower extents in bold at  $x/c_{fs} = 10\%$ , illustrated in Fig. 1. The main element airfoil presents a negative nose droop angle  $\gamma = -5.5^\circ$ , seen by its high trailing edge and  $C_{m0} = -0.05$ . The flap chord corresponds to 1/3 of the hybrid main element chord and is a modified NACA6412 with both gap and overlap of 1.5% of the total hybrid chord  $c_{hyb}$ .

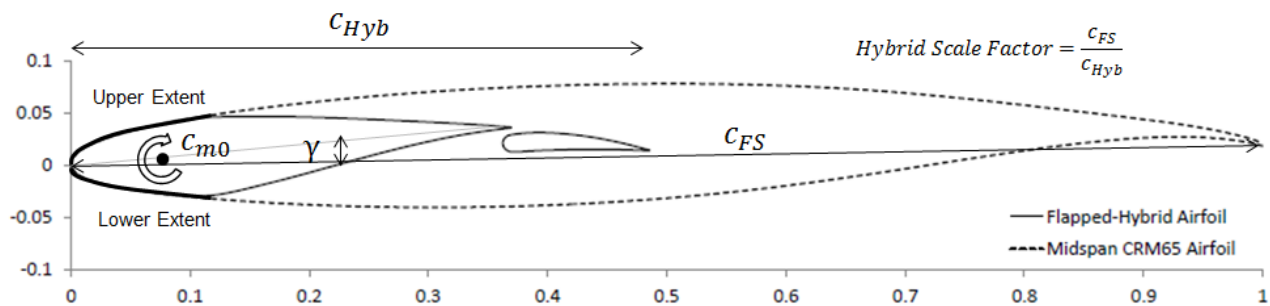


Figure 1. Flapped hybrid airfoil design example

For this project, three CRM65 normal cuts were chosen<sup>16</sup> named IB (Inboard), MS (Midspan) and OB (Outboard), presented in Fig. 2, and the corresponding hybrid airfoils were designed to be later used in the hybrid wing designs. The characteristics of these full-scale normal airfoils and corresponding 2D hybrid designs are presented in Table 1. Note that for the IB case, the normal full-scale cut intercepts the aircraft side of body, so the full-scale airfoil was extrapolated past the leading edge to allow the use of the 2D hybrid design computational tools.<sup>12</sup>

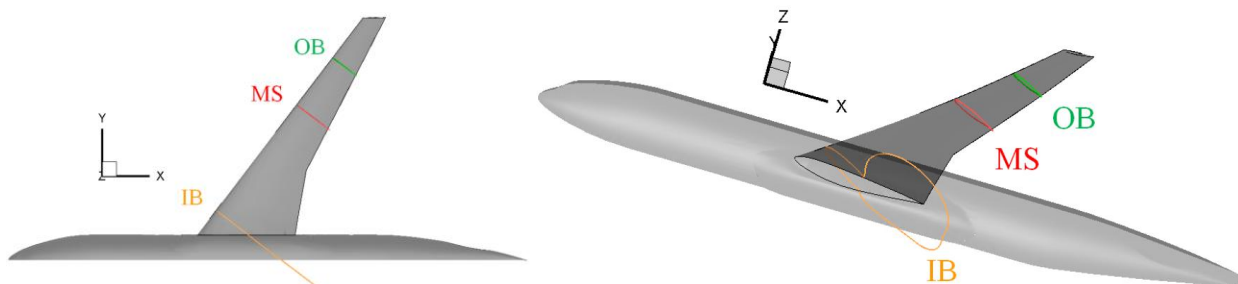


Figure 2. IB, MS, OB normal airfoil cuts from CRM65<sup>16</sup>

**Table 1. IB, MS, OB full-scale normal airfoils and respective hybrid airfoil designs**

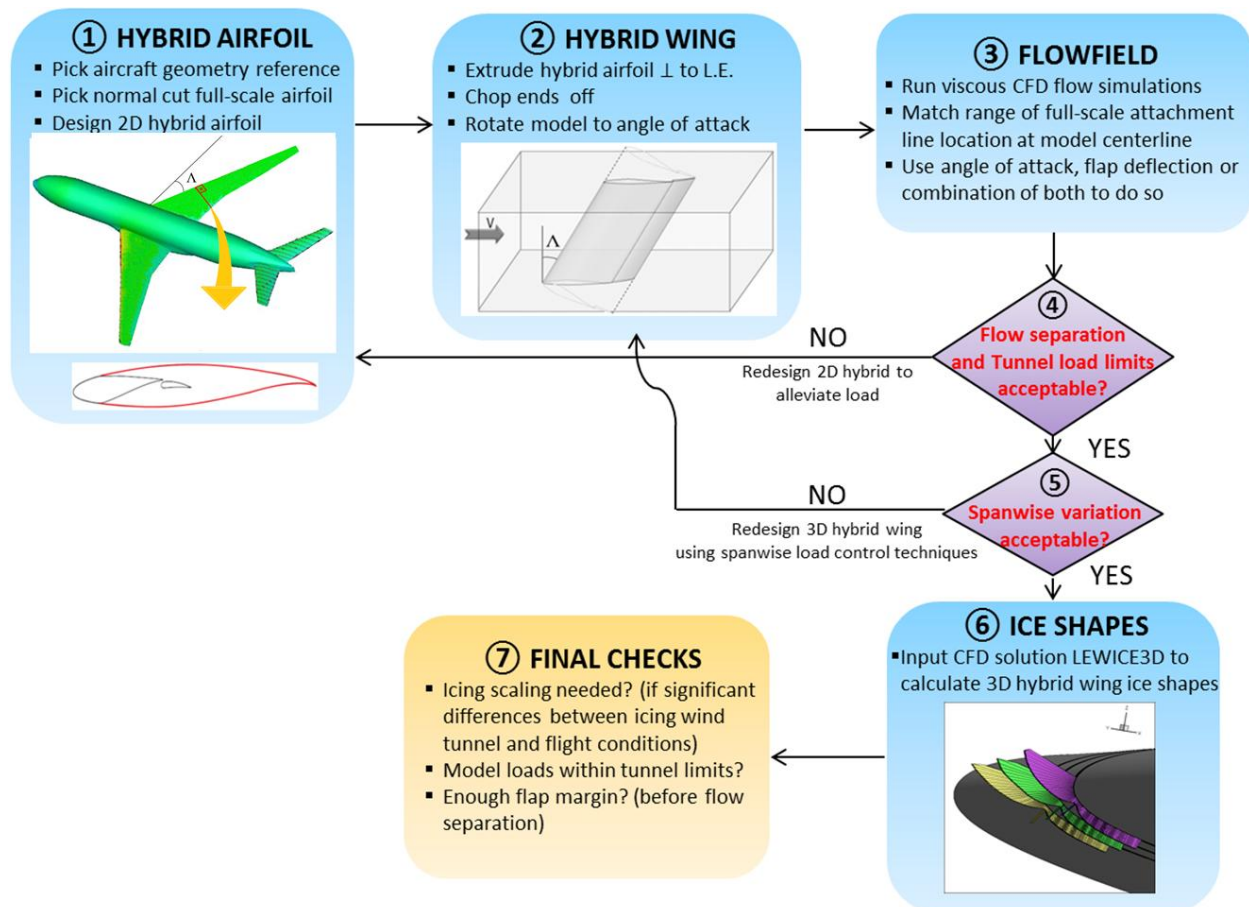
	IB	MS	OB
Model Name	Inboard	Midspan	Outboard
CRM65 spanwise location $\eta$	20%	64%	83%
Full-scale normal chord ( $c_{fs}$ )	297.88 in (7.566 m)	122.72 in (3.117 m)	91.27 in (2.318 m)
Upper LE x/c extent	4%	10%	17%
Lower LE x/c extent	6%	10%	15%
Nose Droop Angle	-11.5°	-5.5°	-3.5°
$C_{m0}$	-0.12	-0.05	-0.08
Scale Factor (SF)	2.25	2	1.5

Full-scale/Hybrid airfoils

**Hybrid Wing Design**

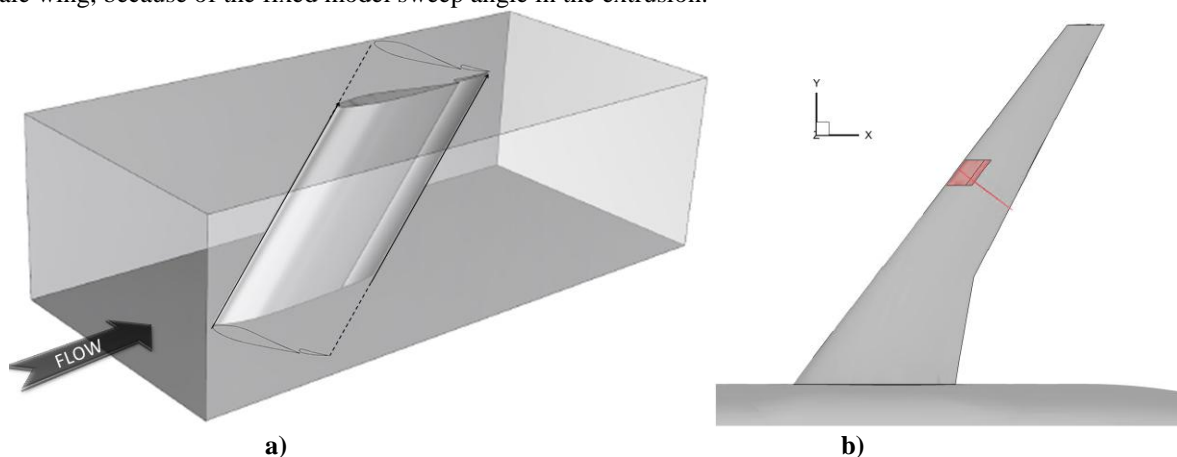
A hybrid wing model can be designed to represent either a region of the reference wing or a single spanwise station. For a wing model representing a region, the entire 3D leading-edge of the full-scale wing region is maintained and a 3D truncated aft section is redesigned. For a single spanwise station, a 2D hybrid airfoil is designed and then extruded to create a hybrid wing whose centerline represent the full-scale station. For this project, the wing model is designed to represent a single spanwise station on the CRM65, so the hybrid airfoil is simply extruded across the wind tunnel test section to create a hybrid wing model.



**Figure 3. Hybrid wing design method workflow**

The hybrid wing model design method utilized for the present work is presented in the workflow of Fig. 3. As previously discussed, the first step is to define the aircraft reference geometry, and establish the set of aerodynamic and icing conditions to be replicated. The hybrid wing design starts with the design of a 2D hybrid airfoil from a normal cut of the full-scale airfoil of the CRM65 to match the stagnation point location for that full-scale airfoil cut. The details and design tradeoffs of this first step are well described by Fujiwara et al.<sup>12</sup> In order to properly represent a swept wing in 2D with simple sweep theory,<sup>37</sup> the hybrid airfoil is designed for a full-scale airfoil that is cut in the direction normal to the leading edge of the full-scale wing.

The second step requires extruding the designed hybrid airfoil in the direction parallel to the full-scale leading edge, maintaining the same wing leading-edge sweep angle. The ends of the hybrid wing model are trimmed in the streamwise direction to create a model that spans from the floor to ceiling in the IRT, as shown for the Midspan hybrid wing model in Fig. 4a. A size perspective of this same model in comparison to the CRM65 is presented in Fig. 4b. Once the hybrid wing geometry is created, the model is then rotated to the desired angle of attack for the CFD simulations that will assess the similarity between the full-scale and hybrid wing's flowfield near the region of interest. The order of operations for this portion of the design is important. The 3D geometry must be created first, and then, the entire swept hybrid model rotated to the desired angle of attack. First rotating the hybrid airfoil to the desired angle of attack and then extruding it to a 3D model generates a 3D model geometry that differs from the full-scale wing, because of the fixed model sweep angle in the extrusion.



**Figure 4. a) Hybrid airfoil extruded parallel to the leading edge then trimmed at the ends (Midspan model)**  
**b) IRT Midspan model compared to the full-scale CRM65 geometry**

The third step is similar to the iterative process done in 2D for the hybrid airfoil. Instead of varying the hybrid airfoil geometry and flap deflection to match the full-scale airfoil stagnation point location, the criterion utilized is to vary the hybrid wing angle of attack and/or flap deflection to match the full-scale attachment line location at the centerline cut of the model inside the tunnel, with 3D viscous CFD simulations. Wiberg et al.<sup>17</sup> show results further supporting the idea that matching the full-scale wing section attachment line location at the centerline of the tunnel generates, indeed, satisfactory ice shapes for the 3D hybrid model. In order to narrow the number of critical baseline cases that drive the design of the hybrid wing model, it is assumed that if the hybrid model is capable of reaching the farthest attachment line location at the tunnel centerline without significant flow separation, then it is capable of reaching all others. The cases requiring the attachment line location to be farthest down the leading edge are considered the most aggressive scenarios because they require the largest circulation, and therefore, impose the highest risk of flow separation to the hybrid wing. Fujiwara et al.<sup>12</sup> show in the 2D hybrid airfoil design method that there is no unique combination of angle of attack and flap deflection that reaches a particular stagnation point location. Instead, there is one corresponding flap deflection for each angle of attack that reaches the same stagnation point location, with very distinct loads. The more front loaded the model, the smaller the load required to reach the same stagnation point. Based on that, if flow separation is observed during step 4 on the main element of the hybrid wing but not on the flap, it means some of the load should be transferred from the main element to the flap by increasing the flap deflection and decreasing the main element camber, while reaching the same attachment line location for that particular angle of attack. The analogy applies similarly if separation occurs on the flap and not on the main element. This process continues iteratively until the farthest attachment line location is reached with no flow separation, within the tunnel load limits.

Once this is achieved, the fifth step is to observe how much the attachment line location on the hybrid wing model changes across the span. If variation is significant, then spanwise load control techniques must be employed. This is discussed later in this paper. Otherwise, the three-dimensional ice shapes are calculated in step 6 using LEWICE3D, and compared to the full-scale ice shapes. For this project, the hybrid wing model ice shapes were only investigated near the centerline region of the model because that is where the model is designed to reach the full-scale attachment line location. This is also region away from the tunnel wall boundary layer, where the icing cloud in the IRT is more uniform. If for some reason the icing wind tunnel cannot reach the flight icing conditions (density, velocity, etc), then icing scaling must be used to correct for the different operating condition, like the similitude method shown by Wiberg et al.<sup>17,38</sup> Otherwise, the hybrid wing is considered complete.

### Computational Tools

The flow solutions were obtained using Fluent,<sup>19</sup> RANS solver with k- $\omega$  SST (Shear Stress Transport) turbulence model, and grids generated by PointWise<sup>39</sup> with from about 16 million nodes for the OB model to about 35 million for the IB model. The boundary layer of the model and tunnel were resolved with a layer of anisotropic tetrahedral elements (T-Rex)<sup>40</sup> to obtain a dimensionless wall distance  $y^+ = 1$ , and isotropic tetrahedral elements elsewhere.

The code utilized to calculate the model ice shapes was LEWICE3D.<sup>20,41</sup> Both the flow solver and the ice accretion code were run at the University of Illinois at Urbana-Champaign computer cluster Taub,<sup>42</sup> and at the University of Washington cluster Hyak, and more details of the mesh topology are given by Wiberg et al.<sup>17,38</sup>

## III. Results and Discussion

### HYBRID WING MODEL DESIGN PARAMETERS

#### Effect of Wind Tunnel Sidewalls

The wind tunnel sidewalls are an important topic from the hybrid wing model design perspective because it affects the attachment line location, the risk of flow separation, and ultimately, the model performance to reproduce full-scale ice shapes. A discussion of the applications of these effects is presented by Wiberg et al.<sup>17</sup> and Wiberg.<sup>38</sup>

The flowfield of an untwisted swept-back wing model confined by sidewalls, like the IRT hybrid models designed for this project, shows a very pronounced three-dimensional feature of increasing outboard load, as shown in Fig. 5 for the RANS solution for the IB hybrid wing model at  $\alpha = 3.67^\circ$ , with a flap deflection of  $\delta = 6^\circ$ , run at approximately 120 m/s. The circulation increases further outboard on the model, leading to higher suction peaks noted by the lower pressure blue color on the upper surface of the model.

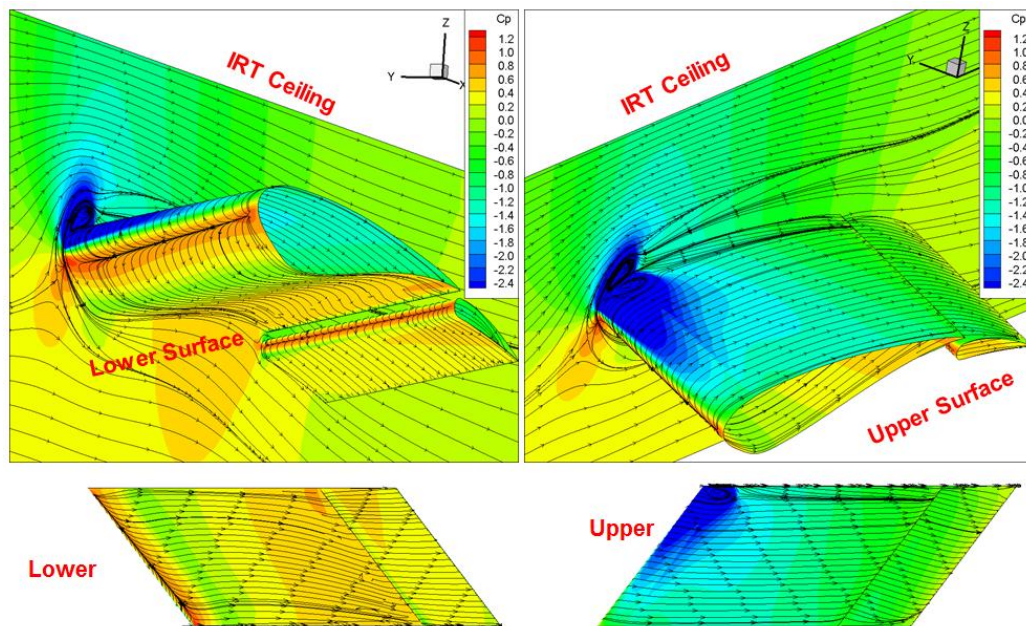
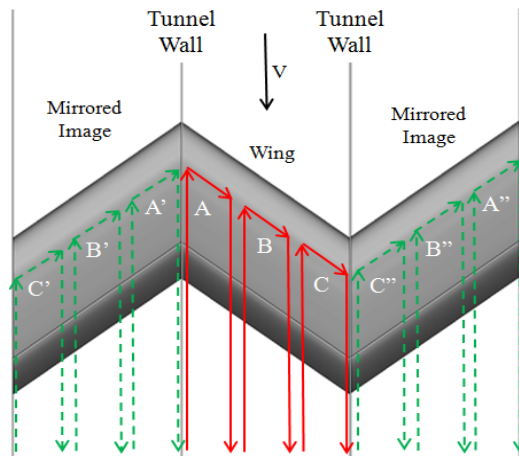


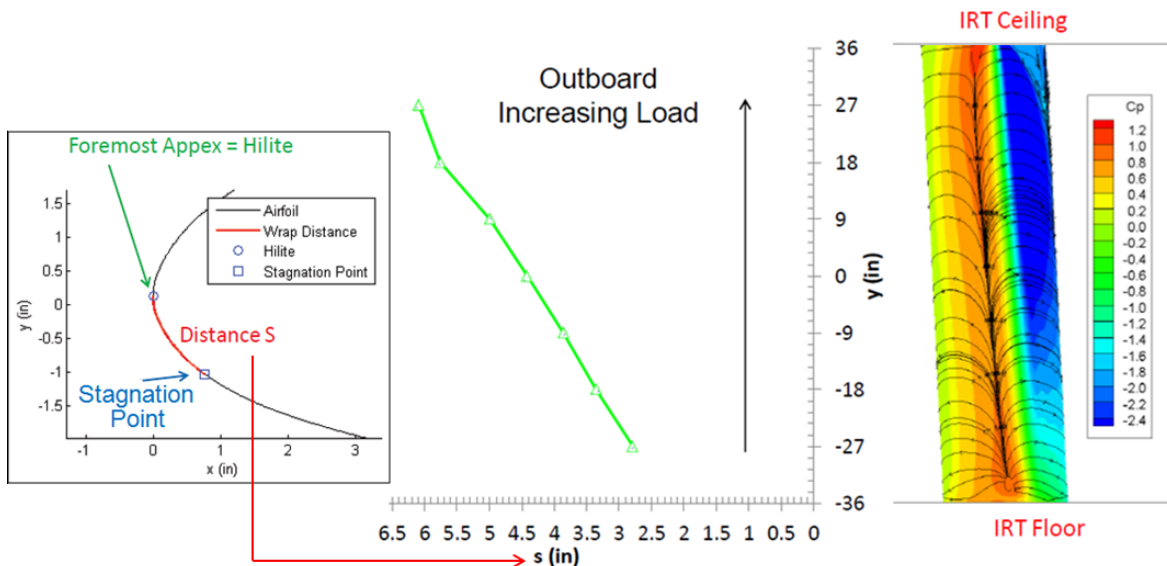
Figure 5. Hybrid wing RANS solution showing spanwise variation:  $\alpha=3.67^\circ$ ,  $\delta=6^\circ$ ,  $V=119.41$  m/s,  $Re=3.45 \times 10^7$

This phenomenon occurs naturally in swept-back wings due to the induced upwash by the stations upstream of the outboard region,<sup>13</sup> but is particularly enhanced for a model bounded by walls because of the symmetry condition imposed by the sidewalls.<sup>17,38</sup> A lifting line representation of the swept wing model inside the IRT is shown in Fig. 6, placing three horseshoe vortices A, B, and C, each composed of two trailing edge vortices connected by a bound vortex, on the wing and on two mirrored images at each side of the wall. It can be observed that the right trailing vortex of the horseshoe vortex C, which primarily contributes to decreasing the outboard local angle of attack by inducing downwash at the wing tip, is cancelled by its image C''. The bound vortex of C'' also induces a greater upwash on the wing outboard region, contributing to increase the outboard load further. The inboard region, on the other hand, sees a much lower effect since the vortices are inducing upwash to the left of the left mirrored image, away from the wing inboard region. Note that both mirror images distort the flow conditions from those that the model is attempting to reproduce with this 3-segment kinked wing, as opposed to the continuous swept-back wing expected in the model neighborhood, as in Fig. 4b. This explains the observed load variation across the span, which initiated the investigations presented here for the use of spanwise load control techniques.



**Figure 6. Lifting line theory representation of swept wing model bounded by sidewalls**

The influence of spanwise load variation on the attachment line location can be observed in Fig. 7. The abscissa axis presents the dimensional distance in inches from the model front most point, also referred to as hilite, to the attachment line. The ordinate axis presents the model spanwise position in inches, with the IRT floor at -36 in and ceiling at +36 in. The CFD RANS solution with pressure contours for the same case is shown at the right.



**Figure 7 – Hybrid wing model attachment line variation with span at  $\alpha = 3.67^\circ$ ,  $\delta = 6^\circ$**



### Effect of Model Sweep Angle

For a given aircraft reference geometry, the leading-edge sweep angle must be preserved in order to attempt to maintain the inherent three-dimensional swept wing icing physics present in the full-scale model. All hybrid wing models designed to the CRM65 were extruded maintaining the leading-edge sweep angle of  $\Lambda = 37.15^\circ$ . Nevertheless, the sweep angle is the primary driver for the spanwise load variation observed in the CFD simulations and would be expected to cause a significant change for an aircraft reference geometry with a different sweep angle than the CRM65. This effect is now investigated comparing the spanwise variation of attachment line and load for four hybrid wings using the MS hybrid airfoil extruded parallel to the leading edge with sweep angles of  $\Lambda = 0^\circ$ ,  $25^\circ$ ,  $35^\circ$ , and  $45^\circ$ , while maintaining the 6-ft span.

The top row of Fig. 8 illustrates the pressure coefficient contours and streamlines on the upper surfaces of each model, while the bottom row illustrates the sectional pressure coefficients extracted from 3 spanwise locations: +18, 0 (centerline cut), and -18 inches for each of the models. It can be observed from Fig. 8 that increasing the sweep angle causes the load to increase outboard of the model, leading to increasing levels of flow separation on the outboard region for the more swept models. Notice that since these hybrid wings were designed starting from the same MS hybrid airfoil normal to the leading edge, the higher sweep angle hybrid wing models see a less thick streamwise airfoil, causing the Cp peaks to be lower for the centerline cut. Still, the increase in spanwise load was large enough to cause flow separation near the ceiling for the  $\Lambda = 35^\circ$  and  $45^\circ$  models.

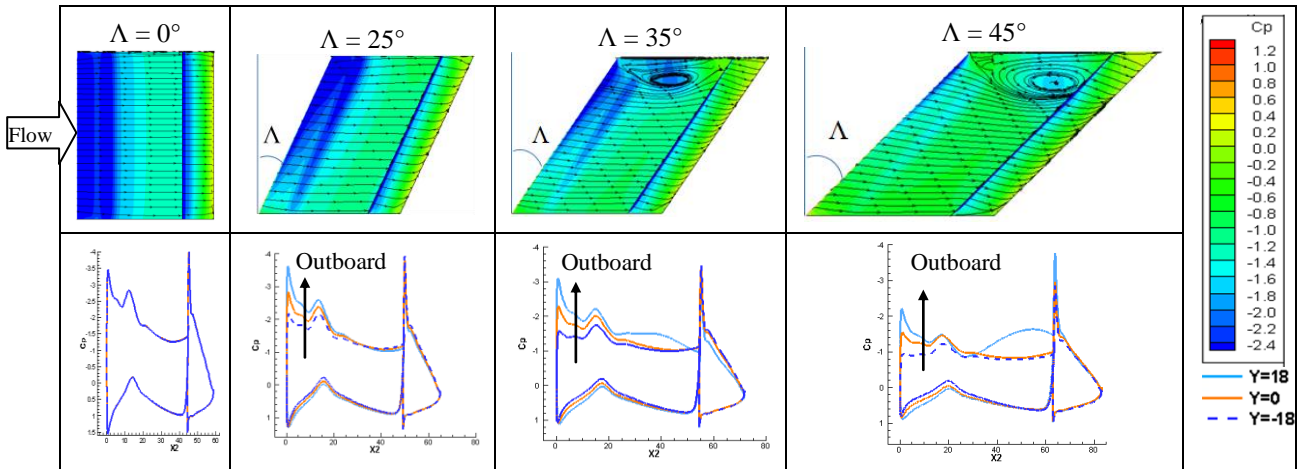


Figure 8. Effect of Sweep Angle on Spanwise Load Distribution

A direct consequence of the load variation along the span can be visualized in the attachment line location across span, Fig. 9. As sweep angle increases, so does the outboard load, causing the attachment line to be located further back on the outboard regions. As expected for a straight wing, the attachment line does not vary across span, indicated by the vertical line on the plot of Fig. 9.

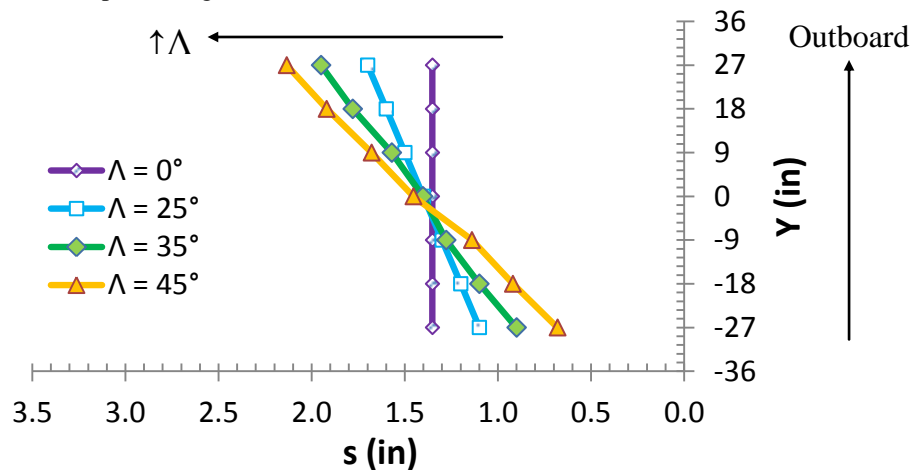


Figure 9. Effect of Sweep Angle on Attachment Line Location

### Effect of Model Aspect Ratio

The hybrid wing aspect ratio, AR, is determined by the scale factor SF chosen for the 2D hybrid airfoil design and the wind tunnel test section height and width. The larger the scale factor and wind tunnel test section dimensions, the larger the hybrid wing model AR will be. For the current project, the icing wind tunnel utilized is the IRT, which is 6-ft high, and the three hybrid wing models, IB, MS, and OB, have scale factors of 2.25, 2, and 1.5, respectively, which yield hybrid wing models with AR of 0.43, 0.94, and 0.94. If aircraft reference geometry, hybrid airfoil scale factors, and/or icing tunnel test section dimensions change, different AR hybrid wing models are expected. For the purposes of evaluating this effect, models with AR values of 0.5, 1, 2, 4, and 8 are now assessed.

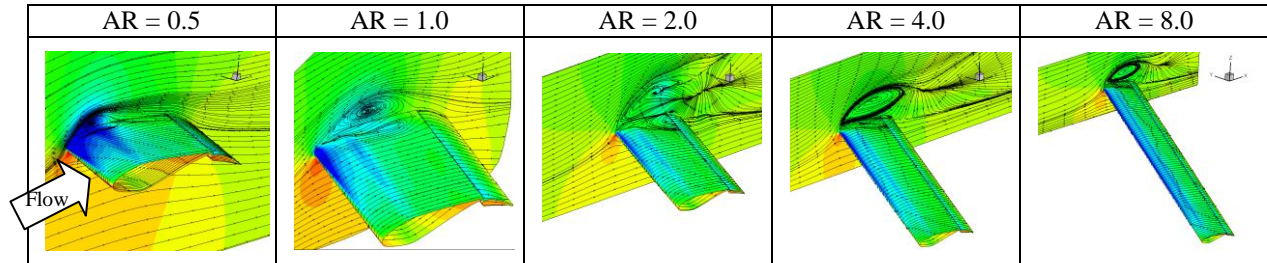


Figure 10. Effect of model AR on pressure distribution for a constant chord

All models kept the same chord in order to maintain the same Reynolds number. The model spans were varied to 38.5, 77, 154, 308, and 616 inches to achieve the AR values previously indicated. The pressure distribution on each of the models can be viewed in Fig. 10, along with the surface streamlines on the upper surfaces and IRT ceiling. One can notice the larger separation bubble near the ceiling for the longer span models (higher AR), but the same overall pressure variation trend along the span for all models. This pressure variation trend along span is confirmed by Fig. 11a, where the attachment line location plotted as function of the non-dimensional span for each model presents similar slopes. On the other hand, plotting the attachment line location as function of the physical span dimension near the centerline of the tunnel, Fig. 11b, reveals that the larger AR models offer way less variation of the attachment line for the given region of +/- 18 inches around the tunnel centerline, due to the greater distance from the sidewalls.

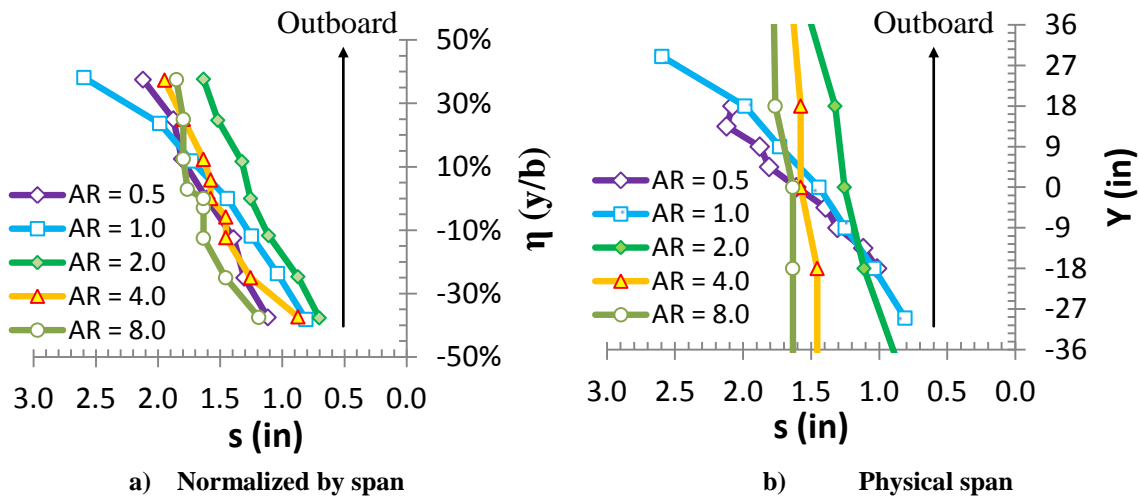


Figure 11. Effect of model AR on attachment line location across span

### Effect of Model Angle of Attack

Fujiwara et al.<sup>12</sup> showed that running the same hybrid airfoil at higher angles of attack with lower flap deflections or even no flaps while reaching the same stagnation point locations leads to similar ice shapes, with a lower load. A similar study is done by Wiberg et al.<sup>17</sup>, running the model at higher angles of attack without the flap, while maintaining the same attachment line location at tunnel centerline. It is shown that good agreement in matching full-scale ice shape is obtained, while also reducing the variation of the ice shapes across the span. These

results from the model design perspective show great benefit from removing the flap from the hybrid wing model, reducing model total load, and its variation across span. It is important to remember that, although the use of angle of attack alone for a single element wing is shown to successfully reproduce the full-scale ice accretion, flaps still provide extra control for fine tuning the exact location of the attachment line location when operating the models in the tunnel.

### Effect of Model Thickness / Wind Tunnel Blockage

Even though hybrid wing models are usually significantly smaller than the full-scale reference geometry, these models can still be fairly large in comparison to the wind tunnel test section. The proximity of the wind tunnel walls to the model cause the flow to accelerate around the model in order to maintain continuity. The model acts as an obstacle blocking the incoming flow, altering the flowfield around the model and significantly limiting the achievable wind tunnel speeds during operations. In order to assess this effect on the model operation, different dimensions for the wind tunnel walls were tested while maintaining the same dimensions of the IB hybrid wing model, to obtain a tunnel height (in this case width due to how the models are positioned spanning from floor to ceiling across the IRT's 6-ft high x 9-ft wide test section) to model chord ratio of  $h/c = 0.5, 1, 2,$  and  $4$ . The resulting flowfields are presented in Fig. 12, in which is possible to see that the closer the walls (top and bottom) are to the model, the more the flow is accelerated around it, causing model loads to increase with the faster speeds. Flow separation occurs due to the adverse pressure gradients that must be recovered past the now higher pressure suction peaks on the model upper surfaces.

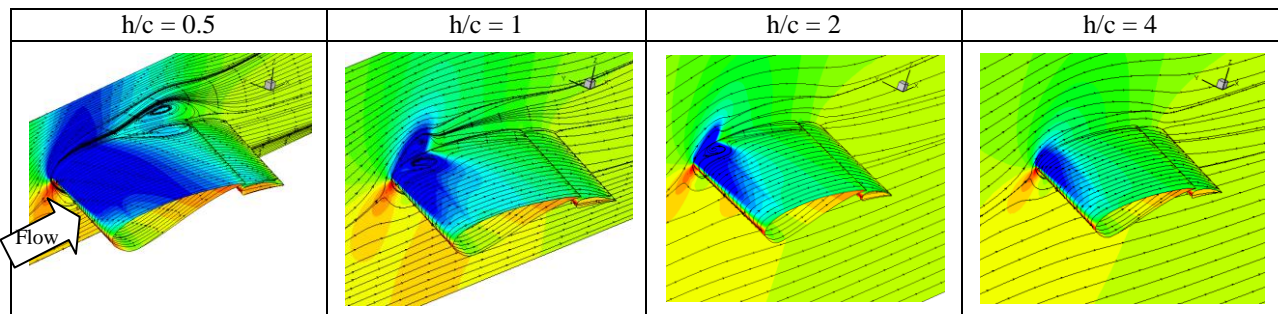


Figure 12. Wind Tunnel Height effect on pressure distribution and attachment line location

Interestingly, the attachment line location is also altered along the span, with tunnel blockage. The accelerated flow that drives higher suction peaks, Fig. 13a, also amplifies the load variation across span, yielding even greater attachment line variations along the span, Fig. 13b. This is especially undesirable for these models because the higher loads (lift) generate more circulation locally, further shifting the attachment line location, which is the primary driver for matching ice shapes. Additionally, the increased suction peaks play a role on the ice shapes by enhancing the heat transfer coefficients locally, which can lead to larger freezing fractions and longer horn lengths.

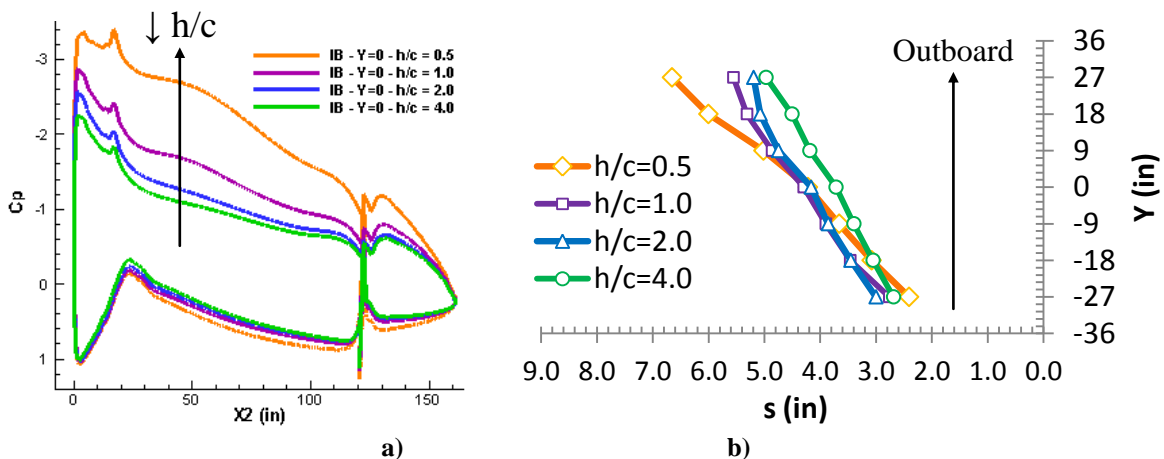


Figure 13. Effect of wind tunnel blockage on: a) Centerline pressure distribution b) Attachment line location

## SPANWISE LOAD CONTROL TECHNIQUES

Because the attachment line location on the hybrid wing model plays such an important role in its ability to reproduce full-scale ice shapes, it is of great interest to investigate means of reducing its variation across the model span. Some of the techniques are described in the next sessions.

### Effect of Sidewall Gap

Sidewall gaps allow the development of wing tip vortices that would not appear if the model spanned all the way between sidewalls, Fig. 6. The Midspan model with no gap between the walls is shown in Fig. 14, where the outboard increasing upwash ahead of the model leading edge is shown, Fig. 14a, and the outboard increasing downwash past the model trailing edge is also illustrated, Fig. 14b.<sup>38</sup>

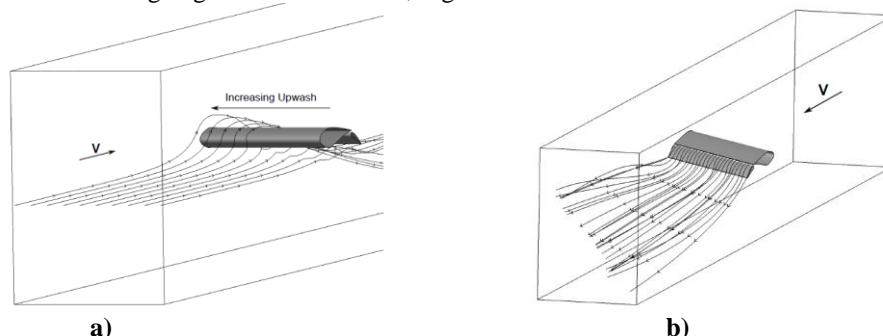


Figure 14. a) Increasing outboard leading-edge upwash, b) Increasing outboard trailing-edge downwash

Creating a 6-inch gap on the inboard side, as shown in Fig. 15a, between the IRT floor and the model, allows the tip vortices to lower the local inboard load due to the induced downwash by the trailing vortices, causing the load distribution and the wake past the model to be even more uneven across the span. On the other hand, a gap on the outboard side, as shown in Fig. 15b, between the IRT ceiling and the model, allows the development of wingtip vortices that help equalize the wake across the model span. The observed problem associated with this approach is that the entire model was unloaded, Fig. 15c, with little change in attachment line slope across span. Thus, a larger flap deflection was now required to reach the same attachment line location which ended up yielding a similar attachment line slope to the no-gap model. Although this approach helped avoiding flow separation at the outboard wall, it did not reduce the attachment line slope across the span for the same centerline attachment line location.<sup>38</sup>

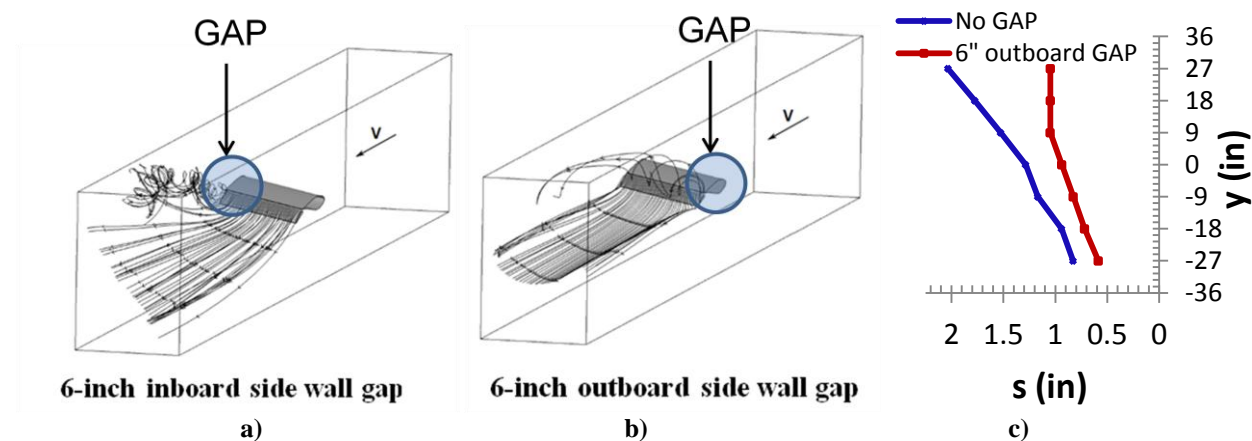


Figure 15. Midspan model a) inboard side wall gap, b) outboard side wall gap, c) Attachment line comparison

### Effect of Model Twist

The use of geometric twist on the model had a better effect on equalizing the wake,<sup>38</sup> Fig. 16, by geometrically increasing the inboard aerodynamic angle of attack and decreasing the outboard. A washout twist of approximately 10° was required on the Midspan main element to start observing significant changes on the attachment line location slope across span. The spanwise load variation reduction was extremely successful, as illustrated in Fig. 17a,b Cp

plots. Like the 2D study presented by Fujiwara et al.,<sup>12</sup> the closer lift is generated to the leading edge, the stronger the effect is has on the attachment line location.

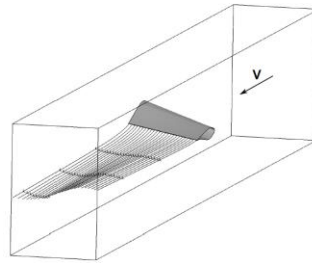


Figure 16. Midspan twisted main element with a 10° washout twist

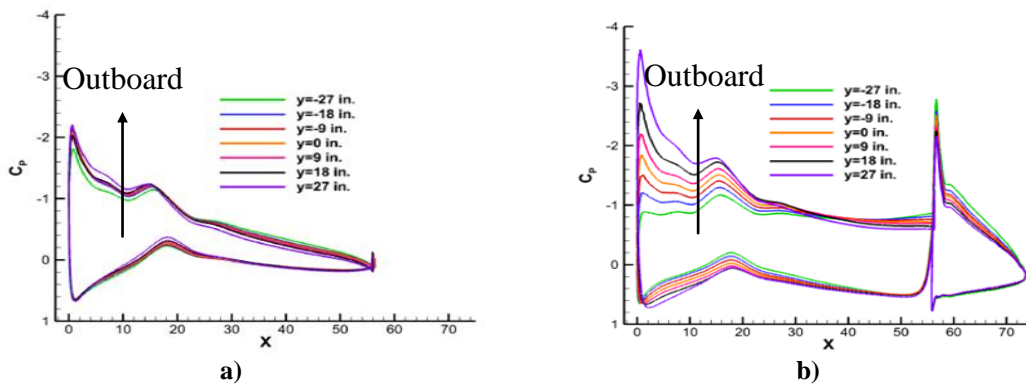


Figure 17.a) Midspan twisted main element only at  $\alpha = 10^\circ$ , b) Original Midspan (untwisted) at  $\alpha = 3.67^\circ$ ,  $\delta = 15^\circ$

### Effect of the Use of Segmented Flaps

As an alternative to applying model twist, segmented flaps can be utilized to change the camber across the span by deflecting the panels independently.<sup>38</sup> Since segmented flaps require independent actuation systems, it poses an operational difficulty to have several on a single model. A configuration with three flap panels was chosen to evaluate its performance in equalizing the spanwise load distribution. Results for the IB and MS models did not show a significant change. The fact that both models have low AR (less than 1) suggested the effectiveness of segmented flaps in successfully equalizing the load distribution is dependent on model AR, as the zone of influence of flaps is closer to affecting just the portion of the wing ahead of it, as illustrated in Fig. 18 a,b,c for different model AR.

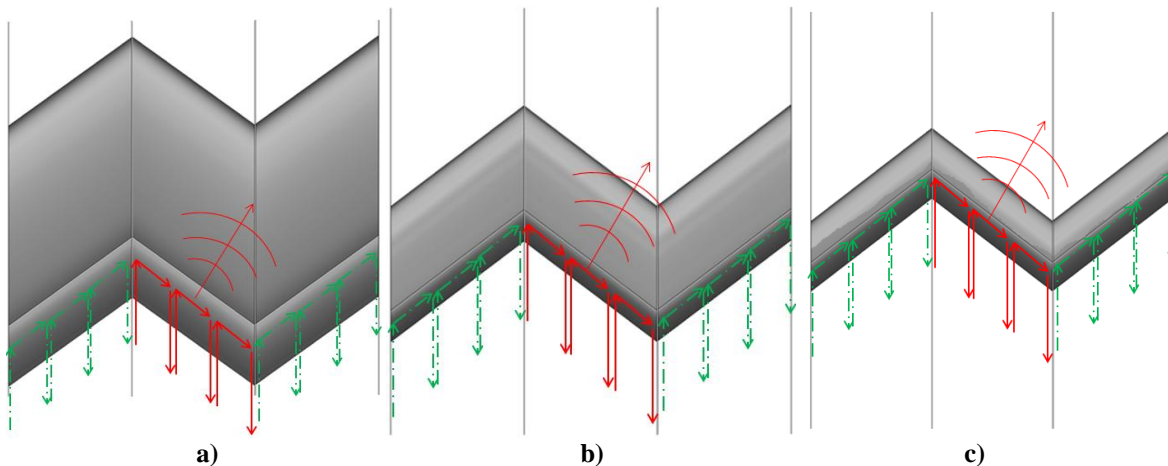


Figure 18. Scheme of 3 hybrid models with three-segmented flaps each for a) AR = 0.5, b) AR = 1, c) AR = 2

The effect of using segmented flaps was studied using hybrid wing models with AR = 0.5, 1, 2, 4, and 8. To avoid numerical convergence issues, all solutions generated for this study are inviscid, using an Euler solver. Notice these are the same models utilized in the effect of AR study, but now with a 3-segment flap instead of the constant  $\delta=15^\circ$  single-segment flap used before. In an attempt to equalize the load distribution, all flaps were deflected to  $20^\circ$  inboard,  $10^\circ$  center,  $0^\circ$  outboard, as seen in Fig. 19. All models chords were also the same to maintain the same Reynolds number.

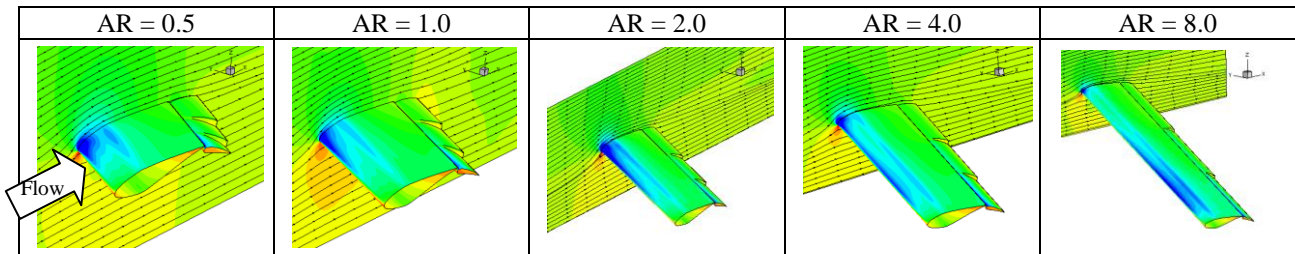


Figure 19. Segmented flaps for models with AR = 0.5, 1, 2, 4, 8

The resulting attachment line locations on the leading edge of the main element of each of the models are presented in Fig. 20, as a function of the non-dimensional span. The slope of the curve remains largely unaffected for AR = 0.5 and 1. For AR = 2, the slope starts getting more vertical near the centerline, as this effect gets more pronounced as AR further increases. It becomes quite clear for AR = 8 that the segmented flaps fully control the spanwise load distribution, shown by the inverted slope that indicates a much higher load near the inboard region compared to the outboard.

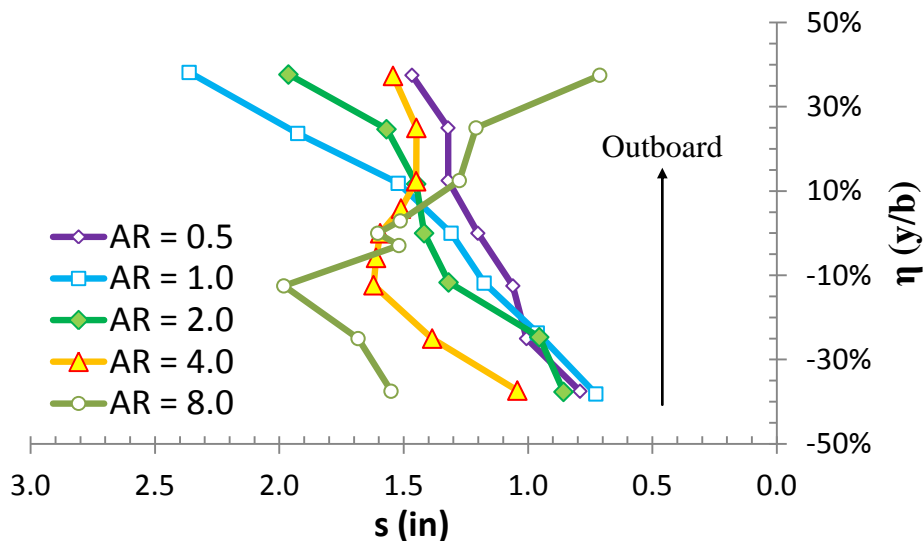


Figure 20. Effect of segmented flaps on attachment line location for different AR

#### IV. Model-Design Tradeoffs and Conclusions

The ultimate goal of designing hybrid wing models for icing wind tunnel tests was to reproduce the full-scale wing ice shapes. An ideal hybrid wing model would produce full-scale ice shape with minimal flow separation, manageable model load, and minimum wind tunnel blockage.<sup>43,44</sup>

An effective hybrid wing design method was presented here. Starting from the design of a 2D hybrid airfoil and extruding it parallel to the full-scale leading edge direction, a hybrid wing model is shown to successfully reproduce free-air ice shapes on the centerline of the wind tunnel model by utilizing the first-order approach of matching the full-scale attachment line location, shown by Wiberg et al.<sup>17</sup>

The sweep angle was the primary cause for attachment line spanwise variation, due to the induced upwash from the upstream inboard stations and the mirrored image imposed by the wind tunnel wall symmetry that amplify the upwash on the outboard region. Since attachment line location matching was first order in matching ice shape, spanwise load control techniques may be required if the spanwise variation is beyond acceptable limits.

Adding sidewall gaps on the inboard side makes attachment line spanwise variation even more asymmetric. Adding sidewall gaps on the outboard side helps unload the model and reduce possible separation bubbles near the wall, but did not change the attachment line location slope along span.

Using segmented flaps, local flap angles can be varied in order to change the attachment line position at local stations. Segmented flaps were not effective in significantly changing the spanwise distribution of load and attachment line position for models with aspect ratio near unity. Increasing the AR of a model simultaneously reduces the spanwise variation in CI and attachment line position caused by sidewalls while increasing the effectiveness of segmented flaps. Because the purpose of this research was to look at large-scale wing models, increasing the aspect ratio of the model was not a practical solution.

Using model twist, the local angle of attack of the model can be varied in order to change the attachment line location at local stations. Twist was more effective in changing the spanwise load distribution by changing circulation closer to the model leading edge, changing the effective angle of attack across the span of the model, and compensating for the increasing upwash across the model. Whether the additional complexity added to the model is justified depends on the requirements of the icing tests to be conducted.

Model thickness and wind tunnel blockage increase suction peaks on the upper surface of the model and amplify the attachment line spanwise variation along span.

Angle of attack and flap deflection can be combined to yield the desirable attachment line location. Model twist and angle of attack effectiveness in moving the attachment line may bring into question the necessity for a flap, as it adds complexity to the model.

The current hybrid wing design method was computationally expensive due to the number of iterations required to generate a satisfactory model. Simultaneously matching full-scale attachment line location, with minimal or no flow separation, within the wind tunnel load limits, and producing good full-scale ice accretion agreement required substantial three-dimensional analysis tools. Although intermediate 2D viscous CFD RANS solutions can be run to mitigate the risks inherent in the use of potential flow codes used for the 2D hybrid airfoil design, the 3D viscous CFD RANS calculations identified a number of undesirable three-dimensional effects that are not captured by 2D analysis. These effects include spanwise load variation, tunnel sidewalls interaction, high tunnel blockage, and 3D flow separation. In the future, a direct 3D design approach might yield a more efficient design method, starting directly from the 3D full-scale leading edge geometry and designing the 3D truncated aft section with an integrated flap, if a flap is necessary or desired. Guided by 3D CFD RANS, wing optimization techniques could help reduce local flow separation risk and match attachment line over a larger wing span, by taking advantage of exploring the greater design flexibility that a fully 3D truncated aft geometry design provides compared to an extruded 2D aft geometry.

## Acknowledgements

The funding for this research was provided by NASA grant NNX12AB04A. The authors kindly thank Andy Broeren, Colin Bidwell, Mark Potapczuk, and others of the NASA Glenn Icing Research Branch as well as Ben Paul, Adam Malone, John Vassberg, Abdi Khodadoust and others from Boeing Commercial Aircraft for their technical contributions. Thanks also to Eric Loth of the University of Virginia and Chris Triphahn of the University of Illinois for their assistance with CFD simulations. Finally, the authors thank Wayne Hoyenga, Jeff Diebold, Phil Ansell, Marianne Monastero, and Stephanie Camello of the University of Illinois for their contributions to this work.

## References

- <sup>1</sup>Bragg, M.B., Broeren, A.P, Blumenthal, L.A., "Iced-Airfoil Aerodynamics," *Progress in Aerospace Sciences*, Vol. 41, No. 5, 2005, pp. 323-418.
- <sup>2</sup>Lynch, F. T. and Khodadoust, A., "Effects of ice accretions on aircraft aerodynamics," *Progress in Aerospace Sciences*, Vol. 37, No. 8, Nov. 2001, pp. 669-767.
- <sup>3</sup>Bragg, M.B., Broeren, A., Addy, H., Potapczuk, M., Guffond, D., Monteruil, E., "Airfoil Ice-Accretion Aerodynamics Simulation", AIAA, Urbana, IL, 2007.

- <sup>4</sup>Broeren, A.P., Bragg, M.B., Addy, H.E., Lee, S., Moens, F., Guffond, D., "Effect of High-Fidelity Ice-Accretion Simulations on Full-scale Airfoil Performance" *AIAA Journal of Aircraft*, Vol. 47, No.1, 2010, pp. 240-254.
- <sup>5</sup>14 CFR Part 25, Appendix C. Part I - Atmospheric Icing Conditions.
- <sup>6</sup>Jeck, R. K., "Icing Design Envelopes: 14 CFR Parts 25 & 29, Appendix C) Converted to a Distance-Based Format," National Technical Information Services, U.S. Department of Transportation Federal Aviation Administration, 2002.
- <sup>7</sup>Mortonson, A. J., "Use of Hybrid Airfoil Design in Icing Wind Tunnel Tests of Large Scale Swept Wings," M.S. Dissertation, Dept. of Aerospace Engineering, University of Illinois at Urbana-Champaign, Champaign, IL, 2011.
- <sup>8</sup>Von Glahn, U.H., "Use of Truncated Flapped Airfoils for Impingement and Icing Tests of Full-scale Leading-Edge Sections," NACA/RM E56E11, 1956.
- <sup>9</sup>Anderson, D. N., "Manual of Scaling Methods," NASA CR-2004-21287.
- <sup>10</sup>Tsao, J.-C. and Lee, S., "Evaluation of Icing Scaling on Swept NACA 0012 Airfoil Models," NASA/CR, National Aeronautics and Space Administration, 2012.
- <sup>11</sup>Saeed, F., Selig, M.S., Bragg, M.B., "Design of Subscale Airfoils with Full-scale Leading-Edges for Ice Accretion Testing", *AIAA Journal of Aircraft*, Vol. 34, No. 1, 1997, pp. 94-100.
- <sup>12</sup>Fujiwara, G. E. C., Woodard, B., Wiberg, B., Mortonson, A. J., and Bragg, M., "A Hybrid Airfoil Design Method for Icing Wind Tunnel Tests," Fluid Dynamics and Co-located Conferences, American Institute of Aeronautics and Astronautics, June 2013.
- <sup>13</sup>Katz, J., Plotkin, A., "Low-Speed Aerodynamics," Cambridge University Press, New York, 2001, pp.331-360.
- <sup>14</sup>Diebold, J., Broeren, A., and Bragg, M., "Aerodynamic Classification of Swept-Wing Ice Accretion," Atmospheric and Space Environments Conference: Aircraft Icing, American Institute of Aeronautics and Astronautics, 2013.
- <sup>15</sup>Vargas, M., "Current Experimental Basis for Modeling Ice Accretions on Swept Wings," *Journal of Aircraft*, Vol. 44, No. 1, Jan. 2007, pp. 274-290.
- <sup>16</sup>Broeren, A. P., Potapczuk, M., Riley, J., Villedieu, P., Moens, F., and Bragg, M., "Swept-Wing Ice Accretion Characterization and Aerodynamics," Fluid Dynamics and Co-located Conferences, American Institute of Aeronautics and Astronautics, June 2013.
- <sup>17</sup>Wiberg, B., Fujiwara, G. E. C., Woodard, B., and Bragg, M., "Large-Scale Swept-Wing Icing Simulations in the NASA Glenn Icing Research Tunnel Using LEWICE3D," AIAA AVIATION, Atlanta, GA, 2014.
- <sup>18</sup>Soeder, R. H., "NASA Lewis Icing Research Tunnel User Manual," National Aeronautics and Space Administration, 1996.
- <sup>19</sup>ANSYS FLUENT 12.0 User's Guide. ANSYS, Inc. April, 2009.
- <sup>20</sup>Bidwell, C. S. and Potapczuk, M. G., "Users Manual for the NASA Lewis Three-Dimensional Ice Accretion Code (LEWICE3D)," TM 105974, NASA, 1993.
- <sup>21</sup>Wright, W., "Validation Results for LEWICE 3.0," Aerospace Sciences Meetings, American Institute of Aeronautics and Astronautics, Jan. 2005.
- <sup>22</sup>Vassberg, J.C., DeHaan, M.A., Rivers, S.M., Wahls, R.A., "Development of a Common Research Model for Applied CFD Validation Studies," AIAA-2008-6919, 2008.
- <sup>23</sup>Eliasson, P. and Peng, S.-H., "Influence of Turbulence Modelling and Grid Resolution In Computations of the DPW4 CRM Configuration," Aerospace Sciences Meetings, American Institute of Aeronautics and Astronautics, Jan. 2010.
- <sup>24</sup>Mani, M., Rider, B., Sclafani, A., Winkler, C., Vassberg, J., Dorgan, A., Cary, A., and Tinoco, E., "RANS Technology for Transonic Drag Prediction; A Boeing Perspective of the 4th Drag Prediction Workshop," Fluid Dynamics and Co-located Conferences, American Institute of Aeronautics and Astronautics, June 2010.
- <sup>25</sup>Vassberg, J., "Introduction: Drag Prediction Workshop," *Journal of Aircraft*, Vol. 45, No. 3, May 2008, pp. 737.
- <sup>26</sup>Hashimoto, A., Murakami, K., Aoyama, T., Yamamoto, K., Murayama, M., and Lahur, P., "Drag Prediction on NASA CRM Using Automatic Hexahedra Grid Generation," Aerospace Sciences Meetings, American Institute of Aeronautics and Astronautics, Jan. 2010.
- <sup>27</sup>Sclafani, A., Vassberg, J., Mani, M., Winkler, C., Dorgan, A., Olsen, M., and Coder, J., "DPW-5 Analysis of the CRM in a Wing-Body Configuration Using Structured and Unstructured Meshes," Aerospace Sciences Meetings, American Institute of Aeronautics and Astronautics, Jan. 2013.
- <sup>28</sup>Vassberg, J., Tinoco, E., Mani, M., Rider, B., Zickuhr, T., Levy, D., Brodersen, O., Eisfeld, B., Crippa, S., Wahls, R., Morrison, J., Mavriplis, D., and Murayama, M., "Summary of the Fourth AIAA CFD Drag Prediction Workshop," Fluid Dynamics and Co-located Conferences, American Institute of Aeronautics and Astronautics, June 2010.
- <sup>29</sup>Rivers, M.B., Dittberner, A., "Experimental Investigation of the NASA Common Research Model" *AIAA Applied Aerodynamics Conference*, AIAA, Chicago. 2010.
- <sup>30</sup>Rivers, M., Hunter, C., and Campbell, R., "Further Investigation of the Support System Effects and Wing Twist on the NASA Common Research Model," Fluid Dynamics and Co-located Conferences, American Institute of Aeronautics and Astronautics, June 2012.
- <sup>31</sup>Paul, B., Malone, A., and Vassberg, J., Personal communications to the author, 2013.
- <sup>32</sup>Robinson, B., Verho, A., and LaBozzetta, W., "Preliminary findings in certification of OVERFLOW," Fluid Dynamics and Co-located Conferences, American Institute of Aeronautics and Astronautics, June 1994.
- <sup>33</sup>Jespersen, D., Pulliam, T., Buning, P., Jespersen, D., Pulliam, T., and Buning, P., "Recent enhancements to OVERFLOW," Aerospace Sciences Meetings, American Institute of Aeronautics and Astronautics, Jan. 1997.
- <sup>34</sup>Saeed, F., Selig, M.S., Bragg, M.B., "Hybrid Airfoil Design Procedure Validation for Full-scale Ice Accretion Simulation", *AIAA Journal of Aircraft*, Vol. 36, No.5, 1999, pp. 769-776.



<sup>35</sup>Saeed, F., Selig, M.S., and Bragg, M.B., "Hybrid Airfoil Design Method to Simulate Full-scale Ice Accretion Throughout a Given  $\alpha$  Range," *AIAA Journal of Aircraft*, Vol. 35, No.2, 1998, pp. 233-239.

<sup>36</sup>Saeed, F., Selig, M., Bragg, M., "A hybrid airfoil design method to simulate full-scale ice accretion throughout a given Cl range," Aerospace Sciences Meetings, American Institute of Aeronautics and Astronautics, Jan. 1997.

<sup>37</sup>McLean, D. J., *Understanding Aerodynamics: Arguing from the Real Physics*, 1<sup>st</sup> Edition, John Wiley & Sons Ltd., November 2012, Chap 8, pp. 444-449.

<sup>38</sup>Wiberg, B. D., "Large-scale swept-wing ice accretion modeling in the NASA Glenn Icing Research Tunnel using LEWICE3D," M.S. Dissertation, Dept. of Aerospace Engineering, University of Illinois at Urbana-Champaign, Champaign, IL, 2013.

<sup>39</sup>Pointwise User Manual, Pointwise, Inc., Fort Worth, Texas. 2013, pp. 306-318.

<sup>40</sup>Steinbrenner, J. P., Abelanet, J. P., "Anisotropic Tetrahedral Meshing Based on Surface Deformation Techniques", AIAA.

<sup>41</sup>Bidwell, C., Personal communication to the author, 2013.

<sup>42</sup>"Campus Cluster Program - Service Level Definition: Taub Instance," University of Illinois at Urbana-Champaign, October, 2011.

<sup>43</sup>Barlow, J.B., Rae, W.H, and Pope.A. *Low Speed Wind Tunnel Testing*, 3<sup>rd</sup> Edition, Wiley-India Pvt. Ltd. New Delhi, 2010, Chap. 9.

<sup>44</sup>Bragg, M.B., Wells, Stephen L. "Effect of Wind-Tunnel Walls on Airfoil Droplet Impingement," *AIAA Journal of Aircraft*, Vol. 31, No.1, 1994 , pp. 175-180.



## **Appendix D.—Large-Scale Swept-Wing Icing Simulations in the NASA Glenn Icing Research Tunnel Using LEWICE3D**

Reprinted by permission of the American Institute of Aeronautics and Astronautics, Inc., from “Large-Scale Swept-Wing Icing Simulations in the NASA Glenn Icing Research Tunnel Using LEWICE3D,” Brock D. Wiberg, Gustavo E.C. Fujiwara, Brian S. Woodard, and Michael B. Bragg (Ref. 41).

# Large-Scale Swept-Wing Icing Simulations in the NASA Glenn Icing Research Tunnel Using LEWICE3D

Brock D. Wiberg\*, Gustavo E. C. Fujiwara†, Brian S. Woodard‡ and Michael B. Bragg§

*University of Illinois at Urbana-Champaign, Urbana, Illinois, 61801, USA*

Computational icing simulations of a hybrid, swept-wing model in the NASA IRT are presented. The results of these simulations are compared to those for the same icing conditions conducted on the full-scale reference wing. The effects of tunnel sidewalls, attachment line position, and altitude are considered. A discussion of icing scaling and the results of one scaling approach are given. The variation of impingement and ice shape with span in the tunnel for different angles of attack and flap deflection are presented.

## Nomenclature

$AR$	aspect ratio
$b$	wing span
$C_{m0}$	zero lift pitching moment coefficient at $c/4$
$c$	chord length
$M$	Mach number
$P$	static pressure
$Re$	Reynolds number
$SF$	hybrid scale factor
$T$	static temperature
$V$	velocity
$\gamma$	nose droop angle
$\Lambda$	sweep angle
$\alpha$	angle of attack
$\delta$	flap angle
$\eta$	dimensionless semispan position, $2y/b$
$\lambda$	taper ratio
$\mu$	dynamic viscosity
$\rho$	density of air

### *Subscripts*

$\perp$	In the direction normal to the leading edge
$sw$	In the streamwise direction
$f$	Flap
$h$	Hybrid
$le$	Leading edge

---

\*Graduate Research Assistant, Department of Aerospace Engineering, currently Member of the Technical Staff at Sandia National Laboratories, Albuquerque, NM, Member AIAA.

†Graduate Research Assistant, Department of Aerospace Engineering, Member AIAA.

‡Post Doctoral Researcher, Department of Aerospace Engineering, Member AIAA.

§Professor of Aerospace Engineering, currently College of Engineering Dean at the University of Washington, Seattle, WA, Fellow AIAA.

## I. Introduction

THE study of aircraft icing is necessary to ensure the safety of commercial, military, and general aviation aircraft. The certification of modern commercial transports requires manufacturers to demonstrate that these aircraft can safely operate during icing conditions consistent with the standards set forth by the Federal Aviation Administration (FAA). While some of these tests are performed on actual aircraft in flight, this is often very expensive and does not provide an adequately controlled matrix of test conditions. Computational tools are used throughout the design and certification of anti-ice systems. However, computational methods alone are not sufficient for aircraft certification. Icing wind tunnels are used for aircraft certification to reduce costs, provide a controlled test matrix of conditions, and validate computational icing tools.

The size of aircraft models that can be tested in wind tunnels is limited by the size and capability of existing facilities. Large wings, such as those found on modern narrow and wide-body commercial transports, cannot fit in existing test sections without being dramatically scaled. Two methods of scaling exist. The first involves geometrically scaling a section of the reference wing to fit inside the tunnel test section and then scaling the icing conditions in an attempt to maintain icing similitude. The second method maintains the full-scale leading edge of the reference geometry but replaces the aft section of the wing with a tail that is designed to produce similar flow around the leading edge but with a considerably shorter chord length, reducing model size and blockage. This type of model is called a hybrid and is used to generate full-scale ice shapes so that in the simplest cases, no icing scaling is necessary.

Modern commercial transport aircraft have large, swept wings. While a broad set of experimental data exist in the literature for airfoil and straight wing icing, there is a distinct lack of data for icing on large, swept wings. Such data is needed in order to better understand the 3D icing physics on swept wings and to allow computational tools to be developed and validated for 3D ice features such as scallops. In order to meet this need, NASA, the FAA, the French Aerospace Lab (ONERA), and the University of Illinois at Urbana-Champaign (UIUC) are collaborating in a research effort that will consider and address the practical challenges that are fundamental to icing on large-scale, swept wings such as those found on modern commercial transport aircraft. An overview of this project and an update of the status as of May 2013 is given by Broeren et al.<sup>1</sup>

The work presented in this paper falls under Phase III of this larger effort. The objective of Phase III is to better understand how ice shapes on a large-scale, swept-wing can be replicated in existing icing tunnels using a hybrid model. Understanding how ice accretes on such models, and identifying key indicators in flowfields that result in successful representation of full-scale icing, is critical to the ultimate goal of performing such testing for aircraft certification as well as considering the ability of Computational Fluid Dynamics (CFD) coupled with icing physics simulations to accurately model ice accretion in this environment.

For this research, computational tools were used to better understand the flow over a large-scale, swept-wing, hybrid model mounted vertically in the NASA Glenn Icing Research Tunnel (IRT). Fluent was used to calculate flows around a flapped-hybrid model in the IRT test section. LEWICE3D was used to simulate droplet impingement and ice accretion on the full-scale leading edge of this model.

## II. Methods

### Reference Wing

The Common Research Model (CRM)<sup>2</sup> was selected as the baseline wing for this research. The CRM is a large, swept-wing transport similar to existing commercial wide-body aircraft. A body of literature for the CRM is available in the public domain including the model geometry,<sup>2</sup> computational results,<sup>3,4,5,6,7</sup> and experimental data.<sup>8,9</sup> Figure 1 shows the full configuration of the CRM including the wing, body, horizontal tail, and nacelle-pylon group.

It was determined that the full configuration of the CRM was not necessary for the objectives of this research. Therefore, the work performed was done on the wing-body only (WB) configuration. Additionally, the full-scale CRM is very large, requiring a very large reduction in size in order to fit models into the IRT test section with acceptable levels of blockage. Furthermore, later objectives of the overall project

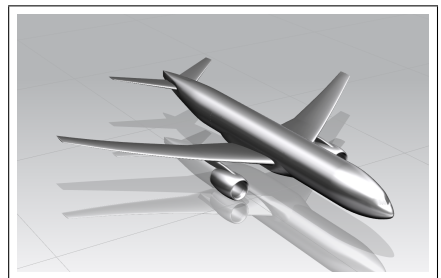


Figure 1. Full configuration of the Common Research Model.<sup>2</sup>

require that artificial ice shapes be created and aerodynamic tests of the full semispan geometry be conducted in the ONERA F1 tunnel. Because this will require scaling of the wing, small features of the ice shapes would not be reproducible if the full-scale CRM were scaled to fit into the F1 tunnel. Therefore, to reduce the risk associated with its size, the reference geometry for the project was chosen to be the CRM scaled to 65% its original size (CRM65). The CRM65 is still a large aircraft, comparable to existing narrow-body commercial transports.

The CRM was designed by Boeing as part of a collaboration with NASA.<sup>2</sup> The CRM features a wide-body fuselage similar to a modern aircraft with a transonic wing having a quarter-chord sweep of  $\Lambda = 35$  deg. The supercritical wing was designed for a cruise Mach number of  $M = 0.85$  and lift coefficient of  $C_L = 0.50$  at a flight Reynolds number of  $Re_c = 40$  million. The aircraft body extends to 10% semispan with a yehudi break at 37% semispan and 8 deg. of washout from side-of-body to tip. The CRM65 has a semispan of  $b/2 = 751.89$  in. (19.10 m) compared to the full-scale CRM semispan of  $b/2 = 1,156.75$  in. (29.38 m). With an aspect ratio of  $AR = 9.0$ , and taper ratio of  $\lambda = 0.275$ , the leading-edge sweep angle is  $\Lambda_{le} = 37.15$  deg.

## Flight Baseline

It was necessary to have a baseline set of icing simulations in order to successfully evaluate the quality of ice shapes that are simulated in the IRT. Aerodynamic flow simulations must be performed before ice accretions can be modeled. To this end, Boeing<sup>10</sup> determined a generic set of icing mission scenarios for a typical large transport aircraft. These scenarios represent all phases of flight with conditions consistent with the U.S. Code of Federal Regulations Appendix C icing clouds. Boeing then reviewed the conditions and determined that a subset of the scenarios would be adequate for determining critical ice shapes. These critical icing scenarios were given case identifiers that will be used hereafter. These identifiers, the aircraft angle of attack associated with a nominal 1G loading, and the flight conditions which they represent are given in Table 1.

**Table 1. Boeing case identifiers and the associated flight conditions.**

Case	Phase	$\alpha$ (deg.)	$P$ (Pa)	$M$	$Re_{c_{ref}}$
WB25	Climb	1.68	30,124	0.81	34.1M
WB33	Hold	3.67	69,702	0.36	28.7M
WB39	Hold	3.64	42,824	0.46	24.8M
WB41	Hold	4.38	84,319	0.35	32.9M
WB47	Hold	4.36	57,209	0.43	28.6M
WB71	ETOPS Hold	4.40	95,956	0.32	33.2M

### *Clean Flight Baseline*

The conditions discussed above were used to conduct flow simulations over the CRM65 reference wing geometry in free air. The well validated, compressible Reynolds Averaged Navier-Stokes (RANS) CFD software OVERFLOW<sup>11,12,13,14</sup> with overset grids was used to perform these calculations. The CFB is used for the icing simulations described below but is also important for direct comparison with the flow simulations of the hybrid-wing model in the IRT. This direct comparison allows the influence of individual flow parameters on ice growth to be considered. Specifically, the attachment line location, sectional pressure distribution, and lift coefficient are important flowfield parameters that help in the initial design and validation of the 3D models.

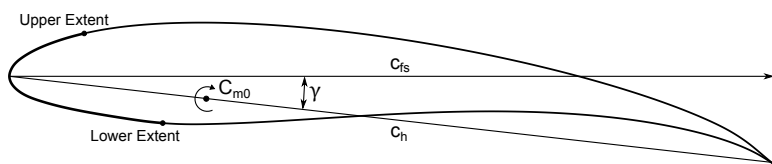
### *Iced Flight Baseline*

The CFB flow solutions provide the velocity vectors used in the calculation of droplet trajectories and the flow state (pressure and temperature) needed to simulate ice accretions. Boeing used the CFB solutions with LEWICE3D to generate a standard set of ice shapes for each of the critical icing scenarios at various temperatures, resulting in the Iced Flight Baseline (IFB). The case identifiers in table 1 are often followed by a temperature designation in Celsius. Icing simulations on the hybrid wing model in the IRT are compared

back to the IFB throughout this paper. Note that the IFB ice shapes in this paper are those reproduced by Wiberg<sup>15</sup> using the CFB flow solutions but with the most recent version of LEWICE3D (which version was also used for the IRT icing simulations in this work).

## Hybrid Model Design

A hybrid model is one that retains the full-scale leading edge of the reference geometry up to a fixed position and uses a redesigned aft section that is considerably shorter than the full-scale. The upper and lower extents up to which the full-scale geometry is maintained are determined based on either the estimated impingement limits or icing limits and are given as a percent of the full-scale chord. The hybrid scale factor,  $SF$ , is the full-scale airfoil chord divided by the total hybrid-model chord and represents the factor by which the baseline geometry is shortened. The nose droop angle,  $\gamma$ , is the angle that the hybrid model chord line makes with the full-scale chord line. This can be viewed as representing the elevation of the hybrid trailing edge with respect to the full-scale chord line. A more positive nose droop angle causes a lower trailing edge elevation or more camber, shifting more load to the aft of the hybrid. The quarter-chord zero-lift pitching moment coefficient,  $C_{m0}$ , affects the camber line curvature of the aft hybrid section such that a more positive  $C_{m0}$  will result in a less cambered aft section and, therefore, reduced aft loading. Values of  $\gamma$  can be both negative and positive but  $C_{m0}$  is usually negative.



**Figure 2. Illustration of the important parameters of a hybrid airfoil design.**

Because ice shapes grown on the nose of the hybrid model are compared to the full-scale baseline airfoil, the hybrid angle of attack is measured relative to the full-scale chord line rather than the hybrid chord line. If present, the deflection of the flap may be measured relative to the full-scale chord or other reference. For the current research, the flap angle is measured relative to the horizontal when the hybrid airfoil is rotated such that the full-scale chord is at the local angle of attack corresponding to the station on the CRM65 wing which it represents. Figure 2 illustrates some of the parameters of hybrid airfoils with the nose from the full-scale airfoil shown bolded. The model shown has  $\gamma = 7$  deg.,  $C_{m0} = -0.32$ ,  $SF = 2$ , and upper and lower extents at  $x/c_{fs} = 5\%$  and  $10\%$ , respectively. The large positive  $\gamma$  brings the tail of the hybrid airfoil well below the full-scale chord line and the negative  $C_{m0}$  causes a high degree of aft camber, seen in the curvature near the trailing edge.

A hybrid wing model can be designed to represent either a spanwise section of the reference wing or a single spanwise station. Generally, if it is desired to test an anti-ice system for aircraft certification, the 3D leading edge from the full-scale wing over a spanwise section will be used on the hybrid model so that the actual icing protection system can be integrated. However, for this research the model is only designed to represent one station of the reference wing. This results in a basic model that has constant sectional geometry from floor to ceiling in the IRT. If modifications to this model such as twist, taper, etc. are used it is for the purpose of better representing the station from the full-scale wing in the region of interest on the hybrid model rather than trying to reproduce ice shapes representative of the reference wing over an entire spanwise section.

The hybrid wing model was first designed in 2D using the method discussed by Fujiwara et al.<sup>16</sup> Designing in 2D allows the use of existing codes and expertise. Because the wing model is designed to represent a single spanwise station on the CRM65, the hybrid airfoil is simply extruded to create a hybrid wing model. However, in order to properly represent a swept wing in 2D, simple sweep theory must be used. Simple sweep theory shows that a 2D cut from a swept 3D wing taken in the direction normal to the leading edge can approximate the flow around that section in 3D if the 2D simulation uses the normal component of the velocity. Sweep theory results in the following equations relating 2D parameters in the normal direction to the equivalent 3D parameters on a wing.

$$\alpha_{3D} = \alpha_{2D} \cos \Lambda_{le} \quad (1)$$

$$c_{3D} = \frac{c_{2D}}{\cos \Lambda_{le}} \quad (2)$$

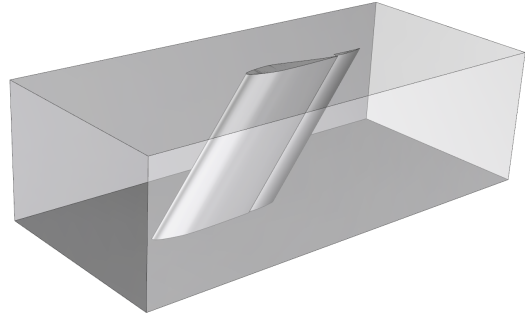
$$C_{P_{3D}} = C_{P_{2D}} \cos^2 \Lambda_{le} \quad (3)$$

$$C_{l_{3D}} = C_{l_{2D}} \cos^2 \Lambda_{le} \quad (4)$$

$$\beta_{3D} = \beta_{2D} \cos \Lambda_{le} \quad (5)$$

Simple sweep theory assumes a geometry that is constant with span (no twist or taper). The sweep angle,  $\Lambda$ , is measured in the plane containing the free stream velocity vector,  $\vec{V}_\infty$ , which is reasonable for small angles of attack. The theory also assumes inviscid flow satisfying the Euler equations. Though none of these assumptions are met by the complex wing geometries on modern commercial transport aircraft, the theory provides a reasonable approximation in the midspan region where flow is similar to that of an infinite swept wing. For this reason, the station represented by the model used in this research was taken from the CRM65 near the midspan of the exposed wing at  $\eta = 0.64$  measured from aircraft centerline. The precise location was selected because it was the point of inflection in the spanwise distribution of upper horn angle from the IFB ice shapes for several important cases.

The final flapped-hybrid wing model is shown in the IRT test section in Fig. 3. The design begins in 2D as a single element airfoil which is able to match the flow characteristics in the leading edge vicinity of the reference airfoil at a single design point. In order to make the hybrid airfoil more useful over a range of test conditions, a flap is often added. A basic external flap was designed for the model of this research by taking a NACA 6412 airfoil and making the radius of curvature constant near the leading edge. This allows the gap and overlap of the flap to remain constant over a large range of deflections with the flap pivot located at the center of the leading-edge cylinder. The flap chord is 1/3 that of the hybrid. The gap and overlap are fixed at 1.5% the total model chord. The scale factor is  $SF = 2$  with the upper and lower leading edge extents both at  $x/c_{fs} = 10\%$ . The zero-lift pitching moment coefficient and nose droop angle are  $C_{m0} = -0.05$  and  $\gamma = -5.5$  deg., respectively.



**Figure 3. Flapped-hybrid wing model in the IRT test section with direction of flow from left to right.**

The wing model was created by extruding the flapped-hybrid airfoil. Because the 2D design was done in the normal plane, the extruded model is rotated by 37.15 deg. about the negative  $z$ -axis. This results in a model that is swept at the proper leading edge sweep angle of the CRM65,  $\Lambda_{le} = 37.15$  deg. The rotated model is then cut in the streamwise direction at  $y = -36$  in. forming the root and again at  $y = +36$  in. forming the tip. The resulting span of the model matches the height of the IRT test section which is 72 in. (1.83 m). A more detailed description of this hybrid wing model design is given by Wiberg<sup>15</sup> with a more general description of hybrid-wing model design and corresponding trade-offs discussed by the authors.<sup>17</sup>

### Mesh Topology

The IRT test section is 20 ft. (6.10 m) in length with a cross section that is 6 ft. (1.83 m) tall and 9 ft. (2.74 m) wide. The center of the floor mounted turntable is 106.5 in. (2.71 m) from the inlet of the test section. Because the hybrid model is mounted from floor to ceiling, the model span is 72 in. (1.83 m). A tunnel fixed reference frame was used with positive  $x$ -axis in the flow direction and positive  $y$ -axis pointing toward the ceiling of the tunnel. The origin of this axis system is centered in the IRT test section with  $x = 0$  at the center of the turntable. This results in the root of the model placed at the floor of the IRT being at  $y = -36$  in. (0.91 m), the tip and ceiling at  $y = +36$  in. (0.91 m), and the walls of the test section at  $z = \pm 54$  in. (1.37 m).

The POINTWISE<sup>®</sup> software package<sup>18</sup> was used for meshing the hybrid wing model in the IRT test section. It features an unstructured solver that uses anisotropic tetrahedra to grow high aspect ratio cells



off surfaces on which it is desired to resolve a boundary layer. Anisotropic tetrahedral meshing (T-Rex for short<sup>19</sup>) allows high resolution boundary layer grid cells to transition smoothly into standard tetrahedral meshes away from walls. The T-Rex solver was used to generate fully unstructured meshes in the IRT test section with boundary layer meshes on all surfaces including the walls. Wiberg<sup>15</sup> describes the meshing process for the IRT simulations in more detail.

### Flow Simulations

ANSYS<sup>®</sup> Fluent v14.5 was used to perform the flowfield calculations for this research. Inviscid simulations using the Euler equations were performed to explore the fundamental flow characteristics around a large, swept-wing model in the tunnel. Viscous simulations made use of the RANS equations with the Menter Shear Stress Transport (SST)  $k-\omega$  turbulence model. These solutions provided the velocity vector fields necessary to integrate droplet trajectories as well as the state of the air in the tunnel needed for icing simulation.

### Icing Simulations

Icing simulations were performed using a 3D grid based ice accretion program called LEWICE3D. The Monte Carlo droplet trajectory calculation method was used for this project to be consistent with the IFB calculations and because the thick, swept hybrid model causes considerable spanwise flow. This spanwise flow component drives highly 3D dispersion of impinging droplets because smaller droplets are carried along the span while larger droplets are not. A parallel version of LEWICE3D, called TRAJMC3D, was used on the UIUC supercomputer Taub to allow this more computationally intensive option. The IFB used the Langmuir D droplet distribution while the IRT icing simulations used a 10-bin IRT spraybar distribution measured by Papadakis et al.<sup>20</sup> in 2003. Details about LEWICE3D can be found in the user’s manual.<sup>21</sup>

## III. Results and Discussion

### Tunnel Sidewall Effects

An inviscid simulation was performed on the hybrid-wing model for the conditions of Case WB33 at  $T = -4^\circ\text{C}$ ,  $\alpha = 3.67$  deg., and  $\delta = 15$  deg. A surface  $C_P$  contour from the resulting solution is shown in Fig. 4(a) for the low pressure surface and Fig. 4(b) for the high pressure surface. The model is oriented such that flow is from left to right. The low pressure surface has a large decrease in pressure from the root (bottom) to the tip (top) near the leading edge. The spanwise variation in pressure on the high pressure surface from root (top) to tip (bottom), by contrast, is not nearly as large in the leading-edge region. On both surfaces, the change in pressure across the model in the aft section is mild.

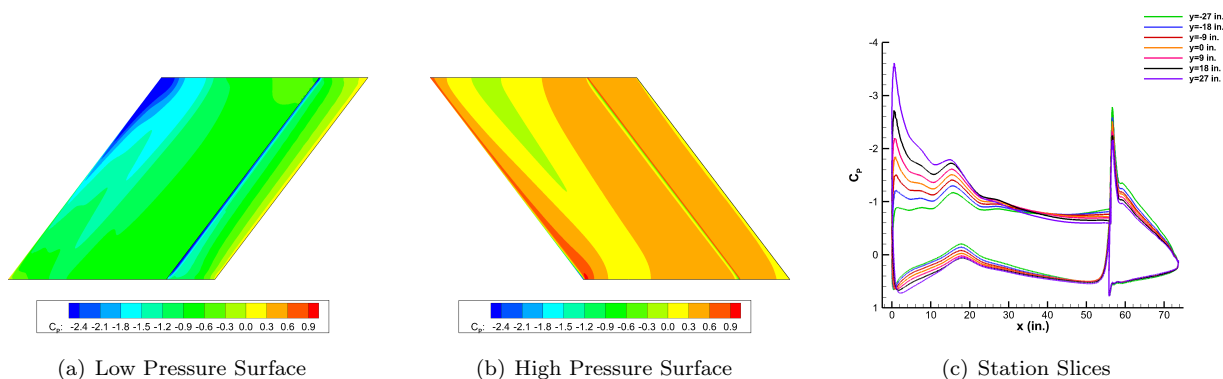


Figure 4. Inviscid  $C_P$  on the hybrid model for Case WB33 T-4 at  $\alpha = 3.67$  deg. and  $\delta = 15$  deg.

This effect is more clear in Fig. 4(c) which shows  $C_P$  distributions at stations across the model for the same case. Recall that the root of the model is found at the floor of the IRT test section at  $y = -36$  in. with the tip at  $y = +36$  in. Again, the pressure is drastically reduced on the low pressure surface near the leading edge from the root to the tip of the model. This is most apparent near the suction peak, which increases

from about -0.8 at root to about -3.6 at the tip. This change in  $C_P$  will clearly result in an increase in local  $C_l$  across the span because the area contained by the  $C_P$  distribution increases with span.

The application of lifting-line theory to a swept-wing model in a tunnel with sidewalls, illustrated in Fig. 5, explains the observed trend in spanwise loading. The model is shown in the center between two walls represented by dashed lines. The effects of the sidewalls are illustrated by placing images of the model to either side, mirrored over the wall boundaries. It should be understood that these images continue *ad infinitum* in either direction but those beyond which are shown have a diminishing effect on the actual model and are omitted for simplicity. Horseshoe vortices are placed along the model span with the bound segment on the lifting line of the model and the semi-infinite trailing segments aligned with the shed vortex sheet. Arrows on each vortex segment indicate the sign of the vorticity according to the right-handed convention. Image vortices are placed on the model reflections in a similar fashion.

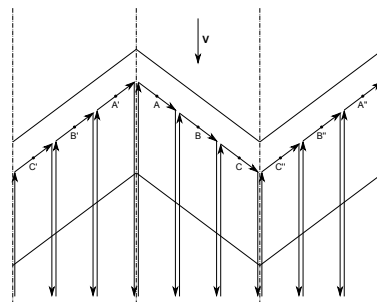
The circulation at any point on the lifting line causes an induced tangential velocity component in the plane normal to the vortex. For a swept wing, this plane is not aligned with the free stream and therefore the circulation at a given station induces an upwash upstream of the leading edge at stations farther outboard. The strength of this induced upwash diminishes with the inverse of the distance from its source point on the lifting line. Considering this effect in the presence of tunnel sidewalls (or floor and ceiling when a wing is mounted vertically, as in the IRT) can illustrate why the inviscid spanwise load increase is so pronounced for the 3D hybrid model.

A vertical (out of the page in Fig. 5) velocity at points upstream of the leading edge at station B is induced by the circulation about the lifting line at station A. This vertical velocity or upwash causes an effectively higher angle of attack resulting in a higher sectional lift at station B due to the circulation at station A. More generally, each station on a swept wing is exposed to an upwash induced by stations farther inboard and induces an upwash upstream of stations which are farther outboard. On an infinite swept wing this essentially results in a uniform upwash at all stations since each has neighbors extending to infinity in either spanwise direction. However, for a model between sidewalls, the situation is quite different. Because station A' is oriented such that it induces upwash ahead of station B', station A does not receive the effective increase in angle of attack due to upwash that would be seen on an infinite swept wing. Nonetheless, station A induces an upwash ahead of station B, increasing the effective angle of attack and thus the circulation at station B. Likewise, the circulation at station B induces an upwash ahead of station C. However, the circulation at station C' also induces an upwash at station C, further increasing the effective angle of attack and circulation at station C. This results in the trend that the sectional lift distribution increases across the span, with an amplification near the downstream wall.

To investigate this effect further, the vortex-lattice method was applied using XF5. Three cases were run at an angle of attack of  $\alpha = 5$  deg. First, a backward-swept wing with constant chord and no twist was simulated. The semispan, normalized by chord, was set to a value of 10 which is approximately the semispan of the CRM65 measured in hybrid model chord lengths. A sweep of  $\Lambda = 37.15$  deg. was used with  $V = 120$  m/s and  $\rho = 1.225$  kg/m<sup>3</sup>. Fig. 6(a) shows the resulting sectional lift coefficient distribution beside a schematic of the wing with symmetry boundary at  $y/c = 0$  and tip at  $y/c = 10$ . A second simulation was performed on the forward-swept wing of Fig. 6(b). The dimensions of the wing and conditions of the simulation are the same as for the backward-swept wing. The symmetry boundary was simply moved to the other side of the model at  $y/c = 10$ , and the former symmetry plane became a wing tip at  $y/c = 0$ .

Near the midspan of the backward-swept wing, the lift distribution is nearly constant, similar to what would be found on an infinite swept wing. Closer to the symmetry boundary, however, the loading begins to drop off due to the lack of upwash that would be contributed if the wing continued farther inboard. The slope of the lift distribution curve is especially steep in the first chord length of the span where the somewhat accumulative effect of increasing spanwise load is acting to asymptotically bring the lift to a steady level. This is similar to the  $C_l$  on a typical swept-wing transport aircraft near the fuselage. The loading near  $y/c = 10$  drops off sharply to zero as expected at a wing tip.

The sectional lift distribution of the forward-swept wing again drops off rapidly near the tip ( $y/c = 0$ ) and approaches a near constant trend at the midspan where the flow is similar to that of an infinite swept



**Figure 5. Lifting-line theory applied to a swept-wing model with sidewalls.**

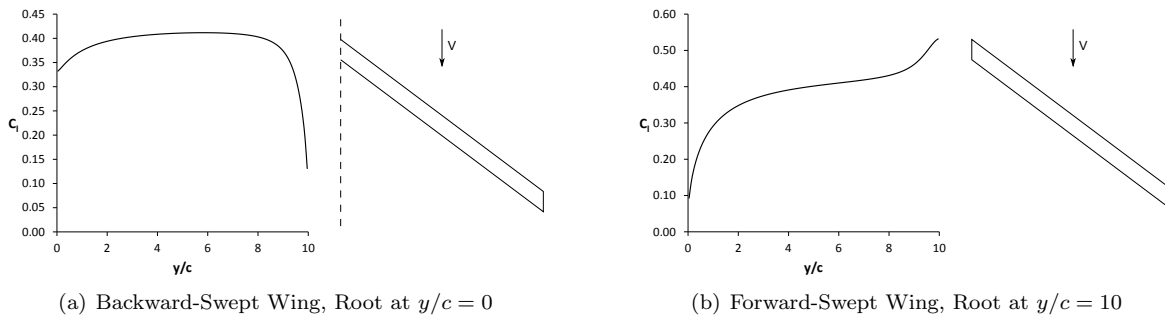


Figure 6. Lift distributions on finite wings predicted by the vortex lattice method.

wing. It is worth noting that the  $C_l$  in the midspan region is roughly 0.40, similar to the backward-swept wing simulation in the same area. The loading trend in the region near the symmetry boundary is exactly as predicted, rising sharply due to the additional upwash and, therefore, circulation near the image vorticity discussed previously. Notice that the slope of the sectional lift coefficient curve is particularly steep over the last chord length of span from  $y/c = 9$  to 10.

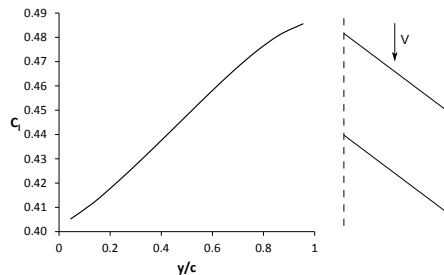


Figure 7. Lift distribution on a swept-wing model between sidewalls predicted by the vortex lattice method.

boundaries. The qualitative features of these results are directly implied by the application of lifting-line theory to the model between sidewalls and are observed in the inviscid solutions that were performed for this research. A more detailed discussion of the effects of sidewalls including the effect of adding gaps at the floor and ceiling is given by Wiberg.<sup>15</sup> Methods for controlling the spanwise load distribution are considered by the authors elsewhere.<sup>17</sup>

### Attachment Line Position Effects

The increase in  $C_l$  with span due to the presence of sidewalls on a swept model results in a significant change in attachment line position relative to the hilite across the span. The hilite is defined as the curve passing through the forwardmost point at each spanwise station on the CRM65 wing (in level flight) in the negative  $x$  direction. For a fixed geometry, an increase in  $C_l$  results in a shift of the attachment line lower on the leading edge of the model. It was shown by Fujiwara et al.<sup>16</sup> that the stagnation point has a first-order impact on ice shape for 2D hybrid models. It would be expected that on a 3D model, the attachment line would have a comparable effect on ice shape, making the attachment line location an important parameter in icing wind tunnel tests. The attachment line on the hybrid model can be adjusted globally by changing the circulation on the model using a change in flap angle or model angle of attack. Viscous simulations were performed for the conditions of Case WB33 T-4 at  $\alpha = 3.67$  deg. and  $\delta = 12, 15,$  and  $18$  deg. and then at  $\alpha = 5.25, 5.50,$  and  $5.75$  deg. and  $\delta = 5$  deg. The attachment line positions versus span are given in Fig. 8. The surface arc length or wrap distance,  $s$ , from the model hilite to the attachment line position is positive for the lower surface of the model.

Because the wrapwise attachment line location changes with span, an attempt was made to match its position to that of the CRM65 at the IRT centerline ( $y = 0$  in.). For  $\alpha = 3.67$  deg., this is accomplished

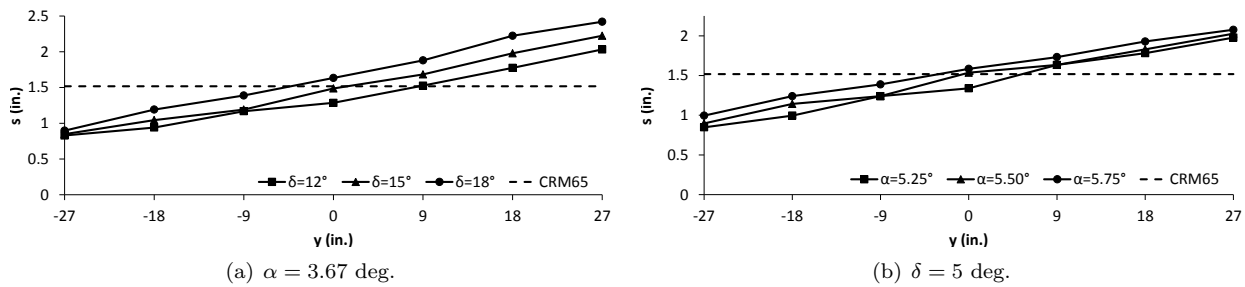


Figure 8. Attachment line position across the span of the hybrid model for Case WB33 T-4.

with the flap at  $\delta = 15$  deg. At  $\delta = 5$  deg., an angle of attack of  $\alpha = 5.50$  deg. is required. By comparing the ice shapes at the IRT centerline that result from the attachment line sweeps shown in Fig. 8, we can determine if the attachment line position has the first-order impact on ice shape we are expecting.

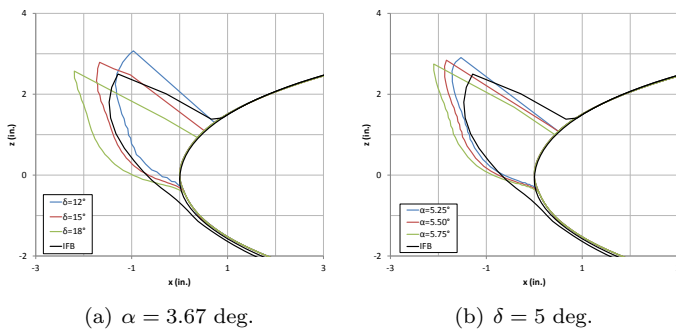


Figure 9. IRT centerline ice shapes on the hybrid model for Case WB33 T-4.

Figure 9 compares the ice shapes that result from running LEWICE3D on the flow solutions giving the attachment lines shown above. From Fig. 9(a) we see that increasing  $\delta$  and, therefore, moving the attachment line farther down the leading edge of the model causes the ice shape to change, reducing the horn angle and lowering the upper extent of the ice. Increasing  $\alpha$  has a similar effect, again reducing the horn angle. Notice that the red ice shapes in both figures best match the horn angle of the IFB, though the horn length is longer in the IRT simulations. These results support the conclusion that the attachment line location on the leading edge of a hybrid wing model has a first-order impact on ice shape, analogous to the first-order impact of stagnation point location on the ice shape on a hybrid airfoil shown by Fujiwara et al.<sup>16</sup> Furthermore, the attachment line can be globally shifted by a change in either angle of attack or flap angle resulting in a range of  $\alpha$ - $\delta$  pairs corresponding to a given attachment line location at the tunnel centerline. Ideally, the model would either have a constant attachment line with span matched to that of the reference wing at the station of interest or the attachment line on the model would have the same position across its span as the reference wing over the same span, either of which require *local* spanwise control of the  $C_l$  distribution. Spanwise load control techniques that can potentially address this need are considered in detail by Wiberg<sup>15</sup> and by the authors<sup>17</sup> in a paper discussing hybrid-wing design.

### Altitude Effects

When the flow simulations are performed for the hybrid model in the IRT to simulate the ice shapes that would be expected during a tunnel experiment, several changes to the flight baseline conditions are made. Rather than using a Langmuir D droplet distribution like was done for the IFB, a circa 2003 IRT 10-bin measured distribution is used which better simulates the icing cloud that is generated by the IRT spraybars.<sup>20</sup> The local air density and pressure at the IRT elevation are also different from that of the flight baseline at altitude and are adjusted accordingly. Due to these adjustments, it is unclear whether differences in the ice shapes that result from the IRT simulations versus the IFB should be attributed to differences in the actual flow or to the effect of droplet distribution and air properties. In order to consider the effects of altitude, simulations can be performed using the IRT flow solutions but with the exact conditions of the flight baseline (not adjusted to local IRT elevation).

In Fig. 10(a), ice shapes at the IRT centerline resulting from the IRT flow solution at both local and flight altitude for  $\alpha = 3.67$  deg. and  $\delta = 15$  deg. are compared to the IFB for Case WB33 T-4. The ice shapes generated using the IRT simulations compare well to each other, though the shape at the local IRT

pressure has less mass. The horn lengths of the IRT ice shapes are greater than the IFB, a trend that will be discussed again.

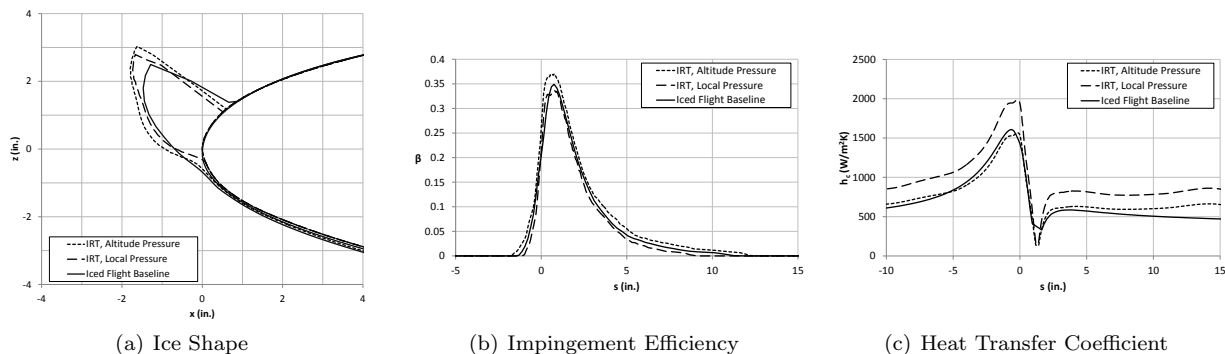


Figure 10. Centerline IRT ice shapes,  $\beta$ , and  $h_c$  for Case WB33 T-4 at local and altitude conditions.

The impingement efficiency,  $\beta$ , and convective heat transfer coefficient,  $h_c$ , distributions corresponding to these ice shapes are shown in Fig. 10(b) and Fig. 10(c), respectively. At altitude conditions, the peak impingement efficiency,  $\beta_{\max}$ , on the IRT model is somewhat higher than that of the IFB while the heat transfer coefficient,  $h_c$ , is well matched. This results in a larger horn due to the extra impinging water mass in the horn area of the upper surface of the model. The  $\beta_{\max}$  value is likely larger due to the lower maximum thickness of the hybrid model as compared to the baseline airfoil, an effect proposed by Malone<sup>22</sup> that is discussed later and isolated by running LEWICE3D at altitude conditions. For the IRT model at local elevation, the effects are reversed with a well matched  $\beta$  distribution but considerably higher  $h_c$ . This also leads to a larger horn on the IRT model than the IFB since more of the water that impinges on (or runs past) the horn is able to freeze due to the higher heat transfer. The increase in magnitude of the heat transfer is caused by the higher density of the air at the elevation of the IRT and is the most apparent effect of altitude.

### Icing Scaling

A flow simulation including viscous effects was run for the conditions of Case WB47 T-6 at the associated baseline angle of attack of  $\alpha = 4.36$  deg. and a flap angle of  $\delta = 16$  deg. in order to match the attachment line location of the CFB at the IRT centerline. It was assumed that the IRT test section velocity is limited to 250 knots (128.6 m/s), leaving the baseline air speed unmatched. This results in a tunnel air speed of  $V = 128.61$  m/s as compared to  $V = 139.60$  m/s from the flight baseline.

Scaled icing conditions that take into account the difference in IRT pressure discussed in the previous section and the reduced test section velocity mentioned above were determined based on the method used by Tsao and Lee<sup>23</sup> using correlation to swept NACA 0012 data. The method attempts to maintain similarity in droplet trajectories, water catch, and droplet freezing by matching the modified inertia parameter,  $K_0$ , accumulation parameter,  $A_c$ , and stagnation plane freezing fraction,  $n_0$ , respectively. Water film dynamics similarity enforced by matching the Weber number,  $We_d$ , was not possible due to a full-scale leading edge with reduced test section velocity. LEWICE3D was then used to generate ice accretions using both the unscaled and scaled IRT conditions. The corresponding ice shapes are compared to the IFB ice shape for Case WB47 T-6 in Fig. 11.

Surprisingly, the IRT ice shape with the unscaled conditions matches the IFB ice shape better than with scaled conditions. To understand why this may be, consider the  $\beta$  and  $h_c$  distributions shown in Fig. 12. Comparing the impingement efficiency distributions in Fig. 12(a) reveals that the droplet trajectory similitude, attempted by matching  $K_0$ , was largely successful. The  $\beta$  distribution from the scaled conditions matches well except for a slightly higher  $\beta$  from about  $s = 0$  to 1 in. whereas the unscaled impingement efficiency is low throughout most of the leading-edge region. Careful examination of Fig. 12(b) reveals that

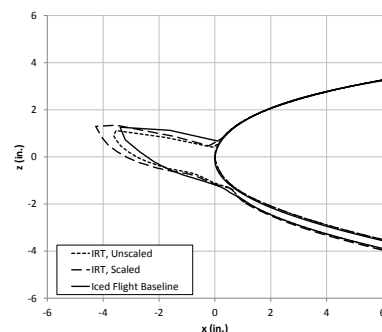
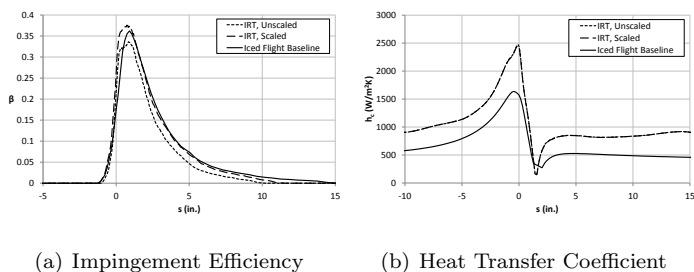


Figure 11. Centerline ice shapes resulting from scaled and unscaled IRT conditions for Case WB47 T-6.

the scaled and unscaled case  $h_c$  distributions are exactly the same, the respective curves being coincident. Though equal, the  $h_c$  for the scaled and unscaled cases are significantly higher than that of the IFB. With a combined low  $\beta$  and high  $h_c$  distribution, the ice thickness of the unscaled shape approximately matches that of the IFB. The  $\beta$  of the scaled case matches that of the IFB well except for the overshoot from about  $s = 0$  to 1 in. Nevertheless, the high  $h_c$  of the scaled case compared to that of the IFB results in ice that is thicker than the IFB, though the horn angle is perhaps matched better. This brings into question whether an effort should be made to directly match  $h_c$  - as Bidwell<sup>24</sup> has done for simulations of a swept NACA 0012 wing in the IRT - rather than the more general matching of  $n_0$ .

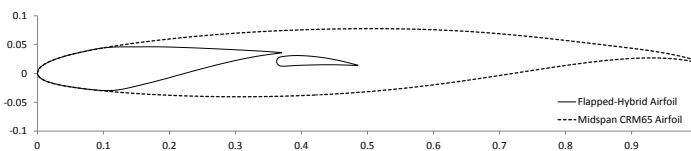


**Figure 12. Centerline IRT  $\beta$  and  $h_c$  for Case WB47 T-6 at scaled and unscaled icing conditions.**

scale, swept-wing model this is actually a favorable constraint because, given the higher density of air at the elevation of the IRT, the test section velocity would need to be lowered in order to match  $h_c$ . Due to blockage effects, it is often the case that the true air speed of the reference case cannot be matched in the tunnel, requiring the tests to be performed at lower velocities anyway. Lowering the IRT test section velocity simultaneously reduces blockage and loading while allowing  $h_c$  to be matched directly, perhaps improving ice shape agreement. However, this precludes surface water dynamics similitude because, with reduced velocity and a full-scale leading edge, the Weber number of the scaled conditions will not match that of the reference case.<sup>23</sup> This highlights the classic challenge of icing similitude; the scaling of icing conditions is limited to a small set of parameters over which the operator has control, namely  $MVD$ ,  $LWC$ ,  $\tau$ ,  $T$ , and perhaps  $V$ . Furthermore, there are often additional constraints on these parameters due to tunnel capabilities such as a limit on test section velocity due to blockage. This short list of variables over which the icing test designer has control limits the allowable number of dimensionless parameters that can practically be adjusted in the tunnel in order to scale the conditions for similitude with the reference case.

Despite the droplet trajectory similarity enforced by matching  $K_0$ , the  $\beta$  distribution for the scaled conditions is somewhat mismatched in the region from about  $s = 0$  to 1 in. A similar trend was found in the ice shapes for Case WB33 T-4 shown in Figure 10(b) and WB47 T-6 (not shown), though in these cases no scaling was attempted. However, the higher impingement efficiency near  $\beta_{max}$  is likely due to the reduced thickness of the hybrid model as compared to the full-scale reference wing.

For a hybrid model, geometry similitude is achieved by retaining the full-scale leading edge. However, for obvious reasons, the full-scale geometry can only be maintained over a small portion of the airfoil, up to the leading-edge extents. The leading-edge extents are generally selected based on the expected impingement limits. Beyond these points the leading-edge is blended with the re-designed aft section of the model. This results in the thickness of the reference airfoil not being maintained beyond the leading-edge extents. This is clear in Fig. 13 which shows the flapped-hybrid airfoil and the full-scale, reference airfoil from which it was designed.



**Figure 13. Comparison of the flapped-hybrid airfoil to the full-scale CRM65 airfoil from which it was designed, in the plane normal to the leading edge.**

The maximum thickness of an airfoil has an important effect on icing, a topic discussed by Malone.<sup>22</sup> At

subsonic velocities, flow upstream of an airfoil or wing is affected by its presence. Streamlines and droplet trajectories upstream of a thick geometry are influenced more than for a thinner body. Icing cloud droplets are consequently spread more thinly on the leading edge of the airfoil. For this reason, hybrid models often result in higher  $\beta_{\max}$  than the reference geometry for the same conditions because the hybrid is substantially thinner than the reference geometry it represents. Such a trend was seen in the icing simulation results for Cases WB33 T-4, WB47 T-6, and WB71 T-6 (see Figures 10(b) and 12(a)).

### Spanwise Variation

It was shown for a swept-wing model that moving from root to tip, the circulation on the model increases, decreasing the  $C_P$  at the suction peak and increasing the local  $C_l$  which causes the attachment line to shift farther down the leading edge. It was also shown that the attachment line position has a first-order impact on ice shape. One important question that results is how this change in attachment line position with span will affect the impingement and ice shape characteristics along the span.

To explore this question further, ice shapes were generated at stations across the entire span for the Case WB33 simulation with  $T = -4^\circ\text{C}$ ,  $\alpha = 3.67$  deg., and  $\delta = 15$  deg. that was discussed previously. Recall that the attachment line location at the IRT centerline agreed well with that of the CFB (see Fig. 8(a)). Figure 14 shows the resulting spanwise variation in impingement and ice shape characteristics. As stated previously,  $y = -36$  in. corresponds to the root of the model at the IRT floor and  $y = +36$  in. to the tip at the ceiling.

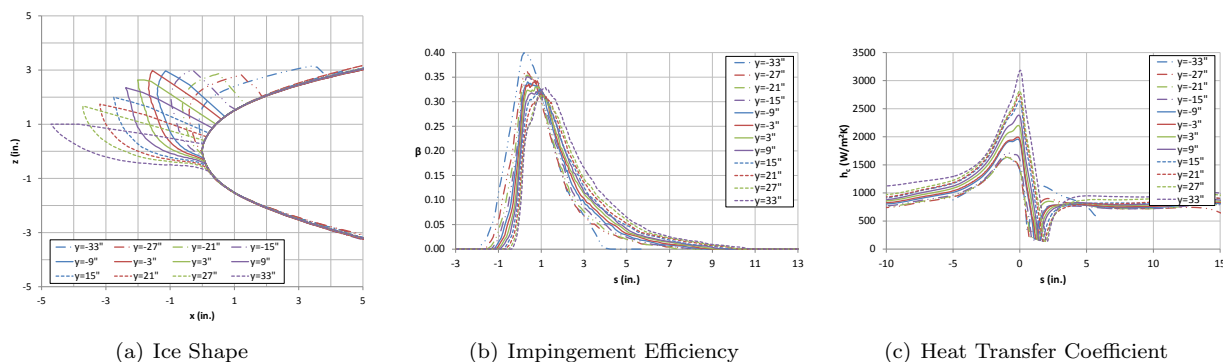


Figure 14. Spanwise variation of impingement and ice shape characteristics for Case WB33 T-4 at  $\alpha = 3.67$  deg. and  $\delta = 15$  deg.

The change in ice shape across the span, shown in Fig. 14(a), is very pronounced. Just as the attachment line moves farther down the leading edge due to the increase in loading across the span, the horn angle of the ice shapes decreases across the span. The ice shapes also transition from short and wide at the floor of the IRT to long and thin at the ceiling. The  $\beta$  distributions across the span of the model in Fig. 14(b) shift to the right (farther down the leading edge) with span (toward tunnel ceiling), tracking the change in attachment line location. The  $\beta_{\max}$  is greatest at the floor and decreases with span.

The  $h_c$  distributions across the span of the model are compared in Fig. 14(c). Again, the shift in the curves caused by the change in attachment line location with span is evident. The heat transfer tends to increase on the upper surface of the model with span, following the trend in suction peak that was observed. The  $h_c$  is considerably lower near the floor, allowing the water film layer to flow further onto the upper surface of the leading edge before freezing. This results in thinner ice shapes with larger bases near the floor. As  $h_c$  increases with span near the hiltite, longer and more distinct horns begin to form until, near the ceiling, very long and thin ice shapes point upstream.

It is clear that the change in ice shape across the model span is significant. Depending on the performance requirements of the hybrid model, it may be desired that the change in impingement and ice shape across the span be mitigated. As mentioned, there are methods for controlling the spanwise  $C_l$  distribution on the model. However, these methods are part of the model design and are thus discussed in another work by the authors<sup>17</sup> which considers hybrid-wing designs and trade-offs in more detail. Nonetheless, there remains a method for reducing spanwise variation in load and attachment line location across the model span which is of value from an operations standpoint and can be used on the most basic swept-hybrid model geometry

without any changes. Recall that the spanwise change in  $C_l$  is driven by the circulation about the lifting line of a swept model and that it is amplified by the presence of sidewalls. It follows that if the circulation on the model can be reduced, the variation in spanwise loading will also be attenuated. Fujiwara et al.<sup>16</sup> showed that for a hybrid airfoil, when the circulation on the model is generated farther forward on the airfoil less total circulation is required to reach the same stagnation point. This results from the fact that the strength of the tangential velocity generated by the circulation goes as the inverse of the distance from the source point. If circulation is generated nearer the leading edge then its influence in the leading edge region is greater. That this same logic applies to the attachment line of swept-wing models will be made clear.

To reduce the total  $C_L$  (and circulation) on the wing model so that the spanwise variation in attachment line would be reduced, simulations were performed over a range of  $\alpha$ - $\delta$  pairs. Starting from  $\alpha = 3.67$  deg. and  $\delta = 15$  deg., the flap angle was reduced to  $\delta = 5$  deg. and the angle of attack changed to match attachment line position at IRT centerline, resulting in  $\alpha = 5.50$  deg. This was repeated for  $\delta = -5$  deg., resulting in  $\alpha = 7.50$  deg. Finally, the flap was removed to explore the option of a single element hybrid model, requiring  $\alpha = 10.0$  deg. to match attachment line at  $y = 0$  in. Note that with a shorter overall model chord length, the scale factor becomes  $SF = 2.67$  for the hybrid with no flap (recall  $SF = 2$  with flap). As the  $\alpha$  is increased and the  $\delta$  decreased, the circulation on the model is shifted farther toward the leading edge, requiring less lift to achieve the same attachment line location at IRT centerline. Comparing the attachment line positions for the four simulations in Fig. 15 confirms the effectiveness of this technique in reducing the spanwise variation. The attachment line slope steadily decreases with increase in angle of attack to the point that, for  $\alpha = 10.0$  deg., the attachment line is nearly constant over portions of the span.

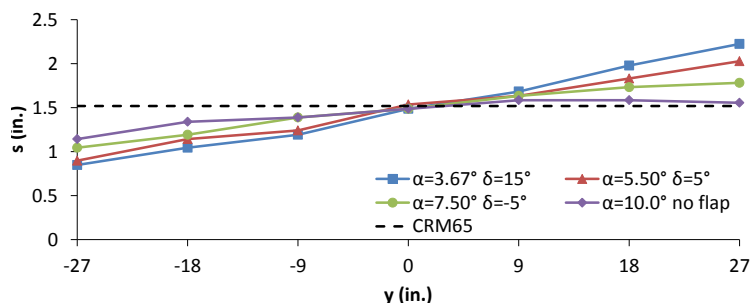


Figure 15. Attachment line position across the span of the hybrid model for Case WB33 T-4 at several angles of attack and flap deflections.

Table 2. Lift coefficient on the hybrid model for Case WB33 T-4 and several  $\alpha$ - $\delta$  pairs.

$\alpha$ (deg.)	$\delta$ (deg.)	$C_L$	diff.
3.67	15	0.666	-
5.50	5	0.549	0.117
7.50	-5	0.429	0.120
10.0	NA	0.273	0.156

$\alpha = 10.0$  deg. are shown in Fig. 16. The ice shape varies substantially less with span, especially along the outboard half of the model. This tracks the trend in attachment line observed in Fig. 15 where the attachment line position nearly matched that of the CFB from  $y = 0$  to 36 in. The  $\beta$  distribution across the span is also much more consistent, varying very little except for just near the floor of the IRT compared to Fig. 14(b) which shows that for  $\alpha = 3.67$  deg. both the extents and peak,  $\beta_{max}$ , change considerably with span. A similar trend is observed for  $h_c$ , which varies much less with span for  $\alpha = 10.0$  deg. compared to  $\alpha = 3.67$  deg. in Fig. 14(c).

A model might need to be operated at an angle of attack other than that of the reference wing for several reasons. For instance, if a flap stalls at an angle lower than predicted by CFD simulations, wind tunnel operators may be forced to increase  $\alpha$  to reach the appropriate attachment line location. Models could also be designed without a flap, relying on the use of  $\alpha$  alone to set attachment line position. This reduces model complexity and fabrication costs while allowing either a less aggressive hybrid design for the same

That a reduction in circulation and thus  $C_L$  in fact caused the favorable change in attachment line slope is clear when the lift coefficient values for each of the four simulations are compared. Table 2 gives the  $C_L$  value for each of the  $\alpha$ - $\delta$  pairs as well as the incremental difference in  $C_L$  that was realized with each reduction in flap angle. As might be expected, removing the flap entirely results in the largest reduction in  $C_L$ .

With the largest reduction in  $C_L$  and the least change in attachment line position with span, the simulation with no flap and  $\alpha = 10.0$  deg. results in spanwise impingement and ice shape characteristics most different from those shown for  $\alpha = 3.67$  deg. and  $\delta = 15$  deg. The ice shapes,  $\beta$  distributions, and  $h_c$  distributions across the span of the hybrid model for



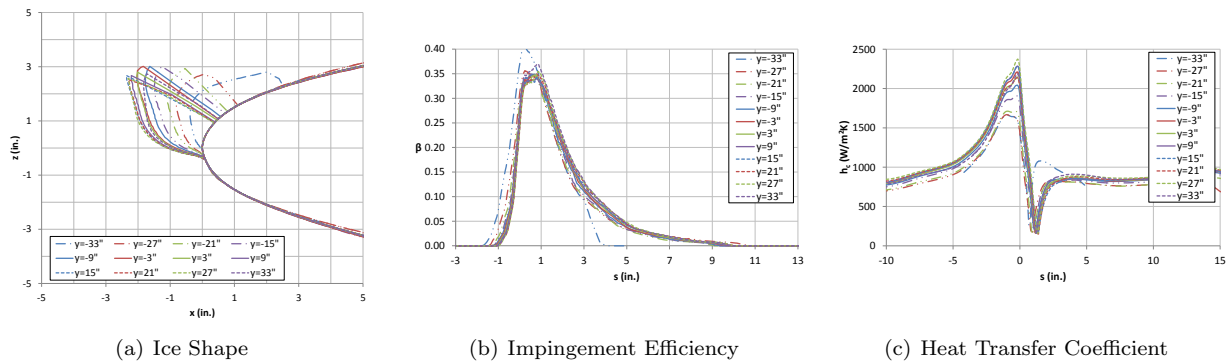


Figure 16. Spanwise variation of impingement and ice shape characteristics for Case WB33 T-4 at  $\alpha = 10.0$  deg. and no flap. Compare to Fig. 14.

$SF$  or a larger  $SF$  for the same model chord length. Regardless of the reason, the advantages of matching attachment line position at a lower  $C_L$  while reducing the spanwise variation of  $C_l$  and attachment line are clear. However, the ultimate goal of a hybrid model is to simulate ice accretions which are representative of those which would be found on the reference wing in flight. Therefore, before running a model at an off-case angle of attack can be done as a general practice, it must be shown that matching the attachment line position at tunnel centerline is sufficient to produce similar ice shapes.

Matching  $\alpha$  to the reference case is generally considered important because it ensures that the droplets from the IRT cloud approach the full-scale leading edge of the model at the same angle of incidence at which droplets approach the baseline wing in flight. It seems clear that matching the global angle of incidence at which the droplets impinge on the model in this way is important, but if the local flow in the region of the leading edge dominates the influence of the flow on droplet trajectories, then it is possible that similar ice shapes will result, regardless of the model angle of attack. To determine whether ice shapes representative of the flight baseline could be generated on the hybrid model at off-case angles of attack, centerline ice shapes were formed on the model using LEWICE3D and the four cases discussed above. The centerline  $C_P$  distributions of the four cases and the ice shapes are compared to the flight baseline in Fig. 17.

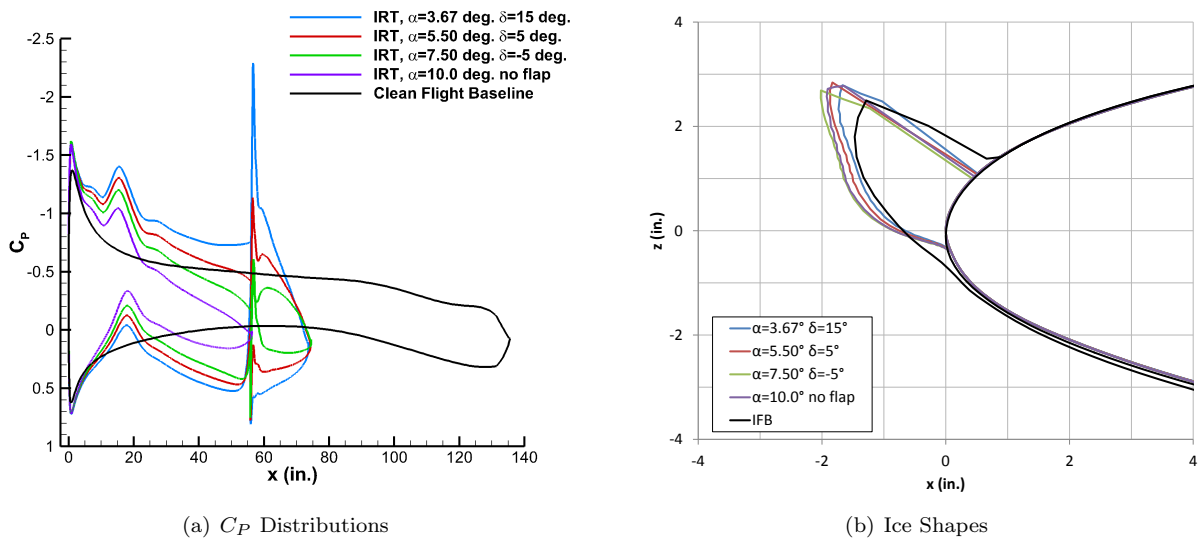


Figure 17. Centerline  $C_P$  distributions and ice shapes for Case WB33 T-4 and several  $\alpha$ - $\delta$  pairs.

The  $C_P$  distributions for all four IRT simulations agree well with one another and match the leading-edge region of the CFB well with a slightly high suction peak, as shown in Fig. 17(a). Farther back on the model, the  $C_P$  distributions begin to diverge, resulting in reduced  $C_l$  values at higher  $\alpha$ . The associated ice shapes of Fig. 17(b) match one another very well and compare reasonably well with the IFB shape, suggesting once

again that attachment line location is sufficient for ice shape similarity.

It was expected that given a high enough  $\alpha$  the ice shapes would begin to differ, however this was not observed. Even at  $\alpha = 10.0$  deg., which is substantially higher than the model was designed for, the ice shapes agree very well. The fact that the ice shapes for the four IRT simulations match each other so well but differ somewhat from that of the IFB suggests that the error, if any, of operating at an off-case angle of attack is small compared to the error associated with trying to replicate flight conditions in a wind tunnel.

#### IV. Conclusions

- The attachment line location on the leading edge of a swept-wing, flapped-hybrid model has a first-order impact on ice shape, analogous to the first-order impact of stagnation point location on the ice shape on a hybrid airfoil shown by Fujiwara et al.<sup>16</sup> The suction peak has a second-order effect, impacting the heat transfer coefficient. Because the attachment line has a first-order impact on ice shape, when the attachment line position is matched for a given case, a good ice shape match can be expected. This makes it the most important metric in early model design. When the attachment line location is matched, the suction peak will generally also be comparable, depending on the geometry.
- The loading on a swept model between sidewalls increases considerably with span due to the increase in effective angle of attack that results from the induced upwash caused by stations farther inboard and amplified by the wall symmetry conditions. This spanwise increase in loading causes the attachment line to move farther down the leading edge at stations farther outboard.
- Changing the angle of attack or flap angle are equivalent methods of adjusting attachment line location uniformly over the span.
- Within the limits of the  $\alpha$  and  $MVD$  ranges of this research, reaching the same attachment line location using different  $\alpha$ - $\delta$  pairs will result in very similar ice shapes, implying that icing tunnel tests do not necessarily have to be conducted at the angle of attack of the reference case. A flap can be removed and angle of attack used to adjust attachment line location, reducing the required  $SF$  of the main element of the hybrid for a given chord length.
- Increasing  $\alpha$  while decreasing  $\delta$  allows the same attachment line location to be achieved at a lower  $C_L$  because the circulation on the model is generated closer to the leading edge, influencing the flow in the region of interest more. In addition to reducing loads on tunnel turntables and balances, the spanwise variation in attachment line position is reduced at lower  $C_L$  values, reducing the spanwise variation in ice shape.
- The most significant effect of altitude on ice shape is that the higher density at the low elevations of icing wind tunnels results in higher heat transfer coefficients compared to icing conditions at departure, cruise, or approach altitudes. If the impingement efficiency is well matched, this can result in thicker ice in glaze ice tunnel tests.
- Droplet trajectory similitude resulted in improved impingement efficiency distribution matching while the overall ice shape did not improve using the scaling method described. The results suggest that directly matching  $h_c$  may improve ice shape agreement for the conditions of this research.
- Though hybrid models with full-scale leading edges are generally considered to maintain geometric similitude, they do not maintain the same thickness as the reference geometry. The lower maximum thickness of hybrid models results in an increase in  $\beta_{max}$  because streamlines and droplet trajectories upstream of the model are influenced less, reducing the spread of the droplets that impinge on the leading edge.
- The flapped-hybrid model designed to be representative of the midspan of the CRM65 is effective in generating ice shapes representative of the IFB when the attachment line location at IRT centerline is matched to that of the CFB. Simulations indicate horn ice shapes in the IRT tend to be longer than those generated on the CRM65 in free air, attributed to a higher  $\beta_{max}$  due to reduced maximum thickness, a higher  $h_c$  due to altitude effects, or both.

## V. Acknowledgements

The funding for this research was provided by NASA grant NNX12AB04A. The authors kindly thank Andy Broeren, Colin Bidwell, Mark Potapczuk, and others of the NASA Glenn Icing Research Branch as well as Ben Paul, Adam Malone, John Vassberg, Abdi Khodadoust and others from Boeing Commercial Aircraft for their technical contributions. Thanks also to Eric Loth of the University of Virginia and Chris Triphahn of the University of Illinois for their assistance with CFD simulations. Finally, the authors thank Wayne hoyenga, Jeff Diebold, Phil Ansell, Marianne Monastero, and Stephanie Camello of the University of Illinois for their contributions to this work. The first author conducted this research under sponsorship from Sandia National Laboratories as part of the Critical Skills Master's Program. Sandia National Laboratories is a multi-program laboratory managed and operated by Sandia Corporation, a wholly owned subsidiary of Lockheed Martin Corporation, for the U.S. Department of Energy's National Nuclear Security Administration under contract DE-AC04-94AL85000. Thanks to Todd Sterk, Maxine Bradley, and Camille Valdez of Sandia Labs for making this opportunity possible.

## References

- <sup>1</sup>Broeren, A. P., Potapczuk, M., Riley, J., Villedieu, P., Moens, F., and Bragg, M., "Swept-Wing Ice Accretion Characterization and Aerodynamics," *Fluid Dynamics and Co-located Conferences*, American Institute of Aeronautics and Astronautics, June 2013, pp. –.
- <sup>2</sup>Vassberg, J., Dehaan, M., Rivers, M., and Wahls, R., "Development of a Common Research Model for Applied CFD Validation Studies," *Guidance, Navigation, and Control and Co-located Conferences*, American Institute of Aeronautics and Astronautics, Aug. 2008, pp. –.
- <sup>3</sup>Eliasson, P. and Peng, S.-H., "Influence of Turbulence Modelling and Grid Resolution In Computations of the DPW4 CRM Configuration," *Aerospace Sciences Meetings*, American Institute of Aeronautics and Astronautics, Jan. 2010, pp. –.
- <sup>4</sup>Mani, M., Rider, B., Sclafani, A., Winkler, C., Vassberg, J., Dorgan, A., Cary, A., and Tinoco, E., "RANS Technology for Transonic Drag Prediction; A Boeing Perspective of the 4th Drag Prediction Workshop," *Fluid Dynamics and Co-located Conferences*, American Institute of Aeronautics and Astronautics, June 2010, pp. –.
- <sup>5</sup>Vassberg, J., "Introduction: Drag Prediction Workshop," *Journal of Aircraft*, Vol. 45, No. 3, May 2008, pp. 737–737.
- <sup>6</sup>Hashimoto, A., Murakami, K., Aoyama, T., Yamamoto, K., Murayama, M., and Lahur, P., "Drag Prediction on NASA CRM Using Automatic Hexahedra Grid Generation," *Aerospace Sciences Meetings*, American Institute of Aeronautics and Astronautics, Jan. 2010, pp. –.
- <sup>7</sup>Sclafani, A., Vassberg, J., Mani, M., Winkler, C., Dorgan, A., Olsen, M., and Coder, J., "DPW-5 Analysis of the CRM in a Wing-Body Configuration Using Structured and Unstructured Meshes," *Aerospace Sciences Meetings*, American Institute of Aeronautics and Astronautics, Jan. 2013, pp. –.
- <sup>8</sup>Rivers, M. and Dittberner, A., "Experimental Investigations of the NASA Common Research Model (Invited)," *Fluid Dynamics and Co-located Conferences*, American Institute of Aeronautics and Astronautics, June 2010, pp. –.
- <sup>9</sup>Rivers, M., Hunter, C., and Campbell, R., "Further Investigation of the Support System Effects and Wing Twist on the NASA Common Research Model," *Fluid Dynamics and Co-located Conferences*, American Institute of Aeronautics and Astronautics, June 2012, pp. –.
- <sup>10</sup>Paul, B., Malone, A., and Vassberg, J., "Personal communications to the author," 2013.
- <sup>11</sup>Robinson, B., Verhoff, A., and LaBozzetta, W., "Preliminary findings in certification of OVERFLOW," *Fluid Dynamics and Co-located Conferences*, American Institute of Aeronautics and Astronautics, June 1994, pp. –.
- <sup>12</sup>Jespersen, D., Pulliam, T., Buning, P., Jespersen, D., Pulliam, T., and Buning, P., "Recent enhancements to OVERFLOW," *Aerospace Sciences Meetings*, American Institute of Aeronautics and Astronautics, Jan. 1997, pp. –.
- <sup>13</sup>Buning, P. G., P., Chiu, I. T., Obayashi, S., Rizk, Y., and Steger, J., "Numerical simulation of the integrated space shuttle vehicle in ascent," *Guidance, Navigation, and Control and Co-located Conferences*, American Institute of Aeronautics and Astronautics, Aug. 1988, pp. –.
- <sup>14</sup>RENZE, K., BUNING, P., and RAJAGOPALAN, R., "A comparative study of turbulence models for overset grids," *Aerospace Sciences Meetings*, American Institute of Aeronautics and Astronautics, Jan. 1992, pp. –.
- <sup>15</sup>Wiberg, B. D., *Large-Scale Swept-Wing Ice Accretion Modeling in the NASA Glenn Icing Research Tunnel Using LEWICE3D*, Master's thesis, University of Illinois at Urbana-Champaign, 2013.
- <sup>16</sup>Fujiwara, G. E., Woodard, B., Wiberg, B., Mortonson, A. J., and Bragg, M., "A Hybrid Airfoil Design Method for Icing Wind Tunnel Tests," *Fluid Dynamics and Co-located Conferences*, American Institute of Aeronautics and Astronautics, June 2013, pp. –.
- <sup>17</sup>Fujiwara, G., Wiberg, B., Woodard, B., and Bragg, M., "3D Swept Hybrid Design Method for Icing Wind Tunnel Tests," *Atmospheric and Space Environments Conference*, American Institute of Aeronautics and Astronautics, 2014.
- <sup>18</sup>Anderson, D. A. and Steinbrenner, J. P., "Grid-Generation Methodology in Applied Aerodynamics," *Progress in Astronautics and Aeronautics*, American Institute of Aeronautics and Astronautics, 1990.
- <sup>19</sup>Steinbrenner, J. and Abelanet, J., "Anisotropic Tetrahedral Meshing Based on Surface Deformation Techniques," *Aerospace Sciences Meetings*, American Institute of Aeronautics and Astronautics, Jan. 2007, pp. –.
- <sup>20</sup>Papadakis, M., Rachman, A., Wong, S.-C., Yeong, H.-W., Hung, K., and Bidwell, C., "Water Impingement Experiments on a NACA 23012 Airfoil with Simulated Glaze Ice Shapes," *Aerospace Sciences Meetings*, American Institute of Aeronautics and Astronautics, Jan. 2004, pp. –.

<sup>21</sup>Bidwell, C. S. and Potapczuk, M. G., “Users Manual for the NASA Lewis Three-Dimensional Ice Accretion Code (LEWICE3D),” *TM 105974*, NASA, 1993.

<sup>22</sup>Malone, A., “Personal communication to the author,” 2013.

<sup>23</sup>Tsao, J.-C. and Lee, S., “Evaluation of Icing Scaling on Swept NACA 0012 Airfoil Models,” *NASA/CR*, National Aeronautics and Space Administration, 2012.

<sup>24</sup>Bidwell, C., “Personal communication to the author,” 2013.

## Appendix E.—Full-Scale and Hybrid Model Airfoil Section Coordinates for Inboard, Midspan, and Outboard Stations

Table E.1 presents chord lengths for the CRM65 full-scale Inboard, Midspan, and Outboard wing stations.

Table E.2 lists coordinates for the normal two-dimensional (2D) full-scale airfoils for each of the three stations (Ref. 11). Coordinates are given in the normal direction, nondimensionalized by the full-scale CRM65 chord.

The coordinates presented in Table E.3 are for the normal 2D flapped hybrid airfoils design used as the basis for the Inboard, Midspan, and Outboard three-dimensional (3D) models. Coordinates are given in the normal direction, nondimensionalized by the full-scale CRM65 chord.

The respective flap pivot points for the Inboard, Midspan, and Outboard models are presented in Table E.4.

TABLE E.1.—CRM65 FULL-SCALE WING STATION CHORD LENGTH

CRM65 full-scale wing station	Normal chord, in. (Angle of attack $\alpha = 0^\circ$ )
Inboard	297.88
Midspan	122.72
Outboard	91.27

TABLE E.2.—COORDINATES FOR 2D FULL-SCALE AIRFOILS FOR INBOARD, MIDSPAN, AND OUTBOARD STATIONS

Inboard full scale		Midspan full scale		Outboard full scale	
<i>x</i>	<i>y</i>	<i>x</i>	<i>y</i>	<i>x</i>	<i>y</i>
1.0000	-0.1620	1.0000	0.0211	0.9991	0.0422
0.9685	-0.1451	0.9899	0.0252	0.9858	0.0476
0.9370	-0.1314	0.9797	0.0284	0.9717	0.0518
0.9056	-0.1185	0.9696	0.0311	0.9575	0.0552
0.8741	-0.1066	0.9595	0.0335	0.9434	0.0581
0.8426	-0.0955	0.9494	0.0356	0.9292	0.0605
0.8111	-0.0849	0.9392	0.0376	0.9151	0.0626
0.7796	-0.0750	0.9291	0.0393	0.9009	0.0645
0.7481	-0.0659	0.9190	0.0410	0.8868	0.0663
0.7167	-0.0573	0.9089	0.0425	0.8726	0.0680
0.6852	-0.0494	0.8987	0.0440	0.8585	0.0696
0.6537	-0.0420	0.8886	0.0454	0.8443	0.0712
0.6222	-0.0349	0.8785	0.0468	0.8302	0.0727
0.5907	-0.0282	0.8684	0.0482	0.8160	0.0742
0.5593	-0.0218	0.8582	0.0496	0.8019	0.0757
0.5278	-0.0157	0.8481	0.0509	0.7877	0.0771
0.4963	-0.0102	0.8380	0.0523	0.7736	0.0784
0.4648	-0.0045	0.8278	0.0536	0.7594	0.0797
0.4333	0.0005	0.8177	0.0550	0.7453	0.0809
0.4019	0.0054	0.8076	0.0563	0.7311	0.0820
0.3704	0.0108	0.7975	0.0577	0.7170	0.0830
0.3389	0.0160	0.7873	0.0590	0.7028	0.0840
0.3074	0.0208	0.7772	0.0603	0.6887	0.0848
0.2759	0.0251	0.7671	0.0616	0.6745	0.0855

TABLE E.2.—COORDINATES FOR 2D FULL-SCALE AIRFOILS  
FOR INBOARD, MIDSPAN, AND OUTBOARD STATIONS

Inboard full scale		Midspan full scale		Outboard full scale	
x	y	x	y	x	y
0.2444	0.0287	0.7570	0.0628	0.6604	0.0861
0.2130	0.0314	0.7468	0.0640	0.6462	0.0866
0.1815	0.0333	0.7367	0.0651	0.6321	0.0869
0.1500	0.0341	0.7266	0.0663	0.6179	0.0872
0.1509	0.0341	0.7165	0.0673	0.6038	0.0874
0.1487	0.0341	0.7063	0.0684	0.5896	0.0875
0.1466	0.0341	0.6962	0.0693	0.5755	0.0876
0.1444	0.0342	0.6861	0.0702	0.5613	0.0875
0.1423	0.0342	0.6759	0.0711	0.5472	0.0874
0.1401	0.0342	0.6658	0.0719	0.5330	0.0872
0.1380	0.0341	0.6557	0.0727	0.5189	0.0869
0.1358	0.0341	0.6456	0.0734	0.5047	0.0865
0.1337	0.0341	0.6354	0.0740	0.4906	0.0861
0.1315	0.0341	0.6253	0.0746	0.4764	0.0856
0.1294	0.0341	0.6152	0.0752	0.4623	0.0851
0.1273	0.0340	0.6051	0.0757	0.4481	0.0845
0.1251	0.0340	0.5949	0.0761	0.4340	0.0838
0.1230	0.0339	0.5848	0.0765	0.4198	0.0831
0.1208	0.0339	0.5747	0.0768	0.4057	0.0823
0.1187	0.0338	0.5646	0.0771	0.3915	0.0815
0.1166	0.0337	0.5544	0.0773	0.3774	0.0805
0.1144	0.0336	0.5443	0.0775	0.3632	0.0796
0.1123	0.0336	0.5342	0.0776	0.3491	0.0785
0.1101	0.0335	0.5241	0.0777	0.3349	0.0774
0.1080	0.0334	0.5139	0.0778	0.3208	0.0762
0.1059	0.0332	0.5038	0.0778	0.3066	0.0749
0.1037	0.0331	0.4937	0.0777	0.2925	0.0735
0.1016	0.0330	0.4835	0.0777	0.2783	0.0721
0.0995	0.0329	0.4734	0.0776	0.2642	0.0705
0.0973	0.0327	0.4633	0.0774	0.2500	0.0689
0.0952	0.0326	0.4532	0.0773	0.2472	0.0686
0.0931	0.0324	0.4430	0.0770	0.2370	0.0674
0.0909	0.0323	0.4329	0.0768	0.2269	0.0661
0.0888	0.0321	0.4228	0.0765	0.2168	0.0648
0.0867	0.0319	0.4127	0.0762	0.2066	0.0634
0.0845	0.0317	0.4025	0.0758	0.1965	0.0620
0.0824	0.0315	0.3924	0.0754	0.1864	0.0606
0.0803	0.0313	0.3823	0.0750	0.1763	0.0590
0.0782	0.0311	0.3722	0.0745	0.1662	0.0574
0.0760	0.0308	0.3620	0.0740	0.1561	0.0558
0.0739	0.0306	0.3519	0.0734	0.1460	0.0541
0.0718	0.0303	0.3418	0.0728	0.1360	0.0523
0.0697	0.0300	0.3316	0.0722	0.1259	0.0504
0.0676	0.0298	0.3215	0.0715	0.1159	0.0485

TABLE E.2.—COORDINATES FOR 2D FULL-SCALE AIRFOILS  
FOR INBOARD, MIDSPAN, AND OUTBOARD STATIONS

Inboard full scale		Midspan full scale		Outboard full scale	
x	y	x	y	x	y
0.0654	0.0295	0.3114	0.0707	0.1058	0.0464
0.0633	0.0292	0.3013	0.0700	0.0958	0.0442
0.0612	0.0288	0.2911	0.0692	0.0859	0.0420
0.0591	0.0285	0.2810	0.0683	0.0759	0.0396
0.0570	0.0282	0.2709	0.0674	0.0660	0.0370
0.0549	0.0278	0.2608	0.0665	0.0562	0.0342
0.0528	0.0274	0.2506	0.0655	0.0481	0.0318
0.0507	0.0270	0.2405	0.0644	0.0462	0.0312
0.0486	0.0266	0.2304	0.0634	0.0442	0.0305
0.0465	0.0262	0.2203	0.0622	0.0423	0.0299
0.0444	0.0257	0.2101	0.0611	0.0404	0.0292
0.0423	0.0253	0.2000	0.0598	0.0385	0.0286
0.0402	0.0248	0.2002	0.0598	0.0365	0.0279
0.0381	0.0243	0.1901	0.0586	0.0346	0.0272
0.0360	0.0237	0.1799	0.0573	0.0327	0.0265
0.0339	0.0232	0.1699	0.0559	0.0308	0.0257
0.0318	0.0226	0.1598	0.0544	0.0289	0.0250
0.0297	0.0220	0.1497	0.0530	0.0270	0.0242
0.0277	0.0213	0.1396	0.0514	0.0252	0.0234
0.0256	0.0206	0.1296	0.0497	0.0233	0.0225
0.0236	0.0199	0.1195	0.0480	0.0215	0.0217
0.0216	0.0192	0.1095	0.0462	0.0196	0.0208
0.0196	0.0184	0.0995	0.0443	0.0178	0.0198
0.0176	0.0175	0.0895	0.0423	0.0160	0.0189
0.0157	0.0166	0.0795	0.0401	0.0143	0.0178
0.0137	0.0157	0.0696	0.0378	0.0126	0.0168
0.0118	0.0146	0.0597	0.0353	0.0109	0.0157
0.0100	0.0135	0.0498	0.0326	0.0092	0.0145
0.0082	0.0123	0.0401	0.0296	0.0076	0.0132
0.0064	0.0109	0.0305	0.0262	0.0060	0.0118
0.0048	0.0095	0.0279	0.0248	0.0046	0.0104
0.0033	0.0079	0.0196	0.0211	0.0033	0.0088
0.0020	0.0061	0.0136	0.0178	0.0021	0.0071
0.0010	0.0042	0.0089	0.0148	0.0011	0.0053
0.0003	0.0022	0.0054	0.0118	0.0004	0.0034
0.0000	0.0000	0.0029	0.0089	0.0000	0.0013
0.0002	-0.0022	0.0013	0.0062	0.0000	0.0000
0.0009	-0.0043	0.0004	0.0037	0.0001	-0.0007
0.0020	-0.0062	0.0000	0.0000	0.0005	-0.0027
0.0034	-0.0079	0.0002	-0.0010	0.0014	-0.0046
0.0049	-0.0095	0.0010	-0.0032	0.0026	-0.0063
0.0065	-0.0110	0.0024	-0.0055	0.0040	-0.0078
0.0082	-0.0124	0.0045	-0.0079	0.0056	-0.0091
0.0099	-0.0137	0.0075	-0.0103	0.0072	-0.0103

TABLE E.2.—COORDINATES FOR 2D FULL-SCALE AIRFOILS  
FOR INBOARD, MIDSPAN, AND OUTBOARD STATIONS

Inboard full scale		Midspan full scale		Outboard full scale	
x	y	x	y	x	y
0.0117	-0.0150	0.0115	-0.0126	0.0090	-0.0113
0.0135	-0.0162	0.0170	-0.0149	0.0108	-0.0123
0.0154	-0.0174	0.0245	-0.0174	0.0126	-0.0132
0.0172	-0.0185	0.0348	-0.0201	0.0145	-0.0140
0.0191	-0.0196	0.0483	-0.0229	0.0164	-0.0148
0.0210	-0.0207	0.0648	-0.0257	0.0183	-0.0155
0.0229	-0.0218	0.0832	-0.0282	0.0202	-0.0161
0.0248	-0.0228	0.1000	-0.0301	0.0222	-0.0167
0.0268	-0.0239	0.1133	-0.0316	0.0242	-0.0173
0.0287	-0.0249	0.1236	-0.0326	0.0261	-0.0179
0.0307	-0.0259	0.1338	-0.0335	0.0281	-0.0184
0.0326	-0.0269	0.1440	-0.0344	0.0301	-0.0189
0.0346	-0.0278	0.1542	-0.0351	0.0321	-0.0194
0.0366	-0.0288	0.1644	-0.0358	0.0341	-0.0198
0.0385	-0.0297	0.1747	-0.0365	0.0361	-0.0202
0.0405	-0.0307	0.1849	-0.0371	0.0381	-0.0207
0.0425	-0.0316	0.1951	-0.0376	0.0401	-0.0211
0.0445	-0.0325	0.2054	-0.0381	0.0421	-0.0214
0.0465	-0.0334	0.2156	-0.0386	0.0441	-0.0218
0.0485	-0.0343	0.2259	-0.0390	0.0461	-0.0222
0.0505	-0.0352	0.2361	-0.0393	0.0481	-0.0225
0.0525	-0.0361	0.2464	-0.0396	0.0501	-0.0229
0.0545	-0.0370	0.2567	-0.0399	0.0564	-0.0239
0.0565	-0.0379	0.2669	-0.0401	0.0665	-0.0253
0.0585	-0.0387	0.2772	-0.0402	0.0767	-0.0266
0.0605	-0.0396	0.2874	-0.0403	0.0868	-0.0277
0.0625	-0.0404	0.2977	-0.0404	0.0970	-0.0288
0.0646	-0.0413	0.3079	-0.0404	0.1072	-0.0297
0.0666	-0.0421	0.3181	-0.0404	0.1174	-0.0305
0.0686	-0.0429	0.3284	-0.0403	0.1276	-0.0313
0.0707	-0.0437	0.3386	-0.0402	0.1378	-0.0319
0.0727	-0.0445	0.3489	-0.0400	0.1480	-0.0325
0.0747	-0.0454	0.3591	-0.0398	0.1582	-0.0330
0.0768	-0.0462	0.3693	-0.0395	0.1684	-0.0335
0.0788	-0.0469	0.3795	-0.0392	0.1786	-0.0339
0.0809	-0.0477	0.3898	-0.0388	0.1888	-0.0342
0.0829	-0.0485	0.4000	-0.0384	0.1990	-0.0345
0.0849	-0.0493	0.4102	-0.0379	0.2092	-0.0347
0.0870	-0.0501	0.4204	-0.0374	0.2194	-0.0348
0.0890	-0.0508	0.4306	-0.0368	0.2296	-0.0349
0.0911	-0.0516	0.4409	-0.0362	0.2398	-0.0350
0.0932	-0.0523	0.4511	-0.0355	0.2500	-0.0350
0.0952	-0.0531	0.4613	-0.0348	0.2500	-0.0350
0.0973	-0.0538	0.4715	-0.0340	0.2642	-0.0348



TABLE E.2.—COORDINATES FOR 2D FULL-SCALE AIRFOILS  
FOR INBOARD, MIDSPAN, AND OUTBOARD STATIONS

Inboard full scale		Midspan full scale		Outboard full scale	
x	y	x	y	x	y
0.0993	-0.0546	0.4817	-0.0332	0.2783	-0.0347
0.1014	-0.0553	0.4919	-0.0323	0.2925	-0.0344
0.1035	-0.0561	0.5021	-0.0314	0.3066	-0.0340
0.1055	-0.0568	0.5123	-0.0304	0.3208	-0.0335
0.1076	-0.0575	0.5225	-0.0294	0.3349	-0.0330
0.1097	-0.0582	0.5326	-0.0283	0.3491	-0.0323
0.1117	-0.0589	0.5428	-0.0271	0.3632	-0.0316
0.1138	-0.0596	0.5530	-0.0259	0.3774	-0.0308
0.1159	-0.0603	0.5632	-0.0247	0.3915	-0.0299
0.1180	-0.0610	0.5734	-0.0234	0.4057	-0.0289
0.1200	-0.0617	0.5835	-0.0220	0.4198	-0.0278
0.1221	-0.0624	0.5937	-0.0206	0.4340	-0.0267
0.1242	-0.0631	0.6039	-0.0192	0.4481	-0.0254
0.1263	-0.0638	0.6140	-0.0177	0.4623	-0.0241
0.1284	-0.0645	0.6242	-0.0161	0.4764	-0.0226
0.1304	-0.0652	0.6343	-0.0146	0.4906	-0.0211
0.1325	-0.0658	0.6444	-0.0129	0.5047	-0.0195
0.1346	-0.0665	0.6546	-0.0113	0.5189	-0.0178
0.1367	-0.0672	0.6647	-0.0096	0.5330	-0.0160
0.1388	-0.0678	0.6748	-0.0079	0.5472	-0.0141
0.1409	-0.0685	0.6849	-0.0061	0.5613	-0.0122
0.1430	-0.0691	0.6950	-0.0044	0.5755	-0.0101
0.1451	-0.0698	0.7052	-0.0026	0.5896	-0.0080
0.1471	-0.0704	0.7153	-0.0008	0.6038	-0.0057
0.1500	-0.0713	0.7254	0.0010	0.6179	-0.0034
0.1815	-0.0804	0.7355	0.0028	0.6321	-0.0010
0.2130	-0.0884	0.7456	0.0046	0.6462	0.0015
0.2444	-0.0955	0.7557	0.0063	0.6604	0.0040
0.2759	-0.1017	0.7658	0.0081	0.6745	0.0067
0.3074	-0.1072	0.7759	0.0098	0.6887	0.0093
0.3389	-0.1121	0.7860	0.0115	0.7028	0.0120
0.3704	-0.1164	0.7961	0.0132	0.7170	0.0147
0.4019	-0.1203	0.8063	0.0148	0.7311	0.0175
0.4333	-0.1245	0.8164	0.0164	0.7453	0.0202
0.4648	-0.1285	0.8265	0.0179	0.7594	0.0229
0.4963	-0.1310	0.8367	0.0194	0.7736	0.0256
0.5278	-0.1329	0.8468	0.0208	0.7877	0.0283
0.5593	-0.1352	0.8570	0.0220	0.8019	0.0308
0.5907	-0.1375	0.8672	0.0232	0.8160	0.0333
0.6222	-0.1400	0.8773	0.0242	0.8302	0.0357
0.6537	-0.1423	0.8875	0.0251	0.8443	0.0380
0.6852	-0.1448	0.8977	0.0259	0.8585	0.0401
0.7167	-0.1470	0.9080	0.0265	0.8726	0.0420
0.7481	-0.1491	0.9182	0.0268	0.8868	0.0436

TABLE E.2.—COORDINATES FOR 2D FULL-SCALE AIRFOILS FOR INBOARD, MIDSPAN, AND OUTBOARD STATIONS

Inboard full scale		Midspan full scale		Outboard full scale	
x	y	x	y	x	y
0.7796	-0.1510	0.9285	0.0270	0.9009	0.0450
0.8111	-0.1527	0.9388	0.0269	0.9151	0.0460
0.8426	-0.1543	0.9491	0.0265	0.9292	0.0465
0.8741	-0.1561	0.9594	0.0258	0.9434	0.0465
0.9056	-0.1577	0.9697	0.0248	0.9575	0.0460
0.9370	-0.1592	0.9799	0.0233	0.9717	0.0446
0.9685	-0.1607	0.9900	0.0213	0.9858	0.0422
1.0000	-0.1620	1.0000	0.0184	0.9993	0.0386

TABLE E.3.—COORDINATES FOR INBOARD, MIDSPAN, AND OUTBOARD HYBRID MODEL SECTIONS WITH FLAPS

Inboard hybrid				Midspan hybrid				Outboard hybrid			
Main element		Flap		Main element		Flap		Main element		Flap	
x	y	x	y	x	y	x	y	x	y	x	y
0.3294	0.0152	0.4327	-0.0042	0.3696	0.0362	0.4855	0.0144	0.4920	0.0494	0.6461	0.0205
0.3261	0.0161	0.4323	-0.0041	0.3658	0.0365	0.4850	0.0145	0.4870	0.0501	0.6457	0.0206
0.3227	0.0169	0.4313	-0.0038	0.3619	0.0369	0.4838	0.0148	0.4820	0.0508	0.6441	0.0210
0.3193	0.0177	0.4296	-0.0033	0.3581	0.0372	0.4819	0.0154	0.4769	0.0515	0.6416	0.0218
0.3160	0.0184	0.4272	-0.0026	0.3542	0.0375	0.4793	0.0162	0.4719	0.0522	0.6380	0.0228
0.3126	0.0191	0.4242	-0.0017	0.3504	0.0378	0.4759	0.0172	0.4669	0.0528	0.6335	0.0242
0.3092	0.0198	0.4206	-0.0006	0.3465	0.0381	0.4718	0.0184	0.4619	0.0533	0.6281	0.0258
0.3058	0.0204	0.4163	0.0006	0.3427	0.0384	0.4671	0.0198	0.4568	0.0538	0.6218	0.0276
0.3024	0.0209	0.4116	0.0019	0.3388	0.0387	0.4618	0.0212	0.4467	0.0546	0.6147	0.0295
0.2990	0.0215	0.4064	0.0032	0.3349	0.0390	0.4559	0.0227	0.4416	0.0549	0.6069	0.0315
0.2955	0.0220	0.4007	0.0045	0.3311	0.0392	0.4495	0.0242	0.4366	0.0551	0.5984	0.0335
0.2921	0.0225	0.3947	0.0058	0.3272	0.0395	0.4428	0.0256	0.4315	0.0553	0.5894	0.0354
0.2886	0.0229	0.3883	0.0070	0.3234	0.0397	0.4356	0.0269	0.4265	0.0556	0.5799	0.0372
0.2852	0.0234	0.3817	0.0081	0.3195	0.0400	0.4282	0.0281	0.4214	0.0559	0.5700	0.0388
0.2817	0.0238	0.3749	0.0090	0.3156	0.0402	0.4206	0.0292	0.4163	0.0562	0.5599	0.0402
0.2783	0.0242	0.3680	0.0098	0.3118	0.0404	0.4129	0.0300	0.4113	0.0565	0.5497	0.0413
0.2749	0.0246	0.3612	0.0103	0.3079	0.0406	0.4052	0.0306	0.4062	0.0568	0.5394	0.0421
0.2715	0.0249	0.3543	0.0107	0.3040	0.0409	0.3975	0.0310	0.4011	0.0571	0.5292	0.0426
0.2680	0.0253	0.3475	0.0107	0.3002	0.0411	0.3899	0.0311	0.3960	0.0574	0.5189	0.0427
0.2646	0.0257	0.3408	0.0104	0.2963	0.0413	0.3824	0.0307	0.3910	0.0577	0.5090	0.0422
0.2611	0.0260	0.3345	0.0097	0.2924	0.0415	0.3754	0.0299	0.3859	0.0580	0.4996	0.0412
0.2577	0.0264	0.3286	0.0087	0.2886	0.0417	0.3688	0.0288	0.3808	0.0583	0.4908	0.0397
0.2542	0.0267	0.3260	0.0076	0.2847	0.0419	0.3658	0.0276	0.3757	0.0586	0.4868	0.0381
0.2508	0.0270	0.3238	0.0052	0.2809	0.0421	0.3633	0.0249	0.3707	0.0590	0.4835	0.0344
0.2473	0.0274	0.3228	0.0020	0.2770	0.0424	0.3623	0.0213	0.3656	0.0593	0.4822	0.0297
0.2439	0.0277	0.3234	-0.0012	0.2731	0.0426	0.3629	0.0177	0.3605	0.0596	0.4829	0.0249
0.2404	0.0280	0.3253	-0.0039	0.2693	0.0428	0.3650	0.0147	0.3554	0.0599	0.4858	0.0209
0.2370	0.0283	0.3281	-0.0055	0.2654	0.0430	0.3682	0.0129	0.3503	0.0602	0.4900	0.0184
0.2336	0.0286	0.3314	-0.0057	0.2615	0.0432	0.3719	0.0126	0.3452	0.0605	0.4950	0.0181
0.2301	0.0289	0.3363	-0.0056	0.2577	0.0434	0.3773	0.0128	0.3402	0.0608	0.5022	0.0183

TABLE E.3.—COORDINATES FOR INBOARD, MIDSPAN, AND  
OUTBOARD HYBRID MODEL SECTIONS WITH FLAPS

Inboard hybrid				Midspan hybrid				Outboard hybrid			
Main element		Flap		Main element		Flap		Main element		Flap	
x	y	x	y	x	y	x	y	x	y	x	y
0.2267	0.0291	0.3421	-0.0052	0.2538	0.0436	0.3838	0.0133	0.3351	0.0611	0.5108	0.0190
0.2233	0.0294	0.3481	-0.0047	0.2499	0.0438	0.3906	0.0138	0.3300	0.0613	0.5199	0.0196
0.2198	0.0297	0.3544	-0.0044	0.2461	0.0440	0.3976	0.0141	0.3249	0.0616	0.5292	0.0201
0.2164	0.0299	0.3609	-0.0042	0.2422	0.0441	0.4050	0.0144	0.3198	0.0618	0.5390	0.0205
0.2129	0.0302	0.3676	-0.0040	0.2384	0.0443	0.4124	0.0146	0.3147	0.0621	0.5490	0.0208
0.2095	0.0304	0.3743	-0.0038	0.2345	0.0445	0.4199	0.0148	0.3096	0.0623	0.5590	0.0211
0.2060	0.0307	0.3809	-0.0036	0.2306	0.0447	0.4273	0.0150	0.3046	0.0625	0.5688	0.0213
0.2026	0.0309	0.3874	-0.0036	0.2268	0.0448	0.4346	0.0151	0.2995	0.0627	0.5786	0.0214
0.1991	0.0311	0.3937	-0.0036	0.2229	0.0450	0.4417	0.0151	0.2944	0.0628	0.5880	0.0214
0.1957	0.0313	0.3998	-0.0036	0.2190	0.0451	0.4485	0.0150	0.2893	0.0630	0.5970	0.0213
0.1922	0.0315	0.4055	-0.0037	0.2152	0.0453	0.4549	0.0149	0.2842	0.0631	0.6055	0.0212
0.1887	0.0317	0.4108	-0.0038	0.2113	0.0454	0.4608	0.0148	0.2792	0.0632	0.6135	0.0210
0.1853	0.0319	0.4156	-0.0040	0.2074	0.0456	0.4663	0.0146	0.2741	0.0633	0.6207	0.0207
0.1818	0.0320	0.4200	-0.0042	0.2035	0.0457	0.4711	0.0144	0.2690	0.0634	0.6272	0.0205
0.1783	0.0322	0.4237	-0.0043	0.1997	0.0458	0.4754	0.0142	0.2639	0.0634	0.6328	0.0202
0.1749	0.0323	0.4269	-0.0045	0.1958	0.0459	0.4789	0.0140	0.2589	0.0634	0.6375	0.0200
0.1714	0.0324	0.4293	-0.0046	0.1919	0.0460	0.4817	0.0139	0.2538	0.0634	0.6412	0.0198
0.1679	0.0325	0.4311	-0.0047	0.1881	0.0461	0.4837	0.0138	0.2487	0.0633	0.6439	0.0196
0.1645	0.0325	0.4322	-0.0048	0.1842	0.0462	0.4849	0.0137	0.2437	0.0633	0.6455	0.0195
0.1610	0.0326	0.4326	-0.0048	0.1803	0.0463	0.4854	0.0137	0.2386	0.0632	0.6461	0.0195
0.1575	0.0326			0.1765	0.0463			0.2335	0.0630		
0.1540	0.0327			0.1726	0.0463			0.2285	0.0628		
0.1506	0.0327			0.1687	0.0463			0.2234	0.0626		
0.1471	0.0327			0.1649	0.0463			0.2184	0.0624		
0.1436	0.0327			0.1610	0.0462			0.2133	0.0621		
0.1401	0.0326			0.1571	0.0462			0.2083	0.0618		
0.1367	0.0326			0.1533	0.0462			0.2032	0.0614		
0.1332	0.0325			0.1494	0.0461			0.1982	0.0610		
0.1297	0.0325			0.1455	0.0461			0.1931	0.0606		
0.1263	0.0324			0.1416	0.0461			0.1881	0.0601		
0.1228	0.0323			0.1378	0.0461			0.1831	0.0596		
0.1193	0.0321			0.1339	0.0462			0.1781	0.0590		
0.1159	0.0320			0.1300	0.0461			0.1730	0.0584		
0.1124	0.0319			0.1261	0.0461			0.1680	0.0577		
0.1089	0.0317			0.1222	0.0460			0.1630	0.0570		
0.1055	0.0315			0.1184	0.0459			0.1580	0.0562		
0.1020	0.0313			0.1145	0.0457			0.1530	0.0554		
0.0986	0.0311			0.1106	0.0455			0.1480	0.0546		
0.0951	0.0309			0.1068	0.0452			0.1430	0.0537		
0.0917	0.0307			0.1029	0.0448			0.1380	0.0528		
0.0882	0.0304			0.0991	0.0442			0.1330	0.0518		
0.0848	0.0302			0.0953	0.0436			0.1281	0.0509		
0.0813	0.0299			0.0915	0.0429			0.1231	0.0499		
0.0779	0.0296			0.0877	0.0422			0.1181	0.0489		
0.0745	0.0293			0.0839	0.0413			0.1131	0.0479		

TABLE E.3.—COORDINATES FOR INBOARD, MIDSPAN, AND  
OUTBOARD HYBRID MODEL SECTIONS WITH FLAPS

Inboard hybrid				Midspan hybrid				Outboard hybrid			
Main element		Flap		Main element		Flap		Main element		Flap	
x	y	x	y	x	y	x	y	x	y	x	y
0.0710	0.0290			0.0802	0.0404			0.1082	0.0469		
0.0676	0.0287			0.0764	0.0395			0.1032	0.0458		
0.0642	0.0283			0.0726	0.0386			0.0983	0.0448		
0.0607	0.0280			0.0689	0.0376			0.0933	0.0437		
0.0573	0.0276			0.0651	0.0367			0.0884	0.0426		
0.0539	0.0272			0.0614	0.0357			0.0834	0.0414		
0.0505	0.0267			0.0576	0.0348			0.0785	0.0402		
0.0471	0.0262			0.0539	0.0337			0.0736	0.0390		
0.0437	0.0257			0.0502	0.0327			0.0687	0.0377		
0.0403	0.0250			0.0465	0.0316			0.0638	0.0364		
0.0369	0.0242			0.0428	0.0304			0.0589	0.0350		
0.0323	0.0229			0.0391	0.0291			0.0541	0.0336		
0.0290	0.0219			0.0355	0.0278			0.0492	0.0321		
0.0257	0.0209			0.0319	0.0264			0.0444	0.0306		
0.0224	0.0198			0.0283	0.0250			0.0396	0.0290		
0.0192	0.0186			0.0247	0.0235			0.0348	0.0273		
0.0161	0.0172			0.0212	0.0218			0.0301	0.0254		
0.0131	0.0156			0.0177	0.0201			0.0254	0.0235		
0.0101	0.0139			0.0143	0.0183			0.0208	0.0213		
0.0073	0.0119			0.0110	0.0162			0.0163	0.0190		
0.0048	0.0096			0.0079	0.0140			0.0120	0.0164		
0.0025	0.0071			0.0050	0.0114			0.0079	0.0134		
0.0008	0.0041			0.0025	0.0084			0.0042	0.0099		
0.0000	0.0000			0.0008	0.0050			0.0013	0.0058		
0.0003	-0.0027			0.0000	0.0000			0.0000	0.0009		
0.0014	-0.0059			0.0008	-0.0026			0.0010	-0.0040		
0.0033	-0.0088			0.0027	-0.0060			0.0042	-0.0080		
0.0055	-0.0113			0.0054	-0.0088			0.0083	-0.0109		
0.0081	-0.0136			0.0086	-0.0110			0.0127	-0.0133		
0.0109	-0.0156			0.0120	-0.0128			0.0175	-0.0152		
0.0137	-0.0175			0.0156	-0.0143			0.0223	-0.0168		
0.0167	-0.0192			0.0192	-0.0157			0.0271	-0.0181		
0.0197	-0.0208			0.0229	-0.0169			0.0321	-0.0194		
0.0223	-0.0221			0.0266	-0.0180			0.0370	-0.0204		
0.0255	-0.0236			0.0304	-0.0190			0.0420	-0.0214		
0.0286	-0.0251			0.0341	-0.0199			0.0470	-0.0223		
0.0318	-0.0265			0.0379	-0.0208			0.0520	-0.0232		
0.0350	-0.0279			0.0417	-0.0216			0.0570	-0.0240		
0.0382	-0.0293			0.0455	-0.0224			0.0620	-0.0247		
0.0414	-0.0306			0.0493	-0.0231			0.0670	-0.0254		
0.0446	-0.0318			0.0531	-0.0238			0.0720	-0.0260		
0.0479	-0.0329			0.0569	-0.0245			0.0771	-0.0266		
0.0513	-0.0338			0.0607	-0.0251			0.0821	-0.0272		
0.0547	-0.0345			0.0645	-0.0257			0.0871	-0.0278		
0.0582	-0.0350			0.0683	-0.0263			0.0922	-0.0283		

TABLE E.3.—COORDINATES FOR INBOARD, MIDSPAN, AND  
OUTBOARD HYBRID MODEL SECTIONS WITH FLAPS

Inboard hybrid				Midspan hybrid				Outboard hybrid			
Main element		Flap		Main element		Flap		Main element		Flap	
x	y	x	y	x	y	x	y	x	y	x	y
0.0616	-0.0353			0.0722	-0.0268			0.0972	-0.0288		
0.0651	-0.0354			0.0760	-0.0273			0.1022	-0.0293		
0.0685	-0.0354			0.0799	-0.0278			0.1073	-0.0297		
0.0720	-0.0352			0.0837	-0.0283			0.1124	-0.0301		
0.0754	-0.0349			0.0876	-0.0287			0.1174	-0.0305		
0.0789	-0.0344			0.0914	-0.0290			0.1225	-0.0309		
0.0823	-0.0339			0.0953	-0.0293			0.1275	-0.0313		
0.0858	-0.0333			0.0992	-0.0296			0.1326	-0.0316		
0.0892	-0.0327			0.1031	-0.0297			0.1376	-0.0319		
0.0926	-0.0320			0.1070	-0.0297			0.1427	-0.0323		
0.0960	-0.0314			0.1108	-0.0296			0.1477	-0.0325		
0.0995	-0.0307			0.1147	-0.0294			0.1528	-0.0326		
0.1029	-0.0301			0.1185	-0.0290			0.1579	-0.0326		
0.1063	-0.0293			0.1223	-0.0284			0.1629	-0.0323		
0.1097	-0.0286			0.1261	-0.0278			0.1680	-0.0320		
0.1130	-0.0278			0.1299	-0.0270			0.1731	-0.0315		
0.1164	-0.0270			0.1337	-0.0262			0.1781	-0.0309		
0.1197	-0.0262			0.1375	-0.0252			0.1831	-0.0301		
0.1231	-0.0253			0.1412	-0.0243			0.1881	-0.0292		
0.1264	-0.0245			0.1450	-0.0233			0.1931	-0.0283		
0.1297	-0.0236			0.1487	-0.0222			0.1981	-0.0272		
0.1331	-0.0227			0.1525	-0.0212			0.2031	-0.0261		
0.1364	-0.0218			0.1562	-0.0201			0.2081	-0.0248		
0.1397	-0.0209			0.1599	-0.0191			0.2130	-0.0235		
0.1431	-0.0200			0.1637	-0.0181			0.2179	-0.0222		
0.1464	-0.0190			0.1674	-0.0170			0.2228	-0.0208		
0.1497	-0.0181			0.1711	-0.0159			0.2277	-0.0193		
0.1531	-0.0172			0.1748	-0.0149			0.2325	-0.0178		
0.1564	-0.0162			0.1785	-0.0138			0.2373	-0.0163		
0.1597	-0.0153			0.1822	-0.0127			0.2422	-0.0147		
0.1631	-0.0143			0.1859	-0.0116			0.2470	-0.0131		
0.1664	-0.0134			0.1896	-0.0104			0.2518	-0.0115		
0.1697	-0.0124			0.1933	-0.0093			0.2566	-0.0099		
0.1731	-0.0115			0.1970	-0.0082			0.2614	-0.0083		
0.1764	-0.0105			0.2007	-0.0070			0.2662	-0.0067		
0.1798	-0.0096			0.2044	-0.0058			0.2710	-0.0051		
0.1831	-0.0087			0.2081	-0.0047			0.2758	-0.0035		
0.1864	-0.0077			0.2118	-0.0035			0.2806	-0.0019		
0.1898	-0.0068			0.2155	-0.0023			0.2854	-0.0004		
0.1931	-0.0059			0.2192	-0.0011			0.2902	0.0012		
0.1964	-0.0050			0.2228	0.0000			0.2951	0.0028		
0.1998	-0.0041			0.2265	0.0012			0.2999	0.0043		
0.2031	-0.0032			0.2302	0.0024			0.3047	0.0058		
0.2065	-0.0023			0.2339	0.0035			0.3095	0.0074		
0.2098	-0.0015			0.2376	0.0047			0.3144	0.0089		

TABLE E.3.—COORDINATES FOR INBOARD, MIDSPAN, AND  
OUTBOARD HYBRID MODEL SECTIONS WITH FLAPS

Inboard hybrid		Midspan hybrid				Outboard hybrid					
Main element		Flap		Main element		Flap		Main element		Flap	
x	y	x	y	x	y	x	y	x	y	x	y
0.2132	-0.0006			0.2413	0.0058			0.3192	0.0104		
0.2165	0.0002			0.2450	0.0069			0.3289	0.0135		
0.2199	0.0010			0.2487	0.0081			0.3337	0.0150		
0.2233	0.0018			0.2524	0.0092			0.3385	0.0165		
0.2266	0.0026			0.2561	0.0103			0.3434	0.0180		
0.2300	0.0034			0.2598	0.0114			0.3482	0.0195		
0.2334	0.0042			0.2635	0.0125			0.3531	0.0209		
0.2368	0.0049			0.2673	0.0136			0.3580	0.0223		
0.2402	0.0056			0.2710	0.0147			0.3628	0.0237		
0.2435	0.0064			0.2747	0.0157			0.3677	0.0251		
0.2469	0.0070			0.2784	0.0168			0.3726	0.0265		
0.2503	0.0077			0.2822	0.0178			0.3775	0.0279		
0.2537	0.0084			0.2859	0.0188			0.3824	0.0292		
0.2571	0.0090			0.2896	0.0198			0.3873	0.0305		
0.2605	0.0096			0.2934	0.0208			0.3922	0.0317		
0.2639	0.0101			0.2971	0.0217			0.3971	0.0330		
0.2673	0.0107			0.3009	0.0227			0.4020	0.0342		
0.2707	0.0112			0.3046	0.0236			0.4069	0.0353		
0.2741	0.0117			0.3084	0.0245			0.4119	0.0365		
0.2775	0.0122			0.3122	0.0254			0.4168	0.0376		
0.2810	0.0126			0.3159	0.0263			0.4218	0.0387		
0.2844	0.0130			0.3197	0.0271			0.4267	0.0397		
0.2878	0.0134			0.3235	0.0279			0.4317	0.0407		
0.2913	0.0138			0.3273	0.0287			0.4367	0.0416		
0.2948	0.0141			0.3311	0.0295			0.4417	0.0426		
0.2983	0.0144			0.3349	0.0302			0.4467	0.0434		
0.3018	0.0146			0.3387	0.0309			0.4516	0.0442		
0.3052	0.0148			0.3425	0.0316			0.4566	0.0450		
0.3087	0.0149			0.3463	0.0322			0.4617	0.0457		
0.3121	0.0151			0.3501	0.0328			0.4667	0.0464		
0.3155	0.0151			0.3539	0.0334			0.4717	0.0470		
0.3190	0.0151			0.3578	0.0340			0.4768	0.0475		
0.3225	0.0151			0.3616	0.0345			0.4818	0.0480		
0.3259	0.0150			0.3654	0.0351			0.4869	0.0483		
0.3294	0.0148			0.3693	0.0355			0.4919	0.0486		

TABLE E.4.—FLAP PIVOT POINTS FOR INBOARD,  
MIDSPAN, AND OUTBOARD MODELS

Inboard hybrid		Midspan hybrid		Outboard hybrid	
Flap pivot		Flap pivot		Flap pivot	
x	y	x	y	x	y
0.33108	0.00147	0.3715	0.02073	0.49445	0.02886

## References

1. Broeren, Andy P., et al.: Swept-Wing Ice Accretion Characterization and Aerodynamics. AIAA Paper 2013–2824 (NASA/TM—2013-216555), 2013. <http://ntrs.nasa.gov>
2. Saeed, Farooq; Selig, Michael S.; and Bragg, Michael B.: Hybrid Airfoil Design Method To Simulate Full-Scale Ice Accretion Throughout a Given  $\alpha$  Range. *J. Aircraft*, vol. 35, no. 2, 1998, pp. 233–239.
3. Saeed, Farooq; Selig, Michael S.; and Bragg, Michael B.: Design of Subscale Airfoils With Full-Scale Leading Edges for Ice Accretion Testing. *J. Aircraft*, vol. 34, no. 1, 1997, pp. 94–100.
4. Saeed, Farooq; Selig, Michael S.; and Bragg, Michael B.: Hybrid Airfoil Design Procedure Validation for Full-Scale Ice Accretion Simulation. *J. Aircraft*, vol. 36, no. 5, 1999, pp. 769–776.
5. Vassberg, J.C., et al.: Development of a Common Research Model for Applied CFD Validation Studies. AIAA–2008–6919, 2008.
6. Sclafani, A.J., et al.: Drag Prediction for the Common Research Model Using CFL3D and OVERFLOW. *J. Aircraft*, vol. 51, no. 4, 2014, pp. 1101–1117.
7. Coder, J.G.: OVERFLOW Analysis of the DLR–F11 High-Lift Configuration Including Transition Modeling. *J. Aircraft*, vol. 1, no. 16, 2015.
8. Robinson, B.; Verhoff, A.; and LaBozzetta, W.: Preliminary Findings in Certification of OVERFLOW. Fluid Dynamics Conference, Fluid Dynamics Conference, Colorado Springs, CO, 1994, p. 2238.
9. Rivers, Melissa B.; and Dittberner, Ashley: Experimental Investigations of the NASA Common Research Model. AIAA Paper 2010–4218, 2010.
10. Federal Aviation Administration: Continuous Maximum Icing. U.S. Code of Federal Regulations, Title 14, Part 25, Appendix C, 2002.
11. Fujiwara, G.E.C.: Design of 3D Swept Wing Hybrid Models for Icing Wind Tunnel Tests. M.S. Thesis, Univ. of Illinois, 2014.
12. Bidwell, C.S.; and Potapczuk, M.G.: Users Manual for the NASA Lewis Three-Dimensional Ice Accretion Code (LEWICE3D). NASA TM–105974, 1993. <http://ntrs.nasa.gov>
13. Wiberg, B.D.: Large-Scale, Swept-Wing Ice Accretion Modeling in the NASA Glenn Icing Research Tunnel Using LEWICE3D. M.S. Thesis, Univ. of Illinois, 2013.
14. NASA: THICK. Ice Shape Analysis Code, Cleveland, OH.
15. McLean, D.J.: Understanding Aerodynamics: Arguing From the Real Physics. First ed., John Wiley & Sons Ltd., New York, NY, Ch. 8, 2012, pp. 444–449.
16. Fujiwara, G.E.C., et al.: Hybrid Airfoil Design Method for Icing Wind Tunnel Tests. AIAA Paper 2013–2826, 2013.
17. Selig, M.S.: PROFOIL—A Multipoint Inverse Airfoil Design Method. Version 2.0, University of Illinois at Urbana—Champaign, Urbana, Illinois, 1999.
18. Drela, M.; and Youngren, H.: XFOIL User Primer. Version 6.9, Aircraft, Inc., Boston, MA, 2001.
19. Bragg, M.B.: AIRDROP. Urbana, IL, 1990.
20. Selig, M.S.; and Mauhmer, M.D.: Multipoint Inverse Airfoil Design Method Based on Conformal Mapping. *AIAA J.*, vol. 30, no. 5, 1992, pp. 1162–1170.
21. ANSYS FLUENT 12.0 User’s Guide. ANSYS, Inc., 2009.
22. Bragg, M.B.; and Wells, Stephen L.: Effect of Wind-Tunnel Walls on Airfoil Droplet Impingement. *J. Aircraft*, vol. 31, no.1, 1994, pp. 175–180.
23. Wright, W.B.: User Manual for the NASA Glenn Ice Accretion Code LEWICE: Version 2.2.2. NASA/CR—2002-211793, 2002. <http://ntrs.nasa.gov>

24. Anderson, David N.: Manual of Scaling Methods. NASA/CR—2004-21287, 2004. <http://ntrs.nasa.gov>
25. Platt, Robert C.; and Abbott, Ira H.: Aerodynamic Characteristics of N.A.C.A. 23012 and 23021 Airfoils With 20-Percent-Chord External-Airfoil Flaps of N.A.C.A. 23012 Section. NACA Report No. 573, 1936, pp. 523–542. <http://ntrs.nasa.gov>
26. Wenzinger, Carl J.: Pressure Distribution Over an N.A.C.A. 23012 Airfoil With an N.A.C.A. 23012 External-Airfoil Flap. NACA Report No. 614, 1938, pp. 85–98. <http://ntrs.nasa.gov>
27. Wenzinger, Carl J.; and Harris, Thomas A.: Wind-Tunnel Investigation of an N.A.C.A. 23012 Airfoil With Various Arrangements of Slotted Flaps. NACA Report No. 664, 1939, pp. 423–453. <http://ntrs.nasa.gov>
28. Clark, Kevin, et al.: Air Flow and Liquid Water Concentration Simulations of the 2012 NASA Glenn Icing Research Tunnel. AIAA 2012–2936, 2012.
29. Ruff, G.A.: Quantitative Comparison of Ice Accretion Shapes. J. Aircraft, vol. 39, no. 2, 2002, pp. 418–426.
30. Bragg, Michael, et al.: Airfoil Ice-Accretion Aerodynamics Simulation. AIAA 2007–85, 2007.
31. Broeren, Andy P., et al.: Effect of High-Fidelity Ice-Accretion Simulations on Full-Scale Airfoil Performance. J. Aircraft, vol. 47, no. 1, 2010, pp. 240–254.
32. Bidwell, C.: NASA Glenn Research Center, Cleveland, OH, Personal communications to the authors, 2013.
33. Malone, A.: Boeing, Chicago, IL, Personal communications to the authors, 2013.
34. Diebold, Jeff D.; Broeren, Andy P.; and Bragg, Michael B.: Aerodynamic Classification of Swept-Wing Ice Accretion. AIAA–2013–2825 (NASA/TM—2013-216556), 2013. <http://ntrs.nasa.gov>
35. Broeren, Andy P.; Diebold, Jeff M.; and Bragg, Michael B.: Aerodynamic Classification of Swept-Wing Ice Accretion. NASA/TM—2013-216381 (DOT/FAA/TC–13/21), 2013. <http://ntrs.nasa.gov>
36. Vassberg, J.C., et al. Comparison of NTF Experimental Data With CFD predictions From the Third AIAA CFD Drag Prediction Workshop. AIAA Paper 2008–6918, 2008.
37. Vassberg, J.: Introduction: Drag Prediction Workshop. J. Aircraft, vol. 45, no. 3, 2008, pp. 737–737.
38. Vassberg, J., et al.: Summary of the Fourth AIAA CFD Drag Prediction Workshop. AIAA Paper 2010–4547, 2010.
39. Paul, B.: Boeing, Chicago, IL, Personal communications to the authors, 2013.
40. Fujiwara, Gustavo E.C., et al.: 3D Swept Hybrid Wing Design Methods for Icing Wind Tunnel Tests. AIAA 2014–2616, 2014.
41. Wiberg, Brock D., et al.: Large-Scale Swept-Wing Icing Simulations in the NASA Glenn Icing Research Tunnel Using LEWICE3D. AIAA 2014–2617, 2014.
42. Katz, Joseph; and Plotkin, Allen: Low-Speed Aerodynamics. Cambridge University Press, New York, 2001, pp. 331–360.
43. Papadakis, Michael, et al.: Water Impingement Experiments on a NACA 23012 Airfoil With Simulated Glaze Ice Shapes. AIAA 2004–0565, 2014.
44. Tsao, J.-C.; and Lee, S.: Evaluation of Icing Scaling on Swept NACA 0012 Airfoil Models. SAE Paper 2011–38–0081 (NASA/CR—2011-217419), 2012. <http://ntrs.nasa.gov>
46. Bidwell, Colin S.: Super Cooled Large Droplet Analysis of Several Geometries Using LEWICE3D Version 3. NASA/TM—2011-216945 (AIAA–2010–7675), 2010. <http://ntrs.nasa.gov>





